Hu Feng
Aofei Guo
Jun Zhao

Ultra-High Ductility Magnesium-Phosphate-Cement-Based Composites (UHDMC)

Springer

Ultra-High Ductility Magnesium-Phosphate-Cement-Based Composites (UHDMC)

Hu Feng · Aofei Guo · Jun Zhao

Ultra-High Ductility Magnesium-Phosphate-Cement-Based Composites (UHDMC)

Springer

Hu Feng
Zhengzhou University
Zhengzhou, China

Aofei Guo
Zhengzhou University
Zhengzhou, China

Jun Zhao
Zhengzhou University
Zhengzhou, China

ISBN 978-981-97-0951-9 ISBN 978-981-97-0952-6 (eBook)
https://doi.org/10.1007/978-981-97-0952-6

This Springer imprint is published by the registered company Springer Nature Singapore Pte Ltd.
The registered company address is: 152 Beach Road, #21-01/04 Gateway East, Singapore 189721, Singapore

Paper in this product is recyclable.

Foreword

As we chart our journey into the relentless pursuit of material innovation, we find ourselves at the threshold of an exciting new venture. The focus of our endeavor revolves around Ultra-High Ductility Magnesium Phosphate Cement-Based Composites (UHDMC)—a promising thread in the fabric of materials science that pledges unmatched strength and toughness. The importance of this breakthrough cannot be overstated in a world increasingly compelled to create sustainable and resilient infrastructures.

Magazines, reviews, and scientific literature abound with research on common construction materials such as concrete. Nonetheless, it has significant carbon footprint and deteriorated performance under extreme cold conditions-cannot normally set and harden. This is where the UHDMC emerges as an undisputed solution, showing remarkable strength, toughness, and environmental friendliness.

Each chapter within this book underscores a vital element of UHDMC. From analyzing the foundational performance of UHDMC with polyvinyl alcohol fiber and hybrid fiber to providing keen insights into its water stability, the authors lay the groundwork for a deeper understanding of these robust materials. The authors' commitment to replacing one of the raw materials, magnesium oxide, with sustainable alternatives is demonstrated in discussions surrounding the development of UHDMC with fly ash and silica fume. This exploration underscores the remarkable adaptability and versatility of UHDMC—a testament to its tremendous potential. The text then turns our attention to the development of UHDMC with polyethylene fiber, yet another remarkable evolution in its composition. The combined versatility and resilience of this fiber-reinforced composite adds a layer of remarkable functionality rarely matched in the cementitious materials science space. Moreover, the authors explore the preparation and performance of sprayable UHDMC, demonstrating its adaptability in different construction techniques and potential for wide applications.

This book sets out to provide an informative guide, serving a variety of readers ranging from academia and research to industry professionals. The exploration within these pages will, hopefully, inspire further studies, expand practical applications, and contribute to the development of sustainable and versatile construction materials.

In writing this Foreword, I am struck by the significance of what's at stake and the potential of what we might achieve. It is my sincere hope that the information and perspectives gathered here serve not just as an enlightening collection of facts, but as a catalyst for further exploration, research, and development in this promising field.

Victor C. Li
James R. Rice Distinguished
University Professor of Engineering
University of Michigan
Ann Arbor, USA

Preface

The continuous evolution of construction materials over the years has culminated in the introduction of ultra-high ductility magnesium phosphate cement-based composites (UHDMC) that are rapidly shaping a new frontier in the world of infrastructure and civil engineering. Evidently, the technologically advanced properties exhibited by the UHDMC are gradually gaining recognition for their beneficial implications and potential use in a wide range of engineering projects.

In the insightful journey toward understanding composites, this book will substantially discuss the workability, mechanical properties, water stability, and material design methods of UHDMC with polyvinyl alcohol (PVA) fibers, polyethylene (PE) fibers, or hybrid fibers. It is noteworthy to mention that UHDMC, so developed, exhibits groundbreaking features such as strain-hardening behavior, multi-cracking, and ultra-high ultimate tensile strain.

The UHDMC has much potential for application in various areas. It can be applied in projects requiring rapid repair and fortification such as airport runways, roads, bridges, and military installations. A significant facet of UHDMC—and one that this book thoroughly explores—is its sprayability. The newly developed sprayable UHDMC extends its application scope, ushering in significant advantages in the field of construction mechanical rehabilitation.

The book is divided into six chapters. Among them, Chaps. 1, 3, and 5 were completed by Hu Feng, Aofei Guo, and Jun Zhao. Chapter 2 was handled by Hu Feng and Xupei Yao. Chapter 4 was completed by Hu Feng and Shuang Nie. The final chapter, Chap. 6, was accomplished by Hu Feng and Zhenyun Yu. In addition, graduate students, Guanghui Liu, Xiangyu Zhao, Lijun Lv, Lulu Li, Yang Wang, Pengfei Zhu, Junhao Liang, Qi Shao, Congguang Yao, and Xuhui Zheng, contribute to the experimental study in this book, and graduate students, Yifang Tian, Xiang Yuan, and Xuhui Zheng, contribute to the formatting of this book.

The primary aim of this book is to provide grounded technical guidance to readers intrigued by the development and design of UHDMC. With in-depth exploration and detailed documentation, it is a comprehensive resource for understanding the nature

and potential of this robust material. By bridging the gap between theoretical understanding and practical implementation, we strive to extend the frontier of composite engineering.

The target readers of this book encompass graduate students looking to further their understanding and prowess in improving the ductility of magnesium phosphate cement-based composites. On the other hand, it serves as a distinct guide for researchers studying the mechanical properties—strength, toughness, and more—, water stability, microstructure, and sprayability of magnesium phosphate cement-based composites. Engineers working on rapid repair of concrete structures would also find this book beneficial.

This book is not just a compilation of technicalities around UHDMC, but it's embedded with the aspiration to encourage further research and innovation in improving the properties and applications of this material. We trust that you will find this book a thoroughly constructively contributing source to advance your knowledge, research, and application of UHDMC in various engineering fields.

Zhengzhou, China

Hu Feng
Aofei Guo
Jun Zhao

Contents

1 Fundamental Performance of UHDMC with PVA Fibers 1
1.1 Introduction 1
1.2 Experimental Program 2
1.2.1 Raw Materials 2
1.2.2 Mixture Proportions 5
1.2.3 Mixing and Curing 6
1.2.4 Slump Test 6
1.2.5 Compressive Test 6
1.2.6 Tensile Coupon Test 6
1.2.7 Four-Point Bending Test 8
1.2.8 Optical Microscopy Test 11
1.3 Results and Discussion 11
1.3.1 Effect of Fly Ash (FA) Content 11
1.3.2 Effect of Fiber Volume Fraction (V_f) 17
1.3.3 Effect of Sand to Binder Mass Ratio (*S/B*) 22
1.3.4 Effect of Water to Solid Mass Ratio (*W/S*) 27
1.3.5 Microstructure 33
1.4 Conclusions 36
References 37

2 Fundamental Performance of UHDMC with Hybrid Fibers 39
2.1 Introduction 39
2.2 Experimental Program 40
2.2.1 Raw Materials 40
2.2.2 Mixed Design 41
2.2.3 Mixing and Curing 43
2.2.4 Slump Test 43
2.2.5 Compressive Test 44
2.2.6 Four-Point Bending Test 45
2.2.7 Investigating the Microstructures 45

2.3 Results and Discussion 46
2.3.1 Workability 46
2.3.2 Compressive Strength 49
2.3.3 Bending Performance 52
2.3.4 Cracking Propagation 56
2.3.5 Microstructure 60
2.4 Conclusions 64
References 65

3 Performance Improvement and Design of UHDMC Using Fly Ash and Silica Fume 67
3.1 Introduction 67
3.2 Background 69
3.2.1 Hydration Mechanism of MPC 69
3.2.2 Design Criteria of ECC 70
3.3 Materials and Experiments 71
3.3.1 Materials 71
3.3.2 Mixture Proportions 75
3.3.3 Mixing and Specimen Preparation 76
3.3.4 Experiments 76
3.4 Results and Discussion 81
3.4.1 Slump of UHDMC 81
3.4.2 Macromechanical Properties of UHDMC 84
3.4.3 Micromechanical Indices 90
3.4.4 Relationship Between Pseudo Strain-Hardening Indices and Ultimate Tensile Strain 106
3.4.5 Microstructure of UHDMC 108
3.4.6 XRD Spectra of MPC Pastes 111
3.5 Conclusions 114
References 117

4 Performance Improvement and Design of UHDMC Using PE Fibers 123
4.1 Introduction 123
4.2 Research Route 125
4.3 Experimental Programs 127
4.3.1 Materials 127
4.3.2 Mix Proportions 128
4.3.3 Mixing and Curing Procedures 130
4.3.4 Compressive Test 131
4.3.5 Tensile Test 131
4.3.6 Micromechanical Tests 132
4.4 Results and Discussion 134
4.4.1 Effect of Sd and *M/P* 134
4.4.2 Effects of *W/S* and *S/B* 143
4.4.3 Effect of Fly Ash (FA) Content 151

4.4.4 Effect of Fiber Content ... 157
4.4.5 Effect of Curing Temperature ... 159
4.4.6 Effect of Curing Age ... 161
4.4.7 Design Method of UHDMC ... 164
4.5 Conclusions ... 166
References ... 167

5 Water Stability of UHDMC ... 171
5.1 Introduction ... 171
5.2 Experimental Program ... 174
5.2.1 Raw Materials ... 174
5.2.2 Mixture Proportions ... 176
5.2.3 Mixing and Curing ... 178
5.2.4 Slump Test ... 178
5.2.5 Compressive Test ... 178
5.2.6 Flexural Test ... 179
5.2.7 Water Stability Evaluation ... 181
5.2.8 Microstructure ... 182
5.3 Results and Discussion ... 182
5.3.1 Effect of Ambient Curing Age and Water Immersion Age ... 182
5.3.2 Effect of *W/B* Ratio ... 185
5.3.3 Effect of *M/P* Ratio ... 188
5.3.4 Effect of NA Content ... 193
5.3.5 Effect of FA Substitution Rate ... 201
5.3.6 Effect of WG Mass Fraction ... 208
5.4 Conclusions ... 212
References ... 215

6 Preparation and Performance of Sprayable UHDMC ... 221
6.1 Introduction ... 221
6.2 Experimental Program ... 223
6.2.1 Raw Materials ... 223
6.2.2 Mixture Proportions ... 225
6.2.3 Mixing and Curing ... 226
6.2.4 Shootability Test ... 228
6.2.5 Rheology Test ... 230
6.2.6 Compressive Strength Test ... 231
6.2.7 Tensile Properties Test ... 232
6.2.8 Pore Structure Test ... 233
6.3 Results and Discussion ... 233
6.3.1 Factors Affecting Shootability and Rheological Properties ... 233
6.3.2 Relationship Between Shootability Factors and Rheological Parameters ... 243

6.3.3 Factors Affecting Compressive Strength 245
6.3.4 Factors Affecting Tensile Properties 250
6.3.5 Pore Structure Analysis 256
6.4 Conclusions 260
References 261

About the Authors

Dr. Hu Feng completed his undergraduate studies at Zhengzhou University, China, in 2004, pursued his master's degree at the same university in 2007, and eventually earned his doctorate from Tongji University, China, in 2010. Post acquiring his Ph.D., he has held a professorial position at Zhengzhou University's School of Civil Engineering.

Dr. Feng dedicates his research to the study of fiber-reinforced composite materials and structures, as well as the development of innovative prefabricated structures. He has been the beneficiary of financial support from sources such as the National Natural Science Foundation, Henan Province's Key Research and Development Project, and the Science and Technology Project of Henan Province. To his credit, he has over 40 scholarly articles published in reputable journals and is the holder of numerous patented inventions.

Currently serving as Deputy Director, Dr. Feng contributes to the Ministry of Education's "Fiber Composite Building Materials and Structures" Engineering Research Center, Henan Province's "New Urban Building Technology" Collaborative Innovation Center, and "Green Composite Building Materials and Structures" International Joint Laboratory of Henan Province. His academic affiliations span the Fiber Reinforced Concrete Special Committee of the China Civil Engineering Society, the Civil Engineering Composite Materials Branch of the China Composite Materials Society, and the American Society of Civil Engineers. He also offers his service as an Editorial Member for the journal Sustainable Structures.

Dr. Aofei Guo completed his undergraduate studies at Henan University of Technology, China, earning his bachelor's degree in 2013, then attained his master's degree from Hunan University, China, in 2016. He continued his academic journey in the United States, where he received his Ph.D. degree from the University of Louisville, USA, in 2020. In May 2021, he joined the School of Civil Engineering at Zhengzhou University as an Associate Research Professor.

Dr. Guo's research is primarily centered on the alteration of lignocellulosic biomass—including the study of nanocellulose—and its integration in cement-based

composites, and the conception and formulation of high ductility magnesium phosphate cement-based composites. His research has been supported by prestigious funding bodies, such as the National Natural Science Foundation, the China Postdoctoral Science Foundation, and the Natural Science Foundation of Henan Province. To date, Dr. Guo has more than 20 technical articles to his name, published in renowned journals like Cement and Concrete Composites, Industrial Crops and Products, and Construction and Building Materials.

As an active member of the academic community, Dr. Guo is part of the inaugural Young Editorial Members of the Sustainable Structures journal and also contributes his expertise as a reviewer for a number of international journals.

Dr. Jun Zhao obtained his Master's degree from Zhengzhou University in 1996, and his Ph.D. from Harbin Institute of Technology in 2000. He was a visiting scholar at the Tokyo Institute of Technology, Japan, and at the University of Florida, USA. He is a professor and has been working at Zhengzhou University for many years.

Dr. Zhao's main research interests include green building materials and structures, disaster prevention and reduction in engineering structures, damage controllable and recoverable seismic structures, high-performance concrete and structure, and key technological applications in engineering. He has led multiple projects such as key projects of the National Key R&D Program for International Scientific and Technological Innovation Cooperation, Innovative Talent International Cooperation Training Projects of the China Scholarship Council, and projects of the National Natural Science Foundation of China. He has published nearly 200 academic papers, authored 6 books, and co-edited 4 national (industry) standards. He has been awarded the National Science and Technology Progress Second Prize and the First, Second, and Third Prizes in Scientific and Technological Progress from the Ministry of Education or in Henan Province.

Dr. Zhao is a national-level mid-young expert with outstanding contributions, selected for the "Talents Project" at the national level, an expert receiving special government allowances from the State Council, recognized by the Ministry of Education as part of the New Century Talents Project. He is the head of the Ministry of Education's Innovative Team for New Building Materials and Structures, and the executive deputy director of the Engineering Research Center for Fiber Composite Building Materials and Structures under the Ministry of Education.

Chapter 1
Fundamental Performance of UHDMC with PVA Fibers

Abstract This Chapter develops ultra-high ductility magnesium phosphate cement-based composites (UHDMC) by adding PVA fibers to magnesium phosphate cement (MPC)-based composites. This chapter introduces the effects of fly ash (FA) content, polyvinyl alcohol (PVA) fiber volume fraction (V_f), sand to binder mass ratio (*S/B*), and water to solid mass ratio (*W/S*) on the workability, compressive strength, tensile properties, and flexural properties of the UHDMC. The optical microscope test is conducted to examine the microstructure of PVA fibers and their bonding with the matrix. Overall, when the FA content is 20% or 30%, the UHDMC can obtain relatively high strength and strain capacity without significant workability loss; the UHDMC can obtain relatively high workability, strength, and strain capacity when the V_f is 1.6% or 1.8%; when the *S/B* is 0 or 0.2, the workability, strength, and strain capacity of the UHDMC are the highest; when the *W/S* is 0.13 or 0.16, the UHDMC can obtain relatively high strength and strain capacity while maintaining good workability. The microstructure analysis shows that PVA fibers are well embedded in the matrix and can effectively bear stress and limit the initiation and propagation of cracks, resulting in multi-cracking.

Keywords PVA fiber · Magnesium phosphate cement · Strain hardening · Tensile property · Workability

1.1 Introduction

The magnesium phosphate cement (MPC) is characterized by high early strength, wear resistance, adhesion, durability, volume stability, and frost resistance, and low dry shrinkage (Feng et al., 2021; Zhang et al., 2022), which attracts extensive attention. The MPC-based composites can be used to rapidly repair and strengthen municipal arterial roads, highways, and airport runways, and also rapidly construct military projects (Seehra et al., 1993). However, similar to many traditional cementitious materials, the MPC-based composites are inherently brittle. Thus, it is necessary to

H. Feng et al., *Ultra-High Ductility Magnesium-Phosphate-Cement-Based Composites (UHDMC)*, https://doi.org/10.1007/978-981-97-0952-6_1

take some measures to overcome the brittle behavior for promoting their large-scale application.

The addition of fibers into the MPC-based composites to develop ultra-high ductility magnesium phosphate cement-based composites (UHDMC) has been successfully implemented in recent years. The fibers are able to bear randomly dispersed cracking stress, which enables the UHDMC exhibit significant strain-hardening characteristics (Feng et al., 2020). Qin et al. (2018) examined the effects of basalt fiber volume fraction on the compression, splitting, stretching, and flexural properties of the MPC-based composite materials and found that the flexural strength, splitting tensile strength, and fracture toughness increased significantly as the fiber volume fraction increases. Similarly, Haque et al. (2020) enhanced the compressive strength and bending properties of MPC-based composites through the addition of micro-steel fibers, polyvinyl alcohol fibers, and basalt fibers.

In addition, the mechanical properties of the UHDMC can be improved by using some supplementary cementitious materials, such as silica fume and fly ash. Ahmad and Chen (2018) examined the effects of basalt fibers and silica fume on the micro-morphology and mechanical properties of MPC-based mortars and found that they could enhance the flexural and compressive strengths of MPC-based mortars. Ahmad et al. (2019) found the ultra-fine fly ash could enhance the mechanical properties of MPC composites reinforced by basalt fibers.

In this chapter, the fly ash (FA) and polyvinyl alcohol (PVA) fibers are combined to develop ultra-high ductility magnesium phosphate cement-based composites (UHDMC). The effects of water to solid mass ratio (*W/S*), fiber volume fraction (V_f), sand to binder mass ratio (*S/B*), and fly ash (FA) content on the fundamental performance (slump, compressive strength, tensile properties, and flexural properties) of the UHDMC were examined in detail. The optical microscope test was conducted to observe the micro-morphology of PVA fibers and their bonding with the matrix. The study results in this chapter can guide the development of the UHDMC with good workability, strength, and strain capacity by controlling FA content, V_f, *S/B*, and *W/S*.

1.2 Experimental Program

1.2.1 Raw Materials

The magnesia oxide (MgO), potassium dihydrogen phosphate (KH_2PO_4), and borax ($Na_2B_4O_7 \cdot 10H_2O$) are three main components of MPC. The MgO is supplied by Jiangsu Huanai magnesium Industry Co., Ltd. Its particle size distribution and chemical composition are shown in Tables 1.1 and 1.2, respectively.

Table 1.1 Particle size distribution of MgO (Provided by the supplier)

Particle size (μm)	Mass percent (%)
≤10	19.19
10–20	12.56
20–45	25.27
45–75	20.68
75–100	10.45
100–200	11.59
200–300	0.26

Table 1.2 Chemical composition of MgO (Provided by the supplier)

Ingredient	Mass percent (%)
MgO	97
Fe_2O_3	0.18
SiO_2	0.7
CaO	1.4
Al_2O_3	0.1

The KH_2PO_4 with two different sizes was purchased from two manufacturers, Sichuan Mianzhu Ronghong Chemical Co., Ltd. and Henan Huaxing Chemical Co., Ltd., which passes through No. 20 sieve and No. 80 sieve, respectively. They are mixed at a mass ratio of 1:1. The particle size distribution of KH_2PO_4 is measured and shown in Table 1.3.

The industrial-grade borax ($Na_2B_4O_7 \cdot 10H_2O$, ≥99.5%) was produced by Liaoning Borda Technology Co., Ltd., which was used as a retarder. Its particles pass through No. 80 sieve with the opening size of 177 μm. The grade of fly ash used in this study is Class 1 as per the Chinese standard GB/T1596-2017, which is purchased from Yulian Power Plant in Gongyi City, Henan Province. The chemical composition of fly ash is listed in Table 1.4.

Table 1.3 Particle size distribution of KH_2PO_4

Particle size (mm)	Mass fraction (%)
≤0.08	0.1
0.08–0.15	12.8
0.15–0.30	21.1
0.30–0.63	51.3
0.63–1.18	14.7

Reproduced from Workability and Mechanical Properties of Tensile Strain–Hardening PVA Fiber-Reinforced Magnesium Phosphate Cement Composites by Shuwen Zhang with permission from ASCE

Table 1.4 Chemical composition of fly ash

Ingredient	Mass fraction (%)
SiO_2	53.97
Al_2O_3	31.15
Fe_2O_3	4.16
CaO	4.01
MgO	1.01
Na_2O	0.89

Reproduced from Workability and Mechanical Properties of Tensile Strain–Hardening PVA Fiber-Reinforced Magnesium Phosphate Cement Composites by Shuwen Zhang with permission from ASCE

Table 1.5 PVA fiber performance index (Provided by the supplier)

Diameter (μm)	40
Length (mm)	12
Tensile strength (MPa)	1560
Elastic modulus (GPa)	41
Elongation at break (%)	6.5
Density (g/cm^3)	1.3

The PVA fibers were purchased from Kuraray Company in Japan, with the specific performance index listed in Table 1.5. The quartz sand was purchased from Henan Zhongbang China Science and Technology Co., Ltd., with the particle size of 149–177 μm. In addition, the tap water was used as mixing water.

The particle size distribution of quartz sand, magnesium oxide, and fly ash is shown in Fig. 1.1.

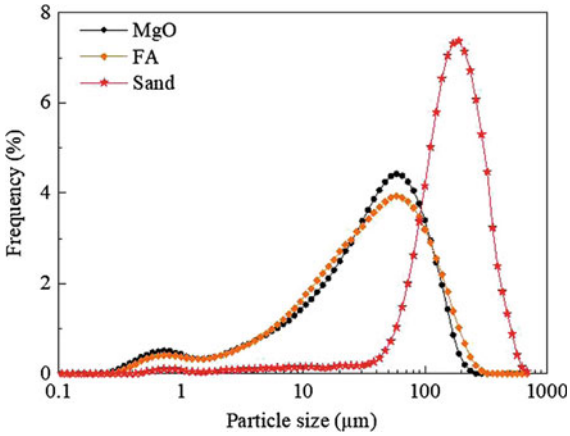

Fig. 1.1 Particle size distribution of quartz sand, MgO, and FA. Reproduced from Deflection hardening behaviour of ductile fibre reinforced magnesium phosphate cement-based composite by Hu Feng with permission from Elsevier

1.2.2 Mixture Proportions

For magnesium phosphate cement (MPC), the borax content is 6% by weight of magnesium oxide, and the magnesium oxide to phosphate mass ratio (*M/P*) is 4. The FA is used to partially replace MPC. The control mixture proportion of UHDMC is: the sand to binder mass ratio (*S/B*), fly ash (FA) content, water to solid mass ratio (*W/S*), and fiber volume fraction (V_f) are 0.2, 20, 0.13, and 1.6%, respectively. The *S/B*, FA, *W/S*, and V_f changes from 0 to 0.6, from 10% to 40, from 0.10 to 0.19, and from 1.2 to 2.0%, respectively. The mixture proportions of UHDMC are shown in Table 1.6.

Table 1.6 Mixture proportions of UHDMC

Mix ID	Fly ash content (%)	Fiber volume fraction (%)	Sand to binder mass ratio	Water to solid mass ratio
FA-10	10	1.6	0.2	0.13
FA-20	20			
FA-30	30			
FA-40	40			
V_f-1.2	20	1.2	0.2	0.13
V_f-1.4		1.4		
V_f-1.6		1.6		
V_f-1.8		1.8		
V_f-2.0		2.0		
S/B-0	20	1.6	0.0	0.13
S/B-0.2			0.2	
S/B-0.4			0.4	
S/B-0.6			0.6	
W/S-0.10	20	1.6	0.2	0.10
W/S-0.13				0.13
W/S-0.16				0.16
W/S-0.19				0.19

Note "FA"-Fly ash content; "V_f"-Fiber volume fraction; "*S/B*"-Sand to binder mass ratio; "*W/S*"-Water to solid mass ratio

Reproduced from Workability and Mechanical Properties of Tensile Strain–Hardening PVA Fiber-Reinforced Magnesium Phosphate Cement Composites by Shuwen Zhang with permission from ASCE

1.2.3 Mixing and Curing

The mixing was conducted by using a cement mortar mixer (model: JJ-5). The internal surface and the blade of the mixer were pre-moistened using some water. The quartz sand, potassium dihydrogen phosphate, magnesium oxide, and fly ash were added to the mixer and mixed at a low speed for 120 s. Meanwhile, the borax (retarder) was uniformly dissolved in the mixing water. The borax aqueous solution was added into the mixer and mixed for 30 s. Afterward, the fibers were manually added into the mixer and mixed at a high speed for 90 s so that they could be uniformly dispersed. The mixture was then quickly cast into the molds and vibrated on a vibrating table for 60 s to compact it. After that, the mixture was kept still for 15 s and then was vibrated again for 30 s. The vibration-molded samples were kept in a curing room with the temperature of 20 ± 2 °C and the relative humidity of 35 ± 5% for about 1.5 h, after which the molds were removed. Then the specimens were stored in the curing room for continuous curing until the age of 7 days.

1.2.4 Slump Test

The slump test (also known as the spread-flow test) was conducted by following JGJ/T283-2012 (Standardization, 2012) to evaluate the workability of UHDMC mixtures. The UHDMC slurry was put into the slump cone first. Then the slurry is allowed to flow freely by lifting the slump cone steadily and vertically. The duration time from the start of lifting to the time when the slurry on the bottom plate extends to the diameter of 500 mm was recorded as T_{500}. In addition, the slump flow diameter (D) of the slurry was recorded when the slurry stops flowing. Lastly, the slump was obtained by calculating the height difference of the slurry before and after slump.

1.2.5 Compressive Test

The compressive test was conducted on $50 \times 50 \times 50\ mm^3$ cubic specimens by using the 2000 kN pressure testing machine (model: YAW-2000B). The loading rate was set as 0.9 kN/s. From this test, the compressive strength was recorded. The average value of three replicates was adopted.

1.2.6 Tensile Coupon Test

The tensile coupon test was conducted on $280 \times 40 \times 15\ mm^3$ specimens by using the 100kN electronic universal testing machine (model: WDW-100), and three samples

were prepared in each group. Prior to this test, some preparation work was done. The specimens were polished to achieve a smooth surface. The carbon fiber cloth tailored to size was attached to both ends of the coupon with epoxy resin and then rolled several times along the fiber direction. Then the aluminum sheet was firmly affixed to the upper surface of the carbon fiber cloth with epoxy resin. The L-shaped iron sheet and the fixed displacement meter were glued to both sides of the aluminum sheet with AB adhesive that consists of two parts of epoxy (Brand: Kafuter, Guangdong Hengda New Materials Technology Co., Ltd.). The appearance of the coupon specimens was examined before testing in case of any damage. To observe the crack propagation phenomenon, the tensile section of specimens was painted with white ash. Then, the specimens were installed as illustrated in Fig. 1.2 to ensure they were subject to axial tension in the tensile test. A pre-tension load of 10–15% of the failure load was applied to the specimens. The specimens were loaded continuously with a loading rate of 0.1 mm/min until a large crack appears. The tensile deformation and the tensile load were recorded automatically.

The tensile stress and tensile strain of the coupon specimens are calculated using Eqs. 1.1 and 1.2, respectively, based on the recorded tensile load and deformation values, from which the direct tensile stress–strain curve is plotted. After the sample cracks, the tensile load drops. When the tensile load is reduced to 85% of the peak tensile load, the corresponding tensile stress and tensile strain are defined as the ultimate tensile stress and ultimate tensile strain, respectively.

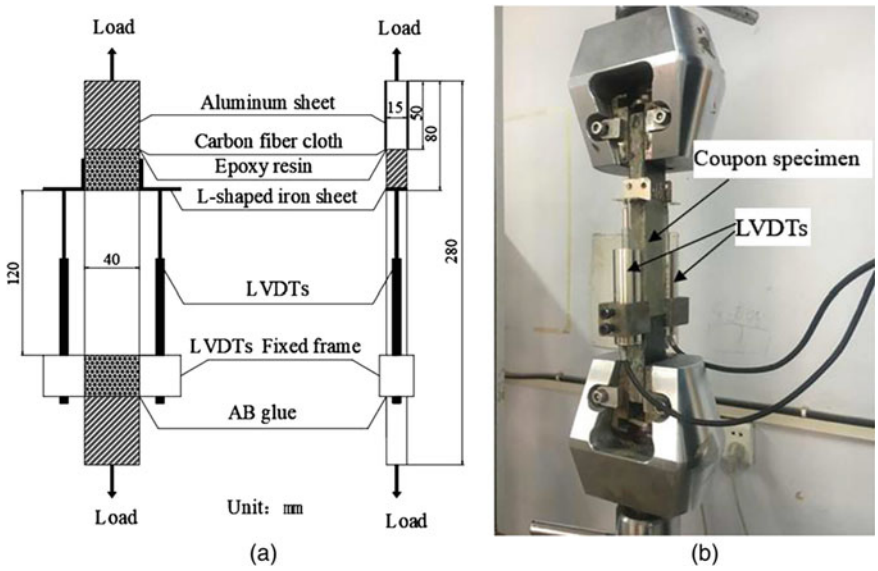

Fig. 1.2 **a** Schematic diagram and **b** loading diagram of tensile coupon test. Reproduced from Workability and Mechanical Properties of Tensile Strain–Hardening PVA Fiber-Reinforced Magnesium Phosphate Cement Composites by Shuwen Zhang with permission from ASCE

$$\delta = \frac{F}{st} \tag{1.1}$$

where δ is tensile stress (MPa); s is the width of test piece (40 mm in this study); F is tensile load (N); and t is the thickness of test piece (15 mm in this study).

$$\varepsilon = \frac{L_o}{L} \times 100\% \tag{1.2}$$

where ε is tensile strain (%); L is the specimen gauge length (120 mm in this study); and L_o is the specimen elongation value under tension (mm).

1.2.7 Four-Point Bending Test

The four-point bending test was conducted to examine the flexural behaviour of panel specimens by using an electronic MTS testing machine, with the displacement-controlled mode. At least three specimens were prepared for each mix. For the purpose of achieving the peak load within the first 30–60 s, the displacement control rate was set 0.18 mm/min following the studies from Martin et al. (2007) and Sarker et al. (2013). A Linear Variable Differential Transformer (LVDT) was adopted to measure the mid-span deflection. From this test, the flexural load-mid-span deflection curves were plotted. The flexural behaviour test setup is schematically shown in Fig. 1.3.

Deflection-hardening and deflection-softening are two types of flexural behaviours for fiber reinforced cement-based composites (FRCC) (see Fig. 1.4) (Joo Kim et al., 2008). The deflection hardening behavior of the FRCC is characterized by a higher load-bearing capacity after first cracking under bending. The FRCC is normally termed as DFRCC (see Fig. 1.4) when it shows the deflection hardening behaviour. The point where the linear stage in the load–deflection curve ends is

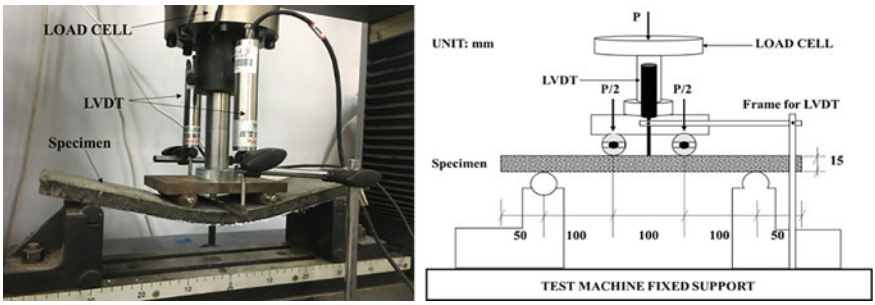

Fig. 1.3 Test specimen and setup. Reproduced from Deflection hardening behaviour of ductile fibre reinforced magnesium phosphate cement-based composite by Hu Feng with permission from Elsevier

termed as limit of proportionality (LOP) referring to ASTM C1018. However, Joo Kim et al. (2008) indicated that it was difficult to exactly locate the LOP in the load–deflection curve. Thus, the point at which the nonlinearity of the load–deflection curve becomes significant could be taken as the LOP (Joo Kim et al., 2008). In this study, the LOP of the load–deflection curves is identified by using the method proposed by Joo Kim et al. (2008). The load and deflection values at LOP are termed as P_{LOP} and δ_{LOP}, as shown in Fig. 1.4. The point where softening happens after the LOP is defined as the ultimate flexural strength, commonly known as modulus of rupture (MOR). The load and deflection values at MOR are termed as P_{MOR} and δ_{MOR}, as shown in Fig. 1.4. The first crack-strength (f_{LOP}) and the MOR can be calculated using Eqs. 1.3 and 1.4 as specified in ASTM C1609.

$$f_{\mathrm{LOP}} = P_{\mathrm{LOP}} \frac{L}{bh^2} \tag{1.3}$$

$$\mathrm{MOR} = P_{\mathrm{MOR}} \frac{L}{bh^2} \tag{1.4}$$

where $b = 100$ mm and $h = 15$ mm are the width and height of the panel, respectively; and $L = 300$ mm is the distance between the supporters of the panel (span length).

In Fig. 1.4, the deflection hardening and multiple-cracking behaviour can be achieved (e.g., curve OA) only when the P_{MOR} of the FRCC exceeds the P_{LOP} If this condition is not satisfied ($P_{\mathrm{MOR}} < P_{\mathrm{LOP}}$), the load drops rapidly after first cracking (e.g., curves OB and OC). The increase in the difference between f_{LOP} and

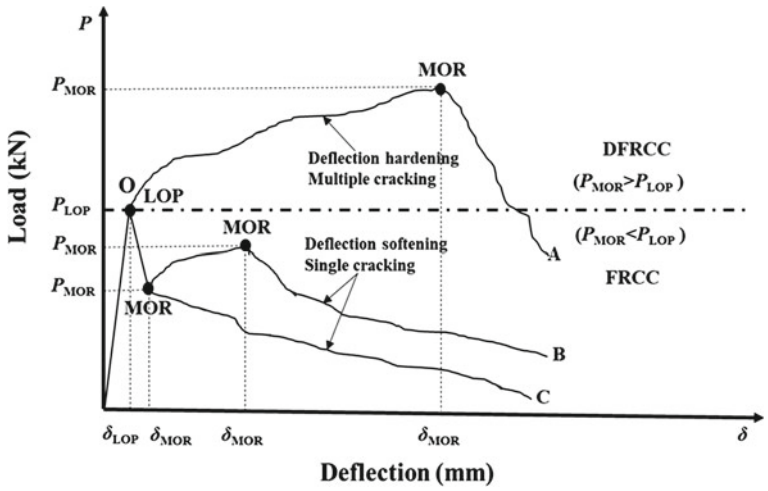

Fig. 1.4 The load–deflection curves of FRCC (Ding et al., 2014). Reproduced from Comparative flexural behavior of four fiber reinforced cementitious composites by Dong joo Kim with permission from Elsevier

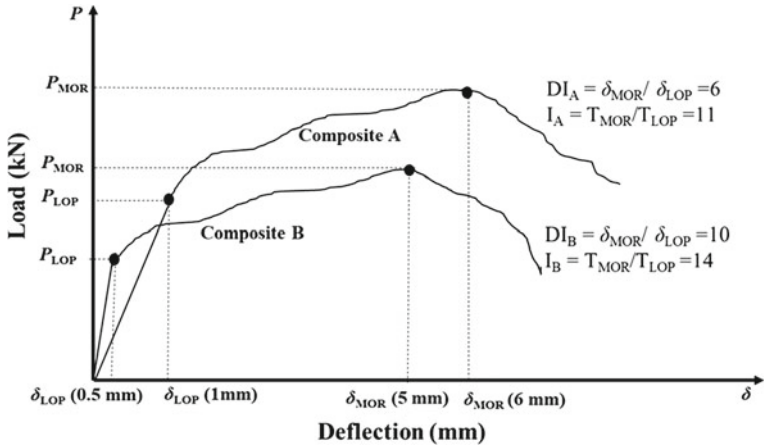

Fig. 1.5 The load–deflection curves of DFRCC. Reproduced from Deflection hardening behaviour of ductile fibre reinforced magnesium phosphate cement-based composite by Hu Feng with permission from Elsevier

MOR and that between their corresponding deflections δ_{LOP} and δ_{MOR} represent the improvement of the deflection hardening behaviour (Banyhussan et al., 2016).

The ductility of DFRCC can be evaluated in multiple ways. Naaman and Reinhardt (1996) quantitatively evaluated the ductility of DFRCC by introducing the ductility index (*DI*) concept. The ratio of the deflection at MOR to the deflection at first-crack ($\delta_{MOR}/\delta_{LOP}$) is defined as the *DI* when the MOR is greater than f_{LOP}. In most cases, the higher the *DI* value, the more ductile the material. However, there are some exceptions. From Fig. 1.5, it can be seen that the *DI* values of composite A and composite B are 6 and 10, respectively, but the deflection hardening capacity of composite B is worse than composite A. In this case, the *DI* value cannot reflect the real phenomenon.

The deflection hardening capacity of DFRCC can be further evaluated by introducing strength gap (f_g) and deflection gap (D_g) in this study. The difference between MOR and f_{LOP} is defined as f_g, and the difference between δ_{MOR} and δ_{LOP} is defined as D_g, as shown in Eqs. 1.5 and 1.6:

$$f_g = \text{MOR} - f_{LOP} \tag{1.5}$$

$$D_g = \delta_{MOR} - \delta_{LOP} \tag{1.6}$$

In addition, there are another two important indices that can be adopted to evaluate the deflection hardening capacity of DFRCC. The first one is the toughness value at peak load (T_{peak}), which is defined as the area under the load–deflection curve up to the δ_{MOR}. The second one is the toughness index (I) that is defined as the ratio of the area under the load–deflection curve up to a given deflection to that up to δ_{LOP}. However, the above two indices do not work well sometimes. From Fig. 1.5, it can be seen that the I_A and I_B of composite A and composite B are 11 and 14, respectively, but the composite B shows worse deflection hardening capacity than the composite A. Thus, the toughness gap is introduced as shown in Eq. 1.7 to evaluate the deflection hardening capacity in this study.

$$T_g = T_{peak} - T_{LOP} \tag{1.7}$$

where the T_{LOP} is the area under the load–deflection curve up to δ_{LOP}.

The flexural behaviour of UHDMC is evaluated using the two groups of indices (f_g and D_g as well as T_{peak} and T_g) in this chapter. Specifically, the higher values of these parameters may lead the composite materials to achieve higher ductility and higher deflection hardening capacity.

1.2.8 Optical Microscopy Test

The UHDMC samples with better tensile properties are selected for optical microscopy analysis. The optical microscope is manufactured by New fiber instruments co., Ltd. Shanghai, China. A small piece is directly cut from the fracture section of samples after tensile test. The micro-morphology of a single PVA fiber and the PVA fiber-matrix interface of the UHDMC were examined to reveal the influence mechanism of PVA fibers on the UHDMC on the microscopic level.

1.3 Results and Discussion

1.3.1 Effect of Fly Ash (FA) Content

(1) **Workability**

The workability of the UHDMC with varying fly ash (FA) contents is shown in Table 1.7. Referring to the technical specification of CCES 02-2004, T_{500} should be 2–5 s, and the slump flow should be 550–750 mm for self-compacting concrete (Society, 2005). Table 1.7 shows that when the FA content is 10%, the UHDMC can reach the self-compacting state. As the FA content increases from 10 to 40%, the T_{500} increases, and the slump and slump flow of the UHDMC decrease, indicating a decreased workability.

Table 1.7 Workability of the UHDMC with varying FA contents

FA content (%)	T_{500} (s)	Slump (mm)	Slump flow (mm)
10	4.1	270	620
20	5.7	265	600
30	6.4	260	550
40	9.9	235	450

Reproduced from Workability and Mechanical Properties of Tensile Strain–Hardening PVA Fiber-Reinforced Magnesium Phosphate Cement Composites by Shuwen Zhang with permission from ASCE

(2) **Compressive strength**

The 7d compressive strength of the UHDMC with varying FA contents is shown in Fig. 1.6. As the FA content increases, an overall decreasing trend can be seen in terms of the compressive strength. However, when the FA content is 30%, the compressive strength of the UHDMC is slightly higher than those at 20% FA and 40% FA, which may be because the structure of the UHDMC is improved by the active effect of FA.

(3) **Tensile properties**

Figure 1.7 shows the direct tensile stress–strain curve of the 7 day UHDMC with varying FA contents. Although three replicates are tested for each mixture, only a representative curve is used to show the comparison clearly and simply, which is not a quantitative analysis, just showing the trend. This is also applicable to all other tensile stress–strain curves in this chapter. Figure 1.7 shows that the strain hardening characteristic is closely dependent on the FA content. The strain hardening

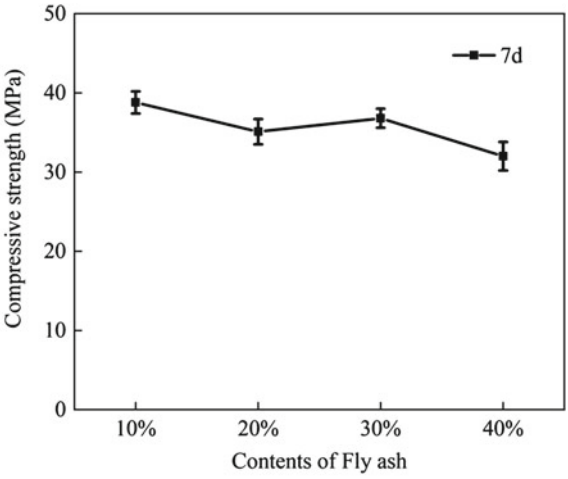

Fig. 1.6 Compressive strength of the UHDMC with varying FA contents. Reproduced from Workability and Mechanical Properties of Tensile Strain–Hardening PVA Fiber-Reinforced Magnesium Phosphate Cement Composites by Shuwen Zhang with permission from ASCE

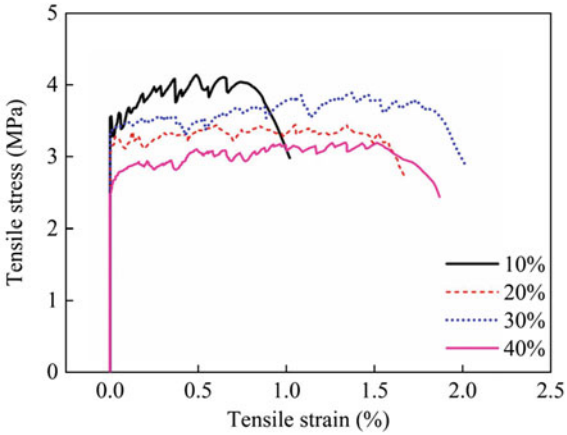

Fig. 1.7 Direct tensile stress–strain curves of the UHDMC with varying FA contents. Reproduced from Workability and Mechanical Properties of Tensile Strain–Hardening PVA Fiber-Reinforced Magnesium Phosphate Cement Composites by Shuwen Zhang with permission from ASCE

characteristic of the UHDMC is obvious when the FA content is 10%, but the peak tensile strain is less than 1%; it becomes less obvious as the FA content increases from 10 to 20%, but the peak tensile strain increases significantly, reaching 1.5%; it becomes more obvious as the FA content increases from 20 to 30%, and the peak tensile strain increases to 1.8%; it becomes less obvious as the FA content increases from 30 to 40%, and the peak tensile strain decreases to 1.5%.

Figure 1.8a shows the peak tensile stress and peak tensile strain of the UHDMC with varying FA contents. Figure 1.8b shows the ultimate tensile stress and ultimate tensile strain of the UHDMC with varying FA contents. As the FA content increases from 10 to 40%, a descending trend can be observed generally for the peak tensile stress and ultimate tensile stress. However, an ascending trend is observed for the peak tensile strain as the FA content increases from 10 to 40%. The ultimate tensile strain reaches the peak when the FA content is 30%. Thus, it can be concluded that when the FA content is 30%, the UHDMC has the best tensile properties.

(4) **Flexural behaviour**

The first cracking strength (f_{LOP}) and its corresponding deflection (δ_{LOP}) and the modulus of rupture (also known as ultimate flexural strength, MOR) and its corresponding deflection (δ_{MOR}) of the UHDMC with varying FA contents are listed in Table 1.8.

The flexural load-mid span deflection response of the UHDMC with varying FA contents is shown in Fig. 1.9. When the FA content is 0 or 10%, the MOR of the UHDMC is equal to the f_{LOP}, so the UHDMC shows deflection-softening response; once the FA content exceeds 10%, the MOR of the UHDMC is higher than the f_{LOP}, so the UHDMC shows deflection-hardening response.

When the FA content is 30%, the f_{LOP} and MOR of the UHDMC are the highest, showing the highest load carrying capacity. The possible reason can be that for the FA-30% specimens, the chemical bonding energy and the frictional bond strength between fibers and the matrix are higher those of the FA-20% and FA-40% specimens,

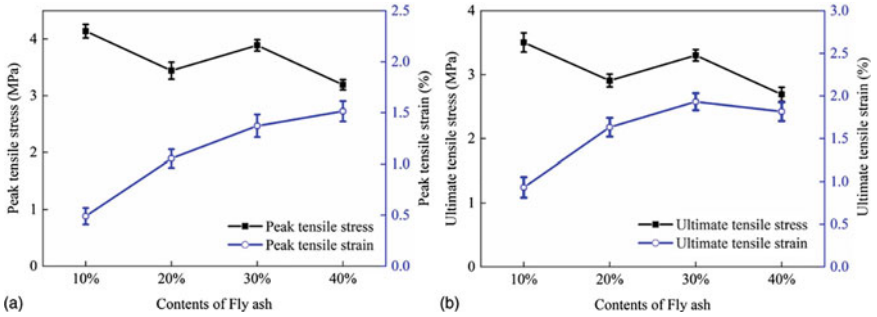

Fig. 1.8 **a** Peak tensile stress and peak tensile strain; and **b** ultimate tensile stress and ultimate tensile strain of the UHDMC with varying FA contents. Reproduced from Workability and Mechanical Properties of Tensile Strain–Hardening PVA Fiber-Reinforced Magnesium Phosphate Cement Composites by Shuwen Zhang with permission from ASCE

Table 1.8 Flexural test results of the UHDMC with varying FA contents

Mix ID (%)	f_{LOP} (MPa)	δ_{LOP} (mm)	MOR (MPa)	δ_{MOR} (mm)
FA-0	8.75	0.43	8.75	0.43
FA-10	7.47	0.45	7.47	0.45
FA-20	6.38	0.65	7.60	25.12
FA-30	6.53	0.48	9.20	21.4
FA-40	4.67	0.59	7.33	22.2

Reproduced from Deflection hardening behaviour of ductile fibre reinforced magnesium phosphate cement-based composite by Hu Feng with permission from Elsevier

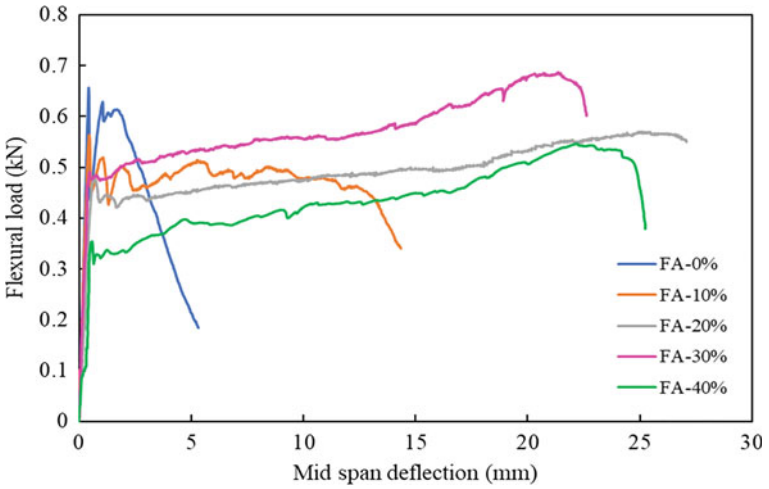

Fig. 1.9 Flexural load-mid span deflection response of the UHDMC with varying FA. Reproduced from Deflection hardening behaviour of ductile fibre reinforced magnesium phosphate cement-based composite by Hu Feng with permission from Elsevier

resulting in higher fiber bridging strength. However, the δ_{LOP} and δ_{MOR} reach the maximum values of 0.69 and 25.4 mm when the FA content is 20%, showing the highest deflection hardening capacity.

The calculated results of f_g and D_g of the UHDMC with different FA contents are shown in Fig. 1.10. It can be seen that the flexural strength gap (f_g) is greater than zero for all UHDMCs, corresponding to MOR > f_{LOP}, resulting in a deflection hardening response. The UHDMC with FA-20% has the highest D_g (24.39 mm), which is 14.2 and 11.4% higher than those with FA-30% and FA-40%, respectively. However, the f_g of UHDMC with FA-20% is the smallest among all UHDMCs, which cannot prove its excellent ductility. Thus, it is necessary to calculate the toughness parameters (T_{peak} and T_g) to provide more alternatives to evaluate the deflection hardening capacity of UHDMCs. The T_{peak} and T_g of UHDMCs are shown in Fig. 1.11. It can be observed that compared to UHDMCs with FA-30% and FA-40%, FA-20% UHDMC has higher T_{peak} (12.23 kN mm) and T_g (12.06 kN mm), which is indicative of more excellent non-elastic energy absorption capacity and peak load energy absorption capacity. In general, it can be concluded that the UHDMC with FA-20% has excellent deflection capacity.

The cracking pattern of UHDMC specimens is shown in Fig. 1.12, which can also reflect the deflection hardening capacity of UHDMC. With the increase of FA content, the crack distribution of specimens becomes more uniform and denser. When the FA content is 20%, the UHDMC specimens have the highest density of cracks. However, when the FA content is over 30%, the density of cracks is greatly reduced.

The number of cracks, crack spacing, and crack width of specimens were measured to quantitatively evaluate the ductility of specimens, as shown in Table 1.9. Specifically, the number of cracks on the samples were manually counted after the flexural

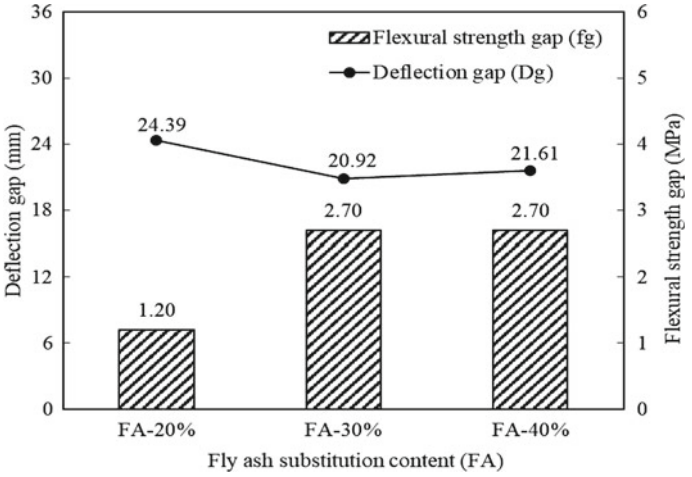

Fig. 1.10 Flexural strength gap and Deflection gap of the UHDMC with varying FA contents. Reproduced from Deflection hardening behaviour of ductile fibre reinforced magnesium phosphate cement-based composite by Hu Feng with permission from Elsevier

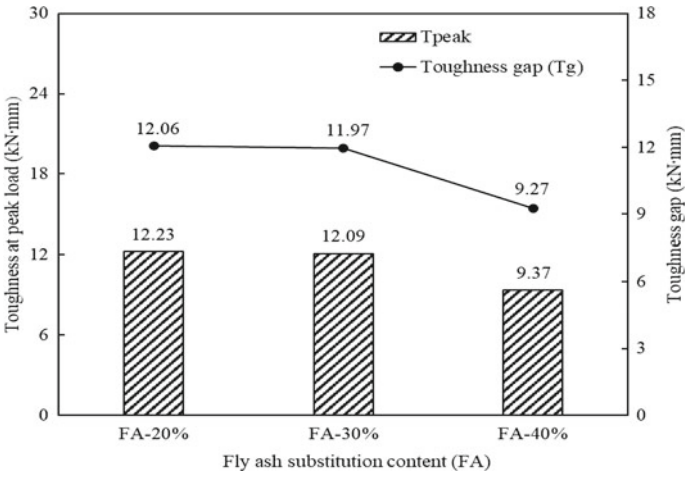

Fig. 1.11 T_{peak} and Toughness gap of the UHDMC with varying FA contents. Reproduced from Deflection hardening behaviour of ductile fibre reinforced magnesium phosphate cement-based composite by Hu Feng with permission from Elsevier

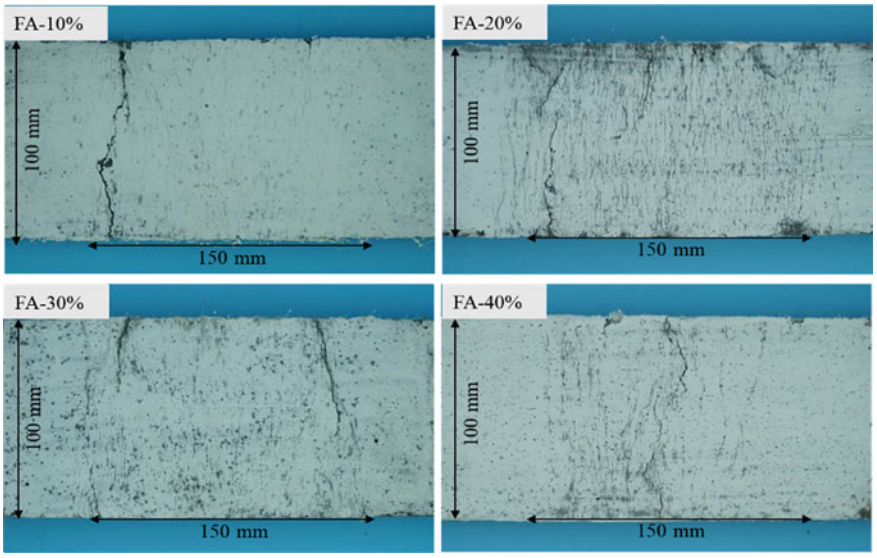

Fig. 1.12 The cracking patterns of UHDMC with varying FA contents. Reproduced from Deflection hardening behaviour of ductile fibre reinforced magnesium phosphate cement-based composite by Hu Feng with permission from Elsevier

Table 1.9 Cracking parameters of the UHDMC with varying FA contents

Mix ID (%)	Number of cracks	Crack spacing (mm)	Crack width (μm)
FA-10	27	4.13	N/A
FA-20	83	1.81	81.7
FA-30	71	2.11	88.8
FA-40	39	3.84	118.7

Reproduced from Deflection hardening behaviour of ductile fibre reinforced magnesium phosphate cement-based composite by Hu Feng with permission from Elsevier

test. The crack spacing was defined as the distance enclosing the cracks divided by the number of cracks. Because some cracks generated during the test are invisible, the actual crack width is less than the calculated crack width. It needs to be noted that the average crack width of FA-10 sample is missing in Table 1.9, because it has smaller deformation in response to the deflection softening behavior. Table 1.9 shows that the FA-20% sample has the largest number of cracks (83) but the smallest crack spacing (1.81 mm) and crack width (81.7 μm), implying the appearance of many tiny cracks, which leads to the significantly higher deflection hardening capacity.

Overall, the deflection hardening response can not be observed for the UHDMC with small amounts of FA contents (e.g., 10%). When the FA content reaches 20%, the UHDMC shows the deflection hardening behavior and even the highest deflection capacity. Afterward, the excess FA content of 30% or 40% reduces the deflection capacity of UHDMC.

1.3.2 Effect of Fiber Volume Fraction (V_f)

(1) **Workability**

Table 1.10 shows the workability of the UHDMC with varying fiber volume fractions (V_f). According to the specification in CCES 02-2004 (Society, 2005), Table 1.10 shows that the UHDMC reaches the self-compacting state when the fiber volume fraction is 1.2% or 1.4%. As the fiber volume fraction increases, the T_{500} increases, but the slump and slump flow reduce, which implies a decrease in workability. When the fiber volume fraction reaches 2.0%, the workability of the UHDMC is decreased greatly, so the T_{500} cannot be recorded and is missing in Table 1.10.

(2) **Compressive strength**

Figure 1.13 shows the 7d compressive strength of the UHDMC with varying fiber volume fractions. The compressive strength of the UHDMC increases gradually as the fiber volume fraction increases from 1.2 to 2.0%. This is because the development of cracks can be prevented by PVA fibers in cement matrix.

Table 1.10 Workability of the UHDMC with varying fiber volume fractions

Fiber volume fraction (%)	T_{500} (s)	Slump (mm)	Slump flow (mm)
1.2	2.7	275	745
1.4	3.2	271	660
1.6	5.7	265	600
1.8	14.6	251	534
2.0	–	233	442

Reproduced from Workability and Mechanical Properties of Tensile Strain–Hardening PVA Fiber-Reinforced Magnesium Phosphate Cement Composites by Shuwen Zhang with permission from ASCE

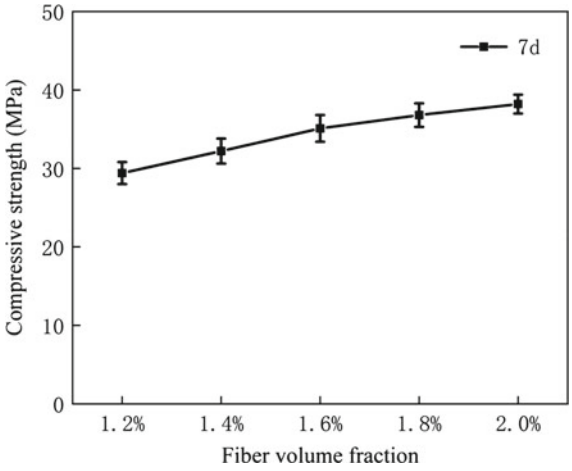

Fig. 1.13 Compressive strength of the UHDMC with varying fiber volume fractions. Reproduced from Workability and Mechanical Properties of Tensile Strain–Hardening PVA Fiber-Reinforced Magnesium Phosphate Cement Composites by Shuwen Zhang with permission from ASCE

(3) **Tensile properties**

Figure 1.14 shows the direct tensile stress–strain curves of the UHDMC with varying fiber volume fractions. It is found that all samples show strain hardening behavior regardless of the fiber volume fraction. The peak tensile stress and peak tensile strain are relatively small when the V_f is 1.2% and then continue to increase when the V_f varies from 1.2 to 1.4%; however, when the V_f varies from 1.4 to 2.0%, only the peak tensile stress increases, and the peak tensile strain changes little.

Figure 1.15a shows the peak tensile stress and peak tensile strain of the UHDMC with varying fiber volume fractions (V_f). It is found that both the peak tensile stress and the peak tensile strain of the UHDMC increase gradually as the V_f increases from 1.2 to 2.0%. Figure 1.15b shows the ultimate tensile stress and ultimate tensile strain of the UHDMC with varying V_f. It is found that the ultimate tensile stress of the UHDMC gradually increases as the V_f increases from 1.2 to 2.0%, while the ultimate tensile strain reaches the peak when the V_f is 1.8%. Overall, it can be concluded that the tensile behavior of the UHDMC is relatively excellent when the V_f is 2.0%.

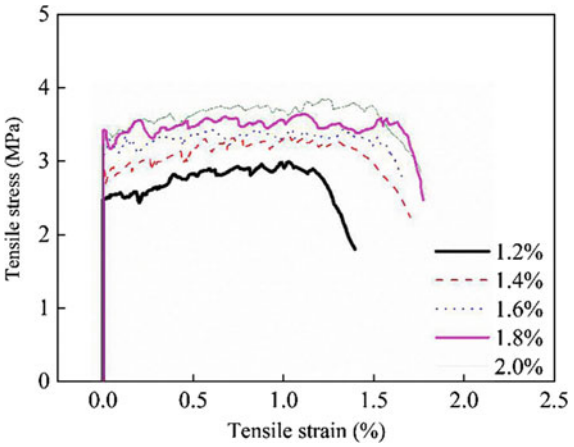

Fig. 1.14 Direct tensile stress–strain curves of the UHDMC with varying fiber volume fractions. Reproduced from Workability and Mechanical Properties of Tensile Strain–Hardening PVA Fiber-Reinforced Magnesium Phosphate Cement Composites by Shuwen Zhang with permission from ASCE

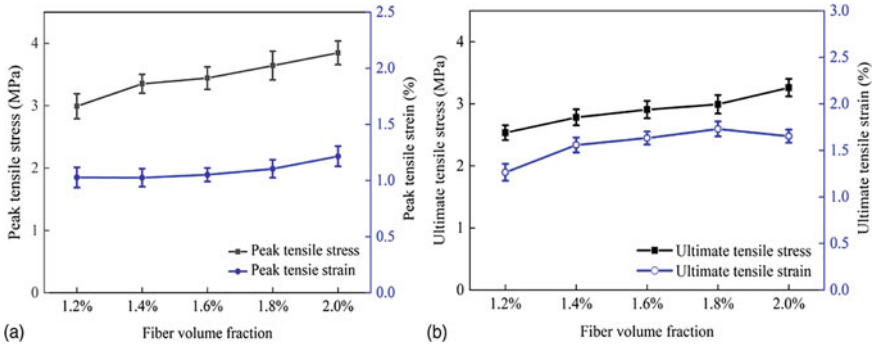

Fig. 1.15 **a** Peak tensile stress and peak tensile strain; and **b** ultimate tensile stress and ultimate tensile strain of the UHDMC with varying fiber volume fractions. Reproduced from Workability and Mechanical Properties of Tensile Strain–Hardening PVA Fiber-Reinforced Magnesium Phosphate Cement Composites by Shuwen Zhang with permission from ASCE

(4) **Flexural behaviour**

Table 1.11 shows the flexural test results of the UHDMC with varying fiber volume fractions. The first cracking strength, modulus of rupture, and their corresponding deflections are listed in Table 1.11, with each data being the average value of three identical specimens.

Figure 1.16 shows the effect of V_f (1.2–2.0%) on the flexural load-mid span deflection response of UHDMC. As shown in this figure, all UHDMC, regardless of V_f, exhibit a deflection hardening response. The f_{LOP}, MOR, and their corresponding

Table 1.11 Flexural test results of the UHDMC with varying fiber volume fractions

Mix ID (%)	f_{LOP} (MPa)	δ_{LOP} (mm)	MOR (MPa)	δ_{MOR} (mm)
V_f-1.2	3.24	0.33	4.55	19.62
V_f-1.4	4.07	0.34	6.06	20.29
V_f-1.6	6.38	0.65	7.60	25.12
V_f-1.8	5.99	0.49	7.65	24.10
V_f-2.0	6.44	0.46	8.09	20.69

Reproduced from Deflection hardening behaviour of ductile fibre reinforced magnesium phosphate cement-based composite by Hu Feng with permission from Elsevier

deflections δ_{LOP} and δ_{MOR}, are listed in Table 1.11. Among these UHDMCs, V_f-1.6% and V_f-2.0% exhibit the highest δ_{MOR} (25.12 mm) and MOR (8.09 MPa), corresponding to their excellent deflection and load-bearing capacities, respectively. Moreover, it is noted that f_{LOP} and MOR increase significantly by 56.8 and 25.4%, respectively, when V_f varies from 1.4 to 1.6%, as shown in Fig. 1.16. This may be because of the greatly enhanced interfacial bond strength between the fibers and the matrix when the V_f varies from 1.4 to 1.6%. Thereafter, this improvement tends to be small as the V_f varies from 1.6 to 2.0%. A similar trend is observed when the V_f varies from 1.4 to 1.6% for the δ_{LOP} and δ_{MOR} of UHDMC. However, a remarkable decrease in δ_{MOR} is observed when the V_f is above 1.8%. This may be due to the excess fiber aggregates in the matrix reducing the deflection capacity of the UHDMC.

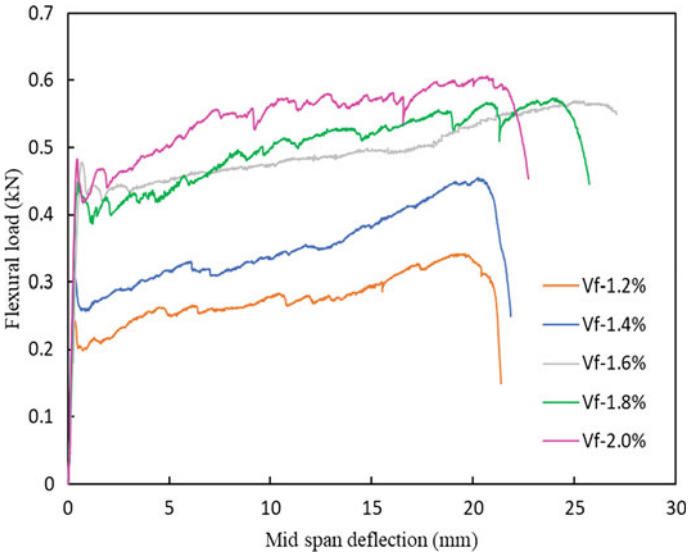

Fig. 1.16 Flexural load–mid span deflection response of the UHDMC with varying V_f. Reproduced from Deflection hardening behaviour of ductile fibre reinforced magnesium phosphate cement-based composite by Hu Feng with permission from Elsevier

In this series, the f_g, D_g, T_{peak} and T_g of the UHDMC as a funcation of V_f are calculated to quantitatively evaluate its deflection hardening capacity. Figure 1.17 shows that the f_g is greater than zero for all UHDMCs, which results in a deflection hardening response. Among all UHDMCs with varying V_f, the V_f-1.6% UHDMC exhibits the highest D_g of 24.47 mm, while the V_f-1.4% UHDMC shows the highest f_g of 1.99 MPa. In this case, it is difficult to confirm which sample has more excellent deflection hardening capacity. Figure 1.18 shows the calculation results of the T_{peak} and T_g of UHDMCs. Among all UHDMCs, the UHDMC with V_f-1.6% has the highest T_{peak} (12.23 kN mm) and T_g (12.07 kN mm), showing excellent deflection capacity.

The cracking patterns of UHDMC with different V_f are shown in Fig. 1.19. It is found that the crack distribution of V_f-1.6% specimen is more uniform and denser than those of other specimens, proving its excellent deflection hardening capacity. The number of cracks, crack spacing, and crack width of the UHDMC with varying V_f were shown in Table 1.12. It is shown that the V_f-1.6% sample has the maximum number of cracks but the smallest crack spacing and crack width, which is consistent with the visible observation. In general, the deflection hardening capacity of UHDMC can be significantly improved with increasing fiber content up to V_f-1.6%. After that, higher fiber amounts may have negative effects.

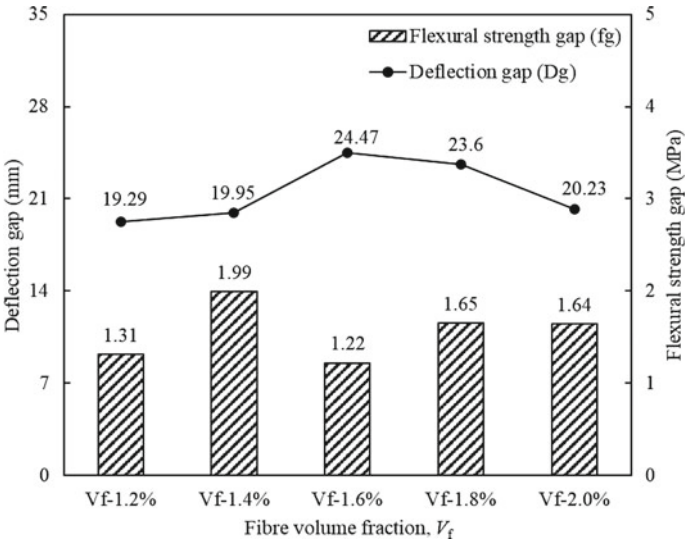

Fig. 1.17 Flexural strength gap and Deflection gap of the UHDMC with varying V_f. Reproduced from Deflection hardening behaviour of ductile fibre reinforced magnesium phosphate cement-based composite by Hu Feng with permission from Elsevier

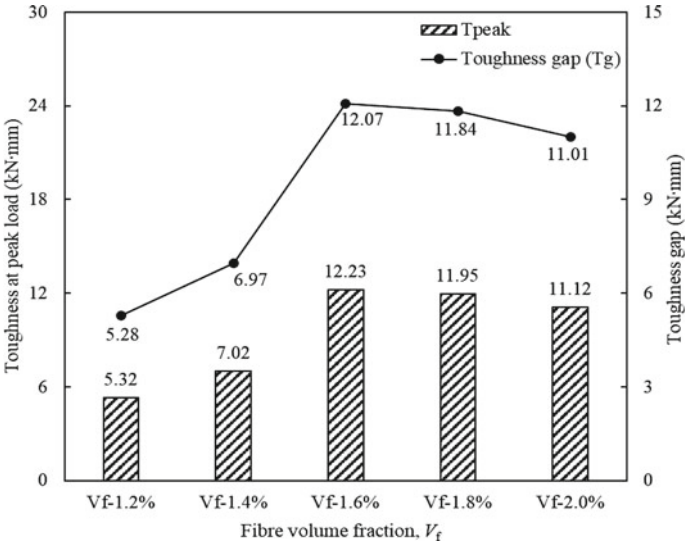

Fig. 1.18 T_{peak} and Toughness gap of the UHDMC with varying V_f. Reproduced from Deflection hardening behaviour of ductile fibre reinforced magnesium phosphate cement-based composite by Hu Feng with permission from Elsevier

1.3.3 Effect of Sand to Binder Mass Ratio (S/B)

(1) **Workability**

The workability of the UHDMC with varying sand to binder mass ratios (*S/B*) is shown in Table 1.13. According to the specification in CCES 02-2004 (Society, 2005), Table 1.13 shows that the UHDMC can achieve the self-compacting properties when the *S/B* is 0. As the *S/B* increases, the T_{500} increases, and the slump and slump flow decrease, which indicates a decrease in workability. Also, the T_{500} does not exist when the *S/B* is 0.4 or 0.6, because the workability of the UHDMC is too bad to record any value.

(2) **Compressive srength**

The 7d compressive strength of the UHDMC with different sand to binder mass ratios is shown in Fig. 1.20. The compressive strength of the UHDMC gradually decreases as the *S/B* increases. This may be because, on one hand, an increase in the amount of quartz sand can reduce the amount of cement paste, weakening the bonding between the paste and quartz sand; on the other hand, the increase in the amount of quartz sand can increase the internal porosity of the composite material (Ding & Li, 2005).

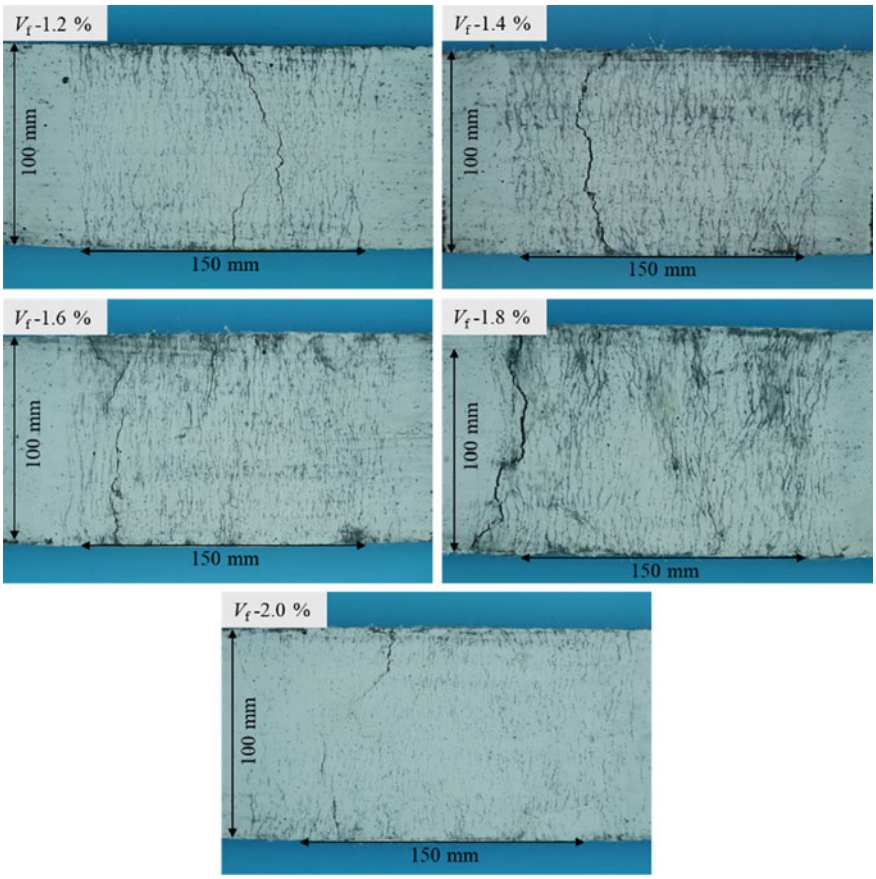

Fig. 1.19 The cracking patterns of the UHDMC with varying V_f. Reproduced from Deflection hardening behaviour of ductile fibre reinforced magnesium phosphate cement-based composite by Hu Feng with permission from Elsevier

Table 1.12 Cracking parameters of the UHDMC with varying V_f

Mix ID (%)	Number of cracks	Crack spacing (mm)	Crack width (μm)
V_f-1.2	65	2.31	93.8
V_f-1.4	68	2.21	91.1
V_f-1.6	83	1.81	81.7
V_f-1.8	75	2.00	87.8
V_f-2.0	71	2.11	89.4

Reproduced from Deflection hardening behaviour of ductile fibre reinforced magnesium phosphate cement-based composite by Hu Feng with permission from Elsevier

Table 1.13 Workability of the UHDMC with varying sand to binder mass ratios

Sand to binder mass ratio	T_{500} (s)	Slump (mm)	Slump flow (mm)
0.0	3.1	275	717
0.2	5.7	265	600
0.4	–	215	390
0.6	–	130	315

Reproduced from Workability and Mechanical Properties of Tensile Strain–Hardening PVA Fiber-Reinforced Magnesium Phosphate Cement Composites by Shuwen Zhang with permission from ASCE

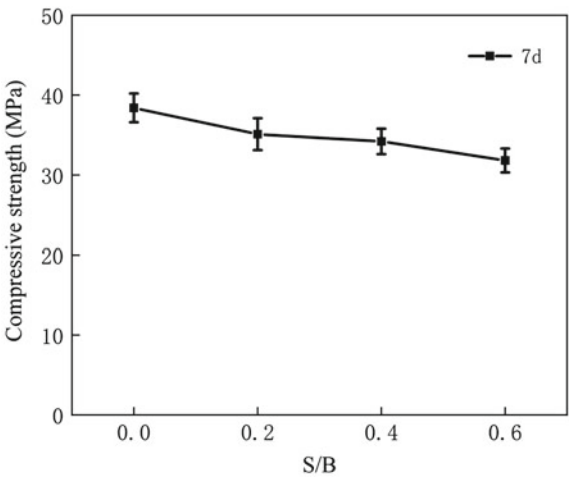

Fig. 1.20 Compressive strength of the UHDMC with varying sand-to-binder mass ratios. Reproduced from Workability and Mechanical Properties of Tensile Strain–Hardening PVA Fiber-Reinforced Magnesium Phosphate Cement Composites by Shuwen Zhang with permission from ASCE

(3) **Tensile properties**

Figure 1.21 shows the effect of sand to binder mass ratio (*S/B*) on the direct tensile stress–strain curve of the UHDMC. When the *S/B* is 0, the strain hardening characteristic of the UHDMC is obvious. When the *S/B* increases from 0 to 0.2, the strain hardening characteristic of the UHDMC fades, so the peak tensile stress and peak tensile strain decrease greatly. When the *S/B* ranges from 0.2 to 0.6, the strain hardening characteristic of the UHDMC changes little, so the peak tensile stress does not change much, but the peak tensile strain decreases greatly. In addition, the sand size also affects the strain hardening of UHDMC. The quartz sand used in this study is rather coarse. However, if finer grained sand is used, more pastes are needed to cover the surface of sand due to its higher specific surface area. Then the flowability of the UHDMC can be reduced, and the PVA fibers cannot be uniformly distributed well, which may increase the porosity of UHDMC and result in less obvious strain hardening behavior (Shen, 2020).

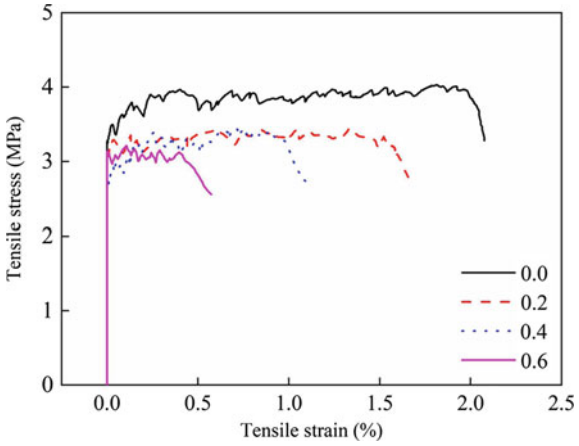

Fig. 1.21 Direct tensile stress–strain curves of the UHDMC with varying sand to binder mass ratios. Reproduced from Workability and Mechanical Properties of Tensile Strain–Hardening PVA Fiber-Reinforced Magnesium Phosphate Cement Composites by Shuwen Zhang with permission from ASCE

Figure 1.22a shows the peak tensile stress and the peak tensile strain of the UHDMC with different sand to binder mass ratios. It is found that the peak tensile stress and peak tensile strain of the UHDMC gradually decrease as the *S/B* increases from 0 to 0.6. Figure 1.22b shows the ultimate tensile stress and the ultimate tensile strain of the UHDMC with different sand to binder mass ratios. Similarly, it is found that the ultimate tensile stress and ultimate tensile strain of the UHDMC gradually decrease as the *S/B* increases from 0 to 0.6. In general, when the *S/B* is 0, the tensile behavior of the UHDMC is the most excellent.

(4) **Flexural behaviour**

Table 1.14 shows the flexural test results of the UHDMC with different sand-to-binder mass ratios. The first cracking strength, modulus of rupture (also known as ultimate flexural strength) and the corresponding deflection are listed in Table 1.14, with each data being the average value of three identical specimens.

From Table 1.14, it can be seen that all UHDMCs, regardless of the *S/B* ratio, have higher MOR than f_{LOP}, resulting in a typical deflection hardening response, as shown in Fig. 1.23. Figure 1.23 shows the flexural load-mid span deflection response of UHDMC with different sand to binder mass (*S/B*) ratios. The ultimate flexural strength and first cracking strength of UHDMC are significantly decreased as the *S/B* ratio increases from 0 to 0.4. This could be because the sand has relatively larger particle size than the MPC, which increases the porosity of the UHDMC matrix, thereby reducing the cracking toughness of the matrix and the bonding strength between fibers and the matrix. As the *S/B* ratio increases from 0.4 to 0.6, the first

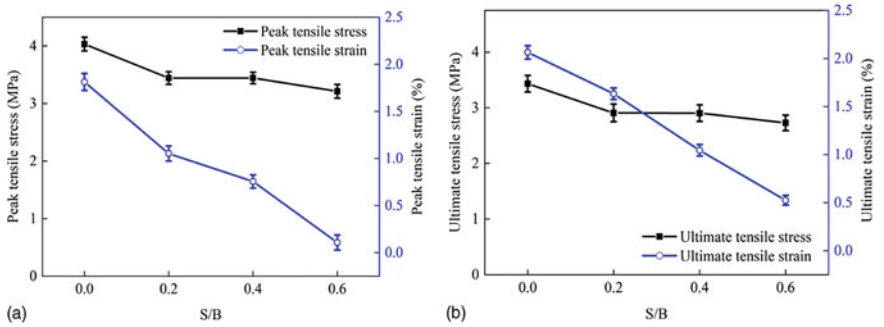

Fig. 1.22 **a** Peak tensile stress and peak tensile strain; and **b** ultimate tensile stress and ultimate tensile strain of the UHDMC with different sand-to-binder mass ratios. Reproduced from Workability and Mechanical Properties of Tensile Strain–Hardening PVA Fiber-Reinforced Magnesium Phosphate Cement Composites by Shuwen Zhang with permission from ASCE

Table 1.14 Flexural test results of the UHDMC with varying sand-to-binder mass ratios

Mix ID	f_{LOP} (MPa)	δ_{LOP} (mm)	MOR (MPa)	δ_{MOR} (mm)
S/B-0	7.81	0.57	8.68	21.38
S/B-0.2	6.38	0.65	7.60	25.12
S/B-0.4	5.35	0.40	6.50	12.59
S/B-0.6	6.82	0.65	6.86	14.85

Reproduced from Deflection hardening behaviour of ductile fibre reinforced magnesium phosphate cement-based composite by Hu Feng with permission from Elsevier

cracking strength of UHDMC increases greatly, while the ultimate flexural strength changes little. This shows that the cracking toughness of the matrix can be increased significantly by the addition of a large amount of sand, but the bonding strength between fibers and the matrix is only slightly improved. In addition, the ultimate cracking deflection of UHDMC can be greatly increased by the addition of a small amount of sand (e.g., *S/B*-0.2) but reduced by the addition of excess sand (e.g., *S/B*-0.4 and *S/B*-0.6). Overall, the UHDMC with *S/B*-0 has the highest f_{LOP} (7.81 MPa) and MOR (8.68 MPa), which reflects its excellent load-carrying capacity, while the UHDMC with *S/B*-0.2 has the highest δ_{LOP} (0.65 mm) and δ_{MOR} (25.12 mm).

The f_g, D_g, T_{peak} and T_g are calculated to further evaluate the deflection hardening capacity of each UHDMC. Figure 1.24 shows the f_g and D_g of UHDMC with different *S/B*. It can be seen that *S/B*-0.6 has the smallest f_g (0.04 MPa) but still exceeds zero, resulting in a deflection hardening response. It is worth noting that the UHDMC with *S/B*-0.6 has the lowest f_g because of its relatively higher f_{LOP} as compared to other UHDMCs. The *S/B*-0.2 UHDMC has the highest f_g of 1.22 MPa and D_g of 24.47 mm among all UHDMCs with different *S/B* ratios, reflecting its excellent deflection capacity. Afterwards, it can be observed that the D_g decreases sharply as the *S/B* varies from 0.2 to 0.4, reflecting a significant decrease in the deflection capacity.

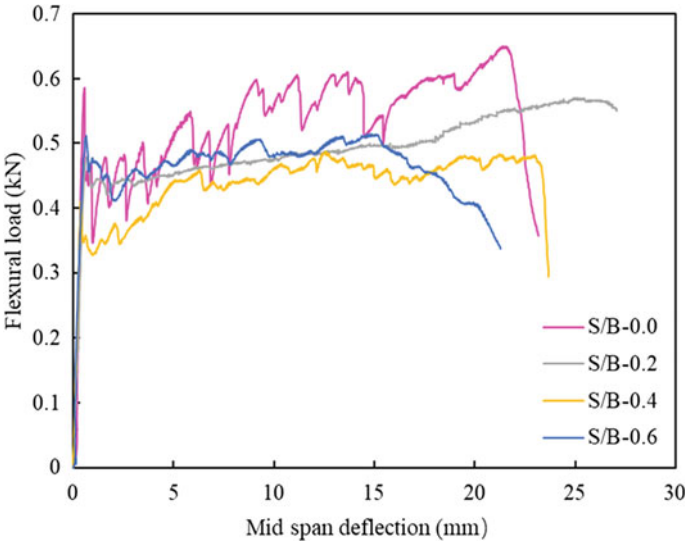

Fig. 1.23 Flexural load-mid span deflection response of UHDMCs with varying *S/B* ratios. Reproduced from Deflection hardening behaviour of ductile fibre reinforced magnesium phosphate cement-based composite by Hu Feng with permission from Elsevier

Nevertheless, the D_g increases slightly as the *S/B* ratio increases to 0.6. Furthermore, Fig. 1.25 shows the calculation results of toughness parameters (T_{peak} and T_g) of UHDMC with different *S/B* ratios. The change of these two parameters shows a similar trend. As the *S/B* ratio increases, the T_{peak} and T_g of UHDMC first reach the peak at *S/B*-0.2 and then drop to the lowest value at *S/B*-0.4.

Figure 1.26 shows the multiple cracking patterns of UHDMCs with different *S/B* ratios. The distribution of cracks for the *S/B*-0.2 sample is more uniform and denser as compared to those of *S/B*-0, *S/B*-0.4 and *S/B*-0.6 samples. The number of cracks, crack spacing, and crack width of the UHDMC with varying *S/B* ratios are listed in Table 1.15. It can be seen that the *S/B*-0.2 has the maximum number of cracks but the smallest crack spacing and crack width, which suggests that the *S/B*-0.2 sample has significantly higher deflection hardening capacity.

1.3.4 Effect of Water to Solid Mass Ratio (W/S)

(1) **Workability**

The workability of the UHDMC with varying water to solid mass ratios (*W/S*) is shown in Table 1.16. According to the specifications in CCES 02-2004 (Society, 2005), Table 1.16 shows that the UHDMC cannot achieve self-compacting performance regardless of the *W/S*. When the *W/S* is 0.10, the T_{500} is missing, which is

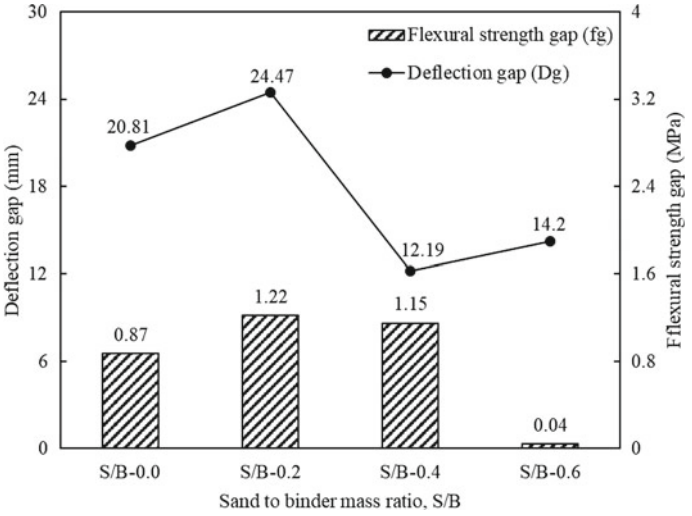

Fig. 1.24 T_{peak} and Toughness gap of UHDMCs with varying *S/B* ratios. Reproduced from Deflection hardening behaviour of ductile fibre reinforced magnesium phosphate cement-based composite by Hu Feng with permission from Elsevier

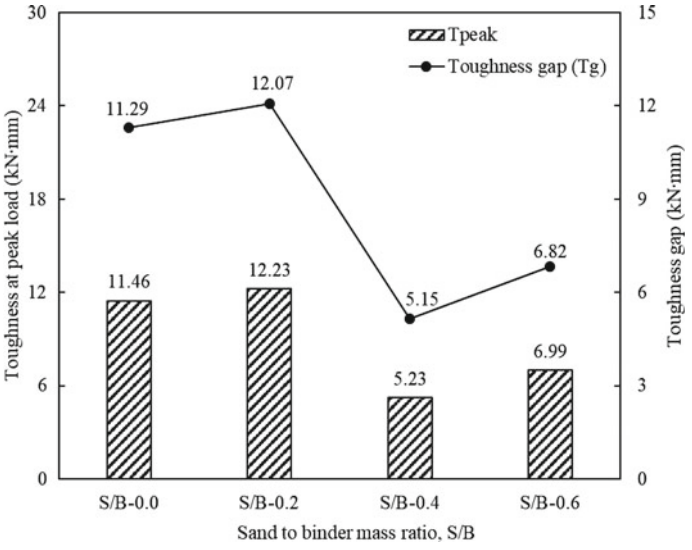

Fig. 1.25 Flexural strength gap and Deflection gap of UHDMCs with varying *S/B* ratios. Reproduced from Deflection hardening behaviour of ductile fibre reinforced magnesium phosphate cement-based composite by Hu Feng with permission from Elsevier

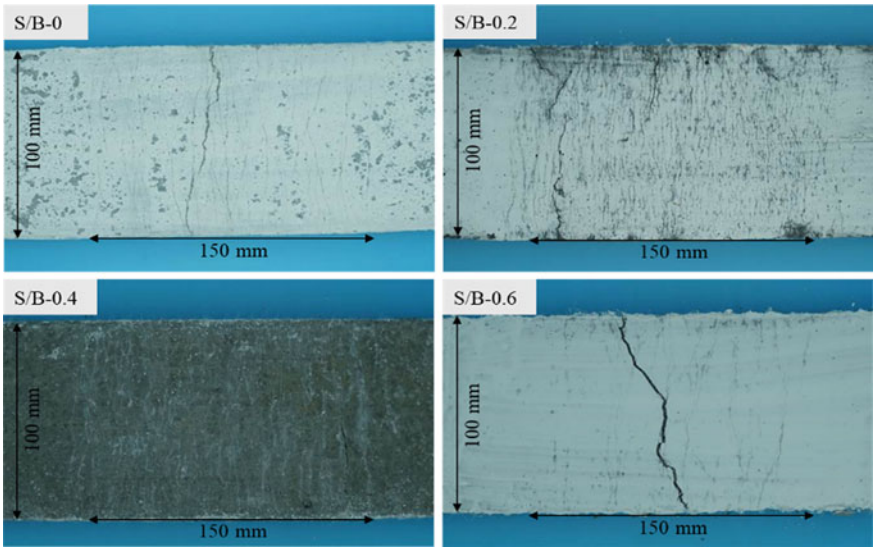

Fig. 1.26 The cracking patterns of UHDMCs with varying *S/B* ratios. Reproduced from Deflection hardening behaviour of ductile fibre reinforced magnesium phosphate cement-based composite by Hu Feng with permission from Elsevier

Table 1.15 Cracking parameters of the UHDMC with varying *S/B* ratios

Mix ID	Number of cracks	Crack spacing (mm)	Crack width (μm)
S/B-0	45	3.41	114.2
S/B-0.2	83	1.81	81.7
S/B-0.4	70	2.14	87.4
S/B-0.6	24	4.75	177.1

Reproduced from Deflection hardening behaviour of ductile fibre reinforced magnesium phosphate cement-based composite by Hu Feng with permission from Elsevier

due to the poor workability of UHDMC. As the *W/S* increases from 0.10 to 0.19, the T_{500} decreases, and the slump and slump flow increase, which indicates an increase in workability.

(2) **Compressive strength**

The 7d compressive strength of the UHDMC with different water to solid mass ratios is shown in Fig. 1.27. As the *W/S* increases from 0.10 to 0.19, the compressive strength of the UHDMC gradually decreases. This is because the porosity in the hardened cement paste increases with the increase of the water–solid ratio, thus reducing the compressive strength.

Table 1.16 Workability of the UHDMC with varying water to solid mass ratios

Water to solid mass ratio	T_{500} (s)	Slump (mm)	Slump flow (mm)
0.10	–	270	365
0.13	5.7	265	600
0.16	1.3	260	660
0.19	1.0	235	740

Reproduced from Workability and Mechanical Properties of Tensile Strain–Hardening PVA Fiber-Reinforced Magnesium Phosphate Cement Composites by Shuwen Zhang with permission from ASCE

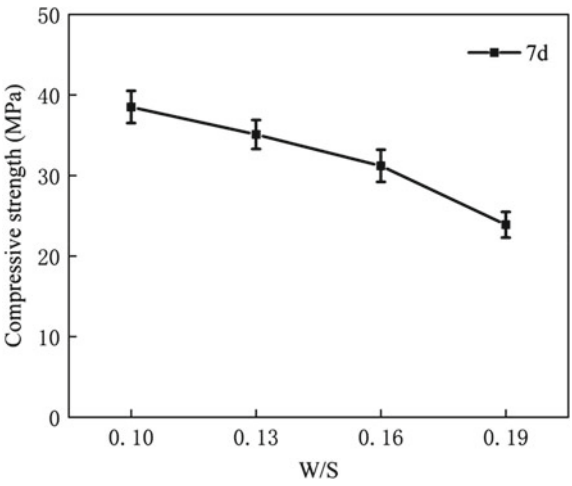

Fig. 1.27 Compressive strength of the UHDMC with varying water-to-solid mass ratios. Reproduced from Workability and Mechanical Properties of Tensile Strain–Hardening PVA Fiber-Reinforced Magnesium Phosphate Cement Composites by Shuwen Zhang with permission from ASCE

(3) **Tensile properties**

Figure 1.28 shows the effect of water to solid mass ratio (*W/S*) on the direct tensile stress–strain curve of the UHDMC. It can be seen that the strain hardening characteristics of the UHDMCs with different *W/S* values are not significant. The peak tensile stress gradually reduces as the *W/S* increases from 0.10 to 0.19. The peak tensile strain is the highest when the *W/S* is 0.16.

Figure 1.29a shows the peak tensile stress and the peak tensile strain of the UHDMC with varying water-to-solid mass ratios. Figure 1.29b shows the ultimate tensile stress and the ultimate tensile strain of the UHDMC with varying water-to-solid mass ratios. It can be seen that with the increase of *W/S*, both the ultimate tensile stress and the peak tensile stress decrease, and both the peak tensile strain and the ultimate tensile strain reach the peak at the *W/S* of 0.16. Therefore, a balance between the tensile stress and the tensile strain needs to be done when determining

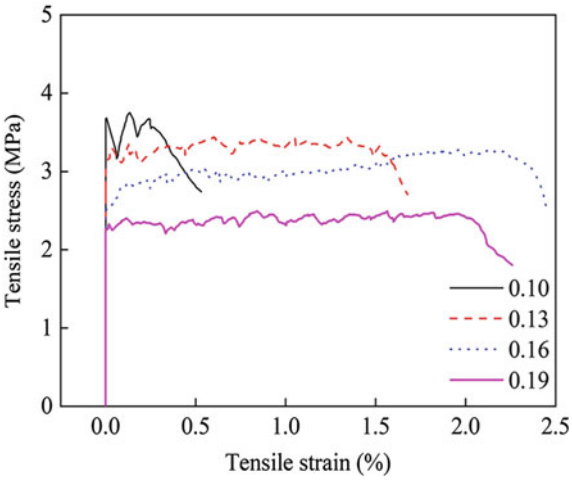

Fig. 1.28 Direct tensile stress–strain curves of the UHDMC with varying water-to-solid mass ratios. Reproduced from Workability and Mechanical Properties of Tensile Strain–Hardening PVA Fiber-Reinforced Magnesium Phosphate Cement Composites by Shuwen Zhang with permission from ASCE

the optimal *W/S* ratio. Overall, the tensile behavior of the UHDMC can be relatively good when the *W/S* is 0.13 or 0.16.

(4) **Flexural behaviour**

Table 1.17 shows the flexural test results of the UHDMC with different water-to-solid mass ratios. The first cracking strength, modulus of rupture (also known as ultimate flexural strength), and the corresponding deflections are listed in Table 1.17, with each data being the average value of three identical specimens.

According to Table 1.17 and Fig. 1.30, the f_{LOP} and MOR of the UHDMC with *W/S*-0.10 are the same, which is indicative of a deflection softening response. The *W/S*-0.13, *W/S*-0.16, and *W/S*-0.19 show MOR > f_{LOP}, showing deflection hardening

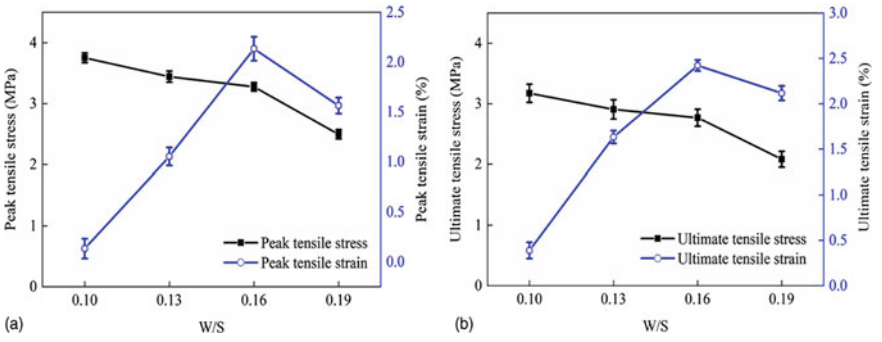

Fig. 1.29 **a** Peak tensile stress and peak tensile strain; and **b** ultimate tensile stress and ultimate tensile strain of the UHDMC with varying water-to-solid mass ratios. Reproduced from Workability and Mechanical Properties of Tensile Strain–Hardening PVA Fiber-Reinforced Magnesium Phosphate Cement Composites by Shuwen Zhang with permission from ASCE

Table 1.17 Flexural test results of the UHDMC with different water-to-solid mass ratios

Mix ID	f_{LOP} (MPa)	δ_{LOP} (mm)	MOR (MPa)	δ_{MOR} (mm)
W/S-0.10	8.32	0.67	8.32	0.67
W/S-0.13	6.38	0.65	7.60	25.12
W/S-0.16	6.57	0.55	8.15	24.05
W/S-0.19	5.06	0.57	6.34	24.26

Reproduced from Deflection hardening behaviour of ductile fibre reinforced magnesium phosphate cement-based composite by Hu Feng with permission from Elsevier

behaviour. For all UHDMCs, as the *W/S* ratio increases from 0.13 to 0.19, both f_{LOP} and MOR first increase and then decrease. When the *W/S* is 0.16, the f_{LOP} reaches the highest value of 6.57 MPa, and the MOR reaches the highest value of 8.15 MPa. When the *W/S* is 0.19, the f_{LOP} reaches the lowest value of 5.06 MPa, and the MOR reaches the lowest value of 6.34 MPa. It is well known that a large amount of mixing water creates some pores inside of the MPC-based matrix, so the UHDMC with *W/S*-0.19 would contain more pores than other samples, resulting in lower f_{LOP} and MOR values. In terms of δ_{LOP} and δ_{MOR}, the UHDMC has the highest δ_{LOP} of 0.68 mm and δ_{MOR} of 25.12 mm at *W/S*-0.13, and then these two values decrease to the lowest at *W/S*-0.16. This shows that the *W/S*-0.16 UHDMC has excellent flexural strength.

The deflection hardening behaviour of UHDMC with varying *W/S* ratios can also be quantitatively evaluated by calculating the f_g, D_g, T_{peak} and T_g of UHDMC. As presented in Fig. 1.31, it is observed that the f_g exceeds zero for all UHDMCs,

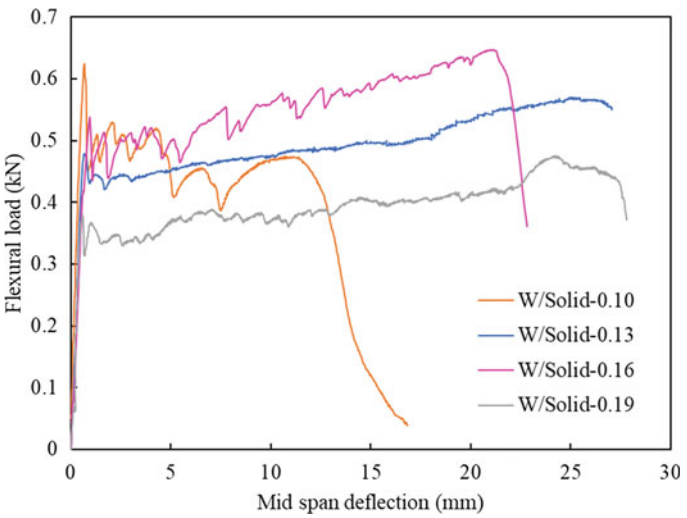

Fig. 1.30 Flexural load-mid span deflection response of the UHDMC with varying *W/S* ratios. Reproduced from Deflection hardening behaviour of ductile fibre reinforced magnesium phosphate cement-based composite by Hu Feng with permission from Elsevier

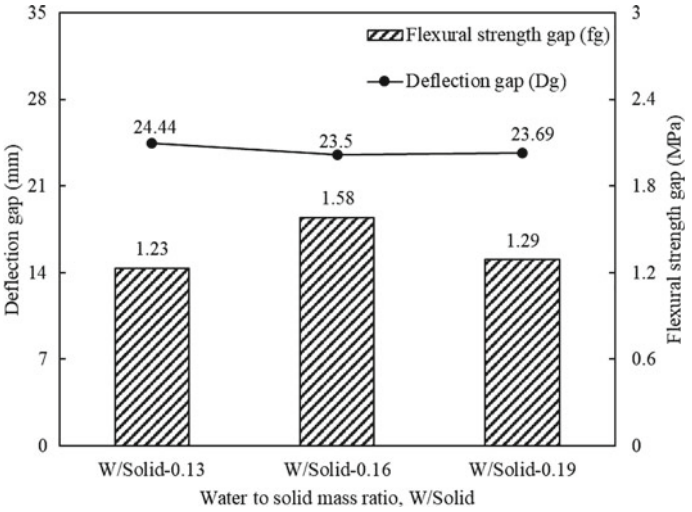

Fig. 1.31 Flexural strength gap and Deflection gap of the UHDMC with varying *W/S* ratios. Reproduced from Deflection hardening behaviour of ductile fibre reinforced magnesium phosphate cement-based composite by Hu Feng with permission from Elsevier

resulting in a deflection hardening response. Furthermore, the UHDMC with *W/S*-0.16 shows the highest f_g, while the UHDMC with *W/S*-0.13 shows the highest D_g. Therefore, it is necessary to calculate the T_{peak} and T_g of UHDMC with different *W/S* ratios. As shown in Fig. 1.32, the UHDMC with *W/S*-0.13 exhibits the largest T_{peak} (12.23 kN mm) and T_g (12.07 kN mm), slightly higher than *W/S*-0.16 UHDMC. These results indicate that the UHDMC with *W/S*-0.13 has excellent deflection hardening capacity.

Figure 1.33 shows the cracking patterns of the UHDMC with different *W/S* ratios. For *W/S*-0.13 samples, the distribution of cracks is more uniform and denser as compared to other samples. The number of cracks, crack spacing, and crack width of the UHDMC with varying *W/S* ratios are listed in Table 1.18. Table 1.18 shows that the *W/S*-0.13 sample has the maximum number of cracks but the smallest crack spacing and crack width, reflecting its excellent deflection hardening capacity.

1.3.5 Microstructure

(1) Micro-morphology of a single PVA fiber

After the tensile failure of UHDMC occurs, the micro-morphology of single PVA fiber was examined through an optical microscope, as shown in Fig. 1.34. Some hydration products are found to be attached to the surface of PVA fibers in Fig. 1.34a, which indicates that the hydrophilic PVA fibers can be well bonded to the matrix.

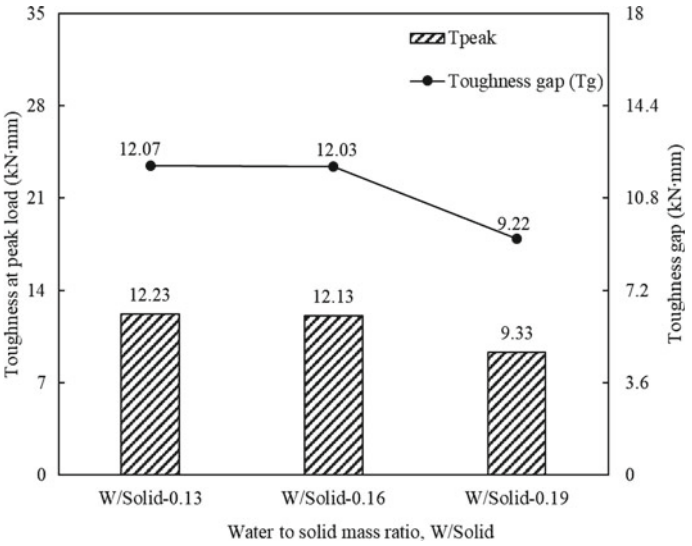

Fig. 1.32 T_{peak} and Toughness gap (T_g) of the UHDMC with varying *W/S* ratios. Reproduced from Deflection hardening behaviour of ductile fibre reinforced magnesium phosphate cement-based composite by Hu Feng with permission from Elsevier

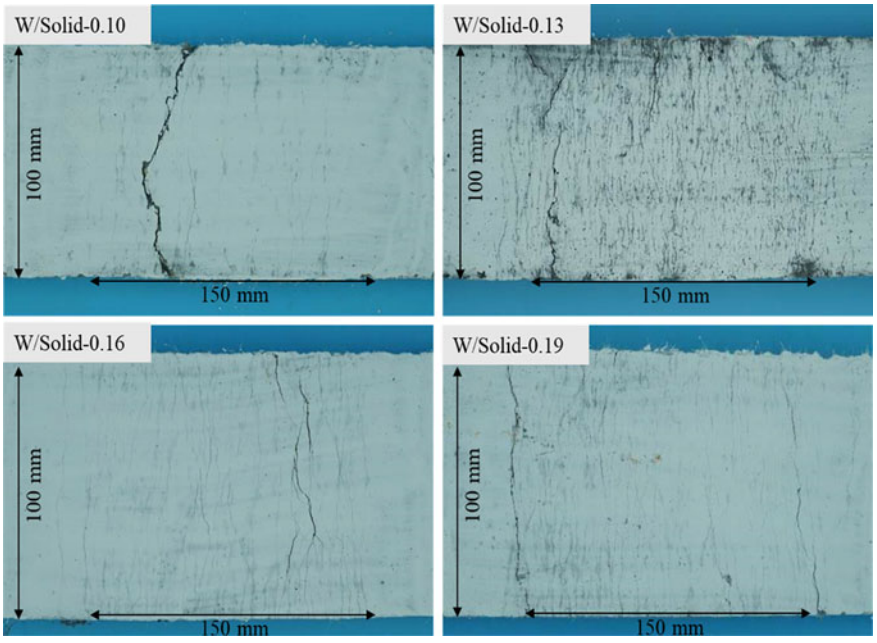

Fig. 1.33 The cracking patterns of UHDMC with varying *W/S* ratios. Reproduced from Deflection hardening behaviour of ductile fibre reinforced magnesium phosphate cement-based composite by Hu Feng with permission from Elsevier

Table 1.18 Cracking parameters of the UHDMC with varying *W/S* ratios

Mix ID	Number of cracks	Crack spacing (mm)	Crack width (μm)
W/S-0.10	23	5.37	N/A
W/S-0.13	83	1.81	81.7
W/S-0.16	53	2.95	107.9
W/S-0.19	56	2.67	105.3

Reproduced from Deflection hardening behaviour of ductile fibre reinforced magnesium phosphate cement-based composite by Hu Feng with permission from Elsevier

Additionally, obvious peeling and fracture marks (see red arrows) can be seen on the PVA fibers in Fig. 1.34b, because the surface of the PVA fibers is scratched by the matrix during the fiber pullout. The processes of peeling, slipping, and pulling out of PVA fibers consume a lot of energy and play a toughening role on the UHDMC.

(2) **Micro-strengthening mechanism of PVA fibers**

The PVA fiber/matrix interface of the UHDMC is examined, as shown in Fig. 1.35. It is found that some hydration products are firmly attached to the PVA fibers, indicating a good bonding. This indicates that the PVA fibers are well compatible with the UHDMC matrix, so they can be closely bonded together. During the tensile test, the PVA fibers play a critical role in preventing the initiation of cracks. If the cracks form unfortunately, the PVA fibers across the cracks can bridge the fractured pieces

Fig. 1.34 Morphology of a single PVA fiber **a** with hydration products and **b** with fracture marks. Reproduced from Workability and Mechanical Properties of Tensile Strain–Hardening PVA Fiber-Reinforced Magnesium Phosphate Cement Composites by Shuwen Zhang with permission from ASCE

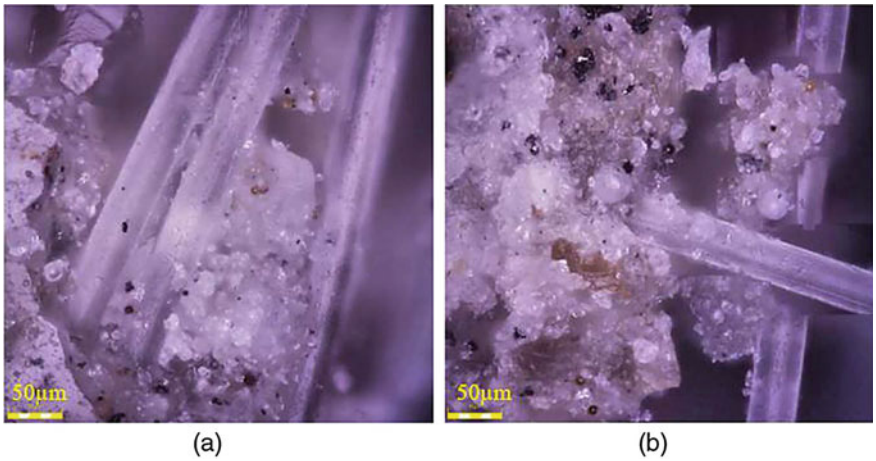

Fig. 1.35 Interface between PVA fibers and the UHDMC matrix: **a** Sample No. 1; and **b** Sample No. 2. Reproduced from Workability and Mechanical Properties of Tensile Strain–Hardening PVA Fiber-Reinforced Magnesium Phosphate Cement Composites by Shuwen Zhang with permission from ASCE

and prevent the propagation of cracks. In the process of crack growth, the frictional shear stress at the interface between PVA fibers and the matrix needs to be overcome to effectively limit the development of cracks.

1.4 Conclusions

In this chapter, the slump test, compressive test, tensile test, and four-point bending test are conducted on the ultra-high ductility magnesium phosphate cement-based composite (UHDMC) to examine its workability and mechanical properties. The effects of fly ash (FA) content, polyvinyl alcohol (PVA) fiber volume fraction (V_f), sand to binder mass ratio (*S/B*), and water to solid mass ratio (*W/S*) on the performance of the UHDMC are discussed and analyzed. Moreover, the optical microscopy test is conducted on the UHDMC to examine the morphology of PVA fibers and the interface between fibers and the matrix. Through this study, some important conclusions are drawn:

(1) As the FA content increases from 10 to 40%, the workability of the UHDMC decreases; when the FA content is 30%, the compressive strength, ultimate tensile stress, and peak direct tensile stress all show a downward trend; the peak tensile strain increases gradually; the ultimate tensile strain reaches the peak at the FA content of 30%. In addition, the flexural test results show that the UHDMC with FA-20% exhibits the highest D_g (24.39 mm), T_{peak} (12.23 kN mm), and T_g (12.06 kN mm) but the smallest f_g. Generally, when the FA

content is 20 or 30%, the UHDMC can obtain relatively high strength and strain capacity without significant workability loss.

(2) As the V_f increases from 1.2 to 2.0%, the workability of the UHDMC decreases; the compressive strength, peak direct tensile stress, ultimate tensile stress, and peak tensile strain gradually increase; the ultimate tensile strain reaches the peak at the V_f of 1.8%. In addition, the V_f-1.6% UHDMC shows the highest D_g (24.47 mm), T_{peak} (12.23 kN mm), and T_g (12.07 kN mm) while V_f-1.4% UHDMC shows the highest f_g (1.99 MPa) among all UHDMCs, which can clearly indicate its superior deflection capacity. Generally, the UHDMC can obtain relatively high workability, strength, and strain capacity at the V_f of 1.6% or 1.8%.

(3) As the *S/B* increases from 0 to 0.6, the workability, compressive strength, peak direct tensile stress, ultimate direct tensile stress, peak tensile strain, and ultimate tensile strain all decrease. In addition, the *S/B*-0.2 UHDMC shows the highest f_g (1.22 MPa), D_g (24.47 mm), T_g (12.07 kN · mm), and T_{peak} (12.23 kN mm) among all UHDMCs with different *S/B* ratios, thus clearly reflecting its excellent deflection capacity. Generally, when the *S/B* is 0 or 0.2, the UHDMC can obtain good workability, strength, and strain capacity.

(4) As the *W/S* increases from 0.10 to 0.19, the workability of the UHDMC increases; the peak direct tensile stress, ultimate tensile stress, and compressive strength decrease; the ultimate tensile strain and peak tensile strain reach the peak at the *W/S* of 0.16. In addition, the UHDMC with *W/S*-0.16 shows the highest f_g (1.58 MPa), while the UHDMC with *W/S*-0.13 shows the highest D_g (24.44 mm), T_{peak} (12.23 kN mm), and T_g (12.07 kN mm). Generally, when the *W/S* is 0.13 or 0.16, the UHDMC can obtain relatively high strain capacity and strength without significant workability loss.

(5) Some hydration products are attached to the surface of PVA fibers for the UHDMC, which indicates that the fibers are well combined with the matrix, thus improving the strength and strain capacity.

References

Ahmad, M. R., & Chen, B. (2018). Effect of silica fume and basalt fiber on the mechanical properties and microstructure of magnesium phosphate cement (MPC) mortar. *Construction and Building Materials, 190*, 466–478.

Ahmad, M. R., Chen, B., & Yu, J. (2019). A comprehensive study of basalt fiber reinforced magnesium phosphate cement incorporating ultrafine fly ash. *Composites Part B: Engineering, 168*, 204–217.

Banyhussan, Q. S., Yıldırım, G., Bayraktar, E., Demirhan, S., & Şahmaran, M. (2016). Deflection-hardening hybrid fiber reinforced concrete: The effect of aggregate content. *Construction and Building Materials, 125*, 41–52.

Ding, Z., & Li, Z. (2005). Effect of aggregates and water contents on the properties of magnesium phospho-silicate cement. *Cement and Concrete Composites, 27*(1), 11–18.

Ding, Z., Dai, J.-G., & Muner, S. (2014). Study on an improved phosphate cement binder for the development of fiber-reinforced inorganic polymer composites. *Polymers, 6*(11), 2819–2831.

Feng, H., Li, L., Zhang, P., Gao, D., Zhao, J., Feng, L., & Sheikh, M. N. (2020). Microscopic characteristics of interface transition zone between magnesium phosphate cement and steel fiber. *Construction and Building Materials, 253*, 119179.

Feng, H., Li, Z., Wang, W., Liu, G., Zhang, Z., & Gao, D. (2021). Deflection hardening behaviour of ductile fibre reinforced magnesium phosphate cement-based composite. *Cement and Concrete Composites, 121*, 104079.

Haque, M. A., Chen, B., & Ahmad, M. R. (2020). Mechanical strength and flexural parameters analysis of micro-steel, polyvinyl and basalt fibre reinforced magnesium phosphate cement mortars. *Construction and Building Materials, 235*, 117447.

Joo Kim, D., Naaman, A. E., & El-Tawil, S. (2008). Comparative flexural behavior of four fiber reinforced cementitious composites. *Cement and Concrete Composites, 30*(10), 917–928.

Martin, J., Stanton, J., Mitra, N., & Lowes, L. N. (2007). Experimental testing to determine concrete fracture energy using simple laboratory test setup. *ACI Materials Journal, 104*(6), 575.

Naaman, A., & Reinhardt, H. (1996). Characterization of high performance fiber reinforced cement composites—HPFRCC. High performance fiber reinforced cement composites.

Qin, J., Qian, J., Li, Z., You, C., Dai, X., Yue, Y., & Fan, Y. (2018). Mechanical properties of basalt fiber reinforced magnesium phosphate cement composites. *Construction and Building Materials, 188*, 946–955.

Sarker, P. K., Haque, R., & Ramgolam, K. V. (2013). Fracture behaviour of heat cured fly ash based geopolymer concrete. *Materials and Design, 44*, 580–586.

Seehra, S., Gupta, S., & Kumar, S. (1993). Rapid setting magnesium phosphate cement for quick repair of concrete pavements—characterisation and durability aspects. *Cement and Concrete Research, 23*(2), 254–266.

Shen, S. (2020). *Experimental study on bending property of high ductility magnesium phosphate cement-based composites under low temperature curing condition*. Zhengzhou University, Zhengzhou, China

Society, C. C. E. (2005). *Guide for design and construction of self-compacting concrete*. China Construction Industry Publishing House, Peking, China.

Standardization, C. A. F. E. C. (2012). *Technical specification for application of self-compacting concrete*. Construction Industry Publishing House, Peking, China.

Zhang, S., Zhu, Y., Feng, H., Guo, A., Shaukat, A. J., & Liu, G. (2022). Workability and mechanical properties of tensile strain-hardening PVA fiber-reinforced magnesium phosphate cement composites. *Journal of Materials in Civil Engineering, 34*(7), 04022138.

Chapter 2
Fundamental Performance of UHDMC with Hybrid Fibers

Abstract This chapter investigated the performance of ultra-high ductility magnesium phosphate cement-based composites (UHDMC) reinforced by multiple types of fibres. Compared with the use of a single type of fibre, the mixed use of multiple fibres can significantly improve both strength and toughness of the cementitious composites, which is referred to as the hybrid effect. Considering polyvinyl alcohol (PVA) fiber, micro steel (MS) fiber and polypropylene (PP) fiber are three of the most widely used fibers for UHDMC, this chapter introduced the hybrid effect of each two of these three fibers. The hybrid effects on workability, compressive strength, and flexural strength were investigated. In addition, the cracking propagation of UHDMC was observed and associated with the deflection by modelling. To further understand the mechanism of the hybrid effect, this chapter also provides the microstructural analysis of the UHDMC. The findings in this chapter indicated that the mixed use of hybrid fibers can effectively improve both strength and toughness of the UHDMC, providing the base for the design of high-performance UHDMC.

Keywords Hybrid fiber · Magnesium phosphate cement · Workability · Mechanical properties · Microstructures

2.1 Introduction

Despite its numerous benefits, the brittleness nature of MPC, significantly limiting its practical application in engineering. Thus, various types of fibres were added to overcome this drawback. For example, incorporating Polyvinyl alcohol fibers (PVA fibers) into MPC significantly enhances the deformability and toughness of MPC-based composites, exhibiting strain-hardening characteristics, greatly improving their ductility (Chen & Zhu, 2016). In addition to PVA fibers, steel fibers, glass fibers, and polypropylene fibers (PP) all contribute to notable improvements in the mechanical properties of MPC.

Different fibers exhibit varying performances at multiple scales, leading to a significantly different reinforcing effect. For instance, PVA fibers significantly

H. Feng et al., *Ultra-High Ductility Magnesium-Phosphate-Cement-Based Composites (UHDMC)*, https://doi.org/10.1007/978-981-97-0952-6_2

enhance the deformability and toughness of MPC-based composites, improving ductility, while PP fibers effectively increase the early flexural strength of MPC, improving its toughness (Jiahuan & Panhui et al., 2017; Quan-Bing et al., 2004). Steel fibers significantly enhance the compressive and flexural strength of MPC mortar, reducing mortar deformation and shrinkage and enhancing the wear resistance (Hongtao et al., 2006; Hu et al., 2018). Glass fiber significantly improves the bending strength of MPC materials (Jian-Ming et al., 2009). However, in engineering applications, various demands are often placed on cement materials, such as high strength, high deformability, and flexural toughness (Li et al., 1992), while the utilization of a single type of fiber cannot always satisfy multiple demands. To overcome this limitation, a combination of different fibers with distinct properties can be added to make UHDMC, which reinforces and toughens MPC at macro and micro levels. Moreover, the incorporation of multiple fibers can complement the advantages of various fibers, which played a significant role in designing UHDMC.

In this chapter, we discussed three types of fibres in pairs, including PVA fibers, PP fibers, and micro steel fibers. The effect of the mixed use of multiple fibres (hybrid effect) on the performance of UHDMC was investigated by analysing the workability, mechanical properties and cracking. Furthermore, the microstructure of UHDMC reinforced by hybrid fibers was also explored, providing insight into the mechanism of the hybrid effects.

2.2 Experimental Program

2.2.1 Raw Materials

The chemical components of magnesia oxide (MgO), potassium dihydrogen phosphate (KH_2PO_4), and borax ($Na_2B_4O_7 \cdot 10H_2O$) are the same as the ones in Chap. 1. Geometries and the mechanical properties of polyvinyl alcohol (PVA) fibers, polypropylene (PP) fibers and micro steel fibers are shown in Tables 2.1, 2.2 and 2.3.

For other materials in the preparation of UHDMC, the physical/chemical properties of silica sand (with grit of 80–120) and fly ash (with grit of 300) are shown in Tables 2.4 and 2.5 respectively.

Table 2.1 Physical and mechanical properties of PVA fibers (Li, 2020)

Diameter (μm)	Length (mm)	Tensile strength (MPa)	Elastic modulus (GPa)	Breaking elongation (%)	Density (g/cm^3)
40	12	1560	41	6.5	1.3

Table 2.2 Physical and mechanical properties of PP fibers (Li, 2020)

Diameter (μm)	Length (mm)	Tensile strength (MPa)	Elastic modulus (GPa)	Breaking elongation (%)	Density (g/cm^3)
25	12	410	3.5	12	0.91

Table 2.3 Physical and mechanical properties of MS fibers (Li, 2020)

Diameter (μm)	Length (mm)	Tensile strength (MPa)	Density (g/cm^3)	Geometry (g/cm^3)
220	13	2850	7.9	Hook end, smooth surface, round cross-section

Table 2.4 Physical properties of silica sand (Li, 2020)

Fraction of SiO_2	Unit weight	Moh's hardness	Porosity	Specific gravity
99.3%	1.8 g/cm^3	7.5	43%	2.66 g/cm^3

Table 2.5 Chemical components of fly ash (Li, 2020)

Components	SiO_2	Al_2O_3	Fe_2O_3	CaO	MgO	Na_2O
Fraction (%)	53.97	31.15	4.16	4.01	1.01	0.89

2.2.2 Mixed Design

Magnesium phosphate cement is composed of MgO, KDP, and borax. The molar ratio of MgO to KDP is 4:1, and the borax content is 6% of the mass of magnesium oxide. The mixed designs are shown in Table 2.6. Here, *S/C* represents the mass ratio of quartz sand to magnesium phosphate cement; *W/S* represents the mass ratio of water to solid components (magnesium phosphate cement, fly ash, and quartz sand); FA content is the mass ratio of fly ash replacing magnesium phosphate cement; Here, *S/C* is fixed at 0.2, *W/S* is 0.16, and fly ash substitution is 40%. As Liu Guanghui (Li)investigated the effect of PVA fiber content on the mechanical properties of magnesium phosphate cement, indicating MPC with the adding 1.6% PVA fibers showed excellent performance, the overall fiber content in this Chapter was designed to be 1.6%.

Table 2.6 Mixed design for UHDMC with hybrid fibers (Li, 2020)

Mixed design	No	*S/C*	*W/S*	FA content	The volume fraction of fibers		
					PVA	MS	PP
Fixed fiber fraction:1.6% Hybrid PVA and MS	1.6% PVA + 0.0% MS	0.2	0.16	40%	1.6%	0.0%	/
	1.2% PVA + 0.4% MS				1.2%	0.4%	
	0.8% PVA + 0.8% MS				0.8%	0.8%	
	0.4% PVA + 1.2% MS				0.4%	1.2%	
	0.0% PVA + 1.6% MS				0.0%	1.6%	
Fixed fiber fraction:1.6% Hybrid PP and MS	1.6% MS + 0.0% PP	0.2	0.16	40%	/	1.6%	0.0%
	1.2% MS + 0.4% PP					1.2%	0.4%
	0.8% MS + 0.8% PP					0.8%	0.8%
	0.4% MS + 1.2% PP					0.4%	1.2%
	0.0% MS + 1.6% PP					0.0%	1.6%
Fixed fiber fraction:1.6% Hybrid PVA and PP	1.6% PVA + 0.0% PP	0.2	0.16	40%	1.6%	/	0.0%
	1.2% PVA + 0.4% PP				1.2%		0.4%
	0.8% PVA + 0.8% PP				0.8%		0.8%
	0.4% PVA + 1.2% PP				0.4%		1.2%
	0.0% PVA + 1.6% PP				0.0%		1.6%
Fixed PP fiber fraction:1.6% Hybrid with MS	1.6% PP + 0.0% MS	0.2	0.16	40%	1.6%	0.0%	/
	1.6% PP + 0.2% MS					0.2%	
	1.6%PP + 0.4% MS					0.4%	

(continued)

Table 2.6 (continued)

Mixed design	No	*S/C*	*W/S*	FA content	The volume fraction of fibers		
					PVA	MS	PP
	1.6% PP + 0.6% MS					0.6%	
Fixed PVA fiber fraction:1.6% Hybrid with MS	1.6% PVA + 0.0% MS	0.2	0.16	40%	/	0.0%	1.6%
	1.6% PVA + 0.2% MS					0.2%	
	1.6% PVA + 0.4% MS					0.4%	
	1.6% PVA + 0.6% MS					0.6%	

Note S/C represents sand to MPC ratio, *W/S* represents water to solid ratio and FA represents fly ash

2.2.3 Mixing and Curing

Firstly, MgO, KDP, quartz sand, fly ash, and borax were added into a concrete mixer, and mixed for 120 s. Next, water was poured into the mixture and mixed for 20 s, followed by the incorporation of fibers and mixing for another 120 s to ensure the even dispersion of fibers in the mixture. Finally, the well-mixed mixture was transferred into cubic moulds with dimensions of 50.9 × 50.9 × 50.9 mm for the compressive test and steel moulds with dimensions of 400 × 100 × 15 mm for the flexural test. The fresh specimens were then placed on a vibrating table for compaction. To prevent fiber floatation, the compaction was completed in three stages. (1) Vibrating for 60 s, continuously patting the slurry with palms during vibration to remove trapped air, and scraping off excess slurry to ensure a smooth surface. (2) Leaving the specimens to stand for 10 s to observe the specimen's formation. (3) Vibrating two more times, each for 20 s. The specimens were demolded after 2 h and placed indoors for curing at 25 ± 2 °C and a relative humidity of 45 ± 5%. For the four-point bending test, a Minicut 40 cutting machine was used to cut the specimens into thin slices with a thickness of approximately 3 mm and an area of about 1 cm^2, ensuring the upper surface is the fractured surface, and the lower surface is smooth, as shown in Fig. 2.1a.

2.2.4 Slump Test

(1) Reference Standard: JGJ/T283-2012 "Technical Specification for Self-Compacting Concrete."
(2) Test Equipment: Concrete mixer, slump cone and base plate, tamping rod.

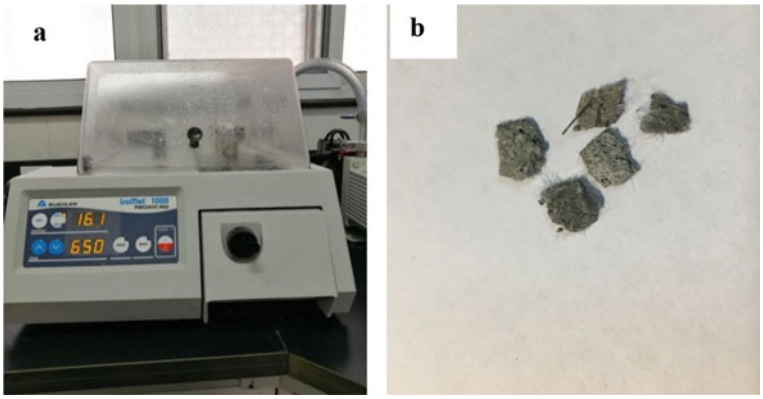

Fig. 2.1 **a** Minicut 40 cutter, **b** samples for microstructural analysis (Li, 2020)

(3) Testing Method: The test begins by moistening the slump cone and base plate and placing the base plate on a level and firm surface. Then, the well-mixed slurry of UHDMC was divided into three portions and filled into the slump cone. After each filling, the slurry was tamped 25 times from the outside to the inside with a rod to eliminate any large voids. When the slurry overflows from the slump cone, the excess slurry is removed from the top of the cone. Finally, the slump cone was raised smoothly and vertically at a constant speed. The time for the slurry to reach an extension of 50 cm (T50) was recorded, and then the final slump and expansion were measured.

2.2.5 Compressive Test

(1) Reference Standard: ASTM C109 "Standard Test Method for Compressive Strength of Hydraulic Cement Mortars"
(2) Testing Equipment: Compression Testing Machine (Model: YAW-2000B, Capacity: 2000 kN)
(3) Testing Procedure: Cubic specimens, aged to the specified curing period, are placed in the centre position of the compression testing machine. Two smooth opposing faces of the specimens are chosen as the load-bearing surfaces. The loading rate of the compression testing machine is set to 0.9 kN/s, and the load is applied until failure. The compressive strength is recorded while observing the failure mode.

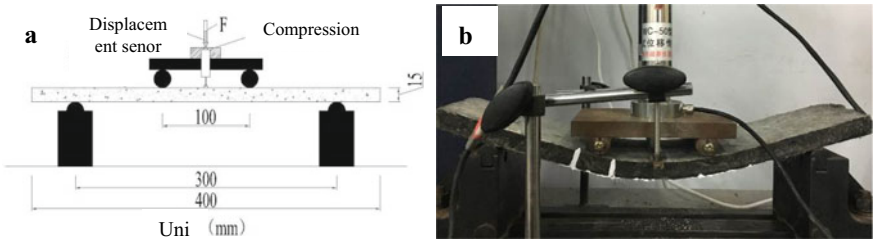

Fig. 2.2 **a** Schematic and **b** photo of the four-point bending test (Li, 2020)

2.2.6 Four-Point Bending Test

(1) Reference Standard: The four-point bending method as outlined in CECS 13:2009 "Standard Test Methods for Fiber-Reinforced Concrete."
(2) Test Equipment: Electronic Universal Testing Machine (Model: WDW-100, Capacity: 100 kN).
(3) Testing Procedure: The loading points on the prepared thin plate flexural specimens were marked and steel pieces were attached on either side of the mid-surface of the specimen. Then, specimens were placed on the electronic universal testing machine, aligning the two lower loading points with the support points., as depicted in Fig. 2.2. The loading speed of the testing machine was set to be 0.3 mm/min, and the strain acquisition system was used for data collection. The loading process was halted when significant cracks appeared at the bottom of the specimen.

2.2.7 Investigating the Microstructures

(1) Test Equipment: Auriga Focused Ion Beam Field Emission Scanning Dual-Beam Electron Microscope (Fig. 2.3).
(2) Testing Procedure: The prepared samples were placed into the RES102 Multi-functional Ion Thinning Instrument for gold sputtering, creating a thin metallic coating on the sample's surface to enhance conductivity for scanning electron microscopy (SEM). Then, the samples were inserted into the SEM chamber for imaging. The distribution of fibers in UHDMC, the fiber/matrix interface and the fiber failure morphology were observed.

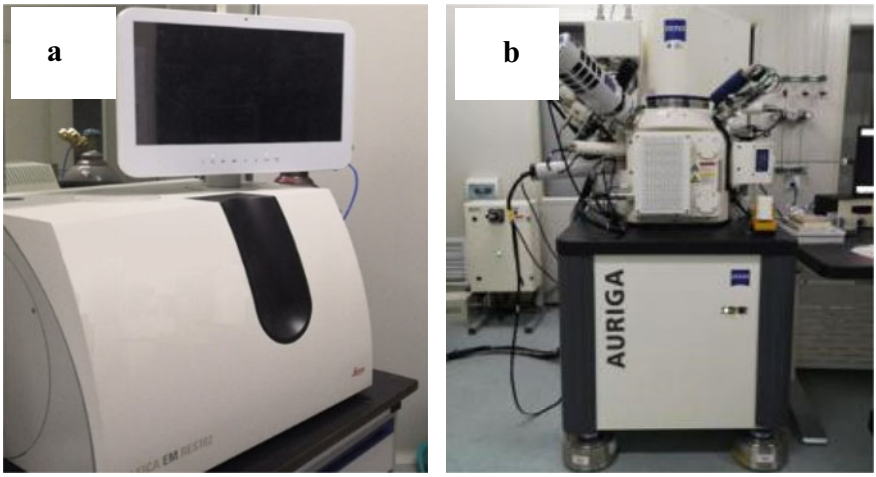

Fig. 2.3 **a** Leica EM RES102 Ion Mill **b** Auriga dual beam Scanning electron microscope (Li, 2020)

2.3 Results and Discussion

2.3.1 Workability

The workability can reflect the plasticity of UHDMC and directly affect the mixing, pouring, and practical application of the material in engineering. When fibers are introduced into MPC, the flowability of the slurry may decrease, potentially affecting its mechanical properties. Therefore, in this section, the hybrid effect of fibers on the workability of UHDMC was introduced.

2.3.1.1 Hybrid PVA and MS

Keeping the total fiber volume content of 1.6%, the hybrid effect of PVA and MS fibers on the workability of UHDMC was examined. Experimental data can be found in Table 2.7, where the time taken for the slurry to extend to 50 cm is denoted as T50, and the expansion refers to the average of the final expansion in both horizontal and vertical directions.

Experimental results reveal that with an increase in PVA fibers and a decrease in MS fibers, the T50 of the UHDMC gradually increases while the expansion decreases. When the hybrid system contains 0.0% PVA and 1.6% MS, the T50 of the UHDMC is 0.9 s, with a final expansion of 75 cm, indicating excellent workability. For 0.4% PVA + 1.2% MS, 0.8% PVA + 0.8% MS, and 1.2% PVA + 0.4% MS, the T50 increases by 55.5, 110.2, and 156.8%, respectively, while the average final spread decreases by 6.6, 13.3, and 20%, indicating a gradual decrease in workability. However, in the

Table 2.7 Fixed fiber fraction:1.6%: Hybrid PVA and MS (Li, 2020)

Fiber fraction		T50 (s)	Slump (mm)	Expansion		
PVA (%)	MS (%)			Horizontal (cm)	Vertical (cm)	Averaged (cm)
0.0	1.6	0.9	281	75	75	75
0.4	1.2	1.4	275	70	70	70
0.8	0.8	1.9	271	66	65	65
1.2	0.4	2.3	272	60	62	60
1.6	0.0	3.5	270	50	50	50

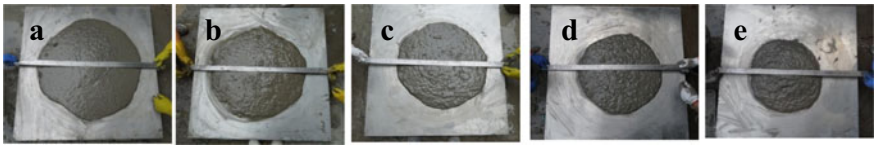

Fig. 2.4 Expansion of the UHDMC reinforced by hybrid PVA and MS: **a** 0.0% PVA + 1.6% MS, **b** 0.4% PVA + 1.2% MS, **c** 0.8% PVA + 0.8% MS, **d** 1.2% PVA + 0.4% MS and **e** 1.6% PVA + 0.0% MS (Li, 2020)

case of 1.6% PVA + 0.0% MS, the T50 is 3.5 s, and the average final spread is 50 cm, which does not meet the self-compacting criteria.

Since PVA fibers have a relatively high water-absorption capacity, they adsorb the water in the slurry of UHDMC, leading to a reduction in the free water content in the slurry and a decrease in its flowability. Furthermore, PVA fibers are flexible, and during the cement mixing process, they tend to wrap and encapsulate a portion of the slurry, increasing the slurry's viscosity, which further reduces the workability of UHDMC. On the other hand, MS fibers have smooth surfaces with almost no water absorption capacity. Besides, the rigidity of MS fibers makes them less likely to tangle or cluster, resulting in a relatively minor impact on the workability of UHDMC (Fig. 2.4).

2.3.1.2 Hybrid PP and MS

As for the hybrid system with PP and MS fibers, the experimental results of the workability of the UHDMC are shown in Table 2.8.

Results showed that with a decrease in PP fibers and an increase in MS fibers, the T50 of UHDMC gradually decreases, while the expansion increases in general. With 1.6% PP fibers only, the T50 of the UHDMC is 2.2 s with an expansion of 53 cm, indicating relatively weaker workability. For 1.2% PP + 0.4% MS, both T50 and the spread decrease slightly. With a continuous increase in PP fibers, T50 consistently decreases, while the spread notably increases. For 0.8% PP + 0.8% MS and 0.4% PP + 1.2% MS, the T50 of the UHDMC decreases by 3.8% and 35.7%, respectively,

Table 2.8 Fixed fiber fraction:1.6%: Hybrid PP and MS (Li, 2020)

Fiber fraction		T50 (s)	Slump (mm)	Expansion		
MS (%)	MS (%)			Horizontal (cm)	Vertical (cm)	Averaged (cm)
1.6	0.0	2.2	261	53	54	55
1.2	0.4	2.1	258	48	50	50
0.8	0.8	2.0	262	62	64	63
0.4	1.2	1.4	273	71	70	70
0.0	1.6	0.9	281	75	75	75

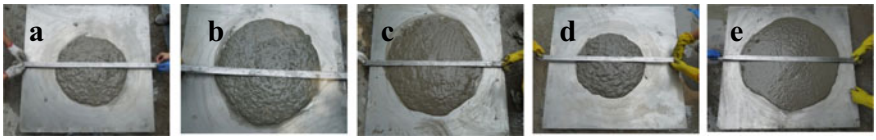

Fig. 2.5 Expansion of the UHDMC reinforced by hybrid PP and MS: **a** 1.6% PP + 0.0% MS, **b** 1.2%P P + 0.4% MS, **c** 0.8% PP + 0.8% MS, **d** 0.4% PP + 1.2% MS and **e** 0.0% PP + 1.6% MS (Li, 2020)

while the spread increases by 14.5 and 27.3%, respectively. For 1.6% MS fibers only, the T50 is the lowest, and the average spread is the highest, indicating the best workability.

Similar to PVA fibers, PP fibers are also considered flexible fibers. During the mixing and pouring process, PP fibers tend to entangle with each other and encapsulate a portion of the slurry, which increases the viscosity and has a significant impact on the workability of UHDMC. When PP fibers are blended with MS fibers, with a decrease in PP fibers and an increase in MS fibers, the phenomenon of PP fibers entangling and encapsulating the slurry gradually weakens, leading to an improvement in workability (Fig. 2.5).

2.3.1.3 Hybrid PVA and PP

As for the hybrid system with PP and PVA fibers, the experimental results of the workability of the UHDMC are shown in Table 2.9.

The result reveals that when for 1.2% PVA + 0.4% PP fibers, in comparison with the addition of 1.6% PVA fibers only, the T50 of the UHDMC decreases, while the expansion slightly increases. As PVA fibers content decrease continuously, and PP fibers content increase, the expansion gradually decreases. For the hybrid system consisting of 0.8% PVA + 0.8% PP and 0.4% PVA + 1.2% PP, the T50 of the UHDMC were unmeasurable, indicating poor workability. Overall, with a decrease in PVA fibers and an increase in PP fibers content, the workability of the UHDMC undergoes a initially reduce and then increases.

Table 2.9 Fixed fiber fraction:1.6%: Hybrid PVA and PP (Li, 2020)

Fiber fraction		T50 (s)	Slump (mm)	Expansion		
PVA	PP			Horizontal (cm)	Vertical (cm)	Averaged (cm)
1.6%	0.0%	3.5	270	50	50	50
1.2%	0.4%	2.6	264	52	52	52
0.8	0.8	–	255	45	46	45
0.4%	1.2%	–	210	36	35	35
0.0%	1.6%	2.2	261	52	54	53

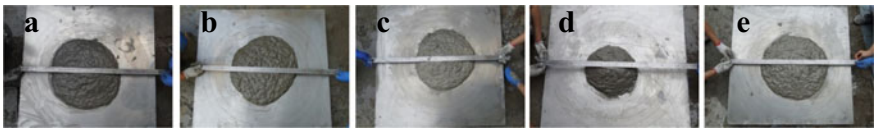

Fig. 2.6 Expansion of the UHDMC reinforced by hybrid PVA and PP: **a** 1.6% PVA + 0.0% PP, **b** 1.2% PVA + 0.4% PP, **c** 0.8% PVA + 0.8% PP, **d** 0.4% PVA + 1.2% PP and **e** 0.0% PVA + 1.6% PP (Li, 2020)

Both PVA and PP fibers lead to a decrease in workability when added to MPC. However, PP fibers have a smaller diameter, which results in a higher quantity of PP fibers per unit volume compared to PVA fibers. Therefore, as the volume content of PP fibers increases and that of PVA fibers decreases, the number of fibers in the slurry increases, which consequently reduces the workability of UHDMC. However, due to the elimination of the interweave between PVA and PP fibers, a sole addition of 1.6% PP fibers increased the workability. The experimental observations are depicted in Fig. 2.6.

2.3.2 Compressive Strength

Magnesium phosphate cement, as a repair material, relies significantly on its strength, In this section, the compressive strength of UHDMC reinforced by hybrid fibers at a curing age of 7 days was investigated. To minimize the operation errors, at least three specimens were tested for each mixture, and averaged values were taken as the compressive strength.

2.3.2.1 Hybrid PVA and MS

Figure 2.7 illustrates the effect of hybrid PVA and MS on the compressive strength of UHDMC with a total fiber fraction of 1.6%. It is evident from the graph that when solely blended with 1.6% MS fibers, the UHDMC exhibits the highest compressive

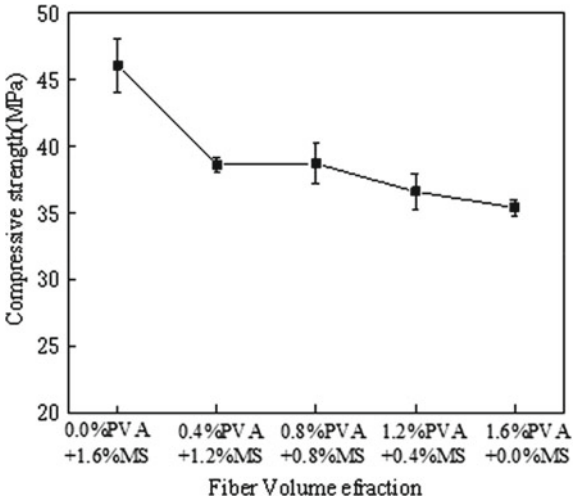

Fig. 2.7 Compressive strength of UHDMC reinforced by hybrid PVA and MS fibres (Li, 2020)

strength, approximately 47 MPa. However, when the hybrid fibers consist of 0.4% PVA + 1.2% MS, the compressive strength of UHDMC significantly decreases. Besides, for 0.8% PVA + 0.8% MS, the compressive strength slightly increases compared to 0.4% PVA + 1.2% MS. In cases where the blended fibers are 1.2% PVA + 0.4% MS and 1.6% PVA + 0.0% MS, the compressive strength continues to decrease. This demonstrates that as MS fibers decrease and PVA fibers increase, the compressive strength of UHDMC gradually declines.

Previous studies have indicated (Chen & Zhu, 2016; Hai-Chao et al., 2013; Hongtao et al., 2006; Tingwei, 2017) that both PVA and MS fibers can carry the load at the crack surface, impeding the development of cracks within the cementitious composites. Compared to PVA fibers, MS fibers have a larger diameter and higher hardness. With a proper design, PVA and MS fibers can creat a structural framework within the matrix. Consequently, the reinforcing effect of hybrid PVA and MS fibers on UHDMC can be enhanced under compressive load.

2.3.2.2 Hybrid PP and MS

Figure 2.8 demonstrate the effect of hybrid PP and MS on the compressive strength of UHDMC with a total fiber fraction of 1.6%. For the addition of PP fiber only, the compressive strength of the cubic specimens is relatively low at 32.2 MPa. However, with a mix of 1.2% PP and 0.4% MS fibers, there is a significant increase in compressive strength. At 0.8% PP + 0.8% MS fibers, the compressive strength decreases slightly compared to the UHDMC of 1.2% PP and 0.4%. It is also noticed that the compressive strength significantly enhanced at 0.4% PP + 1.2% MS and 0.0% PP + 1.6% MS fibers, with increases of 11.6 and 16.7%, respectively. This indicates an

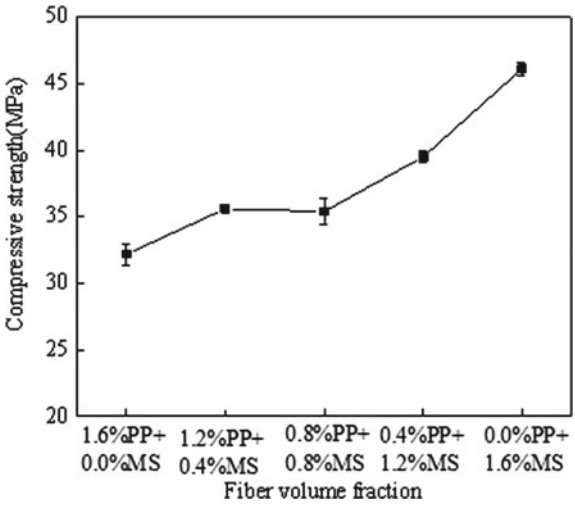

Fig. 2.8 Compressive strength of UHDMC reinforced by hybrid PP and MS fibres (Li, 2020)

overall upward trend in the compressive strength of UHDMC as PP fibers decrease and MS fibers increase.

Compared to the compressive strength of UHDMC reinforced by sole 1.6% PVA or 1.6% MS fibers, the compressive strength of UHDMC reinforced by sole 1.6% PP is the lowest. This may be attributed to the low elastic modulus and strength of PP fibers. Subject to external forces, PP fibers tend to deform and break easily, resulting in a relatively weak reinforcing effect. Therefore, in the condition of the high fraction of PP fiber and low fraction of MS fiber, the compressive strength of UHDMC is generally lower. However, when the MS fiber content reaches 1.2% or higher, there is a significant increase in compressive strength, demonstrating an excellent reinforcing effect of MS for UHDMC.

2.3.2.3 Hybrid PVA and PP

Figure 2.9 demonstrate the effect of hybrid PVA and PP on the compressive strength of UHDMC with a total fiber fraction of 1.6%. Compared to the sole addition of 1.6% PVA fibers, the compressive strength of the composite material slightly increases with the hybrid addition of 1.2% PVA and 0.4% PP fibers. At the combination of 0.8% PVA and 0.8% PP, there is a significant increase in compressive strength, up by 10.2%. However, with a further increase in the fraction of PP fibres to 1.2 and 1.6%, the compressive strength gradually reduced by around 6.2 and 13.6% respectively. This indicates following the increase of PVA fibers and decrease of PP fibers, the compressive strength of UHDMC tends to increase at the initial stage and reduce afterwards.

Based on the discussion in Sect. 2.3.1, the viscosity of UHDMC slurry reinforced by hybrid PVA and PP fibres increased with the increase of PP and decrease of PVA,

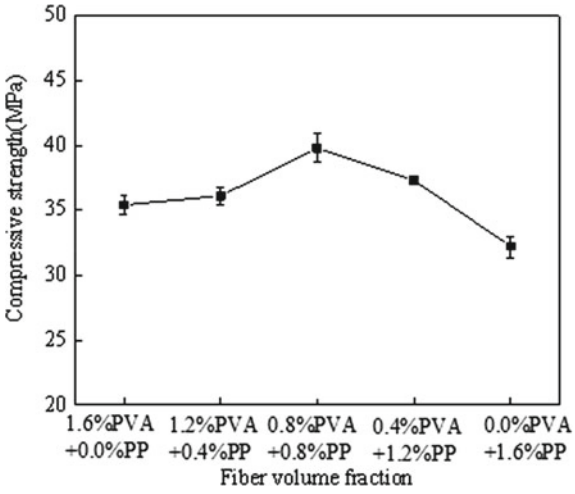

Fig. 2.9 Compressive strength of UHDMC reinforced by hybrid PVA and PP fibres (Li, 2020)

which enhanced the compressive strength of UHDMC. However, due to the relatively weak reinforcing effect of PP fibers, when the PP fiber content exceeds 0.8%, the compressive strength of UHDMC exhibits a decreasing trend.

2.3.3 Bending Performance

Bending performance is crucial for assessing the crack resistance and flexural toughness of fiber-reinforced composite materials. In this section, the effect of hybrid fibers on the strength, flexural toughness and deformation performance of UHDMC is investigated through a four-point bending test.

In this test, the applied load and the mid-span deflection of the prepared specimens were recorded. Figure 2.10 shows a typical strain-hardening curve, indicating a continuous increase in load-bearing capacity after the initial cracking of the specimen. LOP is the point at which the curve transitions from linear to nonlinear behavior and is considered the first cracking point, which is referred to Limit of Proportionality (LOP) in ASTM C1018 (Committee, 1997). However, ASTM C1609 (Committee, 2012) defines the first cracking point as the first peak point in the load–deflection curve, where the slope is zero. Previous research has shown (Kim et al., 2008) that in fiber-reinforced composite materials that exhibit stable strain-hardening behaviors, such as UHDMC, the first peak point in the load–deflection curve is not easily identified. Therefore, the definition of LOP in ASTM C1018 (Committee, 1997) is generally more applicable to UHDMC. Consequently, the load and deflection values corresponding to point LOP are known as the cracking load (P_{LOP}) and cracking deflection (δ_{LOP}). On the other hand, MOR is where the specimen begins to experience softening deformation, with the corresponding load and deflection values

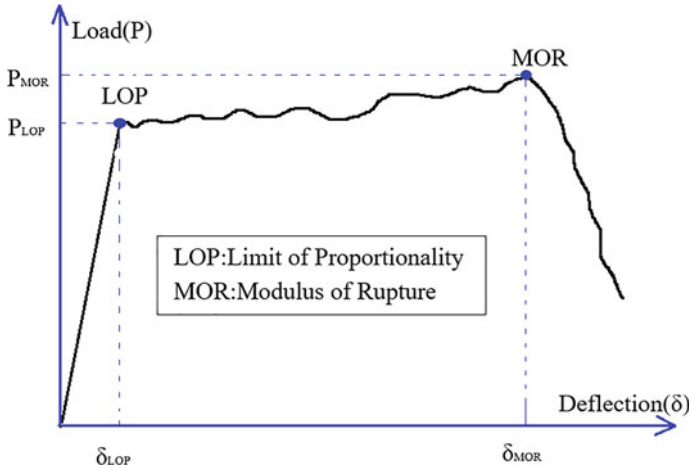

Fig. 2.10 Typical strain hardening curve (Li, 2020)

referred to as the ultimate load (P_{MOR}) (or peak load P_{peak}) and ultimate deflection (δ_{MOR}).

(1) Strength

Based on the P_{LOP}, δ_{LOP}, P_{MOR} and δ_{MOR} obtained from the strain hardening curves, the cracking strength (f_{LOP}) and flexural strength (f_{MOR}) of the specimens can be calculated using Eqs. 2.1 and 2.2. The flexural strength is also referred to as the modulus of rupture (MOR). In this study, cracking strength and flexural strength are used as indicators to evaluate changes in strength under bending loads.

Cracking Strength f_{LOP} (MPa):

$$f_{LOP} = P_{LOP}\frac{L}{bh^2} \tag{2.1}$$

Flexural Strength f_{MOR} (MPa):

$$f_{MOR} = P_{MOR}\frac{L}{bh^2} \tag{2.2}$$

where b and h are the width and height of the thin plate specimen (mm).

(2) Deformation Performance

It is commonly believed that if the P_{MOR} is greater than the P_{LOP}, fiber-reinforced cement composite materials will exhibit strain-hardening characteristics. This strain-hardening characteristic is enhanced if δ_{MOR} is greater than δ_{LOP}. Therefore, Naaman (Naaman & Reinhardt, 1996) used the Damage Index (DI) to quantitatively assess the

deformation performance of fiber-reinforced cementitious composites, as shown in Eq. 2.3. A higher DI value suggests better deformation performance of the UHDMC.

$$DI = \frac{\delta_{MOR}}{\delta_{LOP}} \tag{2.3}$$

(3) Toughness

Toughness refers to the ability of fiber-reinforced composite materials to absorb energy when subjected to external loads, which is calculated by measuring the area under the load–deflection curve up to a given deflection. Shaikh (2013) used the toughness index (I_{peak}) to evaluate the toughness, which is defined as the ratio of the area under the load–deflection curve up to a given deflection to the area under the load–deflection curve up to δ_{LOP}. Although ASTM C 1609 (Committee, 2012) specifies a maximum deflection of 1/150 of the span, this limit needs to be adjusted based on the ductility characteristics of composite materials (Naaman & Reinhardt, 1996). Therefore, for UHDMC, the area under the load–deflection curve up to the ultimate load is denoted as T_{MOR}, and the area under the load–deflection curve up to the cracking deflection (δ_{LOP}) is denoted as T_{LOP}. Equation 2.4 (Shaikh, 2013) is used to calculate I_{peak}, reflecting the hybrid effect of multiple fibres on the toughness of UHDMC.

$$I_{peak} = \frac{T_{MOR}}{T_{LOP}} \tag{2.4}$$

where a higher I_{peak} value indicates greater toughness of the UHDMC reinforced by hybrid fibers.

2.3.3.1 Hybrid PVA and MS Fibers

Based on the load-mid-span displacement curves from the four-point bending tests with varying hybrid fiber contents of PVA and MS fibers, the cracking load, cracking deflection, ultimate load, and ultimate deflection can be determined. Using equations Eqs. 2.1, 2.2, 2.3, and 2.4, the strength, deformation performance, and toughness indices of the specimens can be calculated respectively. The calculation results are shown in Table 2.10.

The reinforcing effect of fibers on UHDMC is mainly due to the fiber's crack-bridging mechanism. Fibers bridge across the cracking surface, limiting or delaying the expansion of the cracks. Consequently, the strength, deformation performance and toughness of UHDMC were enhanced. Based on the results shown in Table 2.10, it is noticed that in the UHDMC with hybrid PVA and MS fibres, MS fibers mainly contributed to the high strength and rigidity. On another hand, PVA fibers, due to their high flexibility and elastic modulus, mainly improved the deformation performance and toughness of the UHDMC. In general, UHDMC with 1.2% PVA and 0.4%

Table 2.10 Flexural performance of UHDMC reinforced by hybrid PVA and MS fibers (Li, 2020)

Mixed design	Strength		Deformation performance			Flexural Toughness		
	f_{LOP}	f_{MOR}	δ_{LOP}	δ_{MOR}	DI	T_{LOP}	T_{MOR}	I_{peak}
0.0%PVA + 1.6% MS	8.2773	10.791	0.741	3.4557	4.6636	0.2662	2.2917	8.6089
0.4%PVA + 1.2% MS	6.9907	8.5827	0.5451	4.8861	8.9637	0.1368	2.8631	20.929
0.8%PVA + 0.8% MS	7.7827	9.7867	0.5763	3.7042	6.4276	0.1746	2.3285	13.336
1.2%PVA + 0.4% MS	7.7907	10.565	0.429	10.689	24.917	0.1425	7.2486	50.867
1.6%PVA + 0.0% MS	5.9467	8.3973	0.6544	24.614	37.614	0.1965	12.925	65.774

MS exhibited excellent performance with high flexural strength, high toughness and outstanding deformation performance.

2.3.3.2 Hybrid PP and MS Fibers

Similarly, the flexural strength, deformation performance, and toughness of UHDMC reinforced by hybrid PP and MS fibers were shown in Table 2.11. Table 2.11 indicated that in the UHDMC with hybrid PP and MS fibers, MS can effectively improve the cracking strength and the flexural strength. It also contributes to the improvement in deformation performance and toughness to some extent. Because of the lower strength and elastic modulus, PP fibers have a limited effect in enhancing the strength and deformability of the UHDMC. However, 0.8% PP and 0.8% MS fibers exhibited a little hybrid effect, leading the UHDMC to a strain-hardening behavior.

Table 2.11 Flexural performance of UHDMC reinforced by hybrid PP and MS fibers (Li, 2020)

Mixed design	Strength		Deformation performance			Flexural toughness		
	f_{LOP}	f_{MOR}	δ_{LOP}	δ_{MOR}	DI	T_{LOP}	T_{MOR}	I_{peak}
1.6%PP + 0.0%MS	6.8133	6.8133	0.2291	0.2291	1.0000	0.1486	0.1486	1.0000
1.2%PP + 0.4%MS	6.0627	6.0627	0.7003	0.7003	1.0000	0.1869	0.1869	1.0000
0.8%PP + 0.8%MS	7.6467	7.7440	0.8854	3.5255	3.9818	0.2723	1.6668	6.1212
0.4%PP + 1.2%MS	7.7960	8.3893	0.8432	2.8268	3.3525	0.3098	1.4034	4.5300
0.0%PP + 1.6%MS	7.7827	10.790	0.741	3.4557	4.6636	0.2662	2.2917	8.6089

Table 2.12 Flexural performance of UHDMC reinforced by hybrid PVA and PP fibers (Li, 2020)

Mixed design	Strength		Deformation performance			Flexural toughness		
	f_{LOP}	f_{MOR}	δ_{LOP}	δ_{MOR}	DI	T_{LOP}	T_{MOR}	I_{peak}
1.6%PVA + 0.0%PP	5.9467	8.3973	0.6544	24.614	37.614	0.1965	12.9245	65.7732
1.2%PVA + 0.4%PP	7.7907	8.9920	0.9285	12.676	13.652	0.2403	7.1469	29.7412
0.8%PVA + 0.8%PP	7.1387	7.6307	0.6372	3.625	5.6890	0.1754	1.7578	10.0221
0.4%PVA + 1.2%PP	6.6347	7.1400	0.716	1.4501	2.0253	0.1865	0.5496	2.9469
0%PVA + 1.6%PP	6.8133	6.8133	0.2291	0.2291	1.0000	0.1486	0.1486	1.0000

2.3.3.3 Hybrid PVA and PP Fibers

Similar to Sects. 2.3.1.1 and 2.3.1.2, the hybrid effect of PVA and PP fibers on UHDMC was also analysed by calculating the strength, deformation performance and toughness of the flexural specimens, as shown in Table 2.12. Generally, in this hybrid system, PVA plays the primary role in strengthening and toughening the UHDMC, while the reinforcing effect of PP fibers is relatively weaker. As the content of PVA fiber decreases while that of PP fiber increases, deformation performance and flexural toughness significantly decrease, and the strain-hardening characteristics gradually weaken, indicating a limited hybrid effect between PVA fibers and PP fibers regarding flexural performance.

2.3.4 Cracking Propagation

Based on the analysis of the flexural performance of UHDMC with different hybrid fiber systems and the observation of failure phenomena, this section summarized the hybrid effect on the load–deflection curve models and the cracking patterns.

(1) 0.0%PVA+1.6%MS

For 0.0% PVA + 1.6% MS, UHDMC exhibits a higher cracking strength. After the initial crack, the load continues to rise, reaching a higher peak load but with a smaller deflection. The corresponding curve model is shown in Fig. 2.11a. The crack pattern

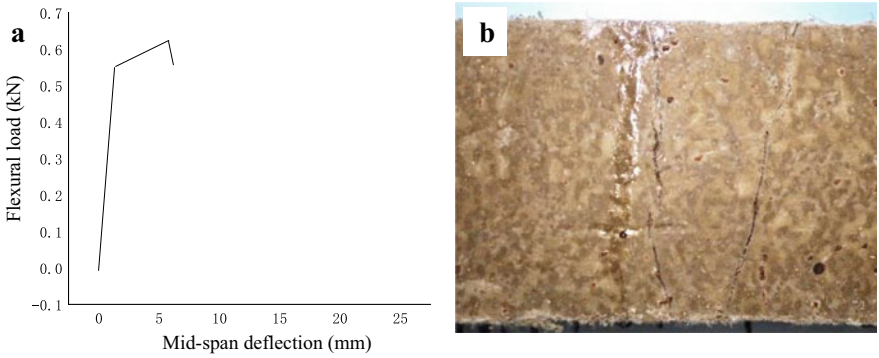

Fig. 2.11 **a** Model of the load–deflection curve and **b** bending crack pattern of 0.0% PVA + 1.6% MS (Li, 2020)

is illustrated in Fig. 2.11b, where two wide cracks are generated at the bottom of the specimen.

(2) 1.6%PVA+0.0%MS

As for 1.6% PVA + 0.0% MS, the crack strength is relatively low. After reaching the cracking strength, the deflection-load curve steadily rises with a lower peak load but greater deflection. The curve model is shown in Fig. 2.12a, and the corresponding crack pattern is indicated in Fig. 2.12b. Figure 2.12b shows that numerous small cracks appeared in the mid-section of the specimen, which indicates a distinct multi-crack pattern with relatively small crack widths and spacing.

(3) 1.2% PVA + 0.4% MS

For 1.2% PVA + 0.4% MS, the displacement-load curve continuously rises after reaching the cracking strength, achieving a higher ultimate strength with greater

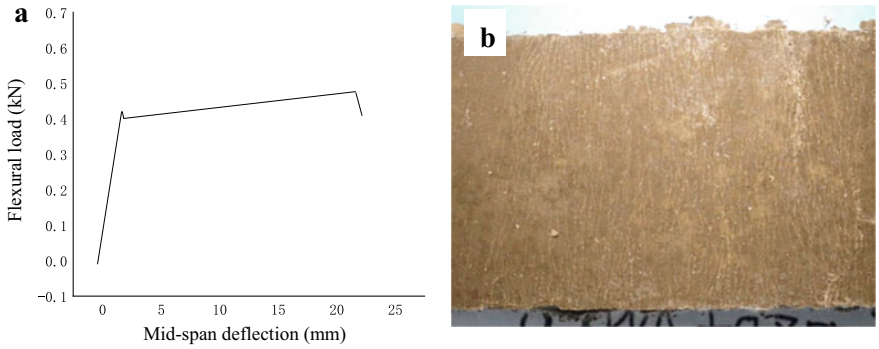

Fig. 2.12 **a** Model of the load–deflection curve and **b** bending crack pattern of 1.6% PVA + 0.0% MS (Li, 2020)

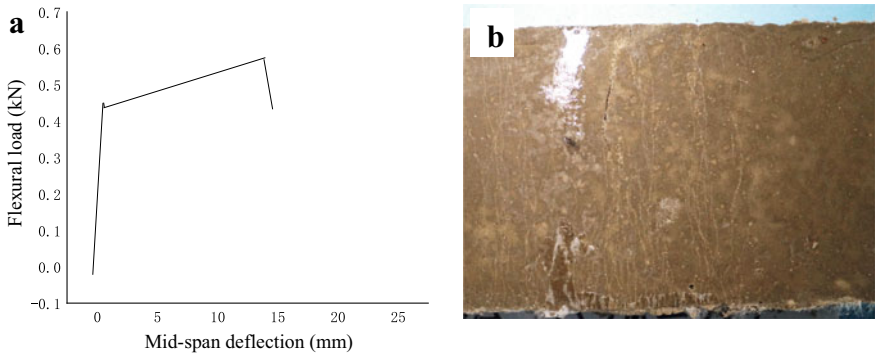

Fig. 2.13 **a** Model of the load–deflection curve and **b** bending crack pattern of 1.2% PVA + 0.4% MS (Li, 2020)

deflection. The curve model is shown in Fig. 2.13a. The crack pattern, as depicted in Fig. 2.13b, shows one main crack at the bottom of the specimen along with several minor cracks.

(4) 1.6% PP + 0.0% MS

For 1.6% PP + 0.0% MS, the flexural load rapidly decreases after reaching the cracking strength, displaying deformation softening characteristics. The curve model is illustrated in Fig. 2.14a. The bending crack pattern, as shown in Fig. 2.14b, includes one main crack at the bottom of the specimen with a large crack width.

(5) 0.8% PP + 0.8% MS

For 0.8% PP + 0.8% MS, the cracking strength is relatively low. After reaching the cracking strength, the flexural load slightly increases, followed by a decrease.

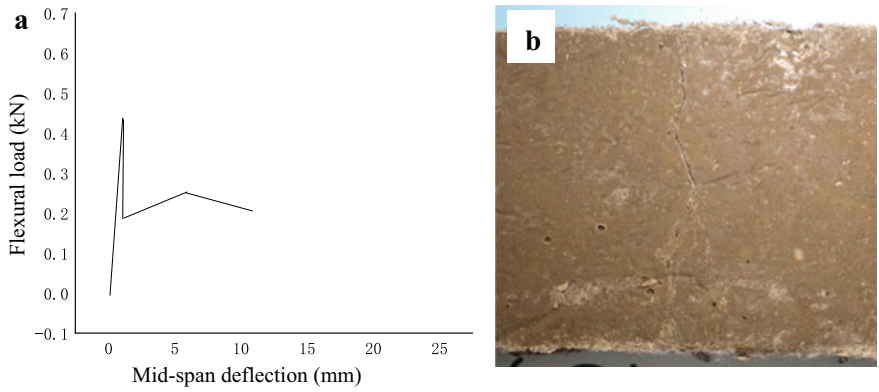

Fig. 2.14 **a** Model of the load–deflection curve and **b** bending crack pattern of 1.6% PP + 0.0% MS (Li, 2020)

Consequently, the ultimate deflection is relatively small. The curve model is depicted in Fig. 2.15a. The crack pattern, as shown in Fig. 2.15b, reveals the presence of 3–4 large cracks at the bottom of the specimen.

(6) 0.8% PVA + 0.8% PP

For 0.8% PVA + 0.8% PP, the cracking strength is also low. After reaching the cracking strength, the flexural load fluctuated, while the failure occurred with a relatively small deflection. The corresponding curve model is illustrated in Fig. 2.16a. The bending crack pattern, as shown in Fig. 2.16b, reveals the presence of multiple cracks at the bottom of the specimen.

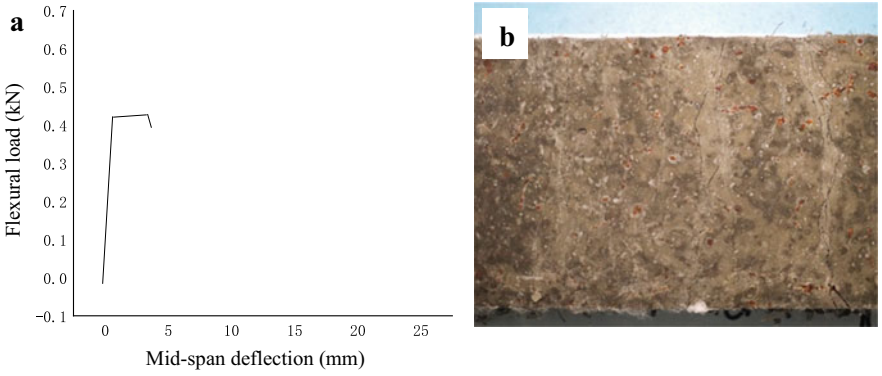

Fig. 2.15 **a** Model of the load–deflection curve and **b** bending crack pattern of 0.8% PP + 0.8% MS (Li, 2020)

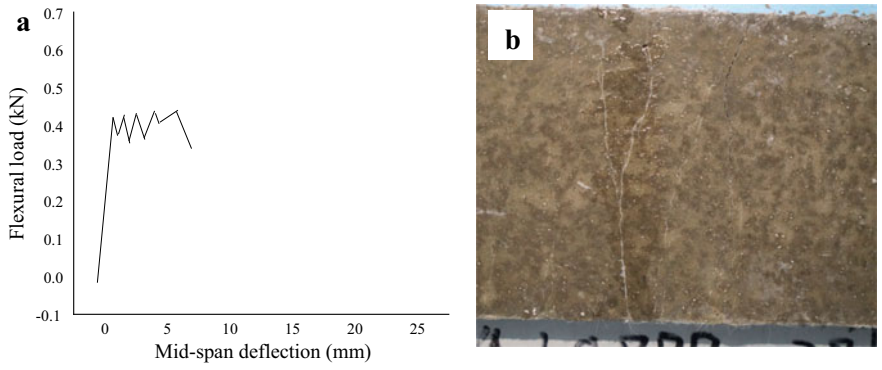

Fig. 2.16 **a** Model of the load–deflection curve and **b** bending crack pattern of 0.8% PVA + 0.8% PP (Li, 2020)

2.3.5 *Microstructure*

The distribution, and orientation of the fibers significantly affect their reinforcing effects in UHDMC. Ideally, uniformly distributed fibers of tight fiber/MPC bond are preferred. However, the distribution of fibers and the bond between fibers and the matrix are influenced by various factors, such as mixing methods and fiber types. In this section, scanning electron microscopy (SEM) is employed to analyze the microstructure of UHDMC reinforced with hybrid fibers. By examining the fiber distribution, fiber/matrix bonding, and correlating these observations with macroscopic mechanical properties, the mechanism of the hybrid effects on the mechanical performance of UHDMC was investigated.

(1) PVA fibers only

Through SEM imaging, a microstructural analysis was conducted on the fracture surface of UHPC reinforced by 1.6% PVA only, as shown in Fig. 2.17. Kong et al. (Xiangqing et al., 2018) indicated that the addition of fibers to the cementitious matrix is beneficial for the uniform distribution of hydration products, which can refine the microstructure of the matrix. Figure 2.17a reveals a relatively even distribution of PVA fibers, with no large voids or cracks within the matrix. This explains the reason why the sole addition of 1.6% PVA fibers significantly enhances the compressive strength of UHDMC. Figure 2.17b, c illustrate the close bonding between PVA fibers and the MPC matrix. After fibers are pulled out from the matrix, the surrounding matrix is relatively compact, and PVA fiber debris remains within the voids. This indicates excellent bonding between PVA fibers and MPC. Figure 2.17d show that there is numerous hydration product attached to the pull-out PVA fiber surface, demonstrating a significant resistance during fiber pull-out, which further prove the strong interface between PVA fiber and MPC matrix.

PVA fibers are hydrophilic materials, and when introduced into the MPC matrix, water molecules migrate to the surface of PVA fibers. Consequently, the surface of PVA undergoes sufficient hydration reactions, with hydration products tightly enveloping the fiber surface. This results in a strong bond between PVA fibers and the MPC matrix, allowing them to jointly withstand external forces. Additionally, PVA fibers exhibit a high elastic modulus and excellent ductility. Consequently, the

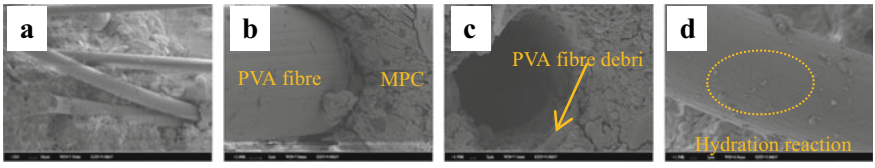

Fig. 2.17 Microstructure of the UHDMC reinforced by PVA fibers **a** fiber distribution, **b** interface between PVA and MPC, **c** fiber pullout hole in MPC matrix, **d** surface of the pulled out PVA fibers (Li, 2020)

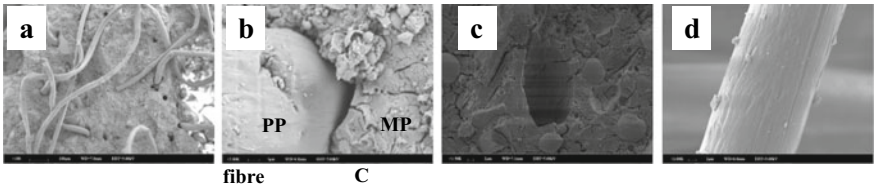

Fig. 2.18 Microstructure of the UHDMC reinforced by PP fibers **a** fiber distribution, **b** interface between PP and MPC, **c** fiber pullout hole in MPC matrix, **d** surface of the pulled out PP fibers (Li, 2020)

addition of 1.6% PVA + 0.0% MS leads to strain-hardening behavior in UHDMC, significantly enhancing their deformation capacity and toughness.

(2) PP fibers only

Figure 2.18 illustrates the microstructure of the fracture surface of UHDMC reinforced by 1.6% PP fiber only. As demonstrated in Fig. 2.18a, PP fibers are uniformly distributed throughout the matrix. Notably, PP fibers exhibit significant curling deformation, which is because of their lower strength making them susceptible to deformation under external forces. In Fig. 2.18b, c, substantial cracks and gaps are observed at the interfaces between PP fibers and the MPC, as well as around the fiber removal holes. This suggests that the bonding interface between PP fibers and MPC is relatively weak. In Fig. 2.18d shows fewer hydration products adhering to the surface of PP fibers, further indicating weaker bonding performance between PP fibers and MPC.

The surface of PP fibers is hydrophobic. Consequently, during the hydration of MPC, there are fewer water molecules near the fiber surfaces, leading to insufficient hydration reactions in the vicinity of the fibers. Additionally, PP fibers are of smaller diameters and lower densities, resulting in a dense distribution within the matrix. This interweave of fibers in weak areas makes them tend to being pulled out under external forces. Consequently, UHDMC with solely 1.6% PP fibers exhibits deformation softening characteristics when subjected to bending loads.

(3) MS fibers only

Figure 2.19 illustrates the fracture surface of the UHDMC reinforced by 1.6% MS, where MS fibers are uniformly and randomly distributed within the matrix. In Fig. 2.19a, b, the bonding between MS fibers and MPC is strong, with the surrounding matrix tightly adhering after fiber pullout. In Fig. 2.19d, the surface of MS fibers exhibits unevenness and some scratches, with adhering MPC particles. Under external loads, the presence of these particles allows MS fibers to create a wedge effect within the matrix, which further enhances their load-carrying capacity. Furthermore, MS fibers possess high tensile strength, enabling them to effectively

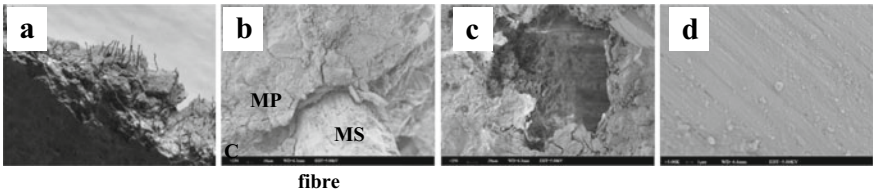

Fig. 2.19 Microstructure of the UHDMC reinforced by MS fibers **a** fiber distribution, **b** interface between MS and MPC, **c** fiber pullout hole in MPC matrix, **d** surface of the pulled out MS fibers (Li, 2020)

disperse and transmit stress, reducing crack formation. Consequently, the addition of 1.6% MS fibers significantly enhances the compressive strength of UHDMC with a slight improvement in flexural toughness and deformation performance.

(4) Hybrid PVA and MS

The microstructure of the UHDMC reinforced by PVA and MS is depicted in Fig. 2.20. PVA fibers are distributed around MS fibers, intertwining together to form a mesh-like structure. At the interface between hybrid fibers and the MPC matrix, no obvious cracks are observed, indicating excellent bonding performance. Within the matrix, the tightly intertwined mesh structure formed by MS and PVA fibers significantly increases the energy consumed when fibers are pulled out, leading to a substantial enhancement in the matrix's load-carrying capacity. Under external forces, PVA fibers cross microcracks, partially bearing the stress during microcrack propagation, thereby improving the matrix's deformation capacity. MS fibers enhance the strength and bridge macroscopic cracks, improving the toughness of the UHDMC. The hybrid effect of these two types of fibers effectively enhances the mechanical properties of UHDMC. Consequently, the addition of 1.2% PVA + 0.4% MS fibers not only results in higher compressive and flexural strength but also significantly improves the deformation performance and toughness of MPC.

(5) Hybrid PP and MS fibers

Figure 2.21 illustrates the microstructure of UHDMC reinforced by PP and MS. Similar to PVA fiber, PP fibers are distributed and entwined with MS fibers. However, cracks were observed at the interface between the PP fiber and the MPC matrix (Fig. 2.21b), indicating a relatively poor bond. Furthermore, the interface between MS fibers and the cement matrix differs significantly from that observed in Fig. 2.19 where only MS are incorporated. When hybrid with PP fiber, the interface between MS fibers and MPC becomes loose with noticeable cracks. This is also attributed to the hydrophobic surface of PP fiber, driving the water from the PP surface to the MS surface. Xiangqing et al. (2018) have demonstrated that as the water-cement ratio increases, the bond between steel fibers and the MPC matrix gradually decreases.

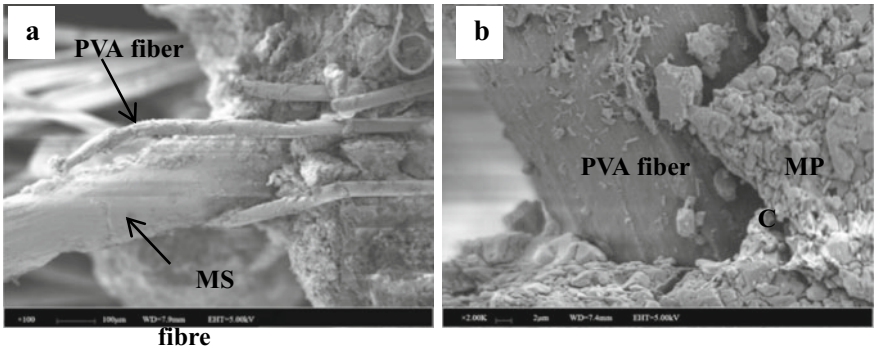

Fig. 2.20 **a** Intertwined MS and PVA fibers in UHDMC, **b** the interface between PVA fiber and MPC matrix (Li, 2020)

Therefore, the interface between MPC and MS fibers becomes loose, leading to a significant reduction in the reinforcing and toughening effects of MS fibers on MPC. Consequently, the addition of hybrid PP and MS fibers leads to a slight increase in the compressive strength of UHDMC but reduces the overall flexural performance.

(6) Hybrid PVA and PP fibers

Figure 2.22 displays the microstructure of the UHDMC reinforced by hybrid PVA and PP fibers. In Fig. 2.22a, PVA fibers are interwoven with PP fibers, and numerous holes are created due to the pull-out of PP fibers. This reflects the relatively poor bonding performance between PP fibers and MPC. In Fig. 2.22b, after the pull-out of PVA fibers, the surrounding matrix is dense with the PVA fiber debris in the pull-out holes, which indicates a good bonding performance between PVA fibers and MPC. In the hybrid system, the interweave of PP and PVA fibers results in a reduced contact area between PVA fibers and MPC, which weakens the bonding between PVA

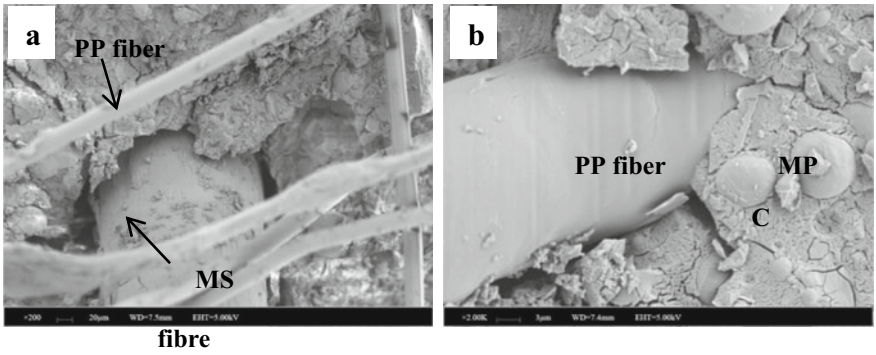

Fig. 2.21 **a** Intertwined MS and PP fibers in UHDMC, **b** the interface between PP fiber and MPC matrix (Li, 2020)

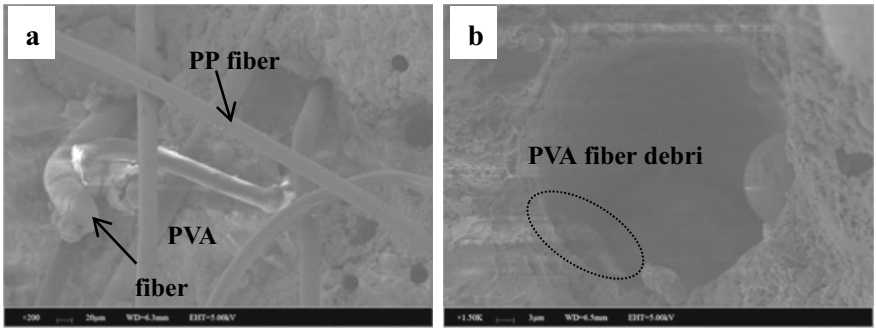

Fig. 2.22 **a** Intertwined PP and PVA fibers in UHDMC, **b** the interface between PVA fiber and MPC matrix (Li, 2020)

fibers and MPC, and consequently weakens their reinforcing effect. Consequently, the UHDMC with a hybrid PVA and PP exhibits increased compressive strength but significantly reduced flexural performance compared to their counterpart with the addition of 1.6% PVA only.

2.4 Conclusions

In this chapter, three types of fibers, namely micro steel fibers, PVA fibers, and PP fibers, were mixed in pairs to make UHDMC reinforced by hybrid fibers. The hybrid effect on UHDMC was studied by investigating the workability, compressive strength, bending performance and microstructures. The main conclusions drawn in this chapter are as follows:

(1) In the hybrid system of PVA and MS fibers, the increase of PVA content and the decrease of MS content lead to a reduction in the workability of UHDMC. MS fibers mainly contribute to the enhanced strength of the matrix, while PVA fibers primarily enhance the deformation performance and later-stage toughness of the UHDMC. The system of 1.2% PVA and 0.4% MS exhibited an excellent performance in flexural strength, deformation performance and toughness, which is attributed to the interweave between PVA and MS fibers forming a mesh structure to withstand the external forces.

(2) In the hybrid system of PP and MS fibers, the increase of PP fibers and the decrease of MS fibers reduced the workability of UHDMC. In this hybrid system, PP fibers had a weaker reinforcing effect on MPC, while MS fibers played the main role in enhancing toughness. Consequently, the flexural performance of the specimens was generally poor. However, with proper mixed design (0.8% PP and 0.8% MS fibers), there was a slight positive hybrid effect between PP and MS fibers, leading to a slight strain-hardening effect in UHDMC.

(3) In the hybrid system of PVA and PP fibers, an increase of PP fiber content and a decrease of PVA fiber content make the workability of UHDMC undergoes an initial decrease but then increase. Microstructure analysis indicates PVA and PP fibers were interwoven with each other. With high PP fiber content, the contact area between PVA fibers and MPC decreased, leading to reduced deformation performance and toughness. As a result, the hybrid effect between PVA and PP fibers is relatively weak, and PVA fibers played the primary role in enhancing the toughness.

References

Chen, S., & Zhu, D. (2016). Study on PVA fiber modified phosphate cement-based materials. *China Concrete and Cement Products,* (12), 44–47.

Committee, A. (1997). ASTM C1018 Standard test method for flexural toughness and first-crack strength of fiber reinforced concrete (Using Beam With Third-Point Loading).

Committee, C. (2012). ASTM C1609/C1609M-12 Standard Test Method for Flexural Performance of Fiber-Reinforced Concrete (Using Beam With Third-Point Loading).

Hai-Chao, W., Ling-Ling, Z., et al. (2013). Experimental study on influence of PVA fiber on mechanical properties of engineered cementitious composites. *Concrete,* (04), 4–7+14.

Hongtao, W., & Jueshi, Q., et al. (2006). Properties and application of steel-fiber reinforced magnesia phosphate cement mortar. *Architecture Technology,* (06), 462–464.

Hu, F., Xiaocong, Z., et al. (2018). Basic mechanical behavior of micro steel fiber reinforced magnesia-phosphate-cement mortar. *New Building Materials, 45*(9), 5.

Jiahuan, Y., Panhui, X., et al. (2017). Effect of polypropylene fiber content on properties of magnesium phosphate cement concrete. *Journal of Shenyang Jianzhu University (natural Science), 33*(02), 266–274.

Jian-Ming, Y., & Ang, Q. C., et al. (2009). Mechanical performance of glass fiber reinforced magnesia-phosphate cements in accelerated aging. *Journal of Building Materials, 12*(05), 590–594.

Kim, D. J., Naaman, A. E., et al. (2008). Comparative flexural behavior of four fiber reinforced cementitious composites. *Cement and Concrete Composites, 30*(10), 917–928.

Li, V., & Ward, R., et al. (1992). Steel and synthetic fibers as shear reinforcement. *Aci Structural Journal*.

Li, L. (2020). Experimental study on the mechanical properties of ductile hybrid fiber magnesium-phosphate-cement-based composite, Master's thesis, Zhengzhou University.

Naaman, A. E., & Reinhardt, H. W. (1996). Characterization of high performance fibre reinforced cement composites. *High Performance Fiber Reinforced Cement Composites, 2*, 1–24.

Quan-Bing, Y., & Sha, S. L., et al. (2004). Effects of polypropylene fiber on properties of phosphate cement-based concrete. *Low Temperature Architecture Technology,* (4), 1–3.

Shaikh, F. U. A. (2013). Deflection hardening behaviour of short fibre reinforced fly ash based geopolymer composites. *Materials and Design, 50*, 674–682.

Tingwei, L. (2017). Research on mechanical properties of fiber reinforced magnesium-potassium phosphate cement mortars. *Journal of Fuzhou University (Natural Science Edition), 45*(04), 528–534.

Xiangqing, K., & Huadong, G. et al. (2018). Fracture properties of hybrid steel- polypropylene fiber recycled aggregate concrete. *Concrete*, (10), 6.

Chapter 3
Performance Improvement and Design of UHDMC Using Fly Ash and Silica Fume

Abstract This chapter endeavored to create an ultra-high ductility MPC-based composite (UHDMC) utilizing fly ash (FA) and silica fume (SF). An initial macro-mechanical examination of UHDMC revealed significant enhancements in both ultimate tensile stress and strain when 30% FA and 20% SF substitutions for MPC were applied. Remarkably, an optimized mix of FA and SF enhanced both the ultimate tensile stress and strain. Subsequent investigation into micro-mechanical behavior of UHDMC led to the calculation of stress-based and energy-based pseudo strain hardening indices (PSH_σ and PSH_J, respectively). It emerged that for UHDMC, both PSH_σ and PSH_J increased with growing proportions of SF or FA substituting MPC. Application of FA, in contrast to SF, resulted in comparable PSH_σ but a superior PSH_J. Moreover, employing a mix of FA and SF yielded substantial enhancements in PSH_σ and PSH_J, with the F30 + S10 mixture found to be the most effective. From these findings, a numerical connection was established between pseudo strain hardening indices and ultimate tensile strain, serving as a roadmap to design UHDMC to a desired ultimate tensile strain. Notably, to achieve UHDMC with ultimate tensile strains up to and beyond 3%, both PSH_σ and PSH_J must collectively exceed 2.2 and 26.7, respectively.

Keywords Engineered cementitious composite · Fly ash · Silica fume · Magnesium phosphate cement · Strain hardening

3.1 Introduction

The concept of Engineered Cementitious Composite (ECC) was first proposed in the 1990s, sparking significant scientifical interest. ECC, a composite grounded on cement and bolstered by fibers, exhibits superior ductility and strain hardening characteristics (Singh & Munjal, 2020; Zhang et al., 2020). Remarkably, a fiber volume percentage of just 2% allows it to achieve an ultimate uniaxial tensile strain capacity exceeding 3% (Li, 2003; Li & Leung, 1992; Li et al., 2002a, 2002b).

H. Feng et al., *Ultra-High Ductility Magnesium-Phosphate-Cement-Based Composites (UHDMC)*, https://doi.org/10.1007/978-981-97-0952-6_3

Yu et al. enhanced the tensile strain capacity of ECC to between 8 and 12% by leveraging additional additives like silica fume, ground granulated blast-furnace slag, and polyethylene fibers in 2017 (Yu et al., 2017). Moreover, with an optimal mix, the compressive strength of ECC can top a significant 210 MPa (Tao et al., 2021). ECC's advent introduces a breakthrough approach to extend the lifespan of concrete structures or components, preventing the typical brittle failures seen with regular concrete under severe loads. In the world of civil engineering, ECC is primarily exploited to reinforce and repair crucial structural elements and concrete edifices, attributed to its strain hardening properties and high ductility (Lim & Li, 1997; Sui et al., 2018; Yu et al., 2018a, 2018b; Zhao et al., 2013).

Traditional ECC consists of common ingredients like ordinary Portland cement (OPC), sand, fibers, and water. However, the OPC component is known to induce shrinkage during hydration, leading to potential cracks that compromise the ECC's strength and long-term durability (Zhenming et al., 2021). Furthermore, OPC's extended setting time and ineffectiveness at low temperatures restrict its useful application in fast repairs, particularly in cold environments. An alternative, magnesium phosphate cement (MPC), characterized by its rapid setting, has seen extensive use in fortifying and speedily remedying structures such as airport runways, roads, and bridges, as well as military facilities (Arora et al., 2019; Haque & Chen, 2019; Hou et al., 2016; Liang et al., 2021). By substituting OPC with MPC in the formulation, an advanced ECC variant emerges, named the ultra-high ductile MPC-based composite (UHDMC). This transformation integrates the merits of MPC (rapid setting, early high strength, and regular setting and hardening even amidst low temperatures) with the distinct properties of ECC (remarkable ductility and steady-state multi-cracking behavior), presenting a more versatile solution for rapid repair and reinforcement projects where regular ECC may fall short.

Currently, UHDMC stands at an early stage of development. Feng et al. introduced a novel ductile fiber-reinforced MPC-based composite revealing flexural hardening characteristics under bending stresses, as well as generating multiple cracks—mirroring the behaviors inherent in ECC (Feng et al., 2021). However, the production process of calcined magnesium oxide (MgO), a primary ingredient in MPC, consumes considerable energy, leaving a substantial environmental burden and CO_2 footprint. As the pursuit for more ecologically friendly infrastructure intensifies, the call for greener construction materials grows. Efforts have been made to adapt a more sustainable MPC-based composite by partly replacing the MPC with mineral wastes like fly ash (FA) and silica fume (SF) (Haque & Chen, 2019; Jin et al., 2021; Liu et al., 2014; Yang et al., 2013). It's observed that FA and SF act not only as inert fillers, effectively filling pores and cracks in MPC-based composites, but also enhance the composite's flexural strengths (Ahmad & Chen, 2018b, 2020; Ahmad et al., 2019; Xu et al., 2020), indicating a potential rise in fiber bridging ability. However, there are downsides. The inclusion of FA weakens the strength of MPC matrix due to the diminished amount of cementing materials and the frail bonding between FA's spherical particles and the matrix (Bilginer & Erdoğan 2021; Li et al., 2015). Also, Wu et al. found that while SF considerably aids in early hydration stages,

this impact wanes over time and its activation proves difficult in MPC's acidic environment, resulting in a decline in 28-day strength of the MPC matrix (Wu et al., 2020). According to the strength criterion in ECC's micromechanical design, matrix cracking strength should be lower than the fiber bridging capacity for multi-cracking to occur (Kanda & Li, 1999; Li, 2019; Yang et al., 2008). Hence, boosting fiber bridging capacity and reducing matrix strength may help MPC-based composites achieve this criterion. Yet, whether the addition of FA or SF benefits the creation of sustainable UHDMC is largely unexplored territory, prompting an investigation into their impact on UHDMC. Moreover, since FA and SF exhibit variabilities in particle sizes, their combined usage might yield superior outcomes. Consequently, this chapter also examines the effects of blending FA and SF on UHDMC.

Within this chapter, both FA and SF were utilized to partially substitute MPC in the formulation, and the design of the ECC was referred to for the inclusion of PVA fibers at a volume content of 2% to create the UHDMC. Initial steps involved applying both compressive and tensile tests to evaluate the macroscopic mechanical properties such as compressive strength and tensile properties inherent in the UHDMC samples. Following this, a series of tests were performed: single crack tensile test for notched UHDMC specimens, uniaxial tensile test for UHDMC matrix (without fiber), and three-point flexural test for notched UHDMC matrix (without fibers). These tests were conducted to unearth UHDMC's micromechanical parameters, and the calculation of pseudo strain-hardening indices was done for the same. To provide insights into optimizing the design of eco-friendly UHDMC by the regulation of the micromechanical parameters, a relationship between pseudo strain-hardening indices and the ultimate tensile strain was formed. Furthermore, to better comprehend the microscale influence mechanisms of FA or SF on UHDMC, the study incorporated X-ray diffraction (XRD) tests to scrutinize the crystalline structures of the MPC pastes, and Scanning Electron Microscopy (SEM) tests to inspect the matrix of UHDMC and the fiber surface.

3.2 Background

3.2.1 Hydration Mechanism of MPC

MPC, as a typical ternary system, is traditionally formed by integrating magnesium oxide (MgO), potassium dihydrogen phosphate (KH_2PO_4), and H_2O. It acts as a cementitious substance which amasses strength via an acid–base neutralization reaction reflected in Eq. 3.1. Under the conditions of a pure MPC system, the main hydration stages unfold as follows: At the outset, KH_2PO_4 breaks down in water into H^+, K^+, and PO_4^{3-}, resulting in an acidic solution which catalyzes the hydrolysis of MgO, generating Mg^{2+} and OH^-. This is followed by a union of K^+, Mg^{2+}, and PO_4^{3-} to produce the principal hydration product, namely magnesium potassium

phosphate hexahydrate ($MgKPO_4 \cdot 6H_2O$ or struvite-K) (Ding et al., 2012). Ultimately, struvite-K coalesces with unreacted MgO forming the structural skeleton of MPC.

$$MgO + KH_2PO_4 + 5H_2O \rightarrow MgKPO_4 \cdot 6H_2O \tag{3.1}$$

The research conducted by Xu et al. presented that the integration of FA into MPC-based materials aided in mitigating the heat produced during early hydration (Xu et al., 2018, 2019). Serving as an inactive filler, FA diluted the binder in MPC-based composites, which led to a postponement in the initial reaction and consequently brought down the release of early heat (Gardner et al., 2015). Additionally, metallic cations in FA could break down into Ca^{2+} and Al^{3+} and take part in the hydration reaction, combining with K^+ and ${PO_4}^{3-}$ to yield minor by-products, specifically calcium potassium hydrogen phosphate ($CaK_3H(PO_4)_2$) and potassium aluminosilicate (Xu et al., 2018). It should be noted that these secondary by-products are detectable only when FA exceeds a concentration of 70%; below this threshold, they are indiscernible (Xu et al., 2018). SF's contribution differs from FA. When SF is added, a $MgO–SiO_2–KH_2PO_4$ system can be established. The highly active SiO_2 in SF undergoes an initial reaction with water to create $Si(OH)_4$, which then binds with OH^- to produce either ${SiO_2(OH)_2}^{2-}$ or ${SiO_2(OH)}^{3-}$. These substances readily capture metallic cations from the solution. Ultimately, ${SiO_2(OH)_2}^{2-}$ or ${SiO_2(OH)}^{3-}$ unites with Mg^{2+}, leading to the formation of an amorphous magnesium silicate gel ($MgSiO_3$). This gel collaborates with $MgKPO_4 \cdot 6H_2O$ (struvite-K) to form a bond (Xie et al., 2020).

3.2.2 Design Criteria of ECC

In order for the composites to exhibit strain-hardening and multiple-cracking characteristics, the fulfillment of both the strength and energy criteria is crucial (Li, 2019). Figure 3.1 illustrates a standard fiber bridging stress-crack opening curve of composites (Li, 2019), where σ_{fc} and σ_0 denote the matrix's cracking strength and the fiber's bridging potential (the maximum stress handled by the bridging fibers), respectively. The strength criterion is pre-set for the beginning of the crack. If a tensile stress needed to cause a new crack exceeds the capacity of the fiber to bridge, a localized fracture will occur at any location where the crack has originated, thus preventing the formation of multiple cracks. Consequently, to enable multiple-cracking, the matrix's cracking strength (σ_{fc}) must be lesser than the fiber bridging capacity (σ_0, observe Fig. 3.1), as specified in Eq. 3.2. The energy criterion is for flat crack propagation. In the case of this mode of propagation, the crack essentially maintains a stable crack opening under a specific load, except for a minor area near the crack's tip. The fiber bridging complementary energy (J_b', refer to Fig. 3.1) should be at least equal to or higher than the matrix's fracture energy (J_{tip}, refer to Fig. 3.1) for the flat crack propagation to continue after the crack's initiation. This is outlined in Eq. 3.3.

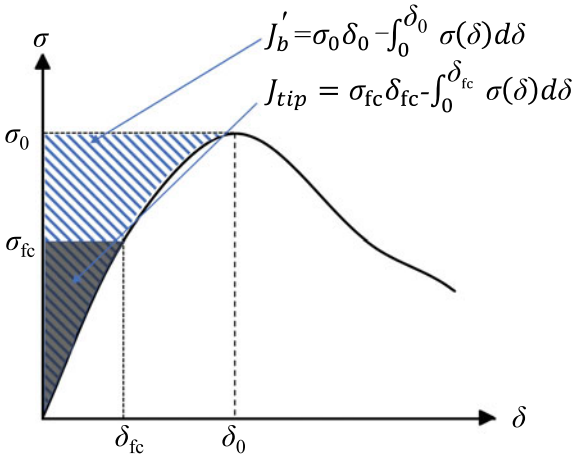

Fig. 3.1 Typical fiber bridging stress-crack opening curve. Reproduced from Development and design of ultra-high ductile magnesium phosphate cement-based composite using fly ash and silica fume by Hu Feng with permission from Elsevier

$$\sigma_{fc} \leq \sigma_0 \tag{3.2}$$

$$J_{tip} \leq J_b' \tag{3.3}$$

where σ_0 is fiber bridging capacity; σ_{fc} is cracking strength of the matrix; J_b' is fiber bridging complementary energy; and J_{tip} is the matrix fracture energy.

To guide the optimized design of ECC, the stress-based pseudo strain hardening index (PSH_σ) and the energy-based pseudo strain hardening index (PSH_J) are articulated in Eqs. 3.4 and 3.5, respectively. These indices serve as effective measures to appraise the level to which a composite can demonstrate strain hardening characteristics.

$$PSH_\sigma = \sigma_0 / \sigma_{fc} \tag{3.4}$$

$$PSH_J = J_b' / J_{tip} \tag{3.5}$$

3.3 Materials and Experiments

3.3.1 Materials

The UHDMC is formulated from a blend of magnesium phosphate cement (MPC), fly ash (FA) or silica fume (SF) or a combination of both FA and SF, polyvinyl alcohol (PVA) fiber, silica sand, and water. The MPC used is a concoction of dead-burned magnesium oxide (MgO), potassium dihydrogen phosphate (KH_2PO_4), and

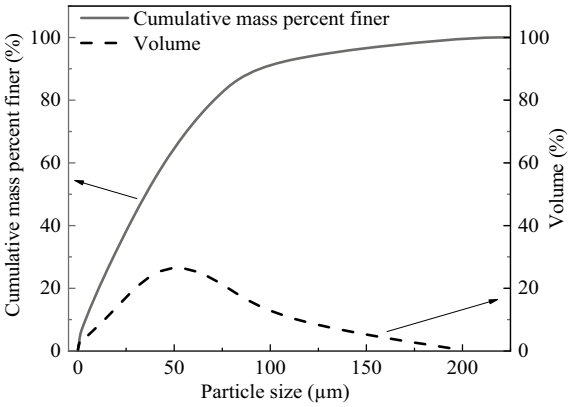

Fig. 3.2 Particle size distribution of MgO. Reproduced from Development and design of ultra-high ductile magnesium phosphate cement-based composite using fly ash and silica fume by Hu Feng with permission from Elsevier

borax (employed as a retarder). The MgO (the purity is no less than 96.5%) is supplied by Jiangsu's Huanai Magnesium Industry Co., Ltd., with its particle size distribution evidenced in Fig. 3.2. An observational study from Fig. 3.3a reveals the irregular formation of MgO particles. Borax of industrial grade, with a purity of 95%, is sourced from Liaoning's Banda Technology Co., Ltd. Two distinct particle size ranges of KH_2PO_4 (a white crystal with a purity of at least 99.5%) are procured from two manufacturers: Sichuan Mianzhu Ronghong Chemical Co., Ltd. and Henan Huaxing Chemical Co., Ltd. It's important to note that the particle size of KH_2PO_4 significantly impacts the chemical reaction rate within the MPC. If KH_2PO_4 particles are overly fine, they accelerate the reaction, and if they're excessively large, they retard the reaction, potentially leading to insufficiency. Thus, these two versions of industrial-grade KH_2PO_4 are amalgamated at a mass ratio of 1:1 and used in this investigation. The particle size distribution of KH_2PO_4 is examined using a particle size analyzer (Model: BT-601, Dandong Baite Instrument Co., Ltd., Dandong, China) and is illustrated in Fig. 3.4.

Fly ash (FA) and silica fume (SF) are incorporated as partial substitutes for MPC. Sourced from Yulian Electricity Plant in Gongyi, Henan, China, the FA utilized is Grade F coal ash—it exhibits a specific surface area of 461.9 m^2/kg. As displayed in Fig. 3.3b, it can be observed that the FA carries a uniform structure with sleek, spherical particles. On the other hand, SF is sourced from Gongyi's Jinfeng Water Purification Material Co., Ltd in Henan, China. It has a high specific surface area ranging between 2×10^4 and 2.8×10^4 m^2/kg. Figure 3.3c presents the SF particles as being spherical, albeit of a smaller size compared to FA. The chemical compositions and particle size distribution for both FA and SF are detailed in Table 3.1 and Fig. 3.5, respectively.

The PVA fiber from Kuraray Company, Japan, is used, with its appearance shown in Fig. 3.6. The technical parameters are shown in Table 3.2.

The silica sand, available in particle sizes of 80–120 mesh (125–178 μm) and 120–150 mesh (100–125 μm), is supplied by Zhongbang Environmental Protection Technology Co., Ltd. from Henan, China. To achieve a more balanced particle size

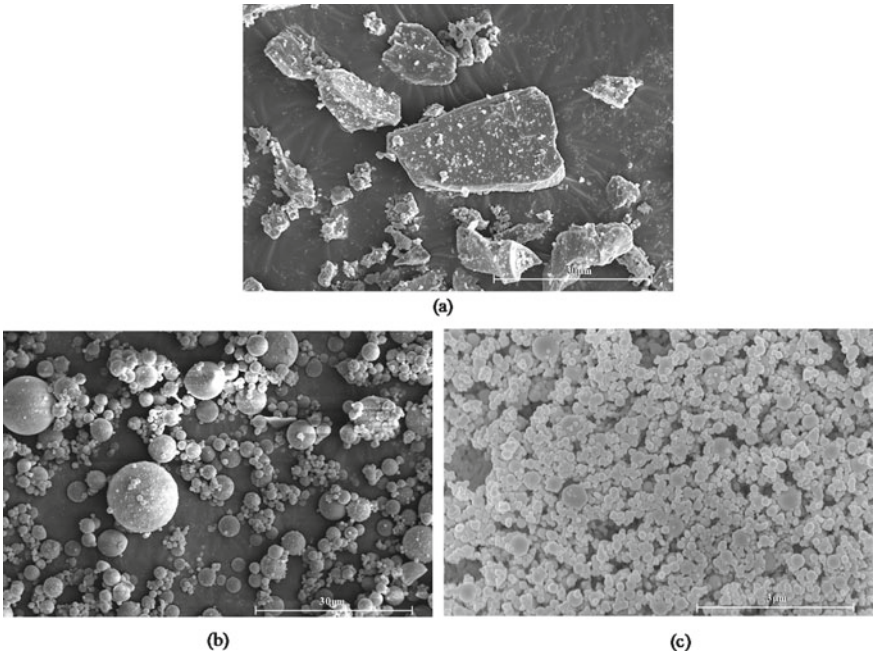

Fig. 3.3 SEM images of **a** MgO, **b** FA, and **c** SF. Reproduced from Development and design of ultra-high ductile magnesium phosphate cement-based composite using fly ash and silica fume by Hu Feng with permission from Elsevier

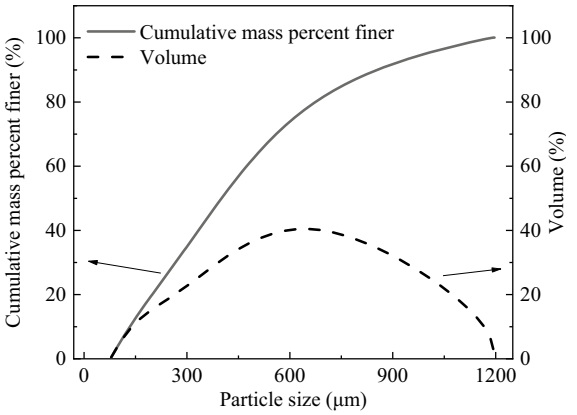

Fig. 3.4 Particle size distribution of KH_2PO_4. Reproduced from Development and design of ultra-high ductile magnesium phosphate cement-based composite using fly ash and silica fume by Hu Feng with permission from Elsevier

distribution, these two variants of silica sand are blended in an equal mass ratio of 1:1 prior to being used. The water used for the UHDMC mixture is derived from the local tap water supply.

Table 3.1 Chemical composition of FA and SF

Chemical composition	Mineral admixture	
	FA (wt.%)	SF (wt.%)
SiO_2	53.97	97
Al_2O_3	31.15	1.0
Fe_2O_3	4.16	0.9
CaO	4.01	0.7
MgO	1.01	0.3
Na_2O	0.89	1.3

Reproduced from Development and design of ultra-high ductile magnesium phosphate cement-based composite using fly ash and silica fume by Hu Feng with permission from Elsevier

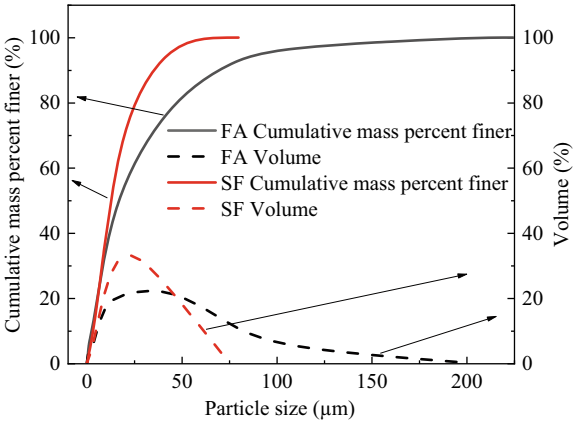

Fig. 3.5 Particle size distribution of FA and SF. Reproduced from Development and design of ultra-high ductile magnesium phosphate cement-based composite using fly ash and silica fume by Hu Feng with permission from Elsevier

Fig. 3.6 Appearance of PVA fiber. Reproduced from Development and design of ultra-high ductile magnesium phosphate cement-based composite using fly ash and silica fume by Hu Feng with permission from Elsevier

Table 3.2 Technical parameters of PVA fibers

Diameter (μm)	Length(mm)	Tensile strength (MPa)	Elastic modulus (GPa)	Elongation (%)	Density (g/cm^3)
40	12	1560	41	6.5	1.3

Reproduced from Development and design of ultra-high ductile magnesium phosphate cement-based composite using fly ash and silica fume by Hu Feng with permission from Elsevier

3.3.2 Mixture Proportions

The UHDMC formulation is composed of a mixture of MPC, FA or SF (or a combination of both FA and SF), silica sand, PVA fiber, and water. The MgO to KH_2PO_4 molar ratio is 4 within the MPC, which draws upon previous research insights (Feng et al., 2021; Yue et al., 2014), while the borax component forms 6% of the MgO mass (Feng et al., 2021; Hall et al., 2001). FA serves as a substitute for 10–50% of the MPC mass in increments of 10%, and SF replaces 5% up to 20% of MPC by mass in 5% increments. In this blend, the mass ratio of silica sand to binders (MPC and any mineral admixtures) is set at 0.2, and water to binder ratio at 0.15. Based on prior studies, the PVA fiber volume has been set at 2% of the UHDMC volume (Arain et al., 2019; Feng et al., 2022). The specific mixing ratios of UHDMC components can be found in Table 3.3. Just to illustrate, the control sample contains a mass ratio of water: MPC: sand: FA: SF at 0.15:1:0.2:0:0, additionally featuring 2% fiber by UHDMC volume.

Table 3.3 Mixture proportions of UHDMC

Samples	Water[a]	MPC[a]	Sand[a]	FA[a]	SF[a]	PVA fibers[b] (%)
Control	0.15	1	0.2	0	0	2
F10	0.15	0.9	0.2	0.1	0	2
F20	0.15	0.8	0.2	0.2	0	2
F30	0.15	0.7	0.2	0.3	0	2
F40	0.15	0.6	0.2	0.4	0	2
F50	0.15	0.5	0.2	0.5	0	2
S5	0.15	0.95	0.2	0	0.05	2
S10	0.15	0.9	0.2	0	0.1	2
S15	0.15	0.85	0.2	0	0.15	2
S20	0.15	0.8	0.2	0	0.2	2

Note [a]The mass ratio relative to the total mass of cementitious materials (MPC + FA + SF); and [b]By volume of UHDMC

Reproduced from Development and design of ultra-high ductile magnesium phosphate cement-based composite using fly ash and silica fume by Hu Feng with permission from Elsevier

3.3.3 Mixing and Specimen Preparation

The preparation of UHDMC adheres to the following protocol. Initially, the predefined mix proportions of MgO, KH_2PO_4, borax, sand, and mineral additives (as outlined in Table 3.3) were introduced into the mixer, where they were blended at a slow speed for 120 s. Subsequently, water was incorporated into this mixture and stirred for an additional 60 s. In the final step, PVA fibers were gradually integrated into the mix and stirred for a duration of 90 s.

Following the mixing process, the resultant UHDMC mixture was transfered into molds and subjected to vibrations on a table in two phases. An initial 45 s vibration aided in the expulsion of gas, after which the mixture surface was leveled using a scraper. The subsequent 15 s vibration helped to increase the compactness of the cast specimens. Following this, the specimens were stationed in a curing chamber maintained at a temperature of 20 ± 2 °C and a relative humidity of 98% for a period of 2 h. Afterwards, the specimens were released from the molds and remained in the curing environment until the targeted test age was reached (seven days in this case). All tests were performed at seven days post-casting, as previous findings reveal that by this time, the strength of MPC can potentially reach 80% or more of the 28-day strength (Chau et al., 2011; Ding & Li, 2005; Xu et al., 2017; Yue & Bing, 2013), and hence the properties of the UHDMC can be reasonably represented by seven-day results.

3.3.4 Experiments

3.3.4.1 Slump Test

The impact of FA and SF on the slump of UHDMC was assessed via slump test conforming to the Chinese standard JGJ/T283-2012. The testing procedure's schematic representation is depicted in Fig. 3.7. The mean value derived from three replicates was utilized for the evaluation.

3.3.4.2 Macromechanical Tests

(1) *Compressive test on* UHDMC *specimens*

The compressive test of UHDMC samples aged seven days was performed following the ASTM C109 procedure to ascertain the compressive strength. The application of force was maintained at a rate of 0.9 kN/s. Three cubic specimens, each measuring 50 mm on all sides, were tested for every mixture, with the mean value utilized for results.

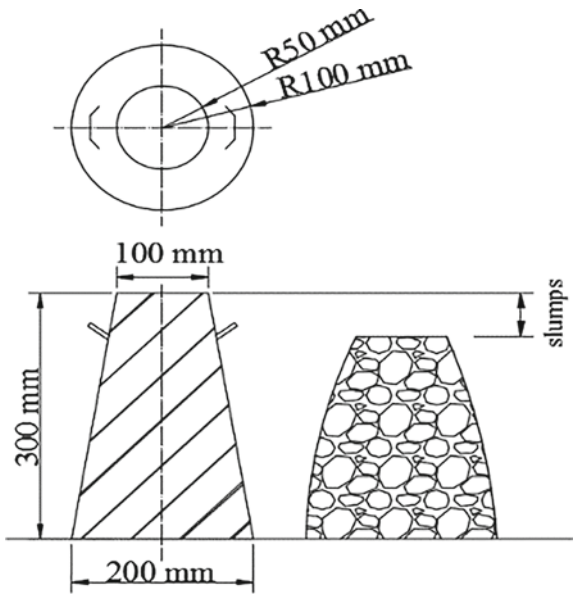

Fig. 3.7 Schematic diagram of slump test. Reproduced from Development and design of ultra-high ductile magnesium phosphate cement-based composite using fly ash and silica fume by Hu Feng with permission from Elsevier

(2) *Tensile test on* UHDMC *specimens*

UHDMC samples shaped like dog bones were molded and went through a curing process for a duration of one week. The tensile test was performed on these samples using a UTM6203 electronic universal testing machine made by Shenzhen Suns Technology Stock Co., Ltd., operating at a stroke control rate of 0.2 mm/min, as displayed in Fig. 3.8. Two YWC-20 model LVDTs by Liyang Chaoyuan Instrument Factory, Jiangsu, acclaimed for their accuracy of 0.025 mv/mm, were stationed on each side of the samples to assess the displacement as tensile force was deployed. The load and displacement data were gathered and consequently translated into a tensile stress–strain graph. The highest tensile stress and its respective tensile strain were designated as the ultimate tensile stress and strain, respectively. Four samples were tested for every mixture, and the mean value for the results was used.

3.3.4.3 Micromechanical Tests

For the evaluation of the strain hardening behavior of UHDMC from the micromechanical perspective using the two design criteria (Eqs. 3.2 and 3.3) of ECC, the corresponding micromechanical parameters need to be acquired through a series of micromechanical tests, *as introduced below.* Four specimens were used for each mixture, and the average value was used.

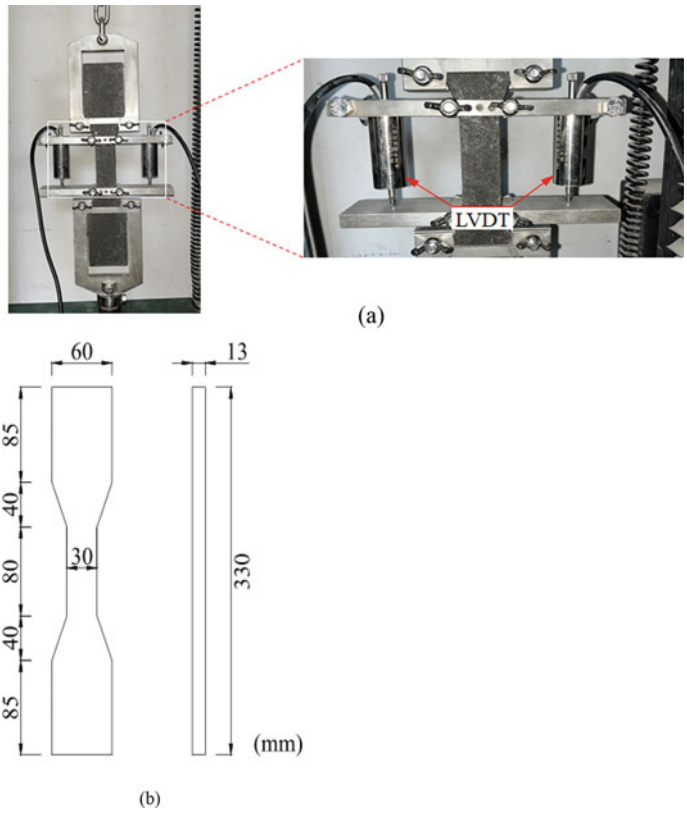

Fig. 3.8 Tensile test on UHDMC specimens: **a** setup and **b** dog-bone-shaped specimen (JSCE, 2008). Reproduced from Development and design of ultra-high ductile magnesium phosphate cement-based composite using fly ash and silica fume by Hu Feng with permission from Elsevier

(1) *Single-crack tensile test on notched* UHDMC *specimens*

The dog-bone-shaped UHDMC samples were finely prepared and then specifically notched, ensuring a single crack to occur, as demonstrated in Fig. 3.9 (Zhou et al., 2019). A single-crack tensile test was then implemented on these seven-day old specimens, following the same procedures detailed in the previous section. Two LVDT devices were deployed to capture the crack opening displacement under tensile stress. From this, the correlation of fiber bridging stress with crack opening displacement was obtained. The maximum fiber bridging stress is denoted as fiber bridging capacity (σ_0), and the fiber bridging complementary energy (J_b') can be calculated using Eq. 3.6 (see Fig. 3.1 for schematical illustration).

$$\sigma_0\delta_0 - \int_0^{\delta_0} \sigma(\delta)\mathrm{d}\delta = J_b' \tag{3.6}$$

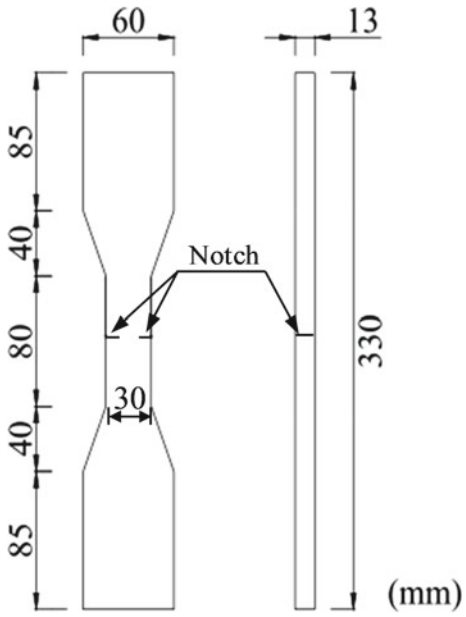

Fig. 3.9 Notched dog-bone-shaped UHDMC specimen for single-crack tensile test. *Note* the depth of the notches on both sides of the specimen is 7.5 mm Reproduced from Development and design of ultra-high ductile magnesium phosphate cement-based composite using fly ash and silica fume by Hu Feng with permission from Elsevier

where σ is fiber bridging stress; δ is crack opening displacement; σ_0 is fiber bridging capacity; δ_0 is crack opening displacement at σ_0; and J_b' is fiber bridging complementary energy.

(2) *Tensile test on* UHDMC *matrix* (without fibers)

Dog-bone-shaped UHDMC matrix (without fibers) was prepared, as illustrated in Fig. 3.8b. Tensile test was then carried out on this 7-day-old, fiber-free UHDMC matrix following the methods discussed in the previous section. The load and displacement responses were tracked and subsequently transformed into a tensile stress–strain graph. The gradient of the graph within the elastic zone was referred to as the elastic modulus (E_c), while the peak tensile stress was marked as cracking strength (σ_{fc}).

(3) Three-point flexural test on notched UHDMC matrix (without fibers).

Beams of dimensions $40 \times 40 \times 160\,mm^3$ were fabricated using a fiber-free UHDMC matrix. A cutting tool engineered a 12 mm-height indentation at the beam's underside, maintaining a notch to beam height ratio of 0.3 (Dao-Yuan, 2004)—evident in Fig. 3.10. To examine these notched UHDMC matrix beams, aged 7 days, a three-point flexural test was executed, adhering to ASTM E399, by utilizing an electronic universal testing apparatus. The individual beam mass and each beam's peak load (F_Q) were systematically recorded. Subsequently, fracture toughness (K_m) was computed through Eqs. 3.7 and 3.8, which subsequently informed the matrix fracture energy (J_{tip}) calculation, employing Eq. 3.9, in tandem with the elastic modulus (E_c) (Victor, 1993; Xu & Reinhardt, 1999).

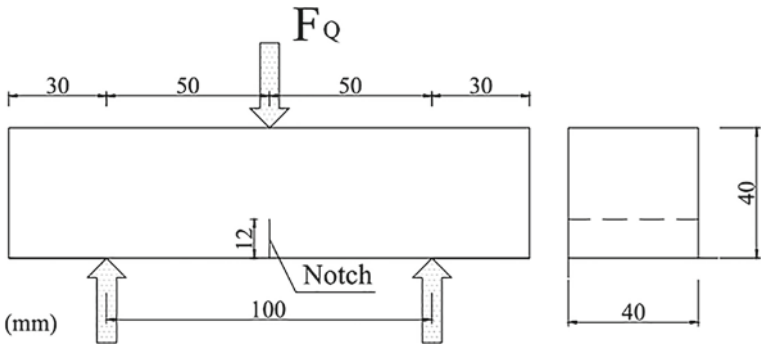

Fig. 3.10 Notched UHDMC matrix beam for three-point flexural test. Reproduced from Development and design of ultra-high ductile magnesium phosphate cement-based composite using fly ash and silica fume by Hu Feng with permission from Elsevier

$$K_m = \frac{1.5 \times \left(F_Q + 0.5\,m \times g \times 10^{-2}\right) \times 10^{-3} \times S \times a_0^{1/2}}{t \times h^2} \times f(a) \tag{3.7}$$

$$f(a) = \frac{1.99 - a \times (1-a) \times \left(2.15 - 3.93a + 2.7a^2\right)}{(1+2a) \times (1-a)^{3/2}}, \alpha = \frac{a_0}{h} \tag{3.8}$$

$$J_{\text{tip}} = K_{\text{m}}^2 / E_{\text{c}} \tag{3.9}$$

where F_Q is the peak load on the beam; m, t, h, and S are the mass, width, height, and span length of a beam, respectively; g is the gravitational acceleration; a_0 is the notch height of a beam; and $f(\alpha)$ is the shape parameter of a beam.

3.3.4.4 X-ray Diffraction (XRD) Test

The D/max-RB X-ray diffractometer, a product of Japan's Rigaku Company, was employed to conduct the XRD test, which evaluated the crystalline phase of 7-day-old MPC paste specimens. This investigation was carried out to determine the impact of FA and SF on the materials' hydration products. In order to condition the samples for this XRD test, they were initially crushed into minute fragments before undergoing a two-day immersion in anhydrous ethanol to halt hydration. Afterwards, the specimens were oven-dried at 50 °C until reaching a constant mass. The subsequent stage involved grinding the dried specimens into refined powders utilizing an agate mortar. Lastly, the milled powders that successfully traversed through a No. 325 (45 μm) sieve were gathered for the XRD test. A diffraction spectrum within the 10–90° (2θ) extent was captured with the assistance of a Cu-Kα radiation source at a scanning pace of (10–20°)/min. The HighScore Plus software was utilized to interpret the diffractive pattern.

3.3.4.5 Scanning Electron Microscopy (SEM) Test

The SEM test was performed using the Helios G4 CX, a system manufactured in the Czech Republic, on UHDMC specimens after a curing period of seven days. The acceleration voltage throughout the test was maintained at 15 kV. The portion under tensile stress from the dog-bone-shaped specimens was chosen for the SEM evaluation. The initial preparation involved slicing these specimens into segments with a thickness of 3 mm, each boasting a cross-section around 1 cm^2, and then immersing these slices in anhydrous ethanol for 48 h to inhibit hydration. The next phase included drying these slices in a 50 °C oven for an equivalent duration. Following this, they were sputter-coated with gold in a vacuum atmosphere to ensure optimal conductivity. The microstructures of the UHDMC matrix and the embedded fibers were meticulously studied to gain insights into the changes in mechanical properties of UHDMC as a result of the inclusion of FA and SF, providing a microscopic viewpoint of the change.

3.4 Results and Discussion

3.4.1 Slump of UHDMC

(a) The addition of mere FA or SF

Figure 3.11 illustrates the impact of FA and SF on the workability, or slump, of UHDMC. As demonstrated, an upward trend in UHDMC's slump is notable when the MPC gets substituted by FA in an escalating percentage from 0 to 30%. This phenomenon can be connected to the smooth and rolling activity of FA's spherical particles (Gardner et al., 2015; Xu et al., 2017). However, when the FA substitutes the MPC beyond 30%, up to 50%, the slump graph indicates a downward trajectory. This slump reduction can possibly be attributed to two factors: one being the excessive FA leading to the dilution of cementitious substances, thus undermining the inter-particle bonding, and the other being the requirement of excess water to wet considerable quantity of FA with a high specific surface area, consequently depleting free water in the matrix and reducing UHDMC's flowability. Furthermore, empirical observations suggest that PVA fibers manifest poor dispersion and considerable clumping if FA replaces less than 10% of MPC. Contrastingly, an FA content increase from 10 to 50% noticeably enhances fiber dispersion. This suggests that higher flowability, and hence greater slump, is achievable when MPC substitution by FA exceeds 10%.

Figure 3.11 also illustrates a pattern where the slump increases incrementally as the MPC gets replaced by SF from 0 to 15%, then sees a slight decrement when the SF substitution for MPC surpasses 15%. The plausible cause for this could be the well-distributed and smaller, more uniform granules of SF when compared to MgO (as shown in Fig. 3.3a, c). These fine SF particles can nestle into spaces between the irregular MgO granules, thus decreasing inter-particle friction and enhancing the

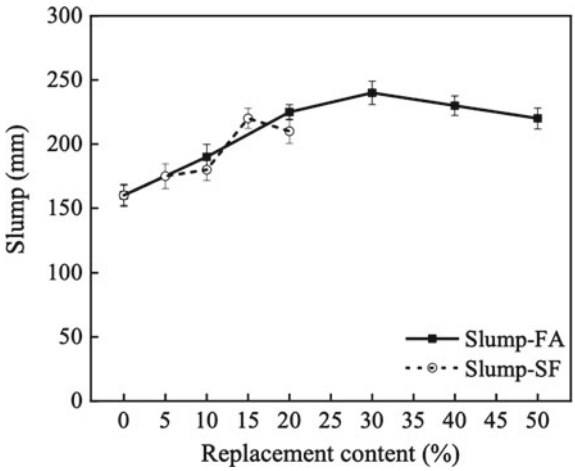

Fig. 3.11 Slump of UHDMC with varying FA and SF contents replacing MPC. Reproduced from Development and design of ultra-high ductile magnesium phosphate cement-based composite using fly ash and silica fume by Hu Feng with permission from Elsevier

fluidity of UHDMC (Xu et al., 2020). However, this beneficial trend reverses when SF's replacement of MPC exceeds 15%, as SF's high water absorption properties outweigh its filling effect, leading to a reduction in UHDMC's fluidity. Experimental observations reveal a pattern parallel to that with FA: under 10% of SF in MPC, suboptimal fiber dispersion occurs due to UHDMC's decreased flowability. Yet, the flowability is improved when SF content is at the 15% or 20%, leading to improved fiber dispersion.

When comparing FA to SF at equivalent percentages, observations indicate that FA results in a marginally larger slump than SF, suggesting a superior capability of FA to boost UHDMC's flowability. More importantly, it's worth highlighting that the integration of either FA or SF into the UHDMC mix, in comparison to the base mix, unequivocally enhances the material's flowability to a significant extent.

(2) The addition of blended FA and SF

Figure 3.12's subplots (a), (b), (c), and (d) present the slump and slump flow of UHDMC, featuring the cumulative quantity of FA and SF at 10, 20, 30, and 40%, respectively. In these illustrations, "F and S" denote FA and SF, and the succeeding digit refers to their substitution rate (%) in MPC. As per these diagrams, the introduction of fly ash and silica fume significantly boosts UHDMC's slump and slump flow, signifying enhanced workability. Particularly, when the combined replacement rate reaches 30%, both the slump and slump flow escalate. Specifically, for F30 + S0, the slump and slump flow can attain values of 240 mm and 56 cm, correspondingly. This is attributed to the spherical effect of both fly ash and silica fume—the spherical particles aid in augmenting the material's flowability (Xiaoying et al., 2020; Zheng et al., 2016).

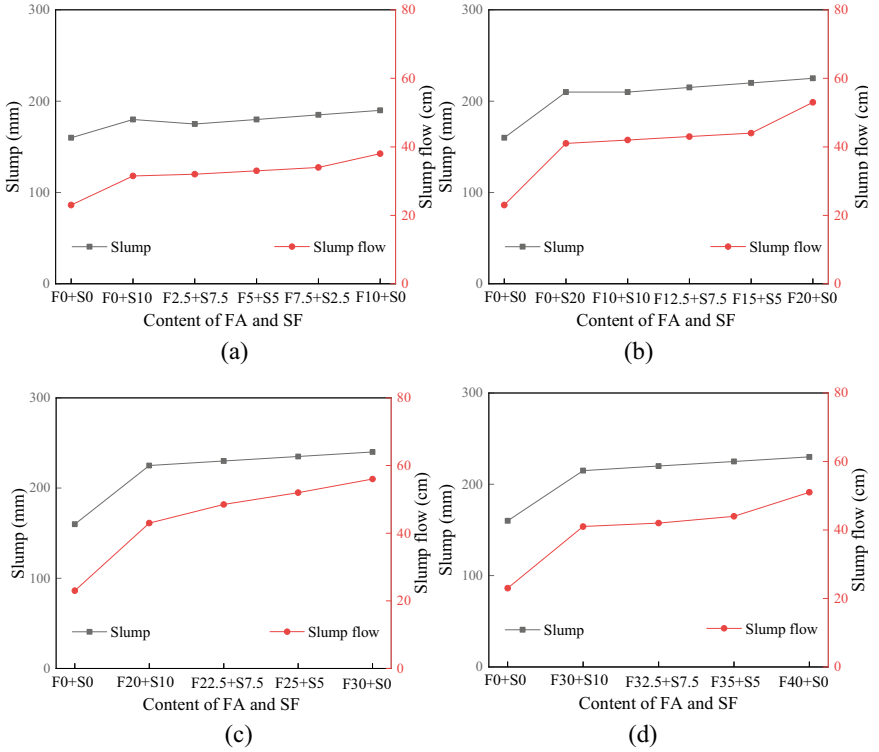

Fig. 3.12 Slump and slump flow of UHDMC with a total content of FA and SF of **a** 10%, **b** 20%, **c** 30%, and **d** 40%. Reproduced from Evaluation on the performance of magnesium phosphate cement-based engineered cementitious composites (MPC-ECC) with blended fly ash/silica fume by Hu Feng with permission from Elsevier

In contrast to the reference group (absent of mineral admixtures), the heightened percentage increments of slump at total substitution contents of 10, 20, 30, and 40% rise to 18.8, 40.6, 50.0, and 43.8%, respectively. Similarly, the maximum increments in slump flow reach 65.2, 130.4, 143.5, and 134.8% correspondingly. Additionally, with each total substitution level, an upward slight trend is observed in the UHDMC's slump and slump flow as the fly ash content amplifies (and the silica fume content decreases). This could potentially be ascribed to the comparably more refined particles of silica fume than fly ash, resulting in a greater water requirement for particle wetting.

3.4.2 Macromechanical Properties of UHDMC

3.4.2.1 Compressive Properties of UHDMC

(a) The addition of mere FA or SF

Figure 3.13 highlights the influence of Fly Ash (FA) and Silica Fume (SF) on the 7 day UHDMC compressive strength. Observable is an initial rise followed by a decline in compressive strength as the FA substitute for MPC mounts from 0 to 50%. At the 20% FA content, it peaks (approximately 1.3 times the control's), but with 50% FA replacement, the strength drops to roughly 0.7 times the control's value. As is evident, an appropriate measure of FA can enhance the UHDMC's compressive strength. This shift can trace its origin to variations in fiber bridging capacity. The compressive strength of the UHDMC is a reflection of the matrix's strength and the bonding strength between the fiber and the matrix. While the former sees a decrease with FA introduction, the fiber bridging capacity experiences a rise. Particularly, at 20% replacement, the fiber bridging capacity peaks, signaling how FA most significantly ameliorates the adhesive vigor between fibers and the matrix, hence, achieving the maximal compressive strength. Similar to FA, an initial increase and subsequent decrease in compressive strength are perceived with an ascent in SF content replacing MPC from 0 to 20%, achieving the peak (118% of the control) at 10% SF content. Interestingly, the compressive strength at any SF content replacing MPC (5–20%) outperforms that of the control, implying SF content below 20% benefits the UHDMC's compressive strength. Moreover, Fig. 3.13 discloses that at 10% MPC replacement, SF induces a compressive strength akin to FA; however, FA brings about superior compressive strength to SF at 20% replacement. This outcome ties closely to the matrix cracking strength and the fiber bridging capacity. While both yield comparable matrix cracking strength and fiber bridging capacity at 10% MPC replacement, at 20% replacement, FA leads to a heightened matrix cracking strength and fiber bridging capacity compared to SF.

(b) The addition of blended FA and SF

Figure 3.14 delineates the 7 day UHDMC's compressive strength with respective total fly ash and silica fume contents of 10, 20, 30, and 40%. Emerging from the data, when the total content is 10%, relative to the control group, F10 + S0 and F0 + S10 register superior compressive strength, escalating by 18.0 and 13.9%, respectively. However, the F5 + S5 and F7.5 + S2.5 categories witness negligible advancements in their respective compressive strengths. When the total content rises to 20%, in contrast to the control group, UHDMC samples comprising fly ash and silica fume exhibit amplified compressive strength. Specifically, the compressive strength of F20 + S0 and F10 + S10 can escalate to 43.7 and 41.7 MPa, up by 29.3 and 23.4% from the control group, respectively. The reason for such outcomes is the micro-aggregate filling effect of both fly ash and silica fume, enabling them to occupy the pores and cracks within the cement matrix (Ahmad & Chen, 2018a; Li & Feng, 2011). Additionally, the SiO_2 in fly ash and silica fume can contribute to the reaction

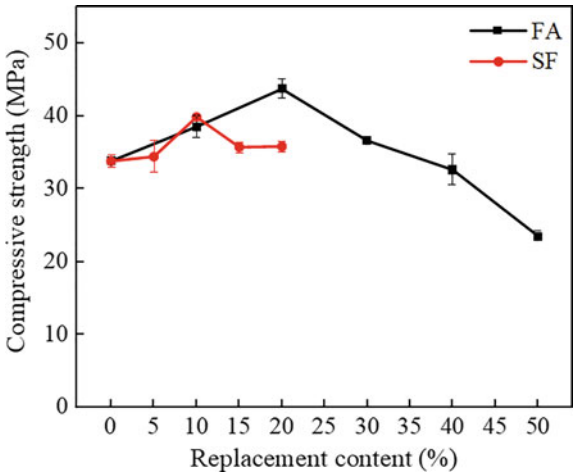

Fig. 3.13 Compressive strength of UHDMC with varying FA and SF contents replacing MPC. Reproduced from Development and design of ultra-high ductile magnesium phosphate cement-based composite using fly ash and silica fume by Hu Feng with permission from Elsevier

system, generating gelling substances like magnesium silicate (Li & Feng, 2011; Lin et al., 2010), which can intertwine with the $MgKPO_4 \cdot 6H_2O$ (MKP) gelling substance and solid particles to enhance compressive strength. However, a total substitution content of 30% results in marginal improvement, and a 40% substitute may even be detrimental to UHDMC's compressive strength. This could be due to the escalating porosity in the UHDMC induced by surplus mineral admixtures (Mo et al., 2018).

3.4.2.2 Tensile Properties of UHDMC

(a) The addition of mere FA or SF

Figure 3.15 illustrates the impact of Fly Ash (FA) and Silica Fume (SF) on the tensile stress–strain relationship in 7 day UHDMC. Due to abnormal damage to specific specimens during the test, fewer than four specimens were utilized in some instances. Figure 3.15a discloses that strain hardening characteristics are barely discernible and the tensile strain capacity is remarkably inferior in the control specimen. Figures3.15b–f, however, reveal an enhancement in the strain hardening behavior as FA increments from 0 to 50%. Specifically, for FA30 and FA40, a substantial tensile strain of 3–4% appears at the point of failure. In a similar vein to FA, Fig. 3.15g–j demonstrate an improvement in the strain hardening behavior as SF increases from 0 to 20%. Nonetheless, SF fails to augment the strain hardening behavior to the same notable extent as FA does.

For a more comprehensive quantitative analysis on the influence of Fly Ash (FA) and Silica Fume (SF) on the strain hardening behavior of UHDMC, Fig. 3.16 provides a summary and comparison of the ultimate tensile stress and strain for 7 day UHDMC supplemented with varying FA and SF proportions. From Fig. 3.16, it is evident that as the FA content escalates from 0 to 50%, the ultimate tensile stress initially diminishes, subsequently rises, and eventually takes a downturn once again. The trajectory of

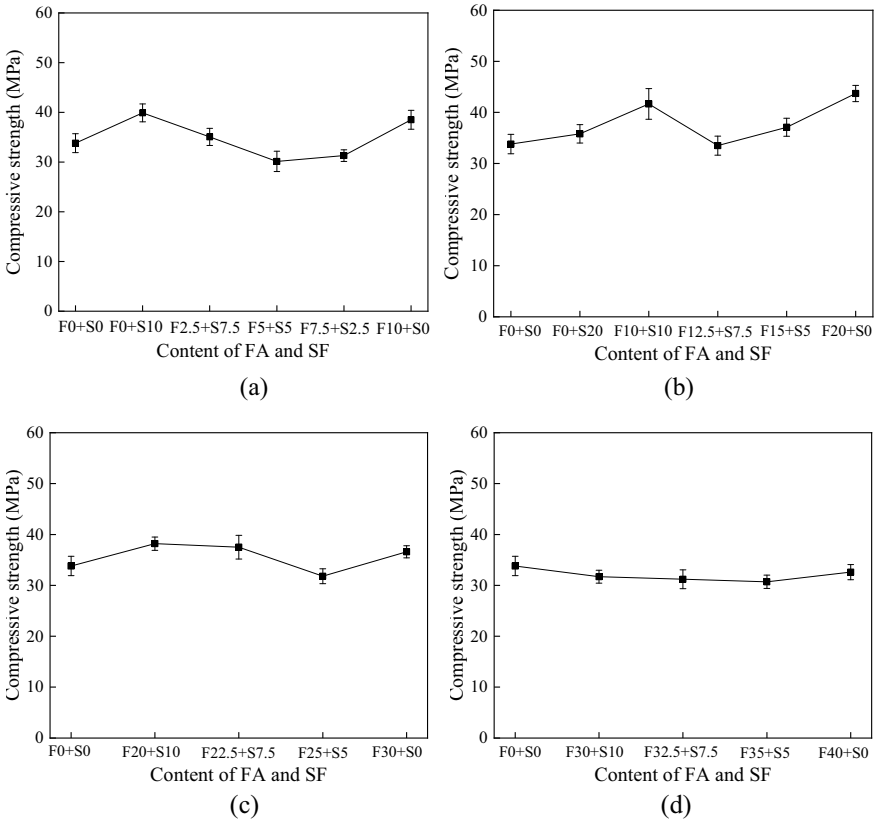

Fig. 3.14 Compressive strength of UHDMC with a total content of FA and SF of **a** 10%, **b** 20%, **c** 30%, and **d** 40%. Reproduced from Evaluation on the performance of magnesium phosphate cement-based engineered cementitious composites (MPC-ECC) with blended fly ash/ silica fume by Hu Feng with permission from Elsevier

the ultimate tensile strain firstly ascends and subsequently descends. When the FA content reaches 30%, both the ultimate tensile stress and strain peak. In comparison to the control, FA30 showcases a superior ultimate tensile stress by 12.46%, possibly due to an enhancement in the interfacial bonding characteristic between the fibers and the matrix. Meanwhile, the ultimate tensile strain of FA30 is 925% higher than the control, which could be attributed to the reduction in matrix cracking strength, lowering the UHDMC's fracture energy, leading to the emergence of additional cracks during the tensile process. Additionally, Fig. 3.16 suggests that as SF content progresses from 0 to 20%, both ultimate tensile stress and strain of UHDMC follow an upward trend. This could be credibly linked to SF's potential in bolstering the fiber/matrix interface, corroborated by the noticeable improvement in fiber bridging capability. Relative to the control, the incorporation of 20% SF amplifies the ultimate tensile stress and strain by 22.5 and 605%, respectively. However, when juxtaposing

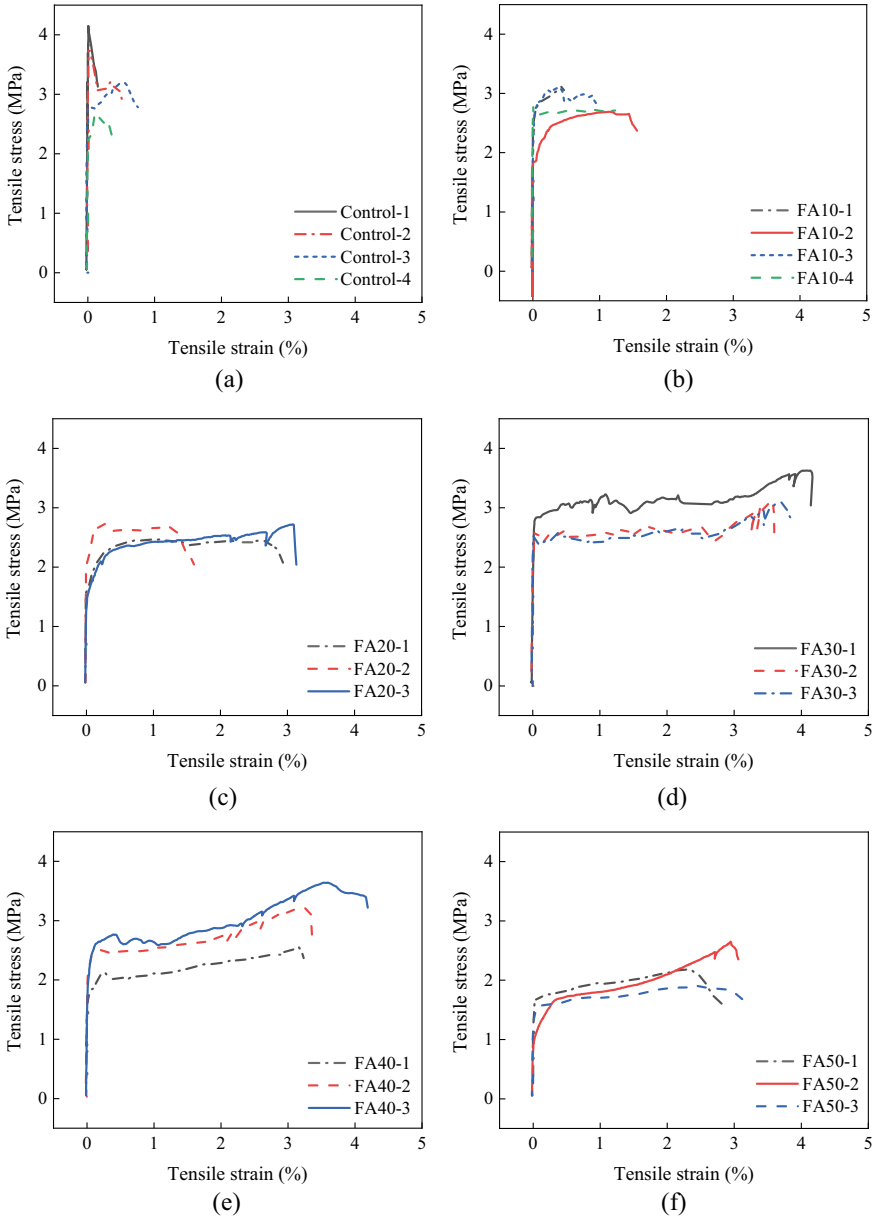

Fig. 3.15 Tensile stress–strain curves of **a** the control, **b** FA10, **c** FA20, **d** FA30, **e** FA40, **f** FA50, **g** SF5, **h** SF10, **i** SF15, and **j** SF20. Reproduced from Development and design of ultra-high ductile magnesium phosphate cement-based composite using fly ash and silica fume by Hu Feng with permission from Elsevier

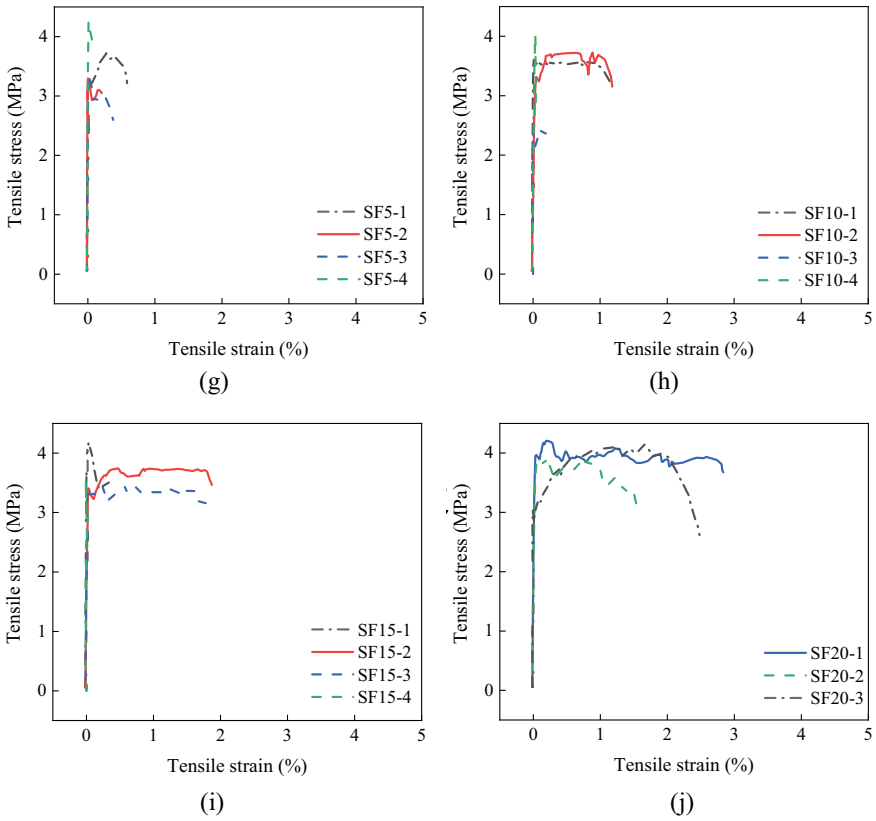

Fig. 3.15 (continued)

20% SF with 30% FA, the former results in increased ultimate tensile stress, yet falls short in terms of ultimate tensile strain.

(b) The addition of blended FA and SF

Figure 3.17a, b, c, d present the tensile stress–strain graphs for UHDMC with blended fly ash and silica fume contents of 10, 20, 30, and 40%, respectively. Conventionally, the strain hardening performance of fiber-reinforced cement-based composites manifests when the ultimate load surpasses the original cracking load, and this characteristic can be further magnified by increasing ductility (Kms et al., 2015). From the data depicted in Fig. 3.17, it becomes apparent that the strain hardening characteristics of UHDMC in the control group, or when total substituted material amounts to 10%, is rather indistinguishable. Nevertheless, as the combined replacement volume ascends from 10 to 40%, the strain hardening performance witnesses a substantial enhancement. This is particularly noticeable in the cases of the F30 + S0 and F30 + S10 groups.

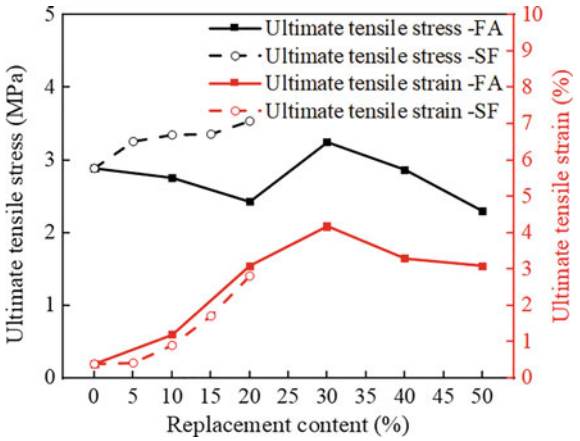

Fig. 3.16 Ultimate tensile stress and strain of UHDMC with varying FA and SF contents replacing MPC. Reproduced from Development and design of ultra-high ductile magnesium phosphate cement-based composite using fly ash and silica fume by Hu Feng with permission from Elsevier

Figure 3.18a, b, c, d depict the ultimate tensile strength and ultimate tensile strain of UHDMC that include a percentage of fly ash and silica fume, ranging incrementally from 10 to 40%. The figures demonstrate that, in comparison to the control group, there is a clear enhancement in ultimate tensile strength and strain as the content of mineral admixtures is incremented. Of particular note is the F30% + S10 group. Here, the ultimate tensile strength peaks at 4.11 MPa, marking an increase of 71% relative to the control group. Moreover, the ultimate tensile strain records an exceptional leap to 4.1%, which translates to 28.3 times the strain observed in the control group.

Holding the total replacement volume constant, reducing the amount of fly ash or escalating the silica fume content generally corresponds to an increase in the ultimate tensile strength. This can potentially be accredited to the silica fume's role in the reaction system of MPC, culminating in the formation of a new gelatinous phase of magnesium silicate (Ahmad & Chen, 2018a; Zheng et al., 2016). This contributes to reinforced bonding between the fibers and the MPC matrix. Despite the participation of SiO_2 in fly ash in the reaction, it has a lower activity level than silica fume. This difference could be due to the smaller particle size of silica fume and its higher SiO_2 content that can partake in the process of reaction. However, there is an anomaly when the total substitution content is at 30%. In this instance, the ultimate tensile strength of the F30 + S0 group exceeds that of the F22.5 + S7.5 and F25 + S5 groups. The explanation for this behavior is still uncertain and warrants further examination. Furthermore, for a consistent total replacement content, the ultimate tensile strain reveals a pattern of initial decrease followed by an increase, co-related with augmenting fly ash content or diminishing silica fume content. For substitution amounts of 20% or 40%, the UHDMC shows superior ultimate tensile strain compared to samples with other replacement contents, with nearly all samples attaining a strain level of 3%. Yet, when the total replacement level is 30%, only the F30 + S0 group exhibits an ultimate tensile strain exceeding 3%, peaking at 4.10%.

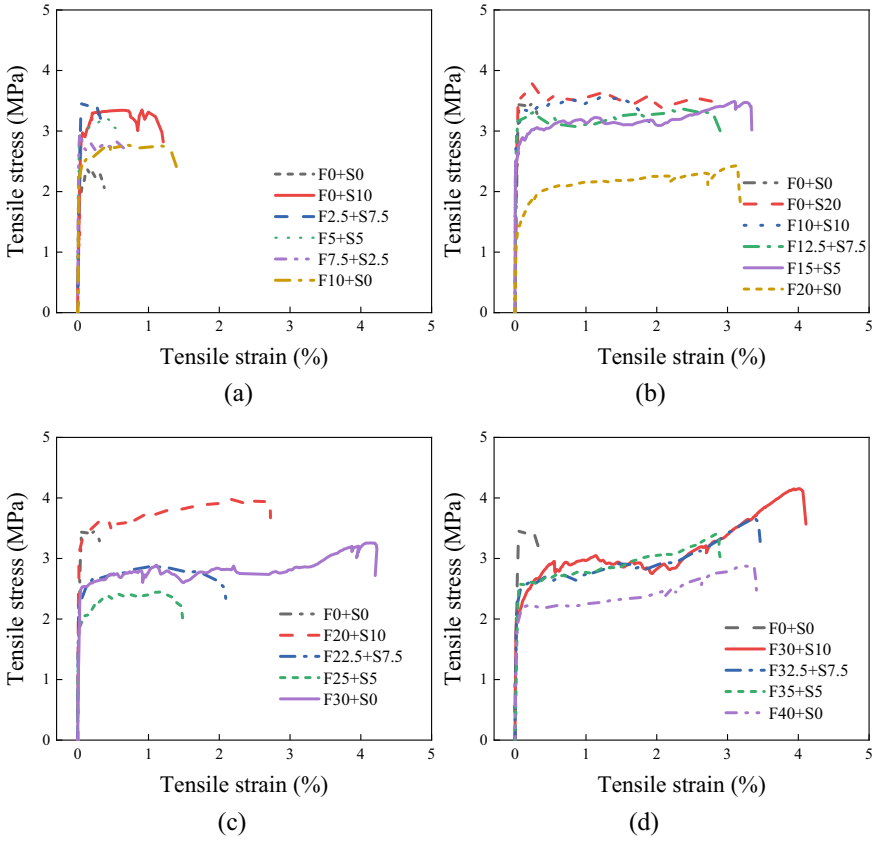

Fig. 3.17 Tensile stress–strain curve of UHDMC with a total content of FA and SF of **a** 10%, **b** 20%, **c** 30%, and **d** 40%. Reproduced from Evaluation on the performance of magnesium phosphate cement-based engineered cementitious composites (MPC-ECC) with blended fly ash/ silica fume by Hu Feng with permission from Elsevier

3.4.3 Micromechanical Indices

3.4.3.1 Fiber Bridging Capacity (σ_0)

(a) The addition of mere FA or SF

The curves portraying the relationship between the fiber bridging stress and the crack opening displacement of UHDMC after 7 days, with different FA and SF levels, are demonstrated in Fig. 3.19. Notably, similar patterns emerge from these curves irrespective of the presence of FA or SF. Prior to the onset of cracking, increase in the fiber bridging stress follows a linear trend, signifying the elastic phase of UHDMC. As cracks begin to form, the rate at which fiber bridging stress increases lessens, yet the association between stress and the displacement of the crack opening remains

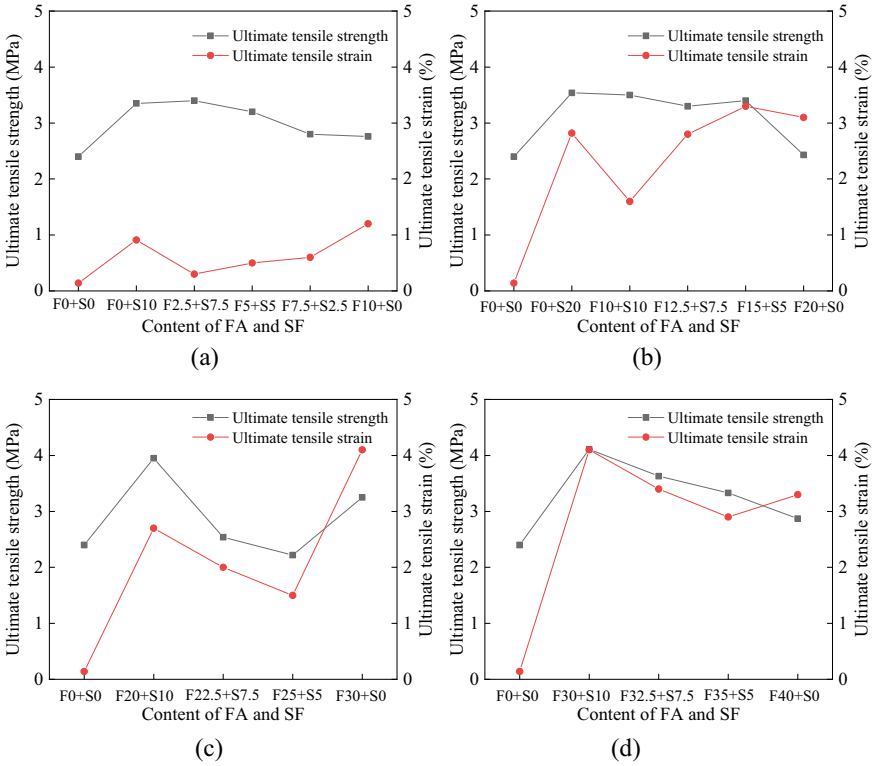

Fig. 3.18 Ultimate tensile strength and ultimate tensile strain of UHDMC with a total content of FA and SF of **a** 10%, **b** 20%, **c** 30%, and **d** 40%. Reproduced from Evaluation on the performance of magnesium phosphate cement-based engineered cementitious composites (MPC-ECC) with blended fly ash/ silica fume by Hu Feng with permission from Elsevier

positive until reaching its peak. Subsequent to this peak, as the evolution of the crack persists, the stress experiences a sharp decline alongside an increase in crack opening displacement. Through analysis of Fig. 3.19, a quantitative examination is carried out concerning the fiber bridging capacity and the apex complementary energy of UHDMC.

Reflecting on Fig. 3.19, the fiber bridging capacity (σ_0) for UHDMC after 7 days can be obtained, as shown in Fig. 3.20. Notably, σ_0 manifests an upward trend with the escalation of FA content from 0 to 20%. It subsequently experiences a decrease as FA content intensifies from 20 to 50%, albeit it remains above the σ_0 of the control group. When juxtaposed with the control, a 38% increase in σ_0 at a 20% FA content and a modest 1.8% increase when FA content hits 50% can be observed. This observation underscores that introducing FA into UHDMC favors an augmentation of the fiber bridging capacity: the optimum substitution percentage is 20%. As mentioned previously, incorporating FA potentially enhances the UHDMC flowability, thereby fostering an improved dispersion of PVA fibers within the matrix.

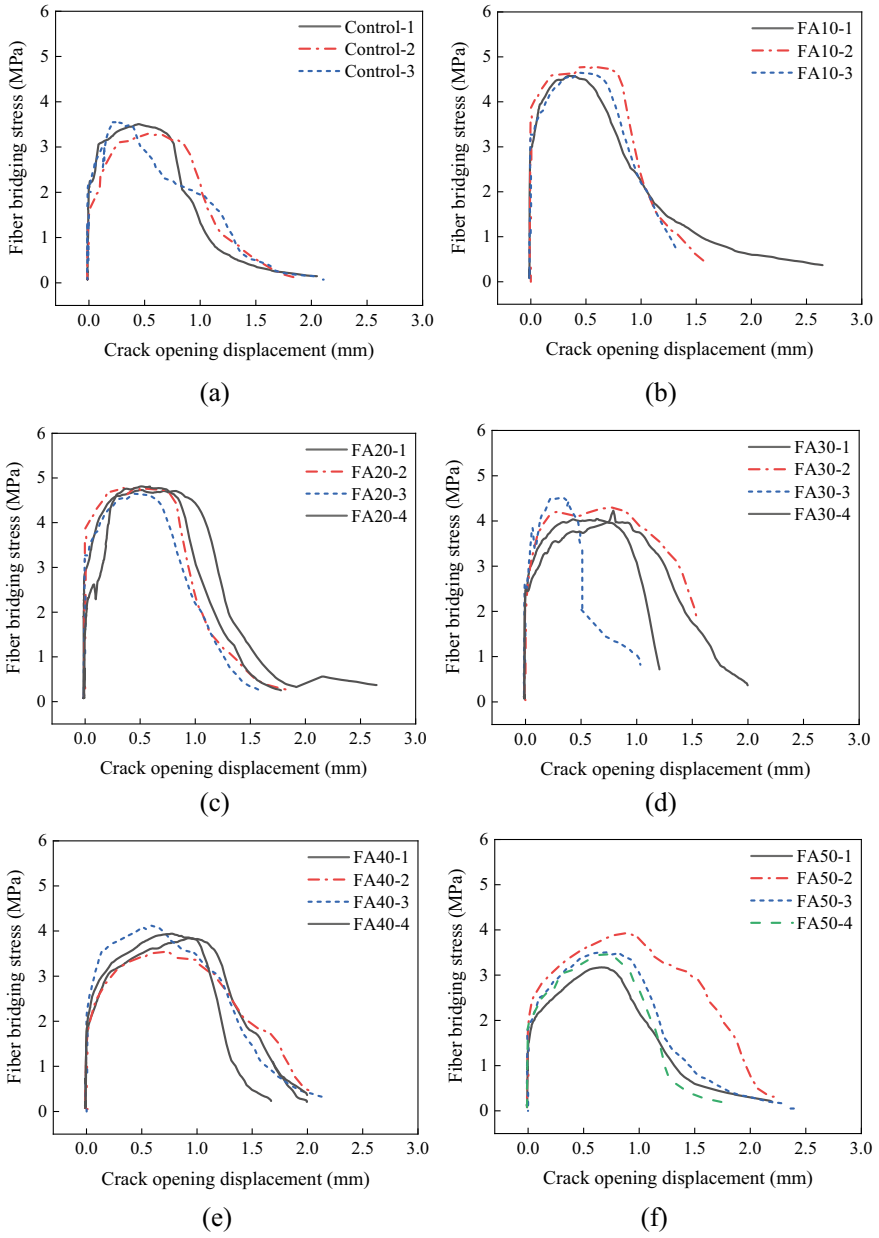

Fig. 3.19 Fiber bridging stress-crack opening displacement curves of **a** Control, **b** FA10, **c** FA20, **d** FA30, **e** FA40, **f** FA50, **g** SF5, **h** SF10, **i** SF15, and **j** SF20. Reproduced from Development and design of ultra-high ductile magnesium phosphate cement-based composite using fly ash and silica fume by Hu Feng with permission from Elsevier

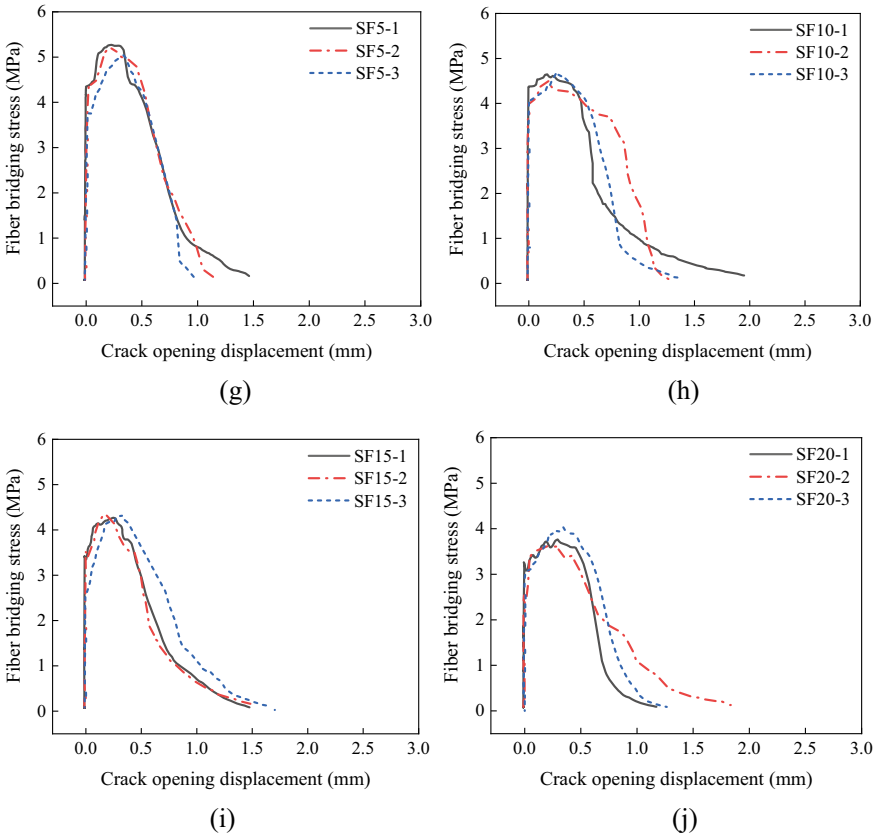

Fig. 3.19 (continued)

Apart from its dominant function as filler, FA may enhance the density of the interface transition zone between the fiber and the matrix, augmenting the interface friction, thereby escalating the σ_0 value (Yang et al., 2007). However, surpassing the 20% FA substitution limit triggers a substantial decline in the quantity of cementitious material, impeding the interphase solid bonding within the transition zone, which in turn leads to σ_0 value reduction.

As indicated in Fig. 3.20, there is a rise in σ_0 value when the content of SF escalates from 0 to 5%, followed by a decline when SF content exceeds 5%. When contrasted with the control, the enhancements in σ_0 value become 50.8, 34.2, 25.4, and 10.5% at SF levels of 5, 10, 15 and 20%, respectively. Thus, the maximum improvement in σ_0 value occurs at 5% SF ccontent, beyond which the enhancement diminishes as the SF level surges from 5 to 20%. This occurs because at 5% SF content, only a minimal proportion of cementitious materials is displaced, causing a slight reduction in the hydration product struvite-K. The reactive silica in SF contributes to the reaction, forming $MgSiO_3$ gel which bolsters the bonding at the fiber/matrix interface, thereby

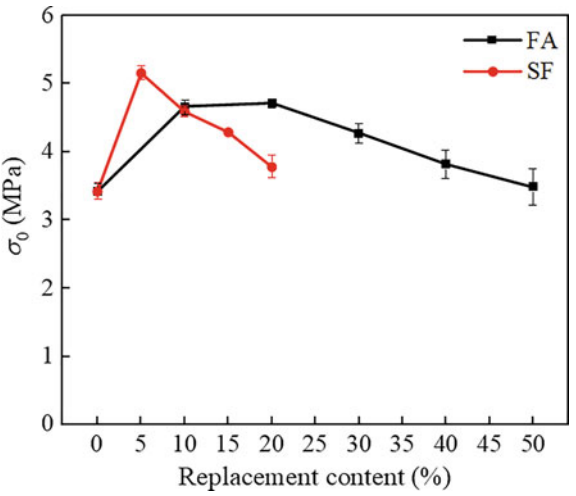

Fig. 3.20 Fiber bridging capacity (σ_0) of UHDMC with varying MPC replacements by FA and SF. Reproduced from Development and design of ultra-high ductile magnesium phosphate cement-based composite using fly ash and silica fume by Hu Feng with permission from Elsevier

elevating the σ_0 value. Nonetheless, as the SF content advances from 5 to 20%, the quantity of struvite-K drastically decreases, lowering the σ_0 value (though it still outperforms the control).

(b) The addition of blended FA and SF

Figure 3.21a, b, c, d illustrate the σ_0—fiber bridging capacity of UHDMC when the combined content of fly ash and silica fume totals 10, 20, 30, and 40% respectively. As compared to the control, we can observe from the graphs that the combination of fly ash and silica fume enhances the σ_0. The F10 + S0, F20 + S0, F30 + S0, and F30 + S10 groups showcase elevated fiber bridging capacity that exceed the control by 36.5, 38.0, 25.1, and 30.4% respectively. The explanation for this might stem from the fact that the SiO_2 present in both fly ash and silica fume contributes to the formation of gel-like substances—for instance, magnesium silicate (Li & Feng, 2011; Lin et al., 2010). This has the net effect of bolstering the bond between the fibers and the matrix.

When compared with the total contents of 10, 30, and 40%, the fiber bridging capacity (σ_0) typically attains a greater value when the combined content is at 20%. Moreover, provided that the total replacement proportion remains constant, an elevated fiber bridging capacity can be achieved when the silica fume makes up 10% of the blend. Nonetheless, as the quantity of fly ash escalates, or the silica fume diminishes, the bridging capacity from fibers tends to trend downward. This phenomenon might be linked to the decrease in silica fume content leading to a reduction in the formation of secondary hydration products like magnesium silicate (Lin et al., 2010). However, when the silica fume content reaches 0%, implying that the mineral admixture consists solely of fly ash, the fiber bridging capacity shows resurgence. This can likely be attributed to the fact that higher content of fly ash significantly amplifies the frictional resistance between the fiber and the matrix (Hu et al., 2021).

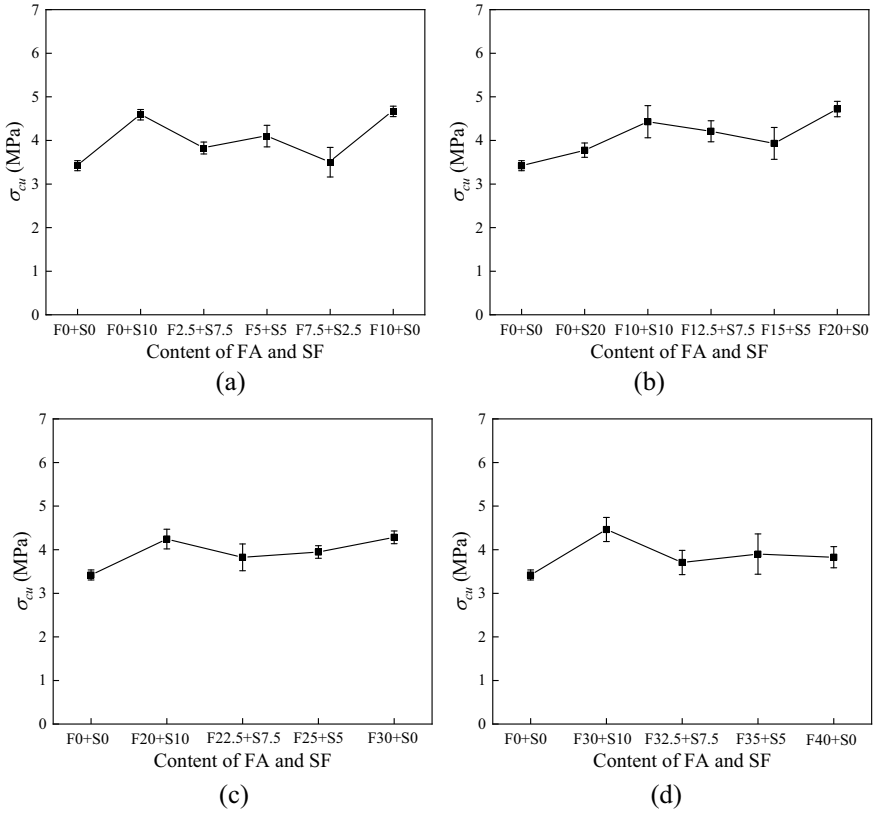

Fig. 3.21 Fiber bridging capacity with a total content of FA and SF of **a** 10%, **b** 20%, **c** 30%, and **d** 40%. Reproduced from Evaluation on the performance of magnesium phosphate cement-based engineered cementitious composites (MPC-ECC) with blended fly ash/ silica fume by Hu Feng with permission from Elsevier

3.4.3.2 Maximum Complementary Energy (J_b') of UHDMC

(a) The addition of mere FA or SF

The variable J_b' significantly influences the pseudo strain hardening index, as a larger J_b' value can prompt the specimen to generate cracks at new locations under a state of tensile stress. Generally, this contributes to the occurrence of the multi-cracking phenomenon in UHDMC. As illustrated by Eq. 3.6, J_b' is not determined solely by the fiber bridging capability (σ_0); instead, it's also correlated with the corresponding crack opening displacement (δ_0). As such, J_b' does not necessarily mirror the alterations in σ_0. Rather, it constitutes the combined outcome of σ_0 and δ_0 actions. The maximum complementary energy (J_b') of 7 day UHDMC, as summarized in Fig. 3.22, shows that J_b' progressively increases as the FA content ascends from 0 to 50%. Relative to the baseline, increases of J_b' at 13.3, 55.5, 83.1, 98.8,

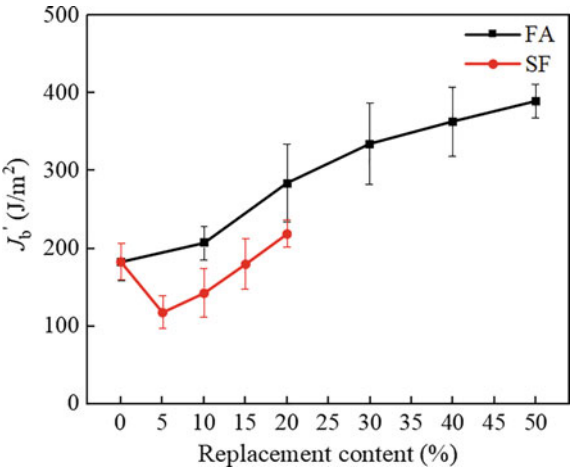

Fig. 3.22 Complementary energy (J_b') of UHDMC with varying FA and SF contents replacing MPC (Reproduced from Development and design of ultra-high ductile magnesium phosphate cement-based composite using fly ash and silica fume by Hu Feng with permission from Elsevier)

and 113.0% occur when the FA contents are 10, 20, 30, 40, and 50% respectively. Therefore, from a J_b'-centric viewpoint, incorporating FA aids the multi-cracking process of UHDMC.

As the SF content supplants MPC ranging from 0 to 20%, the J_b' initially slides down to a SF content of 5%, after which it ascends. The fluctuation in J_b' contradicts that of the σ_0. At 5% SF content, there's a substantial enhancement in the fiber bridging capacity (σ_0), signaling a strengthening of the fiber/matrix interface bonding. Yet, this improved bond is counterproductive to fiber pullout from the matrix during tension, ultimately lowering the ductility and J_b'. As SF content goes beyond the 5%, a decrease in σ_0 triggers an upswing in J_b', promoting multiple-cracking of UHDMC. In contrast to the control, J_b' decreases by 35.5, 21.9, and 1.6% for the SF contents of 5, 10, and 15%, respectively, but escalates by 19.07% for the SF content of 20%. Consequently, an SF content below 20% does not favor the growth of J_b'. However, at 20% SF content, J_b' undergoes a significant elevation.

Furthermore, in a comparison of FA and SF at equivalent replacement contents, FA results in a higher J_b'. This could be attributed to the beneficial dispersion of PVA fibers brought about by the lubricating effect of FA particles.

(b) The addition of blended FA and SF

Figure 3.23a, b, c, d illustrate the fiber bridging complementary energy J_b' of UHDMC when the combined content of fly ash and silica fume is 10, 20, 30, and 40%, respectively. The graphics depict an understated increase in J_b' for the F10 + S0 combination compared to the control group when the total content is 10%. However, the ascent in J_b' becomes pronounced upon reaching the total contents of 20, 30, and 40%; it is particularly remarkable in F20 + S0, F20 + S10, and F30 + S10, where the J_b' surges by 55.2, 145.0, and 350.8%, respectively.

As depicted, the J_b' ascends along with the total substitution content scaling from 10 to 40%. This is because the J_b' is positively related to the ultimate tensile stress

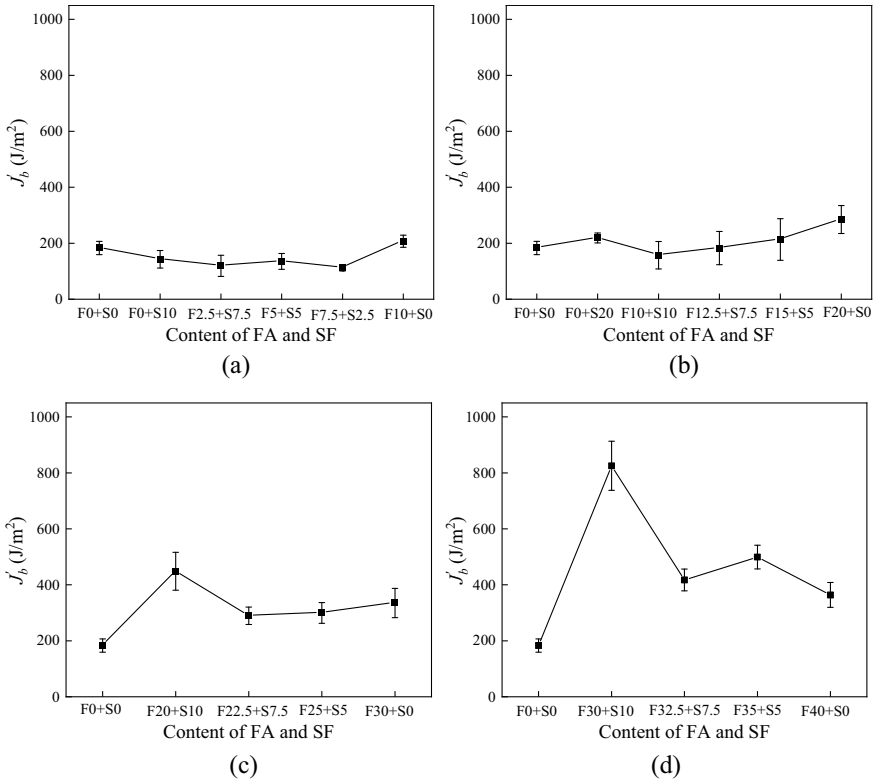

Fig. 3.23 Fiber bridging complementary energy with a total content of FA and SF of **a** 10%, **b** 20%, **c** 30%, and **d** 40%. Reproduced from Evaluation on the performance of magnesium phosphate cement-based engineered cementitious composites (MPC-ECC) with blended fly ash/ silica fume by Hu Feng with permission from Elsevier

and the ductility of the material. With a total content at 20%, raising the fly ash from 10 to 15% or diminishing the silica fume from 10 to 5% causes a steady amplification in J_b'. However, for total contents of 30 and 40%, J_b' significantly contracts as fly ash escalates or silica fume descends. This occurs due to the diminution of the fiber bridging stress capacity σ_{cu} with an increasing proportion of fly ash or a decreasing proportion of silica fume.

3.4.3.3 Cracking Strength (σ_{fc}) of UHDMC Matrix

(a) The addition of mere FA or SF

Figure 3.24 presents the influence of Fly Ash (FA) and Silica Fume (SF) on the cracking strength (σ_{fc}) of the UHDMC matrix after seven days, in the absence of fibers. Observation of the chart reveals that as FA content replaces MPC from 0 to

50%, there is a decrease in σ_{fc} up to 36.6%. Similarly, an increase in SF content replacing MPC from 0 to 20% leads to a reduction in σ_{fc} by as much as 31.9%. This decrease in matrix strength might accelerate the development of cracks when subjected to a tensile load, an attribute which facilitates beneficial multiple-cracking behavior. Previous studies suggest that the strength of the matrix originates from unreacted MgO and the hydration byproduct struvite-K (Xu et al., 2015, 2019). The reduction in cracking strength can primarily be ascribed to two factors: (1) integration of either FA or SF diminishes the level of struvite-K, a hydration byproduct; (2) incorporation of FA or SF escalates the water to MPC ratio, given that the water-cementitious materials ratio maintains a constant value. In addition to these factors, the spherical structure and smooth surface of FA curtail the bond performance among the matrix solid particles, subsequently leading to a reduction in the matrix's cracking strength (σ_{fc}) value. Contrasting with FA, SF serves a dual purpose in the MPC system by not only acting as a filler but also taking an active part in the hydration reaction of MPC to formulate a new cementitious compound, $MgSiO_3$ gel, discernible from the XRD results. Nevertheless, the compensatory capability of recently formed $MgSiO_3$ for the loss in matrix strength is hindered by its inferior cementing performance (Gao et al., 2020). Examining Fig. 3.24 further exhibits that substitutions up to 10% lead FA and SF to result in comparable σ_{fc} values. Conversely, when the replacement surpasses 10%, FA induces a more significant σ_{fc} than SF.

(b) The addition of blended FA and SF

Figure 3.25a, b, c. d depict the tensile cracking strength σ_{fc} of the MPC matrix, encompassing an integrated content of fly ash and silica fume amounting to 10, 20, 30 and 40% respectively. Examination of these figures indicates that introducing fly ash and silica fume into the mix exerts a diminishing effect on the σ_{fc} of the MPC matrix. One potential explanation for this observation could be that the presence of mineral admixtures primarily contributes a micro-aggregate filling function within

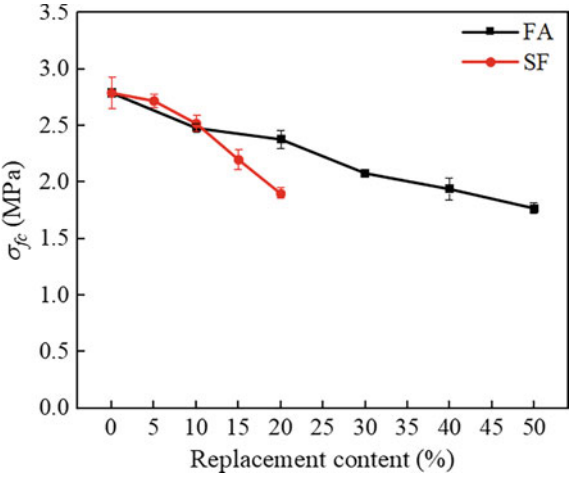

Fig. 3.24 Cracking strength (σ_{fc}) of UHDMC matrix with varying FA and SF contents replacing MPC. Reproduced from Development and design of ultra-high ductile magnesium phosphate cement-based composite using fly ash and silica fume by Hu Feng with permission from Elsevier

the MPC matrix (Xiaoying et al., 2020; Zheng et al., 2016). Also, these mineral admixtures may dilute the reaction system, consequently contributing to a reduced σ_{fc} in the MPC matrix.

Furthermore, while maintaining a constant total content, an elevation in fly ash content or a reduction in silica fume content correspondingly results in a declining σ_{fc}. This is likely attributed to a scenario where, with the decline in silica fume content, smaller voids within the matrix are ineffectively filled and the volume of magnesium silicate gels, produced by the reaction between silica fume and magnesium oxide, is decreased.

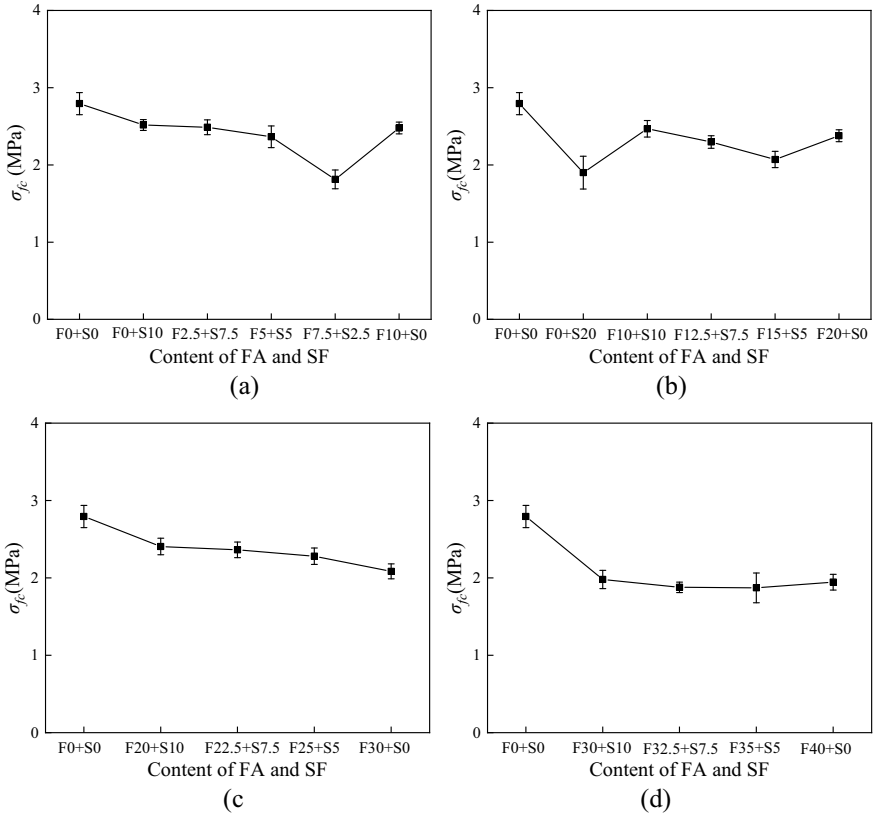

Fig. 3.25 Cracking strength of MPC matrix with a total content of FA and SF of **a** 10%, **b** 20%, **c** 30%, and **d** 40%. Reproduced from Evaluation on the performance of magnesium phosphate cement-based engineered cementitious composites (MPC-ECC) with blended fly ash/silica fume by Hu Feng with permission from Elsevier

3.4.3.4 Fracture Energy (J_{tip}) of UHDMC Matrix

(a) The addition of mere FA or SF

Figure 3.26 presents how Fly Ash (FA) and Silica Fume (SF) affect the 7 day matrix fracture energy (J_{tip}) of UHDMC, devoid of fibers. The evidence from this figure portrays that as opposed to the reference sample, UHDMC matrix incorporated with FA or SF exhibits decreased J_{tip}, suggesting that FA or SF doesn't significantly benefit the J_{tip}. Since a lower J_{tip} value fosters an environment for UHDMC to undergo multiple-cracking, introducing FA or SF assists in realizing strain-hardening behavior. Moreover, the incorporation of FA or SF has a substantial influence on the J_{tip}. As the content of FA rises from 10 to 50%, the J_{tip} first increases, then diminishes, hitting a maximum at a 30% FA addition. On the other hand, with an SF addition climbing from 5 to 20%, the J_{tip} consistently witnesses an uptick. Therefore, it can be inferred that the minimal reduction in the J_{tip} can be achieved with a 30% FA inclusion for FA-laced UHDMC and with a 20% SF involvement for SF-incorporated UHDMC. Further comparison between FA and SF reveals that FA leads to a lesser J_{tip} than SF for identical replacement content. From an energy perspective, this implies that leveraging FA instead of SF likely promotes the development of UHDMC. As delineated by Eq. 3.9, J_{tip} and ${K_m}^2$ hold a direct relationship, and inversely, E_c plays a role in controlling J_{tip}. Therefore, the regulation of J_{tip} can be made possible by adjusting the E_c and K_m properties of the matrix.

Figure 3.27 visually presents how the inclusion of Fly Ash (FA) and Silica Fume (SF) influence the elastic modulus (E_c) of a 7 day UHDMC matrix, lacking fibers. The graph illustrates that moving from 0 to 50% FA content leads to a drop in E_c by up to 39.8%. Similarly, an increase in SF content from 0 to 20% results in up to a 19.5% decrease in E_c. In general, regardless of either FA or SF addition, the E_c value of the matrix falls. As the replacement content heightens, this decrease grows more

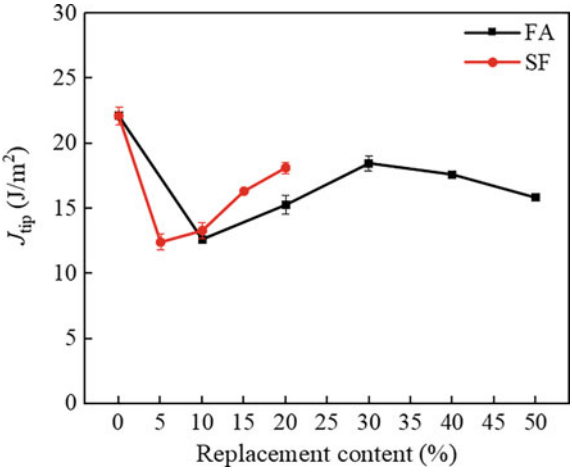

Fig. 3.26 Fracture energy (J_{tip}) of the UHDMC matrix with varying FA and SF contents replacing MPC. Reproduced from Development and design of ultra-high ductile magnesium phosphate cement-based composite using fly ash and silica fume by Hu Feng with permission from Elsevier

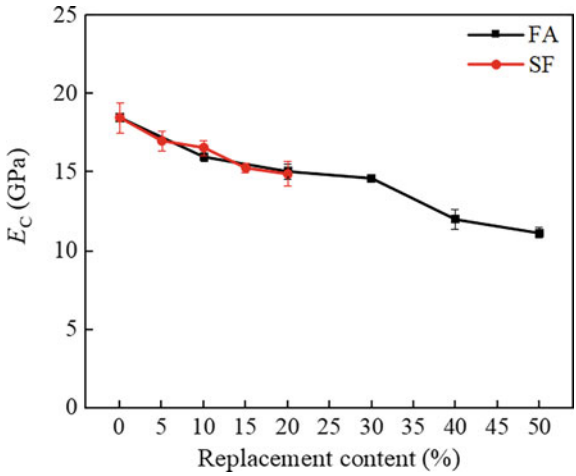

Fig. 3.27 Elastic modulus (E_c) of the UHDMC matrix with varying FA and SF contents replacing MPC. Reproduced from Development and design of ultra-high ductile magnesium phosphate cement-based composite using fly ash and silica fume by Hu Feng with permission from Elsevier

pronounced. Further, at equal replacement levels, FA and SF tend to engender an alike impact on E_c. Therefore, replacement content overshadows the type of mineral admixture as a crucial contributor to the effects on E_c.

Figure 3.28 demonstrates the impact Fly Ash (FA) and Silica Fume (SF) impose on the fracture toughness (K_m) in a 7 day UHDMC matrix (devoid of fibers). Contrasting with the control, the UHDMC matrix featuring either FA or SF yields a diminished K_m. This might be attributable to the FA or SF diluting the reaction system, leading to a reduction in hydration products formation, subsequently impinging on the MPC matrix's fracture toughness. Furthermore, FA or SF markedly factor into the K_m value. When FA incorporation is augmented from 10 to 50%, the K_m initially rises before receding, marking its apex at 30% FA. On the flip side, with an SF incorporation increment from 5 to 20%, the K_m invariably witnesses a hike. Hence, it can be derived that minimal reduction in K_m can be achieved at 30% FA addition for FA-incorporated UHDMC and a 20% SF involvement for SF-incorporated UHDMC. An analysis of Figs. 3.26 and 3.28 reveals that J_{tip} and K_m exhibit a similar trend of change. According to Eq. 3.9, this phenomenon might be due to J_{tip} being more responsive to alterations in K_m than E_c. A comparative assessment suggests FA manifests a lower K_m than an identical replacement content of SF.

(b) The addition of blended FA and SF

The fracture energy J_{tip} of the MPC matrix with varying total contents of fly ash (FA) and silica fume (SF) is displayed across Fig. 3.29a through 3.29d—accounting for accumulated contents of 10, 20, 30, and 40%, respectively. These figures reveal that the inclusion of FA and SF, at total percentages of 10% or 20%, impacts the MPC matrix's fracture energy negatively. Conversely, for total FA and SF contents of 30 and 40% (excluding F30 + S0 and F40 + S0 scenarios), the fracture energy of

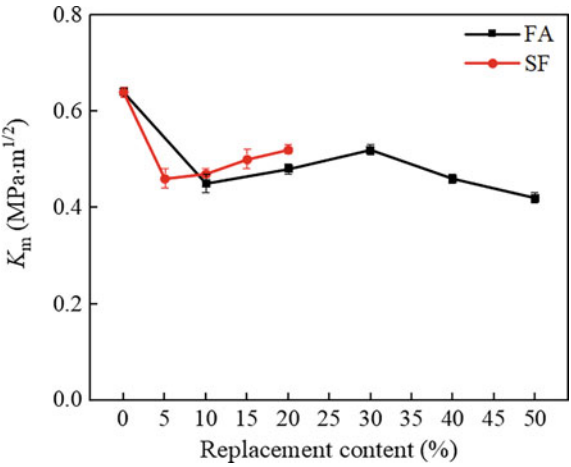

Fig. 3.28 Fracture toughness (K_m) of the UHDMC matrix with varying FA and SF contents replacing MPC. Reproduced from Development and design of ultra-high ductile magnesium phosphate cement-based composite using fly ash and silica fume by Hu Feng with permission from Elsevier

the MPC matrix exhibits an improvement over the control group when infused with these additives. The mixtures of F25 + S5 and F35 + S5 are observed to prompt the most prominent surge in fracture energy, escalating by respective 25.5 and 9.9%. This can be explicated by the fact that fracture energy holds a direct proportionality with K_m and an inverse relation with E_c. When the cumulative replacement is either 10% or 20%, the K_m experiences a more substantial reduction, whereas the decrease in E_c remains relatively moderate. However, at total replacements of 30 and 40%, the drop in K_m is less pronounced, while the E_c exhibits a more severe decrease. Furthermore, an increase in the FA content or a decrement in SF content generally enhances fracture energy. Nevertheless, when SF content diminishes to zero, a drastic tumble in fracture energy is detected, predominantly due to an abrupt plunge in K_m.

Figure 3.30a through 3.30d present the tensile elastic modulus E_c of the MPC matrix inclusive of total fly ash (FA) and silica fume (SF) contents equating to 10, 20, 30, and 40%, respectively. An interpretation of the figures indicates that the integration of FA and SF leads to a decrement in the E_c of the MPC matrix. Furthermore, with a steady total content, an increase in the FA content or a reduction in the SF content leads to a downward trajectory in the elastic modulus E_c.

Figure 3.31a through 3.31d depict the fracture toughness of the MPC matrix, accommodating total concentrations of fly ash (FA) and silica fume (SF) equaling 10, 20, 30, and 40%, correspondingly. Examination of these figures suggests that the introduction of FA and SF diminishes the fracture toughness of the matrix. However, with a constant total content, alterations in the proportions of FA or SF appear to minimally impact the matrix's fracture toughness. While the inclusion of FA and SF tends to densify the MPC matrix, it conversely dilutes the reaction system, thereby reducing its fracture toughness.

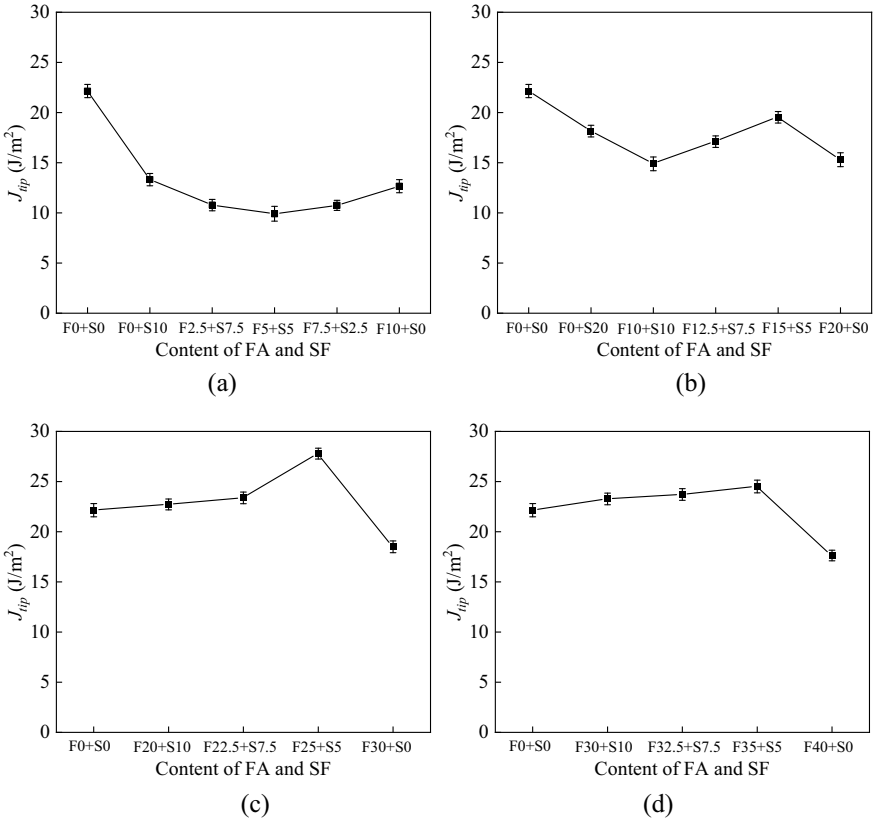

Fig. 3.29 Fracture energy of MPC matrix with a total content of FA and SF of **a** 10%, **b** 20%, **c** 30%, and **d** 40%. Reproduced from Evaluation on the performance of magnesium phosphate cement-based engineered cementitious composites (MPC-ECC) with blended fly ash/ silica fume by Hu Feng with permission from Elsevier

3.4.3.5 Pseudo Strain Hardening Indices

(a) The addition of mere FA or SF

Figure 3.32 demonstrates the influence of FA and SF on the pseudo strain hardening indices (PSH_σ and PSH_J) of UHDMC tested at 7 days. Accepted measures for evaluating the ultimate tensile strain capacity of materials include PSH_σ and PSH_J in terms of strength and energy, respectively (Kanda and Li, 1998). Relative to the control, the inclusion of FA amounts to 10, 20, 30, 40, and 50% has resulted in an increase in PSH_σ by 52.8, 61, 62.6, 60.2, and 53.7%, correspondingly. Concurrently, PSH_J sees increments of 98.1, 125.0, 119.1, 149.6, and 197.6%, respectively. Consequently, the inclusion of FA significantly bolsters PSH_σ and PSH_J. Notably, as FA increments range from 0 to 50%, PSH_σ initially escalates before decreasing, peaking when FA content reaches 30%. In general, PSH_J exhibits a growth pattern

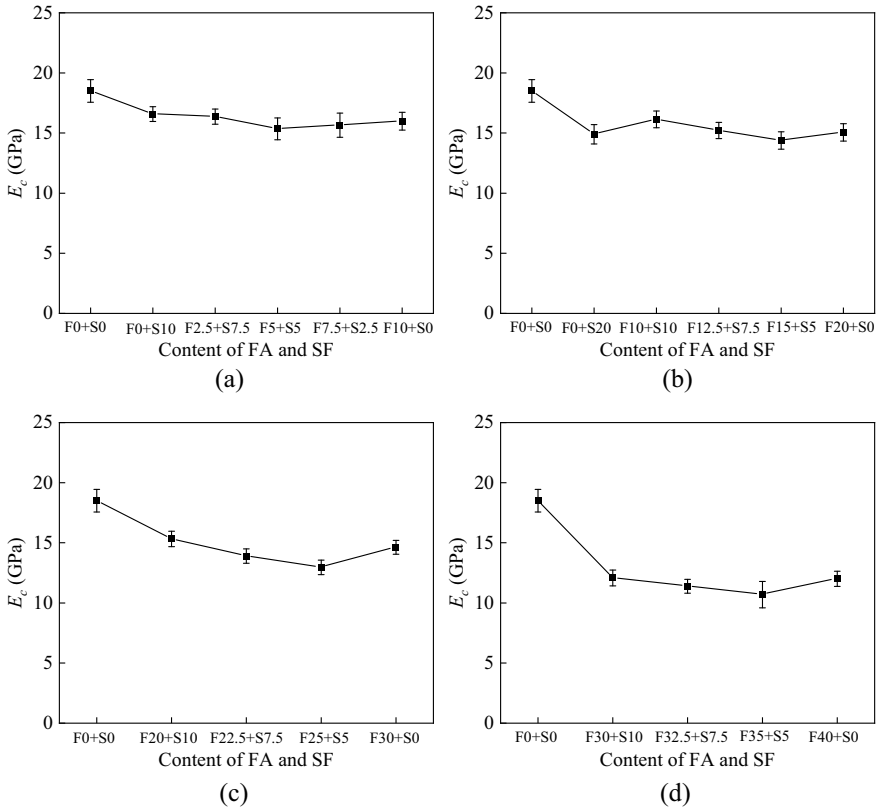

Fig. 3.30 Elastic modulus of MPC matrix with a total content of FA and SF of **a** 10%, **b** 20%, **c** 30%, and **d** 40%. Reproduced from Evaluation on the performance of magnesium phosphate cement-based engineered cementitious composites (MPC-ECC) with blended fly ash/ silica fume by Hu Feng with permission from Elsevier

with FA integration. According to Eq. 3.4, PSH_σ and σ_0 display a positive correlation, hence they show a similar trend. But, as σ_{fc} progressively diminishes with the augmentation of FA, the PSH_σ curve 's decline is more languid than that of the σ_0 curve post-peak.

Figure 3.32 further reveals that as the inclusion of SF advances from 0 to 20%, both PSH_σ and PSH_J demonstrate an upward trajectory. To be precise, when contrasted with the control, SF additions of 5, 10, 15, and 20% result in PSH_σ surges of 52.8, 48.0, 58.5, and 61.8%, correspondingly. Concurrently, PSH_J sees increments of 14.8, 29.7, 33.1, and 45.9%, respectively. These observations signal that the integration of SF can substantially enhance both PSH_σ and PSH_J.

When comparing FA and SF, while there's no substantial differentiation in terms of PSH_σ, FA demonstrates a greater capacity to boost PSH_J compared to SF. For additions of FA ranging from 10 to 50%, PSH_J predominantly surpasses 16, whereas

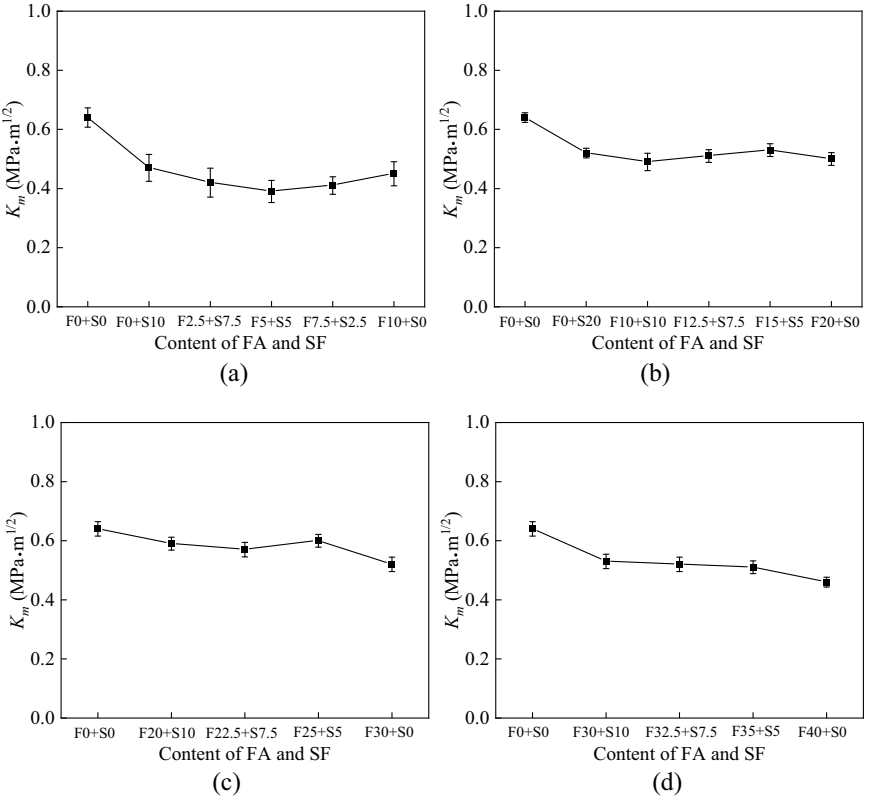

Fig. 3.31 Fracture toughness of MPC matrix with a total content of FA and SF: **a** 10%, **b** 20%, **c** 30%, and **d** 40%. Reproduced from Evaluation on the performance of magnesium phosphate cement-based engineered cementitious composites (MPC-ECC) with blended fly ash/silica fume by Hu Feng with permission from Elsevier

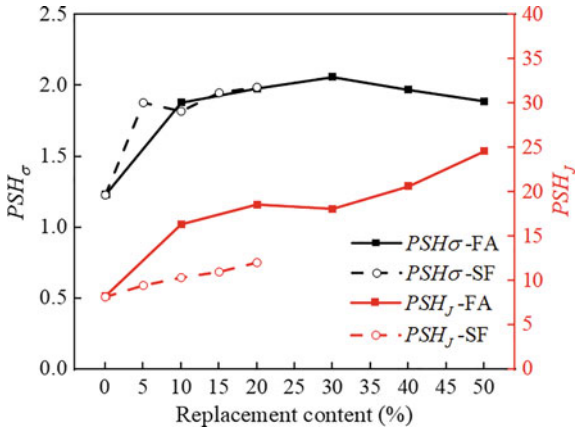

Fig. 3.32 Pseudo strain hardening indices (PSH_σ and PSH_J) of UHDMC with varying FA and SF contents replacing MPC. Reproduced from Development and design of ultra-high ductile magnesium phosphate cement-based composite using fly ash and silica fume by Hu Feng with permission from Elsevier

for SF additions from 5 to 20%, PSH_J hovers just between 9 and 12. This reveals that the integration of FA can provoke more pronounced strain hardening behavior in UHDMC than the SF, aligning with the results from the macromechanical tensile test. As detailed by Kanda and Li (1999), Kanda and Li (1998), achieving strain-hardening behavior necessitates a PSH_σ value in excess of 1.2 and a PSH_J value over 3. Figure 3.32 shows that the pseudo strain hardening indices of UHDMC, whether with FA or SF, conform to this fundamental criterion. Yet, the macromechanical tensile test reveals that certain UHDMC specimens lack apparent strain-hardening behavior. As such, the establishment of new reference values for PSH_σ and PSH_J becomes essential for the design of UHDMC.

(b) The addition of blended FA and SF

Figure 3.33a through 3.33d demonstrate the pseudo strain hardening indices (PSH_σ and PSH_J) of UHDMC when the total content of fly ash and silica fume range from 10 to 40%. Observation of these figures shows that the PSH_σ and PSH_J values for all samples surpass 1. Earlier studies (Jing et al., 2018; Kanda & Li, 2006; Li, 1998; Li et al., 2002a, 2002b; Li, 1998) suggest that if PSH_σ and PSH_J for a material exceed 1.2 and 3 respectively, the material has considerable strain hardening property (ultimate tensile strain over 3%). Nevertheless, our findings do not reflect this. The discrepancies might be due to the fiber bridging stress outpacing the matrix cracking strength, which aligns better with the strength index (PSH_σ). The energy criterion is associated with this phenomenon. The energy criterion is related to the fiber bridging stress and material ductility. The fullfillment of the energy index (PSH_J) is due to the large fiber bridging stress rather than the good ductility of materials.

In observing Fig. 3.33, it is evident that the combination of fly ash and silica fume significantly enhances the pseudo strain hardening indices. While the total content remains constant, an increase in the fly ash proportion or a decrease in the silica fume proportion results in a pattern for PSH_σ and PSH_J, which initially decrease before climbing again. Both the F30 + S0 and those groups with an overall content of 40% show superior strain hardening indices compared to other groups. Remarkably, for F30 + S10, the PSH_σ and PSH_J rates hit 2.25 and 35.47, respectively. The data indicate that to achieve high-quality pseudo strain hardening indices, it is crucial to find an optimal ratio of fly ash to silica fume. Otherwise, the resulting factors may not be as proficient as those derived from samples with a single mineral additive.

3.4.4 Relationship Between Pseudo Strain-Hardening Indices and Ultimate Tensile Strain

Figure 3.34a through 3.34b illustrate the relationship between ultimate tensile strain and PSH_σ, alongside the association between ultimate tensile strain and PSH_J. The data is sourced from UHDMC which exclusively incorporated Fly Ash (FA) or Silica Fume (SF), or a combination of both. A tangible positive correlation is visible. Thus,

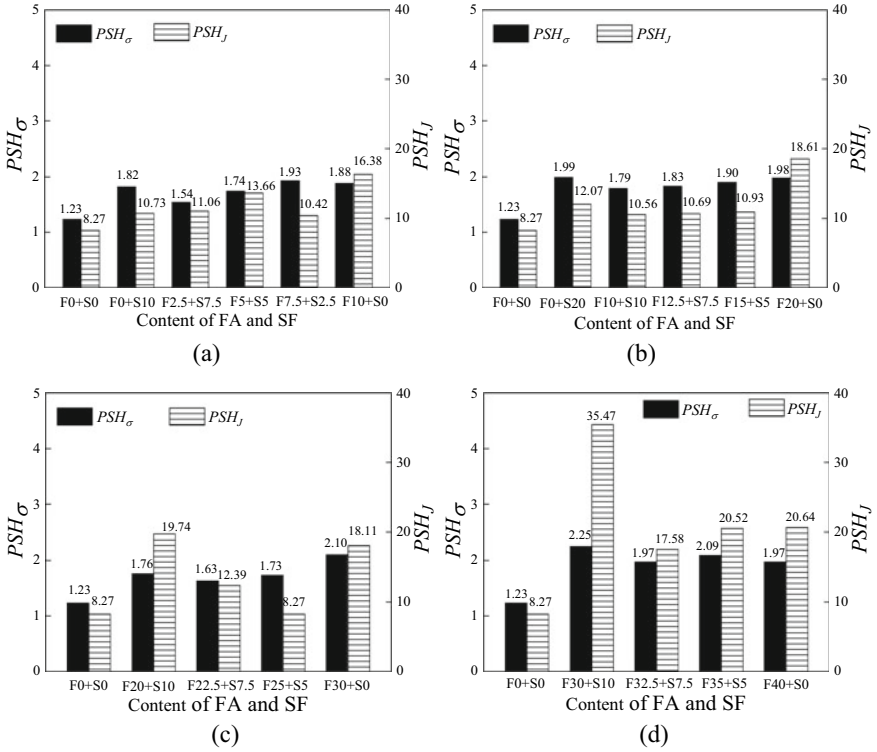

Fig. 3.33 Pseudo strain hardening indices (PSH_σ and PSH_J) of UHDMC with a total content of FA and SF of **a** 10%, **b** 20%, **c** 30%, and **d** 40%. Reproduced from Evaluation on the performance of magnesium phosphate cement-based engineered cementitious composites (MPC-ECC) with blended fly ash/silica fume by Hu Feng with permission from Elsevier

PSH_σ and PSH_J are viable metrics to gauge the ultimate tensile strain capacity and, consequently, the strain-hardening tendencies of UHDMC implementing FA or SF. Figure 3.34 unmistakably displays that when the ultimate tensile strain of UHDMC exceeds 3%, the lowest measured values of PSH_σ and PSH_J are 1.89 and 10.93, respectively. Quantitative design guidelines are formulated via correlation equations (highlighted by the red dotted line in Fig. 3.34), from which the upper and lower boundaries are plotted to encapsulate the complete set of data (indicated by the blue dotted lines in Fig. 3.34). Based on the upper boundary line, it is proposed that to engineer UHDMC with an ultimate tensile strain of 3% or higher, the pseudo-strain hardening indices PSH_σ and PSH_J must concurrently hit minimum values of 2.2 and 26.7.

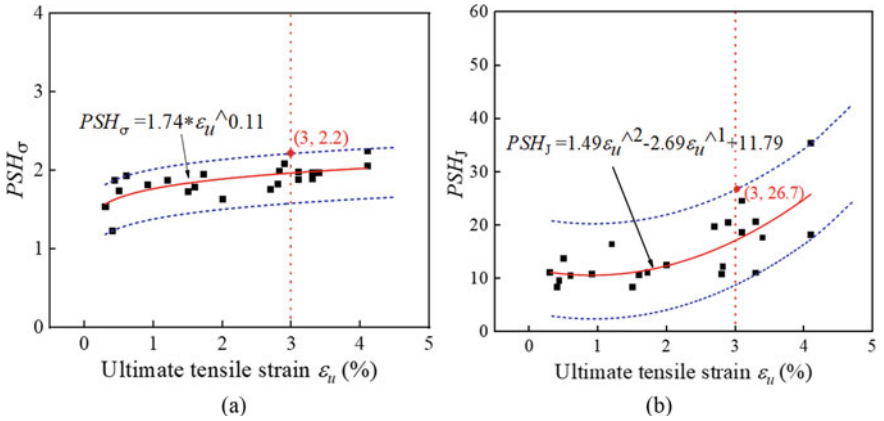

Fig. 3.34 Correlation **a** between ultimate tensile strain and PSH_{σ} and **b** between ultimate tensile strain and PSH_J. Reproduced from Development and design of ultra-high ductile magnesium phosphate cement-based composite using fly ash and silica fume by Hu Feng with permission from Elsevier

3.4.5 Microstructure of UHDMC

(a) The addition of mere FA or SF

To reveal the ductility improvement mechanism of UHDMC by FA and SF, the microstructure of UHDMC specimens with good strain hardening behavior and the control specimen can be examined by scanning electron microscope (SEM). FA30, SF20, and the control samples are selected for the analysis.

Scanning Electron Microscopy (SEM) images of the reference sample, FA30, and SF20 matrices can be observed in Fig. 3.35. For the reference sample (refer to Fig. 3.35a), while microfractures are perceptible on its surface, their dimensions are remarkably small. The FA30 (observed in Fig. 3.35b) boasts embedded spherical FA particles with varying diameters within its matrix, a testament to the excellent adaptability between FA and the UHDMC matrix. However, certain air voids are visible within the matrix. Relative to the reference sample, the addition of FA increases the frequency of air voids. Primary reasons for this increased void prevalence include the spherical FA particle aggregation and the diminished hydration product volume resulting from an FA-substituted portion of MPC (Zhou et al., 2019). This increase in air voids corresponds to the decrease in the FA30's matrix cracking strength (σ_{fc}). For SF20 (see Fig. 3.35c), some SF particles are embedded within the matrix which appears significantly less compact than the reference, with a higher number of microfractures and elevated porosity. Gao et al. (2020) shared a similar finding by demonstrating that when SF content exceeds 5%, the recently-formed magnesium silicate gel in an MPC-based system creates additional pores. SF, with its fine texture and low density, is an exceptionally reactive pozzolanic material (Pedro et al., 2017). The coalescing of SF inhibits the pozzolanic reaction within SF aggregates (Pedro

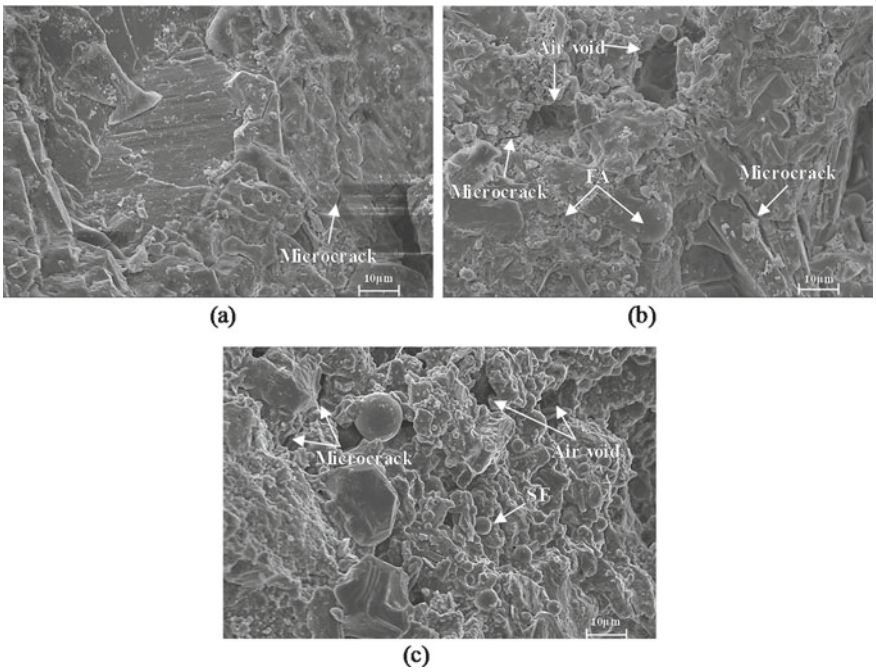

Fig. 3.35 SEM images of the UHDMC matrix: **a** control, **b** FA30, and **c** SF20. Reproduced from Development and design of ultra-high ductile magnesium phosphate cement-based composite using fly ash and silica fume by Hu Feng with permission from Elsevier

et al., 2017) and even cannot lead to uniform hydration reactions within the SF20 matrix. SF20's microstructure corresponds to its reduced matrix cracking strength (σ_{fc}) relative to the control.

Figure 3.36 showcases the SEM imaging of fiber texture within the reference sample, FA30, and SF20. In the case of the reference sample (refer to Fig. 3.36a), the hydration byproducts of MPC are clearly visible on the fiber surface, signaling a strong bond having formed between the fibers and matrix. There's no evident damage on the PVA fiber surface, with the principal mode of fiber failure being direct tensile rupture. This is corroborated by the diminished cross-sectional area at the extremity of the fiber. This mode of direct tensile rupture for PVA fibers isn't conducive to the ductility of UHDMC, lending an explanation for the subpar tensile properties of the reference sample.

Regarding FA30 (as seen in Fig. 3.36b), a noticeable decrease in hydration products on the PVA fiber surface is observed relative to the reference sample. One can see the formation of a planar cutting cross-section at the end of the PVA fibers, which is inherent in fiber production. This finding implies the FA30's fibers have been pulled out without direct breakage. Additionally, evident scuff marks noticeable on the fiber's exterior validate the substantial friction the fibers encounter with

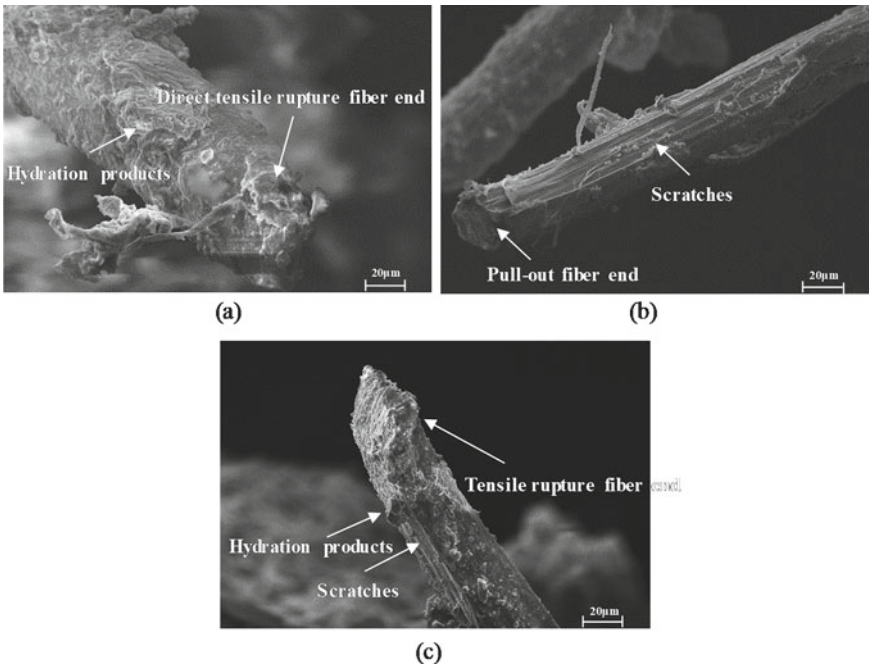

Fig. 3.36 SEM images of PVA fibers at the fracture section of **a** control, **b** FA30, and **c** SF20. Reproduced from Development and design of ultra-high ductile magnesium phosphate cement-based composite using fly ash and silica fume by Hu Feng with permission from Elsevier

the matrix during the pull-out process. Current research highlights that the FA addition promotes fiber failure mode transition from breakage to pull-out in the case of strain-hardening cementitious composites (Lin et al., 2017; Zhang et al., 2021). The PVA fibers are resilient enough to withstand the tensile stress resulting from the pull-out process. As cracks develop and multiply, additional fibers will resist the tensile stress. Consequently, FA30 presents an increased capacity for tensile strain than the reference sample.

In the case of SF20 (refer to Fig. 3.36c), hydration byproducts of MPC are noticeable on the fiber surface, akin to occurrences in the control sample. The main fiber failure mode is direct tensile breakage, evident from significant cross-section contraction at the fiber termination. However, discernible scuff marks are also found on the surface of PVA fibers, indicating that before bearing a tensile rupture, the PVA fibers in SF20 undergo a pull-out process. This pull-out process bolsters the ductility of UHDMC, resulting in SF20 demonstrating a superior strain capacity to the control specimen, albeit inferior to FA30.

(b) The addition of blended FA and SF

The micro-morphology of the MPC matrix, presented in Figs. 3.37, 3.38, and 3.39, varies in the absence of mineral admixtures or presence of F20 + S10 and F30 +

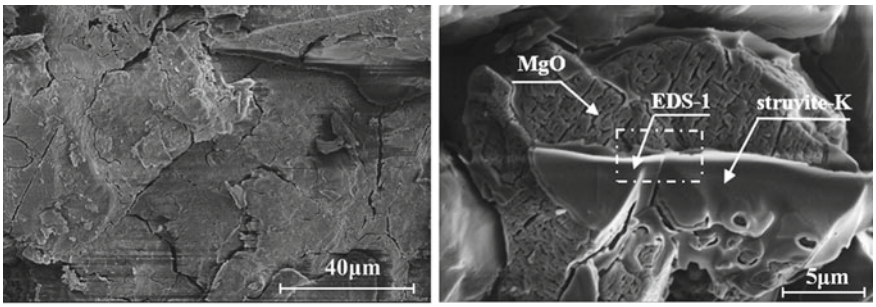

Fig. 3.37 SEM images of MPC matrix without mineral admixtures at the magnification of **a** 1 k and **b** 5 k. Reproduced from Evaluation on the performance of magnesium phosphate cement-based engineered cementitious composites (MPC-ECC) with blended fly ash/ silica fume by Hu Feng with permission from Elsevier

S0 respectively. A plethora of cracks within the matrix are discernible in Fig. 3.37a. Figure 3.37b depicts the characteristic internal MPC structure, where the hydration byproduct MKP encapsulates residual MgO, thus forming an overlapping network structure, albeit not densely packed. Observations from Figs. 3.38 and 3.39 reveal denser microstructures in the samples containing F20 + S10 and F30 + S0 compared to those lacking mineral additives, with F20 + S10 appearing the most densely packed. This appears attributable to two potential factors. Firstly, the varying fineness of FA and SF may yield a superior particle gradation upon their combination, thereby optimally filling the MPC matrix's voids and cracks to ameliorate its pore structure and compactness. Secondly, some silicon oxide in SF may react with MgO to generate $MgSiO_3$ gels, which can effectively bind with MKP, unreacted magnesium oxide, and particles of FA and SF, culminating in a structure that exhibits fewer cracks and pores. This contributes positively to enhancing the fiber bridging stress capacity.

3.4.6 XRD Spectra of MPC Pastes

(a) The addition of mere FA or SF

The XRD spectra for a range of seven-day old MPC pastes—including the control, FA30, FA50, SF5, and SF20—are depicted in Fig. 3.40. The predominant crystalline phase in all samples is $MgKPO_4 \cdot 6H_2O$ (struvite-K), with visible signs of MgO and KH_2PO_4. This evidences that the initial substances have not reacted completely after seven days. Notably, borax's characteristic peaks are absent in the crystal spectra across all specimens, mainly due to its relatively nominal content, just 6% of the MgO mass. The inhibiting mechanism of borax reveals its consumption in the initial phase as it combines with magnesium ions to form magnesium borate. The leftover MgO subsequently serves as minute aggregates within the matrix. Upon comparing

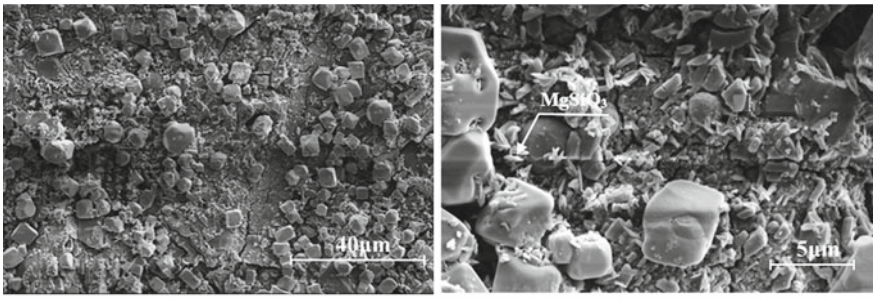

Fig. 3.38 SEM images of MPC matrix with F20 + S10 at the magnification of **a** 1 k and **b** 5 k. Reproduced from Evaluation on the performance of magnesium phosphate cement-based engineered cementitious composites (MPC-ECC) with blended fly ash/silica fume by Hu Feng with permission from Elsevier

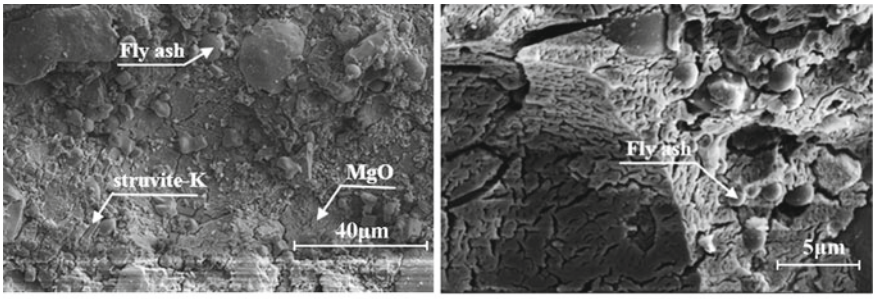

Fig. 3.39 SEM images of MPC matrix with F30 + G0 at the magnification of **a** 1 k and **b** 5 k. Reproduced from Evaluation on the performance of magnesium phosphate cement-based engineered cementitious composites (MPC-ECC) with blended fly ash/silica fume by Hu Feng with permission from Elsevier

Fig. 3.40b, c to 3.40a, it's noticeable that the inclusion of FA does not introduce extra characteristic peaks. The presence of $MgSiO_3$ can't be definitively verified in this study as its peak somewhat coincides with struvite-K. Past studies note that despite active silica in FA contributing to the formation of $MgSiO_3$ gels—increasing cementation of the solid phases—the resultant volume of $MgSiO_3$ is minimal. In essence, FA principally functions as inert fillers (Ahmad et al., 2019). Consequently, the absence of any distinctive $MgSiO_3$ peak in the XRD spectra for FA30 and FA50 seems plausible. Simultaneously, struvite-K peaks diminish corresponding to increased FA addition. This reduction is unsurprising as FA is partially substituting MPC, thereby lowering struvite-K production. However, this decline in struvite-K may hinder the cementing properties of the MPC paste, matching the observed decrease in matrix cracking strength due to FA inclusion.

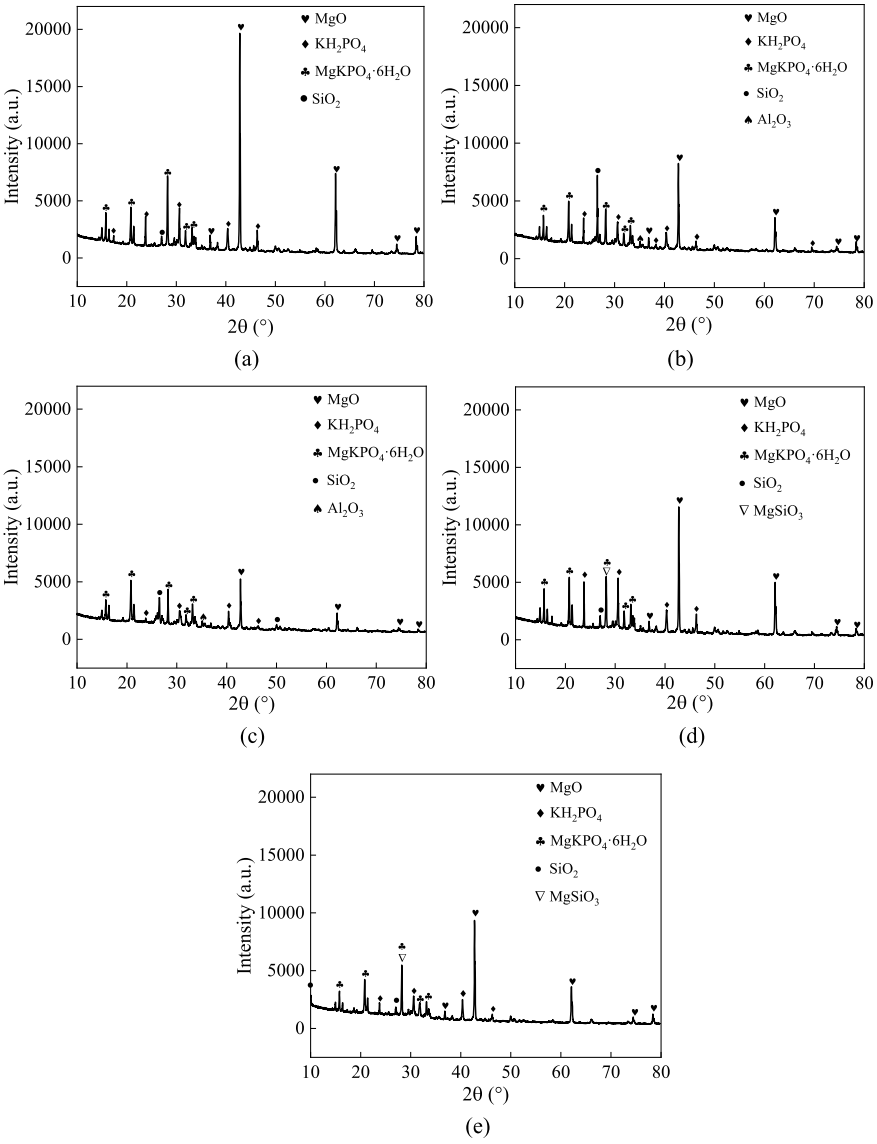

Fig. 3.40 XRD spectra of MPC pastes from **a** control, **b** FA30, **c** FA50, **d** SF5, and **e** SF20. Reproduced from Development and design of ultra-high ductile magnesium phosphate cement-based composite using fly ash and silica fume by Hu Feng with permission from Elsevier

Inspecting Fig. 3.40d, e, we observe that the principal characteristic peak positions of SF5 and SF20 align with those of the control sample. However, the inclusion of SF weakens the diffraction peak intensities of struvite-K and MgO compared to those in the control sample. Interestingly, the characteristic peak of $MgSiO_3$—which results from the reaction between MgO and active silica, a key component of SF—can be detected in both SF5 and SF20. The reduction in struvite-K quantity subsequently diminishes the bond strength between the solid phases of the matrix. While $MgSiO_3$ gel does perform a cementing role within these phases, its bond strength is inferior to that of struvite-K (Gao et al., 2020). In consequence, this results in an overall decrease of the matrix's cracking strength compared to the control.

(b) The addition of blended FA and SF

Figure 3.41a, b, c present the XRD spectra for the MPC matrix, first without any mineral admixtures (F0 + S0), then with F20 + S10, and finally F30 + S0. As Fig. 3.41a illustrates, the F0 + S0 group contains a substantial quantity of unreacted magnesium oxide and potassium dihydrogen phosphate, alongside the hydration product $MgKPO_4 \cdot 6H_2O$ (MKP). Certain impurities also partake in the process, yielding calcium silicate hydrate and mullite. These substances, although not the core hydration products nor present in significant amounts, are still present but unlabelled. Upon examining Fig. 3.41b, it becomes evident that the MKP volume in the F20 + S10 group exceeds that in the F0 + S0 group. Additionally, there is substantial creation of magnesium silicate gels ($MgSiO_3$) within the reaction system. The intertwined hydration products MKP and $MgSiO_3$ lead to a more compact internal structure within the solidified body, thereby enhancing the bond between the fiber and the MPC matrix (Hu et al., 2021). Figure 3.41c shows that for the F30 + S0 group, the quantity of hydration product MKP experiences a notable increase compared to the F0 + S0 group. This implies that the inclusion of fly ash promotes the hydration reaction of MPC, thus fostering an improved bond between the fiber and the matrix. However, the total content of gel (MKP) in the F30 + S0 group falls short compared to the quantity of the gels (MKP + $MgSiO_3$) in the F20 + S10 group. Consequently, the F20 + S10 group exhibits a superior fiber bridging ability and ultimate tensile stress compared to the F30 + S0 group.

3.5 Conclusions

In this chapter, an in-depth examination of both macro- and micromechanical properties of ultra-high ductile MPC-based composites (UHDMC) was carried out. This included the analysis of specimens with added FA or SF, as well as those containing a blend of FA and SF. The evaluation was done in accordance with the design tenets of ECC. A relationship was identified between the pseudo strain hardening indices (derived from micromechanical testing) and the ultimate tensile strain (directly acquired from macromechanical testing). This correlation assists in giving direction for the optimal design of UHDMC. Moreover, to gain a comprehensive understanding

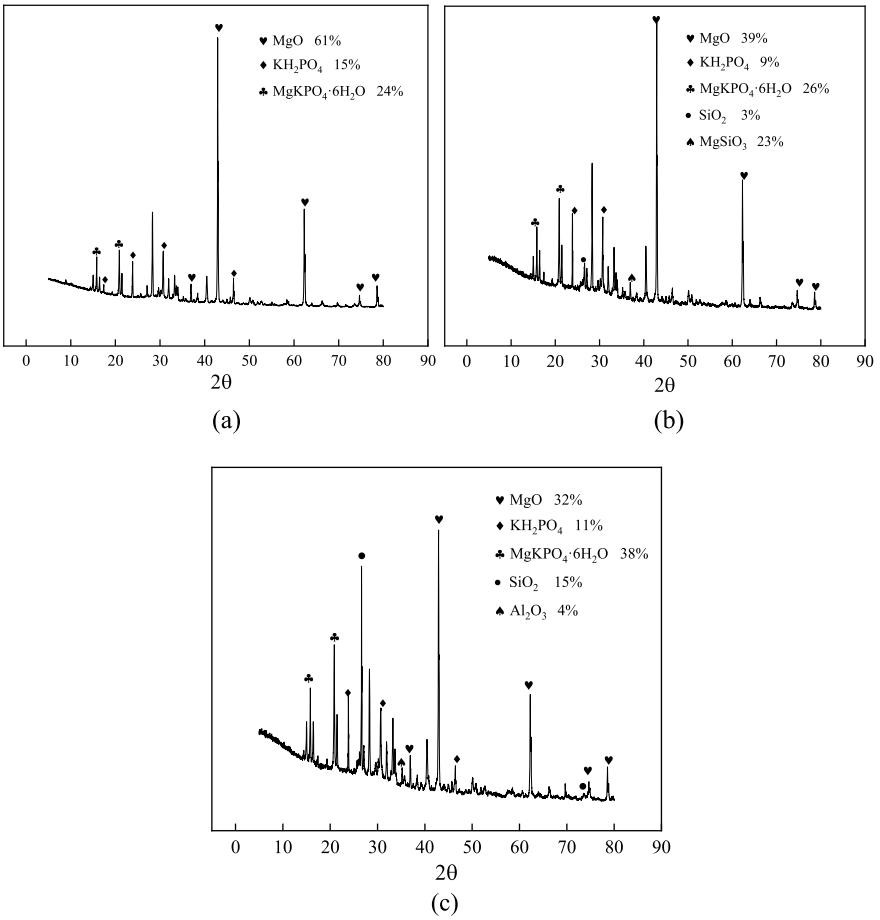

Fig. 3.41 XRD spectra of MPC matrix with **a** F0 + S0, **b** F20 + S10 and **c** F30 + S0. Reproduced from Evaluation on the performance of magnesium phosphate cement-based engineered cementitious composites (MPC-ECC) with blended fly ash/silica fume by Hu Feng with permission from Elsevier

of the micro-level impact of either SF or FA and the combined implementation of FA and SF on UHDMC, X-ray diffraction and scanning electron microscope tests were employed. Some important conclusions are summarized below.

(1) When enhancing the proportion of FA in replacement of MPC from 0 to 50%, or increasing the proportion of SF in place of MPC from 0 to 20%, the UHDMC's flowability initially rises then subsequently falls off. The ideal quantities for FA and SF have been determined to be 30 and 15% respectively. Furthermore, equal replacement of MPC with FA leads to superior flowability compared to SF. In the case of UHDMC amended with a blend of FA and SF, given a fixed

total level of FA and SF, improvements to flowability are greater with a higher FA proportion or lower SF proportion.

(2) Infusing FA or SF remarkably enhances the compressive strength of UHDMC, with their best proportions being 20 and 10% respectively. When it comes to tensile properties, the most optimum ultimate tensile stress and ultimate tensile strain are derived from the integration of 30% FA and 20% SF. In addition, while FA results in less ultimate tensile stress, it contributes to greater ultimate tensile strain compared to SF. The amalgamation of FA and SF into UHDMC serves to boost both its compressive strength and tensile characteristics (ultimate tensile stress and ultimate tensile strain). By combining 30% FA with 10% SF, it is possible for the ultimate tensile stress and the ultimate tensile strain to reach peak values of 3.11 MPa and 4.1% respectively, indicating a significant strain hardening effect.

(3) As the quantity of FA or SF incorporated into UHDMC escalates, the capacity for fiber bridging initially rises before declining, reaching its pinnacle when FA and SF each contribute 20 and 5% respectively. The tendency for UHDMC to crack diminishes incrementally as the dosage of FA or SF increases. The addition of FA up to 30% and SF up to 20% gradually raises the PSH_{σ} in UHDMC respectively. Furthermore, both FA and SF have a comparable effect on enhancing PSH_{σ} at equivalent replacement levels. The combination of FA and SF, totaling either 30% or 40%, bolsters fiber bridging capacity, with the greatest improvement seen in the F30 + S10 blend. On the other hand, mixing FA and SF detracts from the matrix's cracking resistance; as a constant total input, cracking strength lowers as we either increase the FA intake or decrease the SF input. Broadly speaking, a blended addition of FA and SF increases the PSH_{σ} in UHDMC, with F30+

(4) In UHDMC formulated with FA, the highest values for the matrix fracture energy and the maximum complementary energy are achieved with FA contents of 30 and 50%, respectively. Similarly, in UHDMC with incorporated SF, both the matrix fracture energy and the maximum complementary energy attain their peak when the SF encompasses 20% of the blend. Despite leading to an elevated maximum complementary energy, FA contributes less to matrix fracture energy compared to SF. This promotes a consistent growth in PSH_{J} as the FA or SF proportion increases. Additionally, at the same substitution rate, FA outperforms SF in enhancing PSH_{J}. The integration of FA and SF in ratios totaling 30% or 40% ameliorates the complementary energy involved in fiber bridging, with an especially pronounced effect seen in the F30 + S10 combination. When the overall quantity of combined FA and SF is either 10% or 20%, it diminishes the matrix fracture energy. However, an increase to 30% or 40% total content augments the matrix fracture energy. Broadly, the infusion of a FA and SF blend notably heightens PSH_{J}, with F30 + S10 emerging as the superior variant.

(5) A definitive quantitative relationship has been identified linking the ultimate tensile strain and pseudo strain hardening indices (PSH_{σ} and PSH_{J}) in a positive manner, offering guidance for creating UHDMC engineered for a specified ultimate tensile strain. Recommendations indicate that in order to engineer

UHDMC with ultimate tensile strains reaching or exceeding 3%, both pseudo-strain hardening indices, PSH_{σ} and PSH_{J}, must simultaneously exceed values of 2.2 and 26.7, respectively.

(6) Scanning Electron Microscopy (SEM) analysis reveals that the inclusion of FA or SF in the blend leads to an upsurge in the number of air voids compared to the control specimen, accounting for the deterioration in matrix cracking strength. Importantly, when FA or SF are added to the mix, there's a beneficial shift in fiber failure mode from breakage to pullout in UHDMC, consequently enhancing its tensile strain capacity. Furthermore, X-Ray Diffractometry (XRD) examination identifies struvite-K as the dominant reaction product in UHDMC, irrespective of FA or SF levels. The integration of FA or SF is correlated with diminished struvite-K and MgO peaks in XRD spectra. While the FA-MPC system unveils no new hydration products, the SF-MPC system sees emergent hydration product, $MgSiO_3$. The joint understanding derived from SEM and XRD results suggests that an FA and SF combination is more effective in filling MPC matrix gaps and fissures than FA alone, and also facilitates the creation of magnesium silicate ($MgSiO_3$). This substance interacts with MKP to elevate the density of MPC matrix, thereby augmenting the fiber bridging stress capacity in UHDMC.

References

Ahmad, M. R., & Chen, B. (2018a). Effect of silica fume and basalt fiber on the mechanical properties and microstructure of magnesium phosphate cement (MPC) mortar. *Construction and Building Materials, 190*(30), 466–478.

Ahmad, M. R., & Chen, B. (2018b). Effect of silica fume and basalt fiber on the mechanical properties and microstructure of magnesium phosphate cement (MPC) mortar. *Construction and Building Materials, 190*, 466–478. https://doi.org/10.1016/j.conbuildmat.2018.09.143

Ahmad, M. R., & Chen, B. (2020). Microstructural characterization of basalt fiber reinforced magnesium phosphate cement supplemented by silica fume. *Construction and Building Materials*, *237*, Article 117795. https://doi.org/10.1016/j.conbuildmat.2019.117795

Ahmad, M. R., Chen, B., & Yu, J. (2019). A comprehensive study of basalt fiber reinforced magnesium phosphate cement incorporating ultrafine fly ash. *Composites Part B-Engineering, 168*, 204–217. https://doi.org/10.1016/j.compositesb.2018.12.065

Arain, M. F., Wang, M., Chen, J., & Zhang, H. (2019). Study on PVA fiber surface modification for strain-hardening cementitious composites (PVA-SHCC). *Construction and Building Materials, 197*, 107–116. https://doi.org/10.1016/j.conbuildmat.2018.11.072

Arora, A., Singh, B., & Kaur, P. (2019). Novel material i.e. magnesium phosphate cement (MPC) as repairing material in roads and buildings. *Materials Today: Proceedings*, *17*(Pt 1).

Bilginer, B. A., & Erdoğan, S. T. (2021). Effect of mixture proportioning on the strength and mineralogy of magnesium phosphate cements. *Construction and Building Materials*, *277*.

Chau, C. K., Qiao, F., & Li, Z. (2011). Microstructure of magnesium potassium phosphate cement. *Construction and Building Materials, 25*(6), 2911–2917. https://doi.org/10.1016/j.conbuildmat.2010.12.035

Dao-Yuan, Z. G.-J. Z. W.-X. X. (2004). A study on the formulae to test klc in three-point concrete bending beams. *Journal of Jiangsu Ocean University (Natural Science Edition),* (02), 67–70.

Ding, Z., Dong, B., Xing, F., Han, N., & Li, Z. (2012). Cementing mechanism of potassium phosphate based magnesium phosphate cement. *Ceramics International, 38*(8), 6281–6288. https://doi.org/10.1016/j.ceramint.2012.04.083

Ding, Z., & Li, Z. J. (2005). Effect of aggregates and water contents on the properties of magnesium phospho-silicate cement. *Cement and Concrete Composites, 27*(1), 11–18. https://doi.org/10.1016/j.cemconcomp.2004.03.003

Feng, H., Li, Z., Wang, W., Liu, G., Zhang, Z., & Gao, D. (2021). Deflection hardening behaviour of ductile fibre reinforced magnesium phosphate cement-based composite. *Cement and Concrete Composites*, *121*, Article 104079. https://doi.org/10.1016/j.cemconcomp.2021.104079

Feng, H., Nie, S., Guo, A., Lv, L., & Yu, J. (2022). Evaluation on the performance of magnesium phosphate cement-based engineered cementitious composites (MPC-ECC) with blended fly ash/silica fume. *Construction and Building Materials*, *341*, 127861. https://doi.org/10.1016/j.conbuildmat.2022.127861

Gao, M., Liu, N., & Chen, B. (2020). Effect of silica fume on properties of magnesium phosphate cement mortar. *Journal of Building Materials, 23*(1), 29–34.

Gardner, L. J., Bernal, S. A., Walling, S. A., Corkhill, C. L., Provis, J. L., & Hyatt, N. C. (2015). Characterisation of magnesium potassium phosphate cements blended with fly ash and ground granulated blast furnace slag. *Cement and Concrete Research, 74*, 78–87. https://doi.org/10.1016/j.cemconres.2015.01.015

Hall, D. A., Stevens, R., & El-Jazairi, B. (2001). The effect of retarders on the microstructure and mechanical properties of magnesia-phosphate cement mortar. *Cement and Concrete Research, 31*(3), 455–465. https://doi.org/10.1016/s0008-8846(00)00501-9

Haque, M. A., & Chen, B. (2019). Research progresses on magnesium phosphate cement: A review. *Construction and Building Materials*, *211*.

Hou, D., Yan, H., Zhang, J., Wang, P., & Li, Z. (2016). Experimental and computational investigation of magnesium phosphate cement mortar. *Construction and Building Materials*, *112*.

Hu, F., Zeya, L., Weiqiang, W., Guanghui, L., & Danying, G. (2021). Deflection hardening behaviour of ductile fibre reinforced magnesium phosphate cement-based composite. *Cement and Concrete Composites, 121*(2), 104079.

JSCE. (2008). *Recommendations for design and construction of High Performance Fiber Reinforced Cement Composites with Multiple Fine Cracks (HPFRCC).* Japan Society of Civil Engineers.

Kanda, T., & Li, V. C. (1998). Multiple cracking sequence and saturation in fiber reinforced cementitious composites. *Concrete Research and Technology, Japan Concrete Institute, 9*(2), 19–33.

Kanda, T., & Li, V. C. (1999). New micromechanics design theory for pseudostrain hardening cementitious composite. *Journal of Engineering Mechanics-Asce, 125*(4), 373–381. https://doi.org/10.1061/(asce)0733-9399(1999)125:4(373)

Kanda, T., & Li, V. C. (2006). Practical design criteria for saturated pseudo strain hardening behavior in ECC. *Journal of Advanced Concrete Technology, 4*(1), 59–72.

Kms, A., Dkhb, B., & Fuas, C. (2015). Deflection hardening behaviour of jute strands reinforced lightweight cementitious composite. *Construction and Building Materials, 96*, 102–111.

Li, D. X., & Feng, C. H. (2011). Study on modification of the magnesium phosphate cement-based material by fly ash. *Advanced Materials Research, 150–151*, 1655–1661.

Li, V. C. (1998). Engineered cementitious composites—tailored composites through micromechanical modeling. *Journal of Advanced Concrete Technology*, *1*(3).

Li, V. C. (2003). On Engineered Cementitious Composites (ECC) a review of the material and its applications. *Journal of Advanced Concrete Technology*.

Li, V. C. (2019). Engineered Cementitious Composites (ECC): Bendable concrete for sustainable and resilient infrastructure. *Springer*. https://doi.org/10.1007/978-3-662-58438-5

Li, V. C., & Leung, C. K. Y. (1992). steadystate and multiple cracking of short random fiber composites. *Journal of Engineering Mechanics*, *118*(11).

Li, V. C., Wu, C., Wang, S., Ogawa, A., & Saito, T. (2002). Interface tailoring for strain-hardening polyvinyl alcohol-engineered cementitious composite (PVA-ECC). *Materials Journal*, *99*(5).

Li, V. C., Wu, C., Wang, S. X., Ogawa, A., & Saito, T. (2002b). Interface tailoring for strain-hardening polyvinyl alcohol-engineered cementitious composite (PVA-ECC). *Aci Materials Journal, 99*(5), 463–472.

Li, Y., Li, Y., Shi, T., & Li, J. (2015). Experimental study on mechanical properties and fracture toughness of magnesium phosphate cement. *Construction and Building Materials*, *96*.

Liang, J., Fangli, Z., Kai, Y., & Hongjian, D. (2021). Bond performance of repair mortar made with magnesium phosphate cement and ferroaluminate cement. *Construction and Building Materials*, *279*.

Lim, Y. M., & Li, V. C. (1997). Durable repair of aged infrastructures using trapping mechanism of engineered cementitious composites. *Cement and Concrete Composites*, *19*(4).

Lin, C., Kayali, O., Morozov, E. V., & Sharp, D. J. (2017). Development of self-compacting strain-hardening cementitious composites by varying fly ash content. *Construction and Building Materials, 149*, 103–110. https://doi.org/10.1016/j.conbuildmat.2017.05.051

Lin, W., Sun, W., & Li, Z. J. (2010). Study on the Effects of fly ash in magnesium phosphate cement. *Jianzhu Cailiao Xuebao/journal of Building Materials, 13*(6), 716–721.

Jin, L., G. R., Zengqi, Z. (2021). Research progress of magnesium phosphate cement. *Materials Review,* (23), 1–16.

Liu, R. Q., Chen, D. Q., & Hou, T. B. (2014). Study on preparation and the setting time of magnesium phosphate cement. *Advanced Materials Research*, *3593*.

Mo, L., Lv, L., Deng, M., & Qian, J. (2018). Influence of fly ash and metakaolin on the microstructure and compressive strength of magnesium potassium phosphate cement paste. *Cement and Concrete Research, 111*, 116–129.

Pedro, D., de Brito, J., & Evangelista, L. (2017). Evaluation of high-performance concrete with recycled aggregates: Use of densified silica fume as cement replacement. *Construction and Building Materials, 147*, 803–814. https://doi.org/10.1016/j.conbuildmat.2017.05.007

Singh, S. B., & Munjal, P. (2020). Engineered cementitious composite and its applications. *Materials Today: Proceedings*.

Sui, L., Zhong, Q., Yu, K., Xing, F., Li, P., & Zhou, Y. (2018). Flexural fatigue properties of ultra-high performance engineered cementitious composites (UHP-ECC) reinforced by polymer fibers. *Polymers*, *10*(8).

Tao, H. B., Fan, W. K., Xiang, Z. J., Yu, X., Guo, D. J., & C., L. V. (2021). Engineered/strain-hardening cementitious composites (ECC/SHCC) with a compressive strength over 210 MPa. *Composites Communications* (Prepublish).

Victor, C. L. I. (1993). From micromechanics to structural engineering the design of cementitious composites for civil engineering applications. *Doboku Gakkai Ronbunshu*.

Wu, Q., Zou, Y., Gu, J., Xu, J., Ji, R., & Wang, G. (2020). The influence and action mechanization of mineral mixed material on high fluidity potassium magnesium phosphate cement (MKPC). *Journal of Composites Science*, *4*(1).

Xiaoying, X., Xujian, L., Xiaoxin, P., Tao, J., Yongning, L., & Hongru, Z. (2020). Influence of silica fume on the setting time and mechanical properties of a new magnesium phosphate cement. *Construction and Building Materials*, *235*(C), 117544.

Xie, Y., Lin, X., Pan, X., & Ji, T. (2020). Preliminary investigation of the hydration mechanism of $MgO–SiO_2–K_2HPO_4$ cement. *Construction and Building Materials*, *235*, 117471. https://doi.org/10.1016/j.conbuildmat.2019.117471

Xu, B., Lothenbach, B., & Ma, H. (2018). Properties of fly ash blended magnesium potassium phosphate mortars: Effect of the ratio between fly ash and magnesia. *Cement and Concrete Composites, 90*, 169–177. https://doi.org/10.1016/j.cemconcomp.2018.04.002

Xu, B., Ma, H., & Li, Z. (2015). Influence of magnesia-to-phosphate molar ratio on microstructures, mechanical properties and thermal conductivity of magnesium potassium phosphate cement paste with large water-to-solid ratio. *Cement and Concrete Research, 68*, 1–9. https://doi.org/10.1016/j.cemconres.2014.10.019

Xu, B., Ma, H., Shao, H., Li, Z., & Lothenbach, B. (2017). Influence of fly ash on compressive strength and micro-characteristics of magnesium potassium phosphate cement mortars. *Cement and Concrete Research, 99*, 86–94. https://doi.org/10.1016/j.cemconres.2017.05.008

Xu, B., Winnefeld, F., Kaufmann, J., & Lothenbach, B. (2019). Influence of magnesium-to-phosphate ratio and water-to-cement ratio on hydration and properties of magnesium potassium phosphate cements. *Cement and Concrete Research*, *123*, Article 105781. https://doi.org/10.1016/j.cemconres.2019.105781

Xu, S., & Reinhardt, H. W. (1999). Determination of double- K criterion for crack propagation in quasi-brittle fracture, Part II: Analytical evaluating and practical measuring methods for three-point bending notched beams. *International Journal of Fracture*, *98*(2).

Xu, X., Lin, X., Pan, X., Ji, T., Liang, Y., & Zhang, H. (2020). Influence of silica fume on the setting time and mechanical properties of a new magnesium phosphate cement. *Construction and Building Materials*, *235*, Article 117544. https://doi.org/10.1016/j.conbuildmat.2019.117544

Yang, E.-H., Wang, S., Yang, Y., & Li, V. C. (2008). Fiber-bridging constitutive law of engineered cementitious composites. *Journal of Advanced Concrete Technology, 6*(1), 181–193. https://doi.org/10.3151/jact.6.181

Yang, E. H., Yang, Y. Z., & Li, V. C. (2007). Use of high volumes of fly ash to improve ECC mechanical properties and material greenness. *Aci Materials Journal, 104*(6), 620–628.

Yang, N., Shi, C., Yang, J., & Chang, Y. (2013). Research progresses in magnesium phosphate cement–based materials. *Journal of Materials in Civil Engineering*.

Yu, K., Li, L., Yu, J., Wang, Y., Ye, J., & Xu, Q. (2018). Direct tensile properties of engineered cementitious composites: A review. *Construction and Building Materials*, *165*.

Yu, K., Wang, Y., Yu, J., & Xu, S. (2017). A strain-hardening cementitious composites with the tensile capacity up to 8%. *Construction and Building Materials, 137*, 410–419.

Yu, J., Yao, J., Lin, X., Li, H., Lam, J. Y., Leung, C. K., et al. (2018a). Tensile performance of sustainable Strain-Hardening Cementitious Composites with hybrid PVA and recycled PET fibers. *Cement and Concrete Research, 107*, 110–123.

Yue, L., & Bing, C. (2013). Factors that affect the properties of magnesium phosphate cement. *Construction and Building Materials, 47*, 977–983. https://doi.org/10.1016/j.conbuildmat.2013.05.103

Yue, L., Jia, S., & Bing, C. (2014). Experimental study of magnesia and *M/P* ratio influencing properties of magnesium phosphate cement. *Construction and Building Materials, 65*, 177–183. https://doi.org/10.1016/j.conbuildmat.2014.04.136

Zhang, D., Ge, Y., Pang, S. D., & Liu, P. (2021). The effect of fly ash content on flexural performance and fiber failure mechanism of lightweight deflection-hardening cementitious composites. *Construction and Building Materials*, *302*, Article 124349. https://doi.org/10.1016/j.conbuildmat.2021.124349

Zhang, D., Jaworska, B., Zhu, H., Dahlquist, K., & Li, V. C. (2020). Engineered Cementitious Composites (ECC) with limestone calcined clay cement (LC 3). *Cement and Concrete Composites*, *114*.

Zhao, Z. Q., Sun, R. J., Feng, Z. Q., Wei, S. S., & Huang, D. W. (2013). Mechanical properties and applications of engineered cementitious composites (ECC). *Applied Mechanics and Materials*, *2685*.

Zheng, D. D., Ji, T., Wang, C. Q., Sun, C. J., Lin, X. J., & Hossain, K. (2016). Effect of the combination of fly ash and silica fume on water resistance of magnesium–potassium phosphate cement. *Construction and Building Materials*, *106*, 415–421.

Zhenming, L., Brice, D., Tianshi, L., Albina, K., Stéphanie, S., & Guang, Y. (2021). A comparative study on the mechanical properties, autogenous shrinkage and cracking proneness of alkali-activated concrete and ordinary Portland cement concrete. *Construction and Building Materials*, *292*.

Zhou, Y., Xi, B., Sui, L., Zheng, S., Xing, F., & Li, L. (2019). Development of high strain-hardening lightweight engineered cementitious composites: Design and performance. *Cement and Concrete Composites*, *104*, Article 103370. https://doi.org/10.1016/j.cemconcomp.2019.103370

Chapter 4
Performance Improvement and Design of UHDMC Using PE Fibers

Abstract In this chapter, ultra-high ductility magnesium phosphate cement-based composites (UHDMC) was prepared with the polyethylene (PE) fibers. The effect of the magnesium oxide to potassium dihydrogen phosphate mass ratio (*M/P*), quartz sand particle size (Sd), water to solid mass ratio (*W/S*), sand to binder mass ratio (*S/B*), fly ash (FA) content, fiber volume fraction (V_f), curing temperature, and curing age on the micro-mechanical properties and macro-mechanical properties of UHDMC were explored. The results showed that the ultimate tensile strain of UHDMC can reach 7.1%. Even curing at −10°C for 7 days, the ultimate tensile strain can reach 5.6%, and the compressive strength can reach nearly 20 MPa. With the increase of *M/P*, the compressive strength of UHDMC increases, but the ultimate tensile stress decreases. The ultimate tensile strain of UHDMC with the Sd of 150–180 mesh can reach more than 5%. The large *W/S* is helpful to improve strain hardening performance. When the FA content is 40%, the strain hardening performance of UHDMC is significant, and the pseudo strain-hardening indices reach the maximum. The quantitative association model between ultimate tensile strain and pseudo strain-hardening indices was established. According to the association model, the design method of UHDMC was established.

Keywords Magnesium phosphate cement · PE fiber · Ultra-high ductility · Design method · Strain hardening performance

4.1 Introduction

Magnesium phosphate cement (MPC) is a type of inorganic cementitious material, which has many excellent properties, including high early strength (Ma et al., 2021a, 2021b), rapid setting (Jia et al., 2021; Liu et al., 2022; Tonelli et al., 2021), low drying shrinkage (Peng & Chen, 2021; Qin et al., 2022), outstanding durability (Chen et al., 2022; Fang et al., 2018a, 2018b, 2021; Wu et al., 2022; Yang, 2013; Yang et al., 2002), excellent wear resistance (Yang, 2013; Yang et al., 2000; Zhao et al., 2012), and hardening in low temperature environments (Feng et al., 2018a). In addition,

H. Feng et al., *Ultra-High Ductility Magnesium-Phosphate-Cement-Based Composites (UHDMC)*, https://doi.org/10.1007/978-981-97-0952-6_4

MPC can form a good bond with the fibers (Feng et al., 2019; Feng et al., 2018b; Jihui et al., 2018). Therefore, the MPC can be used as a cementitious material to develop high performance ultra-high ductility magnesium phosphate cement-based composites (UHDMC) (Fang et al., 2018a, 2018b; Feng et al., 2021b).

Magnesium phosphate cement-based engineered cementitious composites (MPC-ECC) has been developed in recent years (Feng et al., 2022a, 2022b, 2022c; Haque & Chen, 2019; Jihui et al., 2018). The incorporation of glass fibers, polyvinyl alcohol (PVA) fibers, and basalt fibers can improve the flexural and compressive strengths of MPC mortars (Fang et al., 2018a, 2018b; Haque & Chen, 2019). The incorporation of micro steel (MS) fibers with 0.4–1.6% volume fraction can significantly improve the compressive strength and flexural toughness of MPC mortars (Feng et al., 2018a). The combination of PVA fibers with polypropylene (PP) fibers or MS fibers can significantly improve the ductility and toughness of MPC-based composites (Feng et al., 2022a, 2022b, 2022c). In addition, polyethylene (PE) fiber is also used to develop high ductility ECC due to its excellent strength, modulus of elasticity, corrosion resistance, and durability (Curosu et al., 2017; Ranade et al., 2013a, 2013b; Yu et al., 2017). Tang etc. (Tang et al., 2023) made a preliminary attempt to combine PE fibers with MPC and found that the ultimate tensile strain is only about 1.5%. Therefore, the development of UHDMC using PE fibers still needs further research.

Mineral admixtures also have a significant effect on the strain hardening performance of UHDMC (Feng et al., 2022a, 2022b, 2022c). The components (e.g., SiO_2) in mineral admixtures can participate in the hydration reaction to form new gels (e.g., $MgSiO_3$ gels) (Ahmad & Chen, 2018; Li & Feng, 2011), which is conducive to improving the strengths and the ductility of the composites (Feng et al., 2021b). At present, the research on the UHDMC mainly focuses on examining the effect of fiber types and mineral admixtures. It was reported that magnesia-to-phosphate mass ratio (*M/P*), particle size of quartz sand, water/solid mass ratio (*W/S*), sand/binder mass ratio (*S/B*), etc. have significant impact on the performance of MPC-based composites (Haque & Chen, 2019; Xu et al., 2019; Yue & Bing, 2013). Therefore, these factors are believed to affect the performance of the UHDMC. In addition, the research on UHDMC is not systematic and comprehensive and lacks of a mature design method. Therefore, further research is needed for the UHDMC.

In order to make ordinary Portland cement-based ECC (traditional ECC) possess strain hardening performance, two design criteria were proposed based on the fracture mechanics (Li, 2012; Yang & Li, 2010). One is that the maximum bridging stress of the fibers exceeds the matrix cracking strength, and the other is that the fiber bridging complementary energy is larger than the matrix fracture energy, based on which two pseudo strain hardening performance indices (strength index PSH_σ and energy index PSH_J) were proposed. The strain hardening performance of ECC can be quantified from the perspectives of energy and strength by PSH_σ and PSH_J (Ranade et al., 2013a, 2013b). The design criteria and evaluation method of traditional ECC can provide references for the development of UHDMC. However, the hydration process and products of MPC are different from those of ordinary Portland cement, which results in the difference in the properties of MPC matrix and the interface between the MPC matrix and fibers. Therefore, a systematic design method for high performance

UHDMC needs to be established. In addition, the tensile strain of traditional ECC can already reach 8% (Yu et al., 2017). However, the tensile strain of UHDMC can only reach 4% (Feng et al., 2022a, 2022b, 2022c, 2023a, 2023b), which limits its application to a certain extent. Therefore, it is necessary to develop ultra-high ductility UHDMC and establish its design method.

In this Chapter, the mass ratio of magnesium oxide to potassium dihydrogen phosphate (*M/P*), particle size of quartz sand (Sd), water to solid mass ratio (*W/S*), sand to binder mass ratio (*S/B*), fly ash (FA) content, fiber volume fraction (V_f), curing age, and curing temperature are used as influence factors to develop high performance UHDMC. The micro-mechanical properties (including cracking strength of MPC matrix σ_{fc}, fiber bridging stress capacity σ_{cu}, fracture energy of MPC matrix J_{tip}, fiber bridging complementary energy J_b', fracture toughness K_m and elastic modulus E_c of MPC matrix) and macro-mechanical properties (compressive strength, ultimate tensile stress, and ultimate tensile strain) were tested. The relationship between influencing factors and pseudo-strain hardening indices (PSH_σ and PSH_J) was obtained. In addition, the association model between pseudo-strain hardening indices and ultimate tensile strain was also established, based on which the design method of UHDMC was obtained. The minimum values of PSH_σ and PSH_J of the UHDMC with the ultimate tensile strain more than 3% were recommended eventually.

4.2 Research Route

Figure 4.1 shows the research route of this Chapter. Figure 4.1a shows the overall design flowchart of UHDMC. Firstly, the influence of the *M/P* and the Sd on the mechanical properties of UHDMC is investigated, from which the suitable *M/P* and Sd are obtained. And then the influence of *W/S* and *S/B* on the mechanical properties of UHDMC is studied, from which the suitable *S/B* and *W/S* are obtained. Afterward, the effects of FA content and V_f are investigated in turn. Finally, the effects of curing age and curing temperature on the early strength performance and mechanical properties of UHDMC are examined.

Figure 4.1b shows the specific design method of UHDMC based on its micro-mechanical and macro-mechanical properties. The micro-mechanical properties include σ_{fc}, σ_{cu}, J_{tip}, J_b', K_m and E_c, which are measured by tensile test, single-crack tensile test and three-point bending test. The macro-mechanical properties include compressive strength, ultimate tensile stress, and ultimate tensile strain. Then, the association model between micro-mechanical properties and macro-mechanical properties is obtained by data fitting. Based on this association model, the design method of UHDMC is established. The macro-mechanical properties of UHDMC can be adjusted through the micro-mechanical properties as a function of influencing factors, so the UHDMC with desired ductility can be realized.

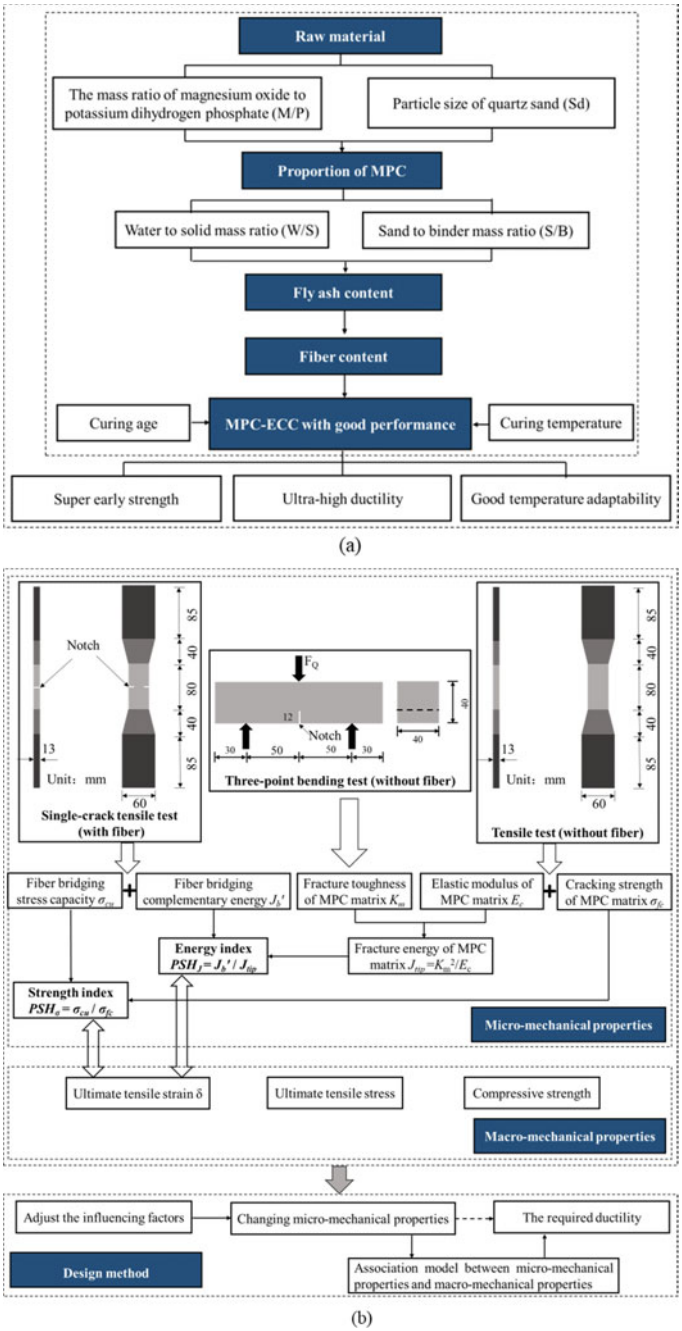

Fig. 4.1 Research route: **a** design flowchart and **b** design method

4.3 Experimental Programs

4.3.1 Materials

Magnesium oxide (MgO), potassium dihydrogen phosphates (KH_2PO_4), borax ($Na_2B_4O_7 \cdot H_2O$), quartz sand, fly ash (FA), polyethylene fiber (PE), and tap water are used to prepare UHDMC. The MgO (purity: ≥96.5%) is obtained from Guizhou Phosphorus Magnesium Material Co., Ltd., and its specific surface area is 451.0 m^2/kg. The KH_2PO_4 (purity: ≥99.5%) containing two different particle sizes of 30 (from Sichuan Mianzhu Ronghong Chemical Co., Ltd.) and 80 (Henan Xinxiang Huaxing Chemical Co., Ltd.) mesh are mixed, and the mass ratio is 1:1. The $Na_2B_4O_7 \cdot H_2O$ (purity: ≥99.5%) is provided from Liaoning Borda Technology Co., Ltd. The fly ash with the specific surface area of 461.9 m^2/kg is obtained from Yulian Power Plant. The quartz sand with an approximate size of 200 mesh, 150–180 mesh and 80–120 mesh are represented by S, M, and L, respectively, which are obtained from Henan Zhongbang Environmental Protection Technology Co., Ltd. Figure 4.2 shows the particle distributions of MgO, KH_2PO_4, quartz sand and FA. Table 4.1 shows the chemical composition of fly ash. The polyethylene (PE) fibers are purchased from Zhejiang Quanmit New Material Technology Co., Ltd., and Table 4.2 shows their specific performance indicators.

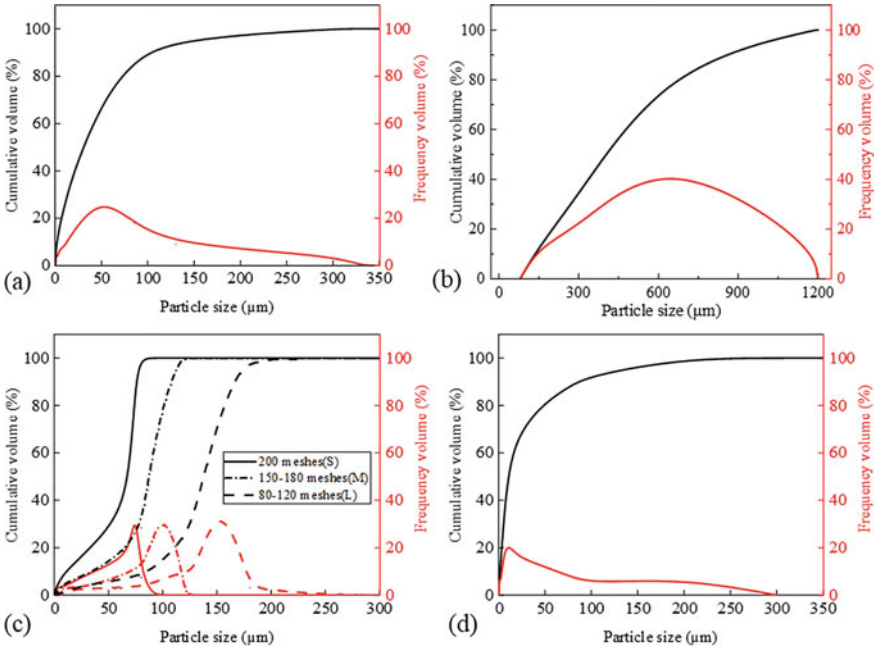

Fig. 4.2 Particle distribution: **a** MgO, **b** KH_2PO_4, **c** quartz sand, and **d** FA

Table 4.1 Chemical composition of FA

Ingredient	Mass fraction (%)
SiO_2	53.97
Al_2O_3	31.15
Fe_2O_3	4.16
CaO	4.01
MgO	1.01
Na_2O	0.89

Reproduced from Workability and Mechanical Properties of Tensile Strain–Hardening PVA Fiber-Reinforced Magnesium Phosphate Cement Composites by Shuwen Zhang with permission from ASCE

Table 4.2 Performance indices of PE fibers (Provided by the supplier)

Diameter (μm)	24
Length (mm)	12
Tensile strength (MPa)	3000
Elastic modulus (GPa)	110
Elongation at break (%)	2–3
Density (g/cm^3)	0.97–0.98

4.3.2 Mix Proportions

In order to further develop ultra-high performance UHDMC and establish a systematic design method, referring to previous research previous studies, a relatively good UHDMC ratio is set as the control sample (Feng et al., 2022a, 2022b, 2022c, 2023a, 2023b; Feng et al., 2021b), for which the specific mix proportion is that the content of $Na_2B_4O_7 \cdot H_2O$ is 6.0% by weight of MgO, the fly ash content is 30% by weight of MPC (MgO, KH_2PO_4, borax), the water to solid (MgO, KH_2PO_4, FA, quartz sand) mass ratio (*W/S*) is 0.14, the sand to binder (MgO, KH_2PO_4, FA) mass ratio (*S/B*) is 0.2, and the PE fibers volume fraction (V_f) is 2%. On the basis of the control sample, the UHDMC is gradually optimized from the perspectives of macro-mechanics and micro-mechanics. Firstly, the effect of the *M/P* and Sd were investigated, and then the optimal *M/P* and particle size of quartz sand were selected, denoted as $O_{M/P}$ and O_s, respectively. Secondly, the effect of *W/S* and *S/B* were investigated, and the optimal *W/S* and *S/B* were selected, denoted as $O_{W/S}$ and $O_{S/B}$, respectively. Thirdly, the effect of FA content was explored, and the optimal FA content was selected, denoted as O_{FA}. Fourthly, the effect of fiber content was explored, and the optimal fiber content was selected. Finally, the UHDMC with high performance is obtained. And the effects of curing temperature and curing age on the obtained UHDMC were also investigated. Tables 4.3, 4.4, 4.5, 4.6 and 4.7 show the specific mix proportion.

Table 4.3 Mixture proportions with different *M/P* and Sd

M/P	*S/B*	Sd	*W/S*	V_f (%)	FA (%)
1.0	0.2	S	0.14	2	30
		M			
		L			
1.2	0.2	S	0.14	2	30
		M			
		L			
1.4	0.2	S	0.14	2	30
		M			
		L			

Table 4.4 Mixture proportions with different *S/B* and *W/S*

M/P	*S/B*	*W/S*	V_f (%)	FA (%)
$O_{M/P}$	0.1	0.12	2	30
		0.14		
		0.16		
$O_{M/P}$	0.2	0.12	2	30
		0.14		
		0.16		
$O_{M/P}$	0.3	0.12	2	30
		0.14		
		0.16		
$O_{M/P}$	0.4	0.12	2	30
		0.14		
		0.16		

Table 4.5 Mixture proportions with different FA content

M/P	*S/B*	*W/S*	V_f (%)	FA (%)
$O_{M/P}$	$O_{S/B}$	$O_{W/S}$	2.0	0
				10
				20
				30
				40

Table 4.6 Mixture proportions with different Fiber content

M/P	*S/B*	*W/S*	V_f (%)	M
$O_{M/P}$	$O_{S/B}$	$O_{W/S}$	1.2	O_{FA}
			1.4	
			1.6	
			1.8	
			2.0	

Table 4.7 UHDMC with different Age (D) and temperature (T)

M/P	*S/B*	*W/S*	V_f	FA	D/T
$O_{M/P}$	$O_{S/B}$	$O_{W/S}$	O_V	O_{FA}	8h
					1d
					3d
					7d
					28d
$O_{M/P}$	$O_{S/B}$	$O_{W/S}$	O_V	O_{FA}	0 °C
					−5 °C
					−10 °C

4.3.3 Mixing and Curing Procedures

Following the specimen preparation process indicated in the literature (Feng et al., 2022a, 2022b, 2022c), potassium dihydrogen phosphate, magnesium oxide, borax, quartz sand, and fly ash were mixed in the mixer and stirred for 120 s to achieve uniform dispersion. Then the water was added into the mixer gradually and mixed for another 60 s. Finally, PE fibers were added, and then continue stirring for 90 s. For MPC matrix, the mixing method is the same as that of UHDMC except without fibers. After the mixing was completed, the prepared mixture was cast into the mold and vibrated for 30 s to remove air bubbles. Then specimens were cured in specific environment. Regarding the effect of curing age, the specimens were cured at the temperature of 20 ± 2 °C and the relative humidity of 98% for specific curing ages (8 h, 1 day, 3 days, 7 days, and 28 days). Regarding the effect of curing temperature, the specimens were cured at the specific curing temperatures (0, −5, and −10 °C) for 7 days. Regarding the effect of other influencing factors (such as *M/P*, Sd, *S/B*, *W/S* etc.), the specimens were cured at the temperature of 20 ± 2 °C and the relative humidity of 98% for 7 days.

4.3.4 Compressive Test

The compressive strength of UHDMC was tested by using the cubic specimen (size: 50 mm × 50 mm × 50 mm) by referring to ASTM C109 (Cabinets et al., 2010), and the loading rate was 0.9 kN/s. Three specimens of each ratio were tested, and the average value was used.

4.3.5 Tensile Test

Figure 4.3 shows the dimension of the specimen and the loading diagram (Yokota et al., 2008). Two linear variable displacement sensors (LVDTs) were used to record tensile displacement. The loading speed was 0.2 mm/min. The load and displacement of the specimen were recorded. The tensile stress was obtained by dividing the tensile load by the cross-sectional area, and the tensile strain was obtained by dividing the tensile displacement by gauge length. Then, the stress–strain curve was obtained, in which the maximum tensile stress is the ultimate tensile stress, the strain corresponding to maximum tensile stress is the ultimate tensile strain.

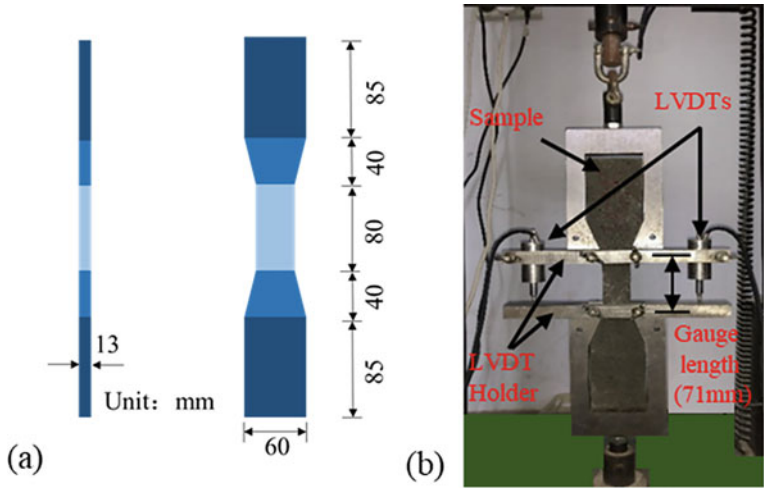

Fig. 4.3 Axial tensile test: **a** specimen and **b** loading diagram. Reproduced from Evaluation on the performance of magnesium phosphate cement-based engineered cementitious composites (MPC-ECC) with blended fly ash/silica fume by Hu Feng with permission from Elsevier

4.3.6 Micromechanical Tests

The development of ECC is on the basis of the synergistic interaction of cement matrix, fiber, and fiber/matrix interface, which is characterized by $PSH_\sigma\left(\sigma_{cu}/\sigma_{fc}\right)$ and PSH_J (J_b'/J_{tip}) (Kiran, 2012). In order to develop the design method of UHDMC with high performance, the micro-mechanical analysis was conducted to provide a further understanding on the UHDMC. Figure 4.4 shows the σ_{cu}, σ_{fc}, J_b', and J_{tip}, which are all obtained through the following experiments.

The single-crack tensile test was conducted to obtain the J_b' and the σ_{cu} (Zhou et al., 2019). In order to ensure that UHDMC cracks in single-crack failure pattern under tension, a notch is made on the specimen. Figure 4.5 is the schematic illustration of the remained area. The maximum load was divided by the remained area to obtain the σ_{cu}, and the J_b' was calculated using Eq. 4.1.

$$J_b' \equiv \sigma_{cu}\delta_{cu} - \int_0^{\delta_{cu}} \sigma(\delta)d\delta \tag{4.1}$$

where J_b' is the fiber bridging complementary energy, σ_{cu} is the fiber bridging stress capacity, and δ_{cu} is the displacement corresponding to σ_{cu}.

The σ_{fc} and E_c were obtained by tensile test. The schematic illustration of the specimen is the same as that of UHDMC with fibers (see Fig. 4.3). During the test, the load and displacement are recorded to obtain the tensile stress–strain curve, from which the σ_{fc} (maximum tensile stress) and the E_c can be obtained.

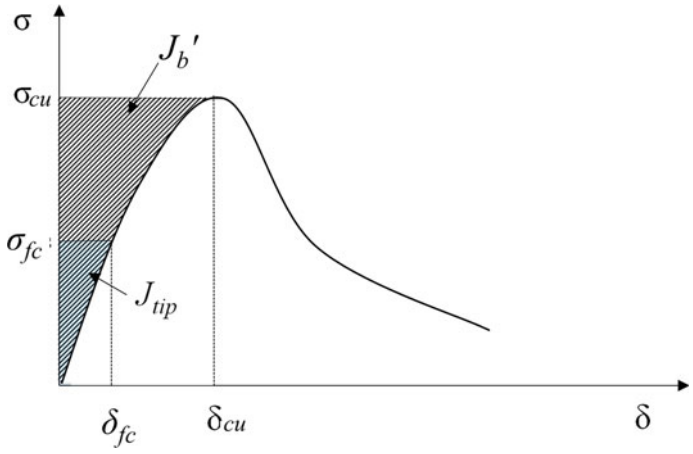

Fig. 4.4 Tensile stress–strain curve of ECC. Reproduced from Development of high strain-hardening lightweight engineered cementitious composites: Design and performance by Yingwu Zhou with permission from Elsevier

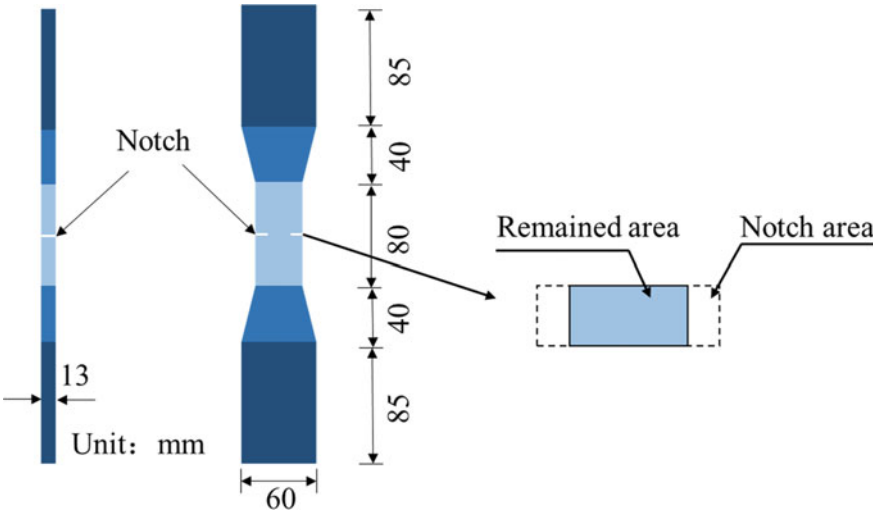

Fig. 4.5 Schematic illustration of single-crack tensile specimen. Reproduced from Evaluation on the performance of magnesium phosphate cement-based engineered cementitious composites (MPC-ECC) with blended fly ash/silica fume by Hu Feng with permission from Elsevier

The K_m was obtained by three-point bending test by referring to ASTM E399 (2012) ("Astm," 2009). Figure 4.6 shows the size of the specimen (notched beam) (Guang-Jun et al., 2004). During the test, the peak load F_Q is recorded. The K_m is calculated by Eqs. 4.2 and 4.3 (Xu & Reinhardt, 1999). And the J_{tip} can be obtained by Eq. 4.4.

$$Km = \frac{1.5(FQ + 0.5mg \cdot 10^{-2}) \cdot 10^{-3} \cdot S \cdot a_0^{1/2}}{th^2} f(\alpha) \tag{4.2}$$

$$f(\alpha) = \frac{1.99 - \alpha(1-\alpha)(2.15 - 3.93\alpha + 2.7\alpha^2)}{(1+2\alpha)(1-\alpha)^{3/2}}, \alpha = \frac{a0}{h} \tag{4.3}$$

where m is the mass of the specimen; g is the acceleration of gravity; S is the span of the beam; a_0 is the notch height of the beam; t is the width of the beam; h is the height of the beam; $f(\alpha)$ is the shape parameter of the beam.

$$J_{tip} = K_m^2 / E_c \tag{4.4}$$

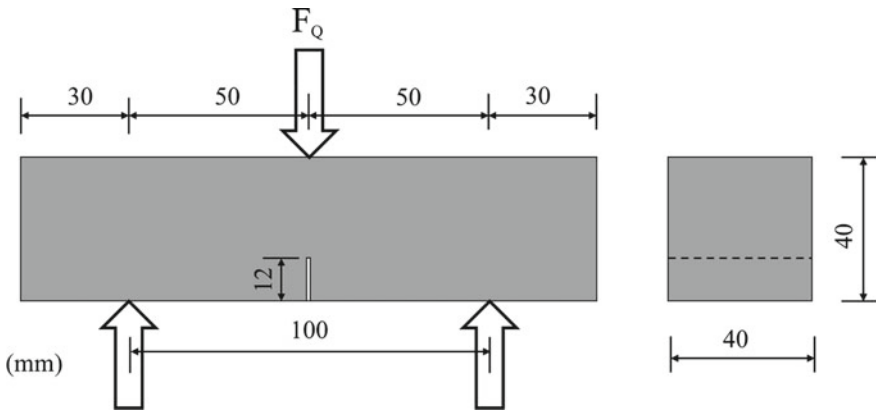

Fig. 4.6 Schematic illustration of three-point bending test specimen. Reproduced from Evaluation on the performance of magnesium phosphate cement-based engineered cementitious composites (MPC-ECC) with blended fly ash/silica fume by Hu Feng with permission from Elsevier

4.4 Results and Discussion

4.4.1 Effect of Sd and M/P

(1) **Compressive strength**

Figure 4.7 shows the effect of the Sd and *M/P* on the compressive strength of UHDMC. When the *M/P* is constant, the compressive strength increases with the decrease of Sd. When the *M/P* is 1.0, 1.2, and 1.4, the compressive strength increases by 3.9, 2.1, and 2.5 MPa with the Sd changes from 80 to 120 mesh to 200 mesh, respectively. Compared to MPC, the quartz sand has a relatively larger particle size, which will increase the porosity of the cement matrix (Feng et al., 2021b), Therefore, the larger Sd will adversely affects the compressive strength more. When the Sd is 80–120 mesh, 150–180 mesh and 200 mesh, respectively, the compressive strength of UHDMC slightly increases by 4.2, 2.5 and 2.4 MPa with the increase of *M/P* from 1.0 to 1.4, respectively. Theoretically, when the molar ratio of potassium dihydrogen phosphate to magnesium oxide is 1, the KH_2PO_4 and MgO can react completely. However, the *M/P* used in this Chapter were 1.0, 1.2, and1.4, equivalent to the molar ratios of 3.3, 4.0, and 4.7, respectively. The content of magnesium oxide in the reaction system is more than the content required for the reaction. In addition, the main source of MPC strength is the overlapping network structure, which is formed by the hydration product, MKP, wrapping the remaining MgO (Liu et al., 2012). The magnesium oxide particles are small and very hard, and the unreacted magnesium oxide can fill pores and cracks in MPC matrix, leading to dense cement matrix (Qiao et al., 2010).

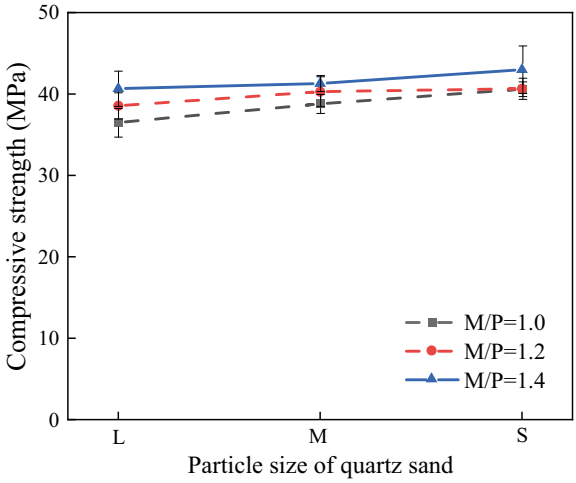

Fig. 4.7 Compressive strength of UHDMC with different quartz sand particle sizes and M/P

(2) **Tensile properties**

Figures 4.8, 4.9 and 4.10 show the tensile stress–strain curves of UHDMC with different Sd and *M/P*. From Fig. 4.8, when the quartz sand particle size is 150–180 mesh or 200 mesh, the UHDMC with the *M/P* of 1 shows good strain hardening performance. However, when the quartz sand particle size is coarse (80–120 mesh), the UHDMC with the *M/P* of 1 shows poor strain hardening performance. Figure 4.9 shows that when the *M/P* is 1.2, the UHDMC all show good strain hardening performance, especially for that with quartz sand of 150–180 mesh particle size. Figure 4.10 shows that when the *M/P* is 1.4, the UHDMC with the Sd of 80–120 mesh and 150–180 mesh show obvious strain hardening performance. However, when the quartz sand particle size is 200 mesh, the UHDMC does not show good strain hardening performance. In general, when the *M/P* changes from 1.0 to 1.4, the UHDMCs with the quartz sand particle size of 150–180 mesh all show obvious strain hardening performance.

Figure 4.11a, b show the effect of *M/P* and Sd on the ultimate tensile stress and ultimate tensile strain of UHDMC. From Fig. 4.11a, the ultimate tensile stress increases with the Sd becoming finer. When the *M/P* ratios are 1.0, 1.2 and 1.4, the ultimate tensile stress increases by 11.7, 12.1, and 21.4%, respectively, with the change of the Sd from 80 to 120 mesh to 200 mesh, which is because large Sd increases the porosity of the cement matrix and reduces the bridging ability of the fiber (Feng et al., 2021b). In addition, when the particle sizes of quartz sand are 80–120 mesh, 150–180 mesh and 200 mesh, the ultimate tensile stress decreases by 17.0, 10.5, and 10.4% with the increase of the *M/P* from 1.0 to 1.4, respectively. This is because in the magnesium phosphate cement reaction system, the magnesium oxide content is greater than the required, and the content of magnesium oxide increases

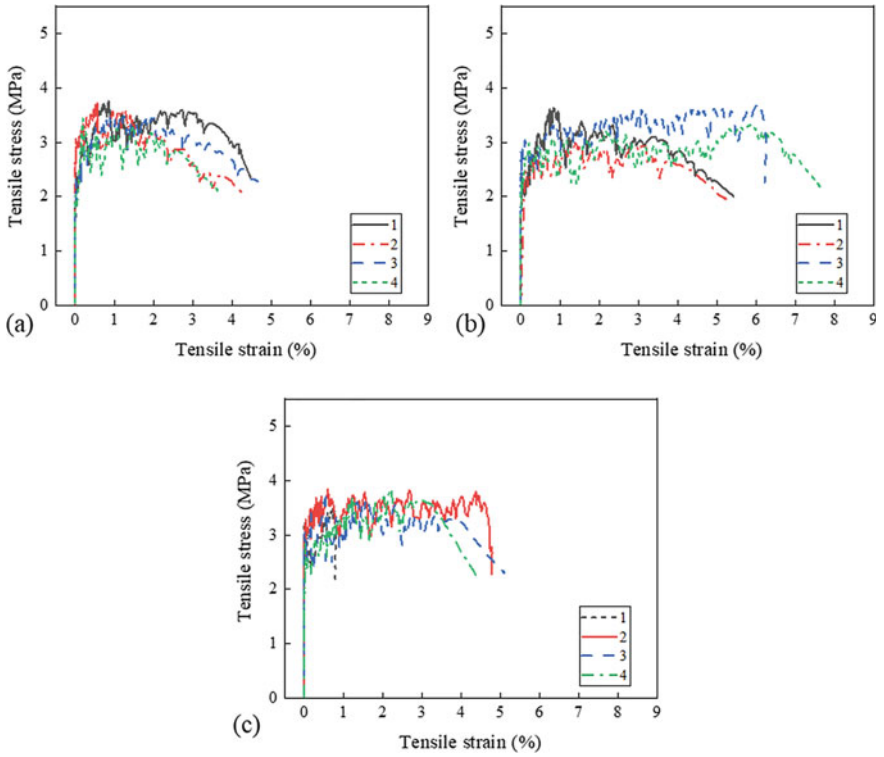

Fig. 4.8 Tensile stress–strain curves with $M/P = 1.0$ and Sd of **a** 80–120 mesh, **b** 150–180 mesh, and **c** 200 mesh

with the increase of the *M/P*, which will result in the decrease of hydration product (MKP). Therefore, the bonding performance between the matrix and the fiber is reduced.

From Fig. 4.11b, when the Sd is 80–120 mesh or 150–180 mesh, the ultimate tensile strain increases gradually with the increase of the *M/P*. This may be due to that although the bonding strength between the matrix and the fiber decrease with the increase of the *M/P*, some fibers are pulled out from the matrix rather than broken, which will lead to an increase in the ultimate tensile strain. When the Sd is 200 mesh, the ultimate tensile strain decreases slightly with the increase of the *M/P*. The Sd also has a greatly effect on the ultimate tensile strain. When the *M/P* is 1.0, 1.2, and 1.4, the ultimate tensile strain is significantly increased from 0.62, 1.50, and 1.84% to 5.25, 5.49, and 5.85%, and then decreased to 1.02, 0.86, and 0.46%, respectively, with the Sd changing from 80 to 120 mesh to 150–180 mesh and then to 200 mesh. This indicates that when the *M/P* is 1.0, 1.2 or 1.4, the UHDMC with quartz sand particle size of 150–180 mesh has a very good ultimate tensile strain.

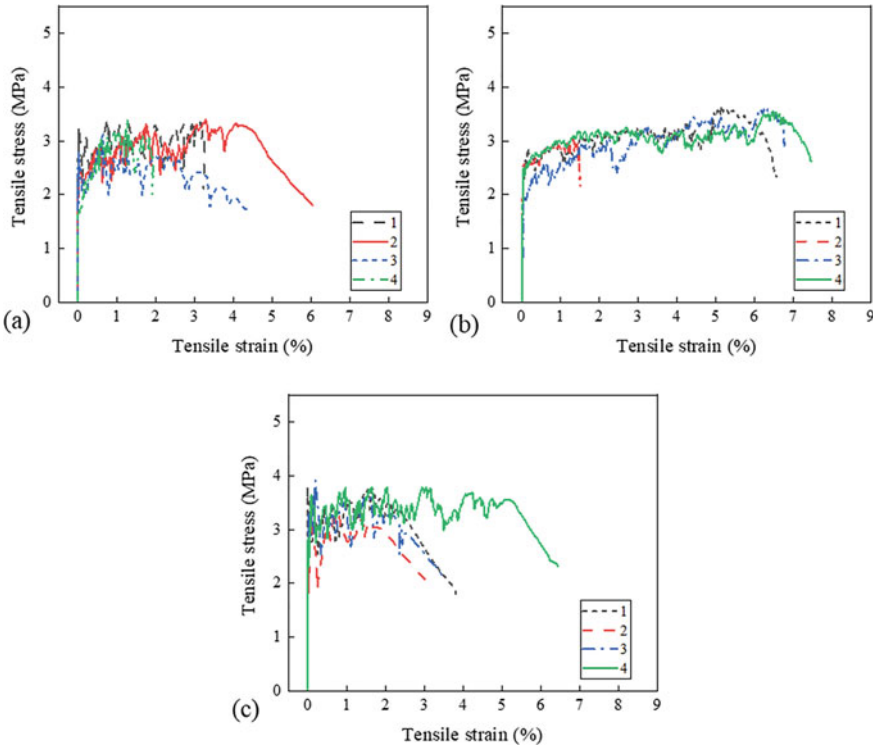

Fig. 4.9 Tensile stress–strain curves with $M/P = 1.2$ and Sd of **a** 80–120 mesh, **b** 150–180 mesh, and **c** 200 mesh

(3) **Micromechanical indices**

Figure 4.12 shows the effect of Sd and *M/P* on the σ_{cu} of UHDMC. When the *M/P* were 1.0, 1.2, and 1.4, the fiber bridging stress increased by 18.8, 16.0, and 26.1%, respectively, with the quartz sand particle size changing from 80 to 120 mesh to 150–180 mesh and then to 200 mesh. On other hand, when the quartz sand particle size is 80–120 mesh, 150–180 mesh and 200 mesh, the fiber bridging stress is decreased by 15.8, 14.1 and 10.7%, respectively, with the *M/P* gradually increasing from 1.2 to 1.4, which is similar to the change of ultimate tensile stress. The increase of magnesium oxide content leads to the decrease of MKP content, thus resulting in the decrease of fiber bridging stress.

Figure 4.13 shows the effects of Sd and *M/P* on the cracking strength of MPC matrix. When the *M/P* were 1.0, 1.2 and 1.4, the cracking strength of the matrix increases by 19.3, 14.1 and 26.2%, respectively, with the Sd changing from 80 to 120 mesh to 200 mesh. This indicates that the reduction in the Sd is helpful to enhance the cracking strength of the matrix. When the Sd is 80–120 mesh, 150–180 mesh and 200 mesh, respectively, the cracking strength of MPC matrix decreases by 15.7, 16.8 and 10.9% with the *M/P* gradually increasing from 1.0 to 1.4.

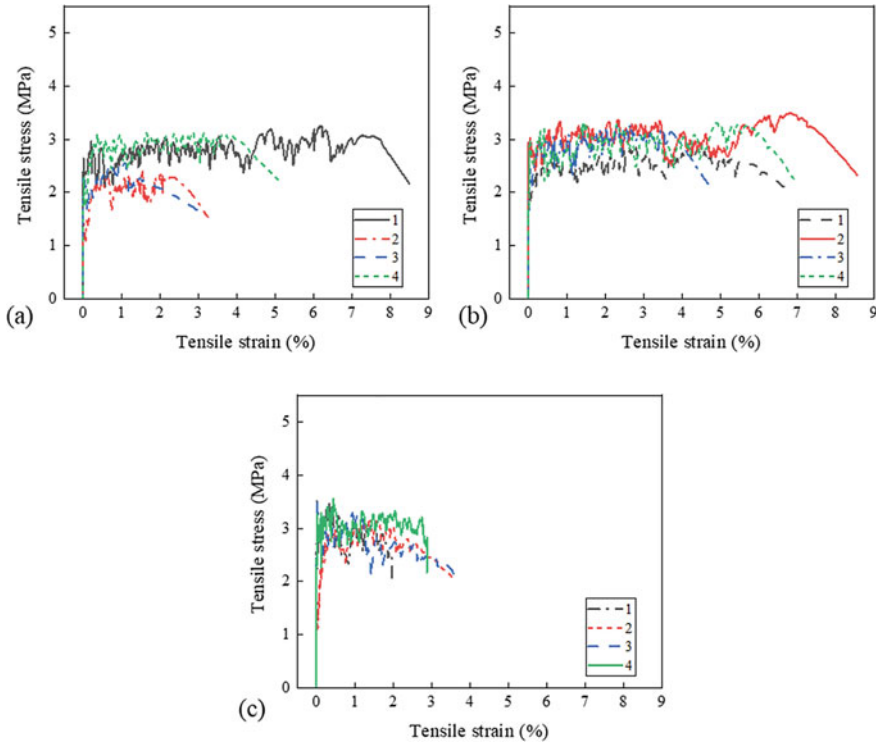

Fig. 4.10 Tensile stress–strain curves with $M/P = 1.4$ and Sd of **a** 80–120 mesh, **b** 150–180 mesh, and **c** 200 mesh

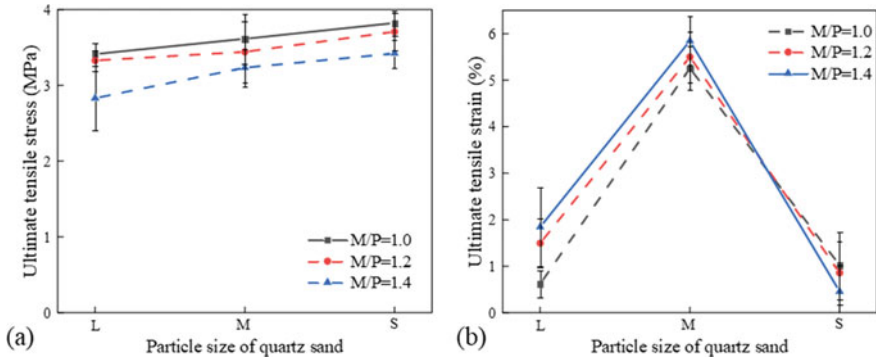

Fig. 4.11 The effect of *M/P* and Sd on **a** ultimate tensile stress and **b** ultimate tensile strain

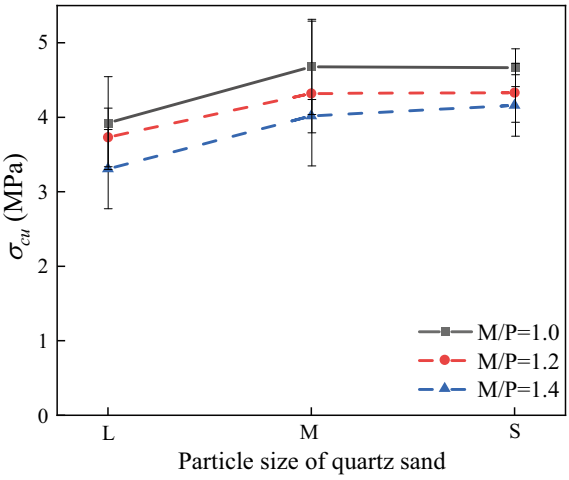

Fig. 4.12 The σ_{cu} of UHDMC with different Sd and *M/P*

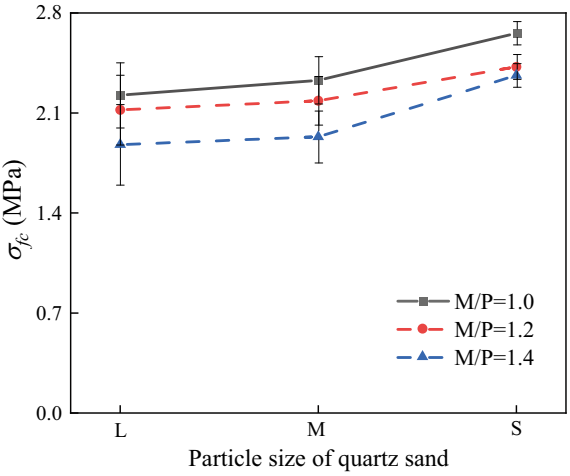

Fig. 4.13 The σ_{fc} of MPC matrix with different Sd and *M/P* ratios

Figure 4.14 shows the effect of Sd and *M/P* on fiber bridging complementary energy J_b'. It can be seen from the figure that when 150–180 mesh quartz sand is used, the fiber bridging complementary energy reaches the maximum values, 573.7, 621.9 and 715.3 J/m^2, at the *M/P* of 1.0, 1.2 and 1.4, respectively. The J_b' is related to the ductility of UHDMC and the σ_{cu}. Although the difference among the values of fiber bridging stress with different *M/P* and Sd is small, there is a significant difference in ductility. When 150–180 mesh quartz sand is used, the ultimate tensile strain corresponding to the *M/P* of 1.0, 1.2 and 1.4 can reaches 5.25, 5.49 and 5.85%, respectively. In addition, when the Sd is constant, the fiber bridging complementary energy shows an increasing trend with the increase of *M/P*, which is mainly due to

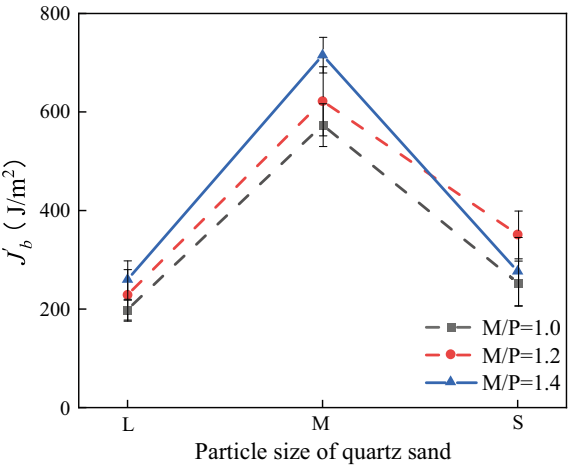

Fig. 4.14 The J_b' of UHDMC with different Sd and *M/P* ratios

that the effect of *M/P* on the ductility of UHDMC is greater than that on the tensile stress.

Figure 4.15 shows the effect of Sd and *M/P* on the elastic modulus of MPC matrix. When the *M/P* is constant, the elastic modulus increases first and then decreases with the Sd changing from 80 to 120 mesh to 200 mesh. When the *M/P* ratios are 1.0, 1.2 and 1.4, the MPC matrix with the Sd of 150–180 mesh has the maximum elastic modulus, 31.97, 31.70, and 27.41 GPa, respectively. In addition, when the Sd is 80–120 mesh, 150–180 mesh, and 200 mesh, respectively, the elastic modulus of MPC matrix gradually decreases with the increase of *M/P* from 1.0 to 1.4, decreased by 7.7, 14.3 and 18.2%, respectively, which is mainly because the elastic modulus is directly proportional to the tensile cracking strength, and the cracking strength decreases with increase of the *M/P* (see Fig. 4.13).

Figure 4.16 shows the effect of Sd and *M/P* on the fracture toughness K_m of MPC matrix. When the *M/P* ratios are 1.0, 1.2 and 1.4, the fracture toughness increases slightly by 13.2, 7.0 and 3.8%, respectively, with the Sd changing from 80 to 120 mesh to 200 mesh, which indicates that quartz sand with finer particle size has a more favorable effect on K_m. In addition, the K_m of the matrix increases first and then decreases with the increase of *M/P* from 1.0 to 1.4. When the particle sizes of the quartz sand are 80–120 mesh, 150–180 mesh and 200 mesh, the fracture toughness reach the maximum, 0.57, 0.61, and 0.61 MPa m$^{1/2}$, respectively, at the *M/P* of 1.2.

Figure 4.17 shows the effect of Sd and *M/P* on the fracture energy J_{tip} of MPC matrix. When the *M/P* ratios are 1.0, 1.2 and 1.4, the fracture energies of the matrix increase by 27.2, 48.1 and 23.7%, respectively, with the Sd changing from 80 to 120 mesh to 200 mesh, which shows that the Sd has a significant effect on the J_{tip}. In addition, when the Sd is constant, the J_{tip} increases first and then decreases with the increase of the *M/P*. When the quartz sand particle sizes are 80–120 mesh, 150–180 mesh and 200 mesh, respectively, the maximum fracture energies reach 15.31, 18.03 and 22.67 J/m^2, respectively, at the *M/P* of 1.2.

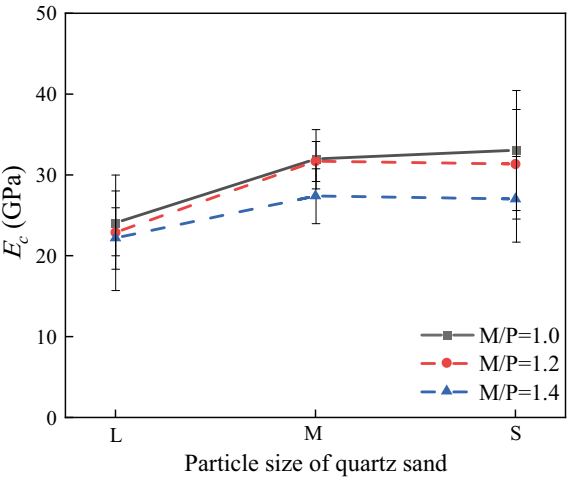

Fig. 4.15 The E_c of MPC matrix with different Sd and *M/P* ratios

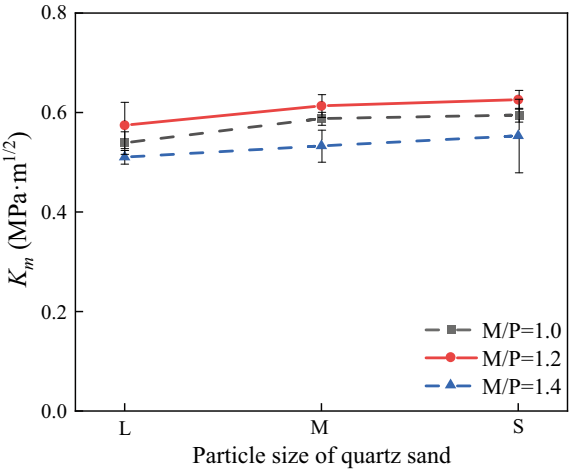

Fig. 4.16 The K_m of MPC matrix with different Sd and *M/P* ratios

Figure 4.18 shows the effect Sd and *M/P* on pseudo strain hardening indices (strength index PSH_σ and energy index PSH_J) of UHDMC. From Fig. 4.18a, when the Sd is constant, the *M/P* has little influence on the PSH_σ. When the *M/P* ratios are 1.0, 1.2 and 1.4, the PSH_σ increases first and then decreases with the change of quartz sand from 80 to 120 mesh to 200 mesh. When the Sd is 150–180 mesh, the strength index PSH_σ reaches the maximum.

From Fig. 4.18b, *M/P* and Sd both have a great influence on the PSH_J. When the *M/P* is constant, the PSH_J increases first and then decreases with the particle size of quartz sand changing from 80 to 120 mesh to 200 mesh. When the Sd is 150–180 mesh, the energy index reaches the maximum. The UHDMC with the Sd of 150–180 mesh shows good strain hardening performance. In addition, when the

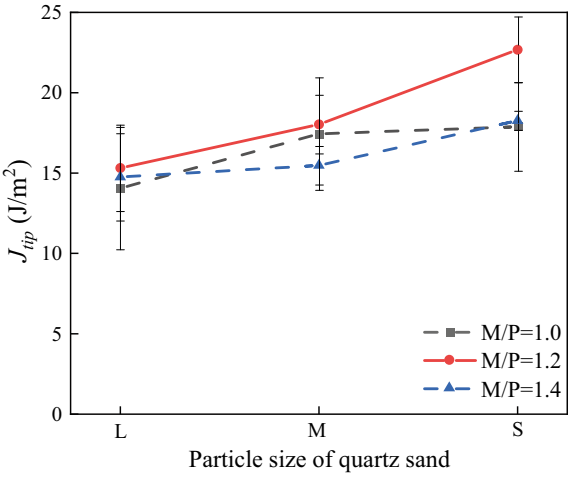

Fig. 4.17 The J_{tip} of MPC matrix with different Sd and *M/P* ratios

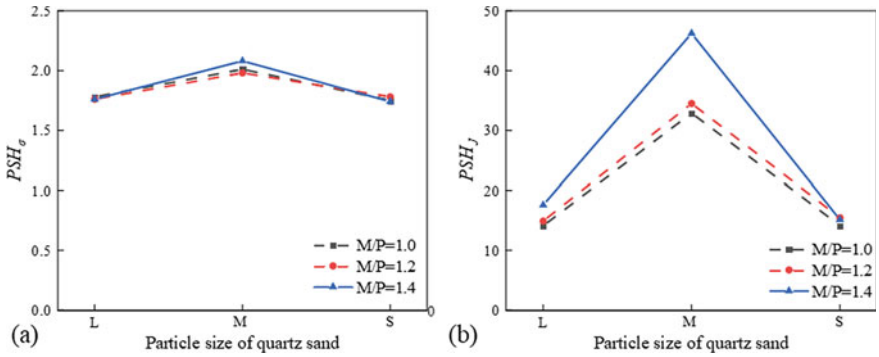

Fig. 4.18 **a** PSH_σ and **b** PSH_J of UHDMC with different Sd and *M/P* ratios

Sd are 80–120 mesh, 150–180 mesh and 200 mesh, respectively, the energy index increases by 24.5, 40.5 and 7.0%, respectively, with the increase of *M/P* from 1.0 to 1.4. Especially when the *M/P* is 1.4 and the Sd is 150–180 mesh, the energy index of UHDMC reaches 46.20, showing obvious strain hardening performance. Therefore, the *M/P* of 1.4 and the Sd of 150–180 mesh were selected to explore the effect of water–solid ratio and sand-binder ratio on UHDMC performance.

4.4.2 *Effects of W/S and S/B*

(1) **Compressive strength**

Figure 4.19 shows the effect of the *W/S* and *S/B* on the compressive strength of UHDMC. When the *S/B* are 0.1, 0.2, 0.3, and 0.4, the compressive strength decreases by 20.83, 17.46, 19.17 and 6.83 MPa, respectively, with the increase of the *W/S* from 0.12 to 0.16. This is because the free water content in MPC matrix will increase with the increase of *W/S*, which will result in the increase of porosity of MPC matrix (Qiao et al., 2010). When the *W/S* is constant, the compressive strength also decreases with the increase of the *S/B*. When the *W/S* is 0.12, the compressive strength decreases by 13.99 MPa with the increase of the *S/B* from 0.1 to 0.3, and when the *W/S* is 0.14 and 0.16, the compressive strength decreases by 14.16 and 12.82 MPa with the *S/B* increases from 0.1 to 0.4, respectively, which is because the quartz sand has a relatively larger particle size than the MPC, higher content of quartz sand will lead to higher porosity (Feng et al., 2021b). On the other hand, large quartz sand content will lead to a significant decrease in fluidity of the MPC matrix (Feng et al., 2021a), which leads to that fibers cannot be uniformly distributed, impairing the strength of the UHDMC. In addition, the compressive strength of the UHDMC with the *W/S* of 0.12 and *S/B* of 0.4 is missing, which is due to poor workability of the UHDMC resulting from low water content and high quartz sand content.

(2) **Tensile properties**

Figures 4.20, 4.21 and 4.22 show the tensile stress–strain curves of UHDMC with different *W/S* and *S/B*. When the *W/S* is 0.12, the UHDMC with the *S/B* of 0.1, 0.2, 0.3 or 0.4, respectively, exhibits poor strain hardening performance. While when the *W/S* is 0.14 or 0.16, the UHDMC with the *S/B* of 0.1, 0.2, 0.3 or 0.4, respectively, shows

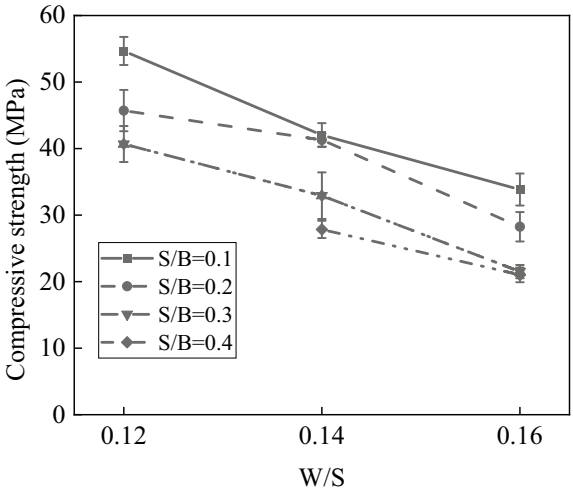

Fig. 4.19 Compressive strength of UHDMC with different *W/S* and *S/B*

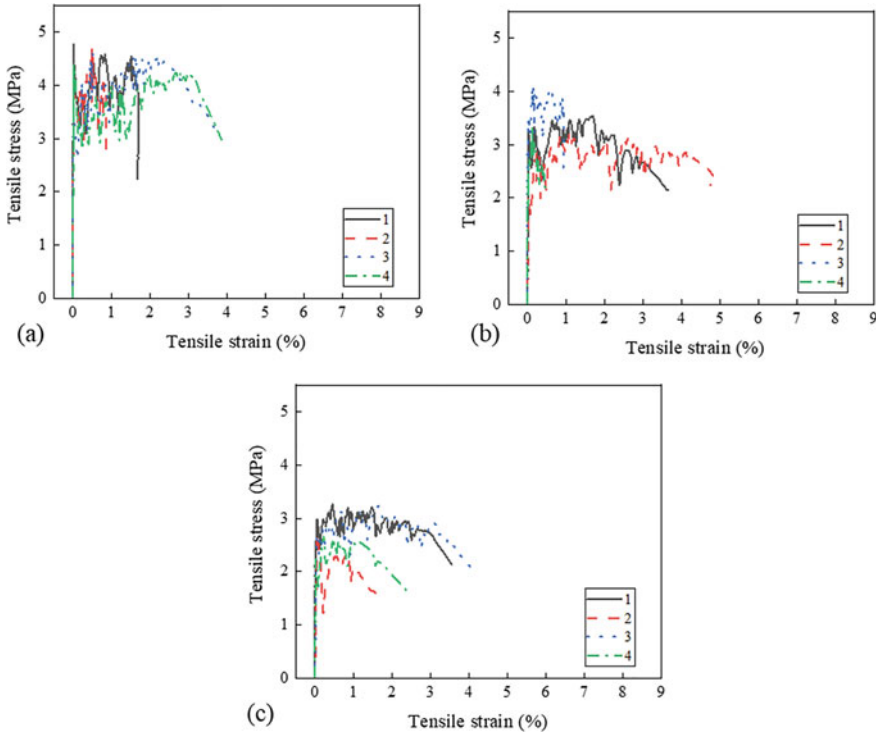

Fig. 4.20 Tensile stress–strain curves with *W/B* of 0.12 and *S/B* of **a** 0.1, **b** 0.2, and **c** 0.3

good strain hardening performance and excellent ductility properties. In addition, when the *W/S* is constant, the change of strain hardening performance is not obvious with the change of *S/B* from 0.1 to 0.4.

Figure 4.23 shows the effect of the *W/S* and *S/B* on the ultimate tensile stress and ultimate tensile strain of UHDMC. From Fig. 4.23a, when the *S/B* is 0.1, 0.2, and 0.3, the ultimate tensile strength decreases by 58.6, 43.4 and 17.8% with the increase of the *W/S* from 0.12 to 0.16, respectively. And when the *S/B* is 0.4, the ultimate tensile stress also slightly decreases with the increase of the *W/S* from 0.14 to 0.16. This is due to that the increase of the *W/S* leads to the increase of the porosity of MPC matrix (Qiao et al., 2010) and then decreases the adhesion between the fiber and the matrix. When the *W/S* is 0.12, 0.14 and 0.16, the ultimate tensile stress decreases by 87.0, 58.5 and 16.5% with the *S/B* increases from 0.1 to 0.3 or 0.4, respectively. This is because the quartz sand has a relatively larger particle size, and large content of quartz sand will increase the porosity of the matrix, thus reducing the bond strength between the fibers and the matrix (Feng et al., 2021b). Furthermore, the increase of the *S/B* will significantly reduce the fluidity of the UHDMC (Feng et al., 2021a), which will lead to that the fibers cannot be uniformly distributed in the matrix, impairing the ultimate tensile stress of the UHDMC.

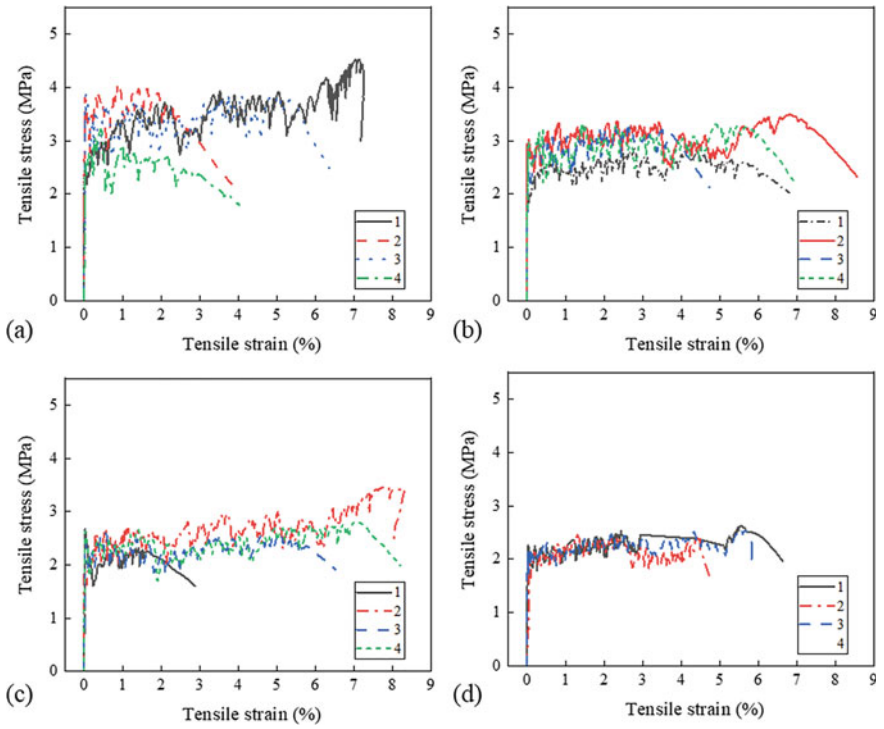

Fig. 4.21 Tensile stress–strain curves with *W/B* of 0.14 and *S/B* of **a** 0.1, **b** 0.2, **c** 0.3, and **d** 0.4

From Fig. 4.23b, when the *S/B* is constant, the ultimate tensile strain of UHDMC increases first and then decreases with the increase of *W/S* from 0.12 to 0.16. When the *S/B* is 0.1, 0.2, 0.3 and 0.4, and the *W/S* is 0.14, the maximum ultimate tensile strain reaches 5.71, 5.84, 7.46 and 5.56%, respectively. When the specimen of UHDMC is failure, there are two cases of fiber breaking and pulling out. When the ultimate tensile strength is large, the fiber is pulled off, and the ultimate tensile is only the fiber tensile deformation. However, when the fiber is pulled out, the ultimate tensile includes fiber slip and tensile deformation. Therefore, when the number of fibers pulled out is relatively large, UHDMC will have a larger ultimate tensile strain. However, when the *W/S* is large (e.g. 0.16), the porosity will increase, the bond strength between the matrix and the fibers will be reduced (Qiao et al., 2010), which will also lead to premature failure of the specimen, thereby reducing the ultimate tensile strain. Therefore, the UHDMC with the *W/S* of 0.14 has significant strain hardening performance. When the *W/S* is constant, the ultimate tensile strain also increases first and then decreases with the increase of the *S/B*. However, when the *W/S* is greater than 0.14 (including 0.14 and 0.16) and the *S/B* is 0.1, 0.2, 0.3 and 0.4, respectively, the UHDMC shows large ultimate tensile strain.

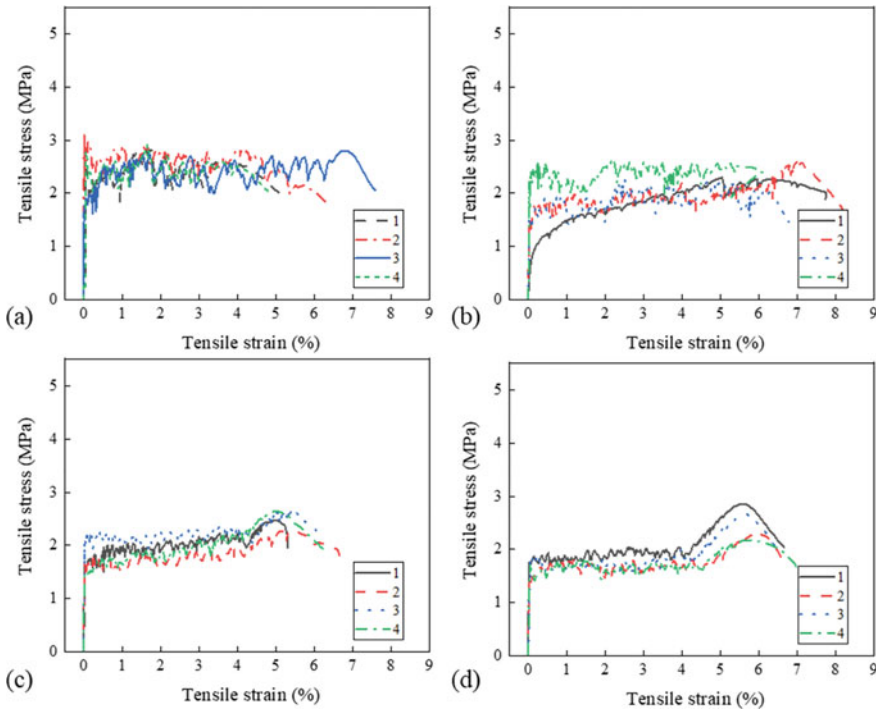

Fig. 4.22 Tensile stress–strain curves with *W/B* of 0.16 and *S/B* of **a** 0.1, **b** 0.2, **c** 0.3, and **d** 0.4

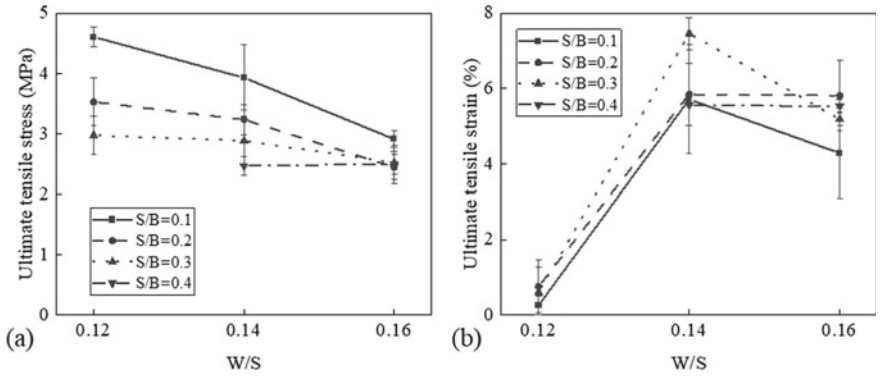

Fig. 4.23 The effect of *W/S* and *S/B* on **a** ultimate tensile stress and **b** ultimate tensile strain

(3) **Micromechanical indices**

Figure 4.24 shows the effect of *W/S* and *S/B* on fiber bridging stress capacity. When the *S/B* is 0.1, 0.2 and 0.3, the fiber bridging stress decreases by 32.4, 27.1 and 24.6%, respectively, with the *W/S* gradually increases from 0.12 to 0.16. And when the *S/B*

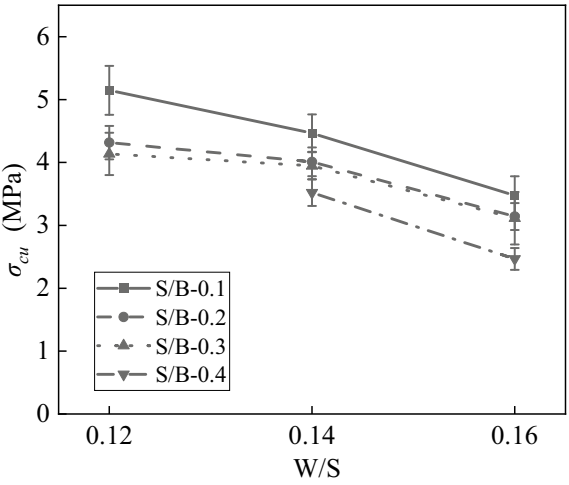

Fig. 4.24 The σ_{cu} of UHDMC with different *W/S* and *S/B*

is 0.4, the fiber bridging stress decreases by 30.1% with the *W/S* gradually increases from 0.14 to 0.16. This is mainly due to that the increase of the *W/S* will lead to the increase of the porosity of the MPC matrix and the decrease of the compactness, thus reducing the σ_{cu}. In addition, when the *W/S* is constant, the σ_{cu} also gradually decreases with the increase of the *S/B*. When the *W/S* is 0.12, the fiber bridging stress decreases by 19.6% with the *S/B* increasing from 0.1 to 0.3. And when the *W/S* is 0.14 and 0.16, the fiber bridging stress decreases by 21.1 and 29.1%, respectively, with the *S/B* increasing from 0.1 to 0.4. This is because the increase of the *S/B* will dilute the cementitious material, it will have an adverse effect on the fiber bridging stress.

Figure 4.25 shows the effect of *W/S* and *S/B* on the tensile cracking strength of MPC matrix. When the *S/B* is 0.1, 0.2 and 0.3, the cracking strength decreases by 24.4, 44.3 and 53.0%, respectively, with the *W/S* increasing from 0.12 to 0.16. And when the *S/B* is 0.4, the cracking strength of the MPC matrix decreases by 21.2% with the *W/S* increasing from 0.14 to 0.16. This indicates that the increase of *W/S* will also adversely affect the σ_{fc}. In addition, when the *W/S* is 0.12 and 0.14, the σ_{fc} increases first and then decreases with the increase of the *W/S*. When the *S/B* is 0.3, the cracking strength reaches the maximum of 2.54 and 2.15 MPa respectively. However, when the *W/S* is 0.16, the cracking strength reaches the maximum of 1.85 MPa when the *S/B* is 0.1, which is because the higher *W/S* will lead to larger porosity, and the increase of *S/B* also has the effect (Feng et al., 2021b). Therefore, when the *W/S* is 0.16, the cracking strength decreases with the increase of *S/B*.

Figure 4.26 shows the effect of *W/S* and *S/B* on fiber bridging complementary energy J_b'. It can be seen from the figure that when the *S/B* is constant, the J_b' first increases and then decreases with the increase of the *W/S* from 0.12 to 0.16. When the *W/S* is 0.14, the J_b' reaches the maximum of 513.5, 715.3, 561.1 and 418.5 J/m^2, respectively. In addition, when the *W/S* is constant, the J_b' also first increases and

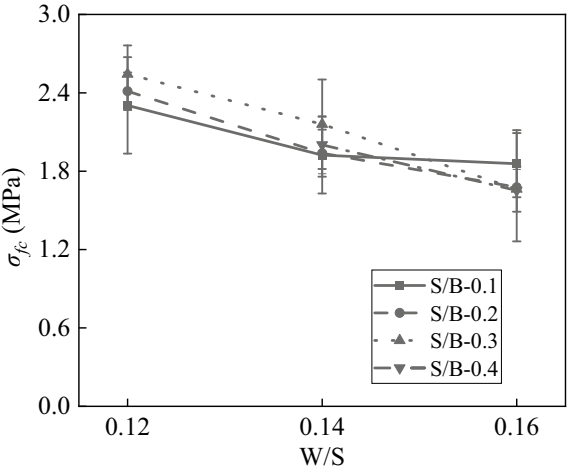

Fig. 4.25 The σ_{fc} of MPC matrix with different *W/S* and *S/B*

then decreases with the increase of the *S/B*. When the *S/B* is 0.2, the J_b' reaches the maximum. Especially for the UHDMC with the *W/S* of 0.14 and the *S/B* of 0.2, the J_b' can reach 715.3 J/m^2, which is due to that the J_b' is related to fiber bridging stress and ductility of UHDMC, when the *S/B* is 0.2 and the *W/S* is 0.14, the high fiber bridging stress and good ductility are obtained.

Figure 4.27 shows the effect of *W/S* and *S/B* on the elastic modulus of MPC matrix. When the *S/B* is 0.1, 0.2 and 0.3, the elastic modulus of MPC matrix gradually decreases by 59.3, 77.0, 48.2%, respectively, with the increase of the *W/S* from 0.12 to 0.16. And when the *S/B* is 0.4, the elastic modulus of MPC matrix decreases by 46.1% with the increase of the *W/S* from 0.14 to 0.16. In addition, when the *W/S* is 0.12 and 0.14, the elastic modulus increases first and then decreases with the increase

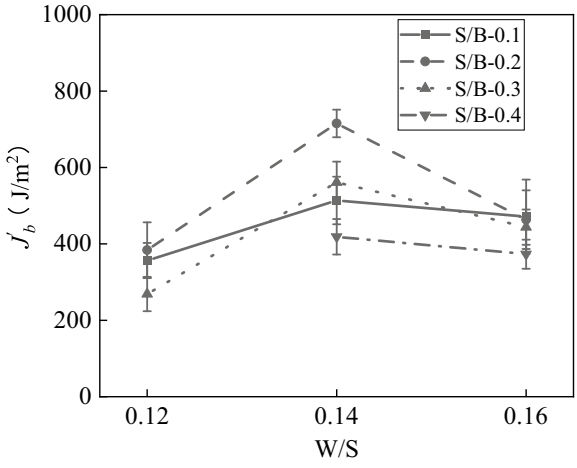

Fig. 4.26 The J_b' of UHDMC with different *W/S* and *S/B*

of the *S/B*. When the *S/B* was 0.2, the elastic modulus reaches the maximum of 27.95 and 27.41 J/m^2, respectively. When the *W/S* is 0.16, the elastic modulus gradually decreases with the increase of the *S/B* from 0.1 to 0.4.

Figure 4.28 shows the effect of *W/S* and *S/B* on the fracture toughness (K_m) of MPC matrix. When the *S/B* is 0.1, 0.2 and 0.3, the fracture toughness of MPC matrix gradually decreases by 18.1, 25 and17.0%, respectively, with the increase of the *W/S* from 0.12 to 0.16. And when the *S/B* is 0.4, the fracture toughness of MPC matrix decreases by 31.8% with the increase of the *W/S* from 0.14 to 0.16. In addition, when the *W/S* is constant, the K_m of the MPC matrix also decreases with the increase of the *S/B*.

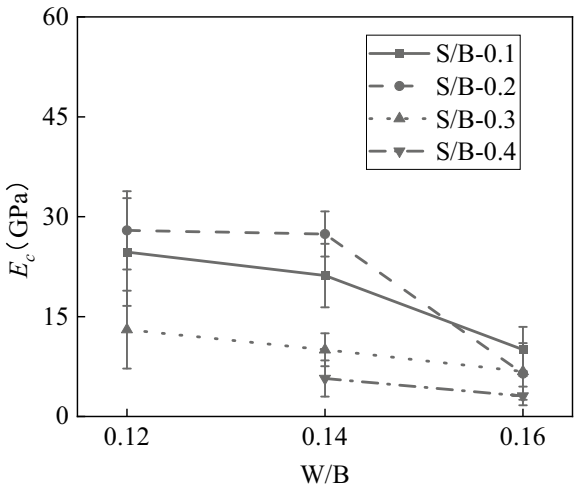

Fig. 4.27 The E_c of MPC matrix with different *W/S* and *S/B*

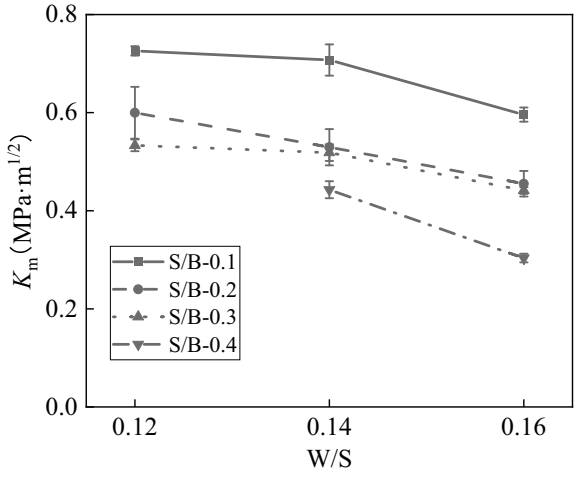

Fig. 4.28 The K_m of MPC matrix with different *W/S* and *S/B*

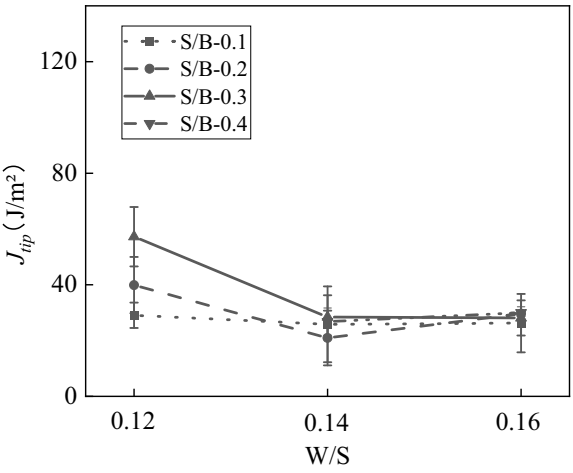

Fig. 4.29 The J_{tip} of MPC matrix with different *W/S* and *S/B*

Figure 4.29 shows the effect of *W/S* and *S/B* on the fracture energy (J_{tip}) of MPC matrix. When the *S/B* is 0.1, 0.2 and 0.3, the fracture energy firstly decreases and then slightly increases with the increase of the *W/S* from 0.12 to 0.16. And when the *S/B* is 0.4, the fracture energy of MPC matrix also increases with the increase of the *W/S* from 0.14 to 0.16. In addition, when the *W/S* is 0.12, the fracture energy of MPC matrix gradually increases by 44.5% with the increase of the *S/B* from 0.1 to 0.3. When the *W/S* is 0.14 and 0.16, respectively, the matrix fracture energy is almost unchanged with the increase of the *S/B*. The change of fracture energy is caused by the change of elastic modulus and fracture toughness. The J_{tip} is proportional to the fracture toughness and inversely proportional to the elastic modulus.

Figure 4.30a, b show the effect of *W/S* and *S/B* on pseudo strain hardening indices of UHDMC. From Fig. 4.30a, when the *S/B* is 0.1, 0.2, 0.3 and 0.4, the PSH_σ increases with the *W/S* increases from 0.12 to 0.14, while it decreases with the *W/S* increases from 0.14 to 0.16. The maximum PSH_σ are 2.32, 2.07, 1.83 and 1.76, respectively. However, when the *W/S* is 0.12, PSH_σ shows a gradually decreasing trend with the increase of the *S/B* from 0.1 to 0.3, decreased by 27.4%. when the *W/S* is 0.14 and 0.16, PSH_σ decreases by 24.1 and 20.3%, respectively, with the increase of the *S/B* from 0.1 to 0.4. From Fig. 4.30b, when the *S/B* is constant, the PSH_J first increases and then decreases with the increase of the *W/S* from 0.12 to 0.16. And when the *W/S* is constant, the PSH_J also first increases and then decreases with the increase of the *S/B*. Especially when the *S/B* is 0.2 and the *W/S* is 0.14, the PSH_J reaches 46.14, which also corresponds to the good strain hardening performance.

In addition, from Fig. 4.30a, when the *W/S* is 0.12, the PSH_σ is relatively large, but the axial tensile specimens do not show good strain hardening performance, which indicates that UHDMC needs to have high PSH_σ and PSH_J at the same time to show good strain hardening performance. Through comprehensive evaluation of strain hardening performance, compressive strength and pseudo strain hardening

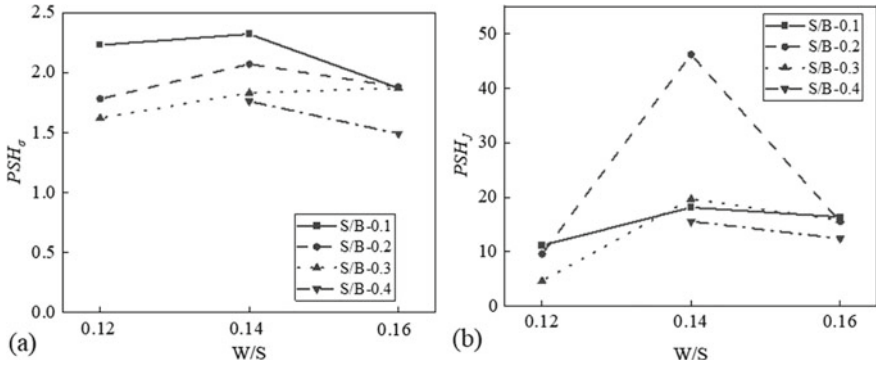

Fig. 4.30 **a** PSH_σ and **b** PSH_J of UHDMC with different *W/S* and *S/B*

indices, the *W/S* of 0.14 and *S/B* of 0.2 were used to explore the effect of FA content on UHDMC properties.

4.4.3 Effect of Fly Ash (FA) Content

(1) **Compressive strength**

Figure 4.31 show the effect of FA content on the compressive strength of UHDMC. The compressive strength increases first and then slightly decreases with the increase of FA content, and reaches the maximum value of 41.28 MPa when the FA content is 30%. This shows that the appropriate content of FA is helpful to the improve the compressive strength, while the excessive FA content will have an adverse effect. The compressive strength increases by 9.2% with the increase of FA content from 0 to 30%, which is due to the addition of appropriate FA content, the particles of FA can fill the cracks and pores to obtain a denser MPC matrix (Li & Feng, 2011), resulting in the improvement of the compressive strength. While when the FA content increases from 30 to 40%, the compressive strength of UHDMC slightly decreases by 3.3%, which is because the high FA content leads to the decrease of internal adhesion of MPC hydration products, resulting in a decrease in compressive strength (Lei et al., 2019).

(2) **Tensile properties**

Figure 4.32 show the tensile stress–strain curves of UHDMC with different FA content. The strain hardening performance of UHDMC was significantly improved with the increase of FA content from 0 to 40%. When the FA content is 0, 10 and 20%, the strain hardening performance is not significant, however, the strain hardening performance is particularly obvious when the FA content is 30 and 40%.

Figures4.33a, b show the effect of FA content on ultimate tensile stress and ultimate tensile strain. From Fig. 4.33a, with the increase of fly ash content from 0

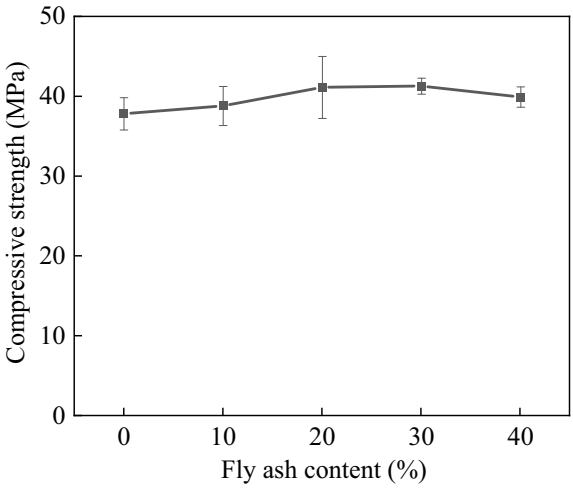

Fig. 4.31 Compressive strength of UHDMC with different FA contents

to 40%, the ultimate tensile stress decreases first and then increases. The ultimate tensile stress is reduced by 31.9% with the increase of fly ash content from 0 to 30%. And when the fly ash content increases from 30 to 40%, it increases by 32.5%. Based on previous research, Some scholars believe that FA is an inert filling material (Bilginer & Erdogan, 2021; Shao et al., 2017), but some scholars believe that FA will participate in the hydration reaction of MPC to generate new gelling (Li & Feng, 2011; Provis et al., 2015). Therefore, combined with the experimental results of this Chapter, it is considered that when the content of FA is relatively small, FA mainly plays an inert filling role, which can enhance the density of MPC matrix. However, the incorporation of fly ash leads to a relative decrease of cement content, thus reducing the bonding properties between fiber and matrix. However, when the FA content is 40%, due to the large content of fly ash, More fly ash components (e.g. Al_2O_3 and SiO_2) participate in the hydration reaction and generate new gelling (e.g. $MgSiO_3$) (Feng et al., 2022c), therefore, the bonding properties between fiber and matrix is improved. From Fig. 4.33b, with the increase of fly ash content from 0 to 40%, the ultimate tensile strain increases from 1.87 to 5.98%, which shows that the increase of FA content has obvious influence on the ultimate tensile strain of UHDMC.

(3) **Micromechanical indices**

Figure 4.34 show the effect of FA content on the σ_{cu}. With the increase of fly ash content from 0 to 40%, the fiber bridging stress capacity first decreases and then increases. The fiber bridging stress capacity gradually decreased by 27.9% with the FA content increased from 0 to 30%. However, when the FA content increased from 30 to 40%, the fiber bridging stress capacity increased by 28.7%.

Figure 4.35 shows the effect of FA content on the σ_{fc} of MPC matrix. The σ_{fc} decreases by 40.6% with the increase of FA content from 0 to 40%, which is because

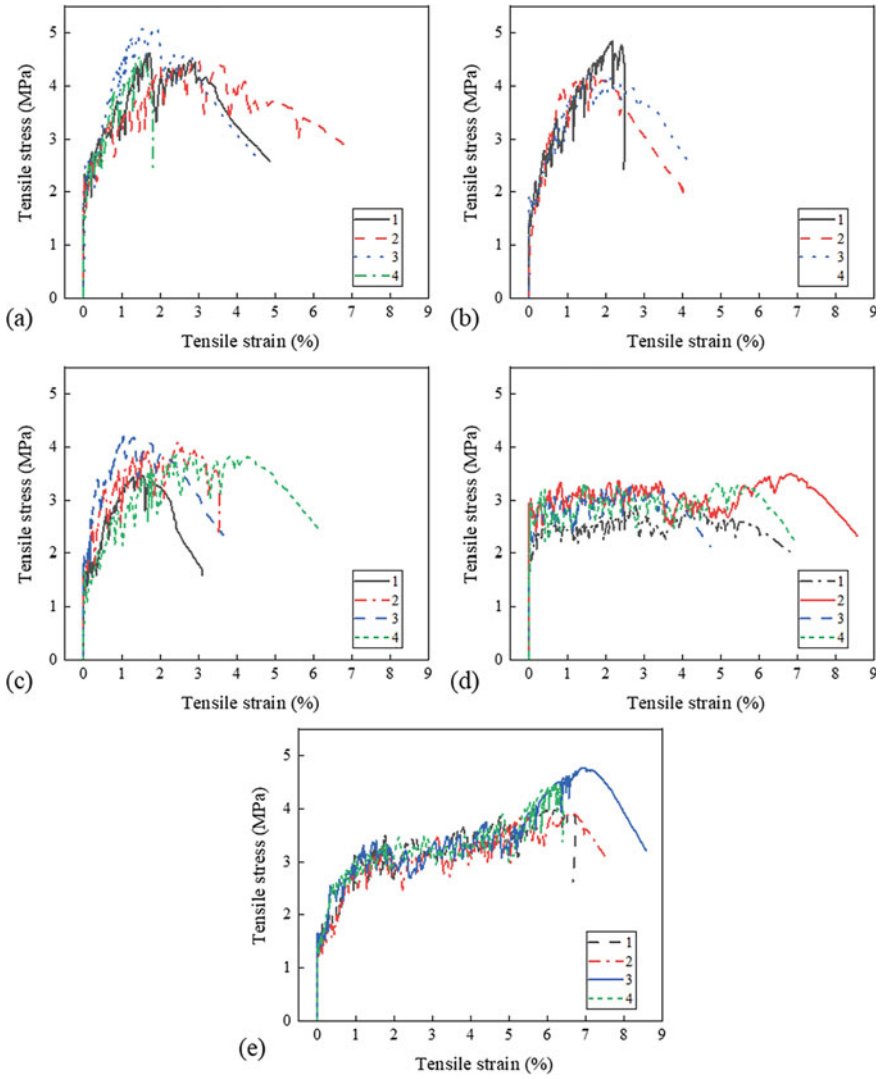

Fig. 4.32 Tensile stress–strain curves with FA content of **a** 0%, **b** 10%, **c** 20%, **d** 30%, and **e** 40%

that micro-aggregate filling effect is the main function of mineral admixtures (Zheng et al., 2016). Furthermore, the reaction system can be diluted by FA content, resulting in a decrease of the σ_{fc}.

Figure 4.36 shows the effect of FA content on the J_b'. The J_b' generally increases with the increase of FA content, which is because the J_b' is related to the maximum bridging stress of the fiber and the ductility of the material. Although the UHDMC with 30% fly ash content has a relatively low bridging stress, it has a good ductility (see Fig. 4.32), so it also has a high J_b'. In addition, the J_b' increased by 81.6% with

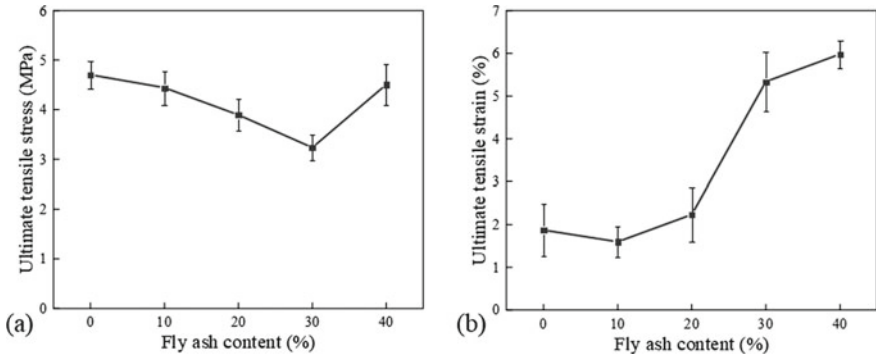

Fig. 4.33 The effect of FA content on **a** ultimate tensile stress and **b** ultimate tensile strain

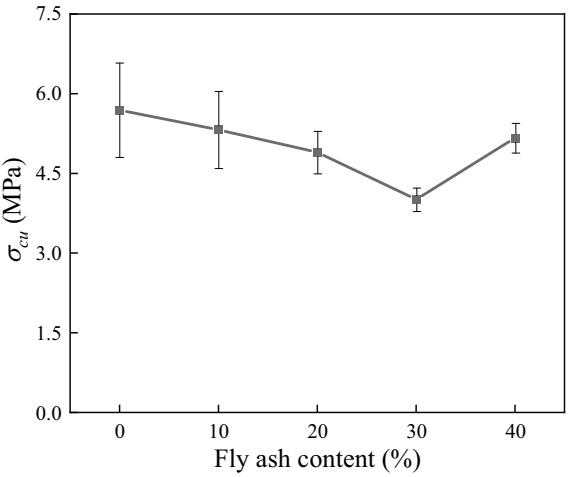

Fig. 4.34 The σ_{cu} of UHDMC with different FA content

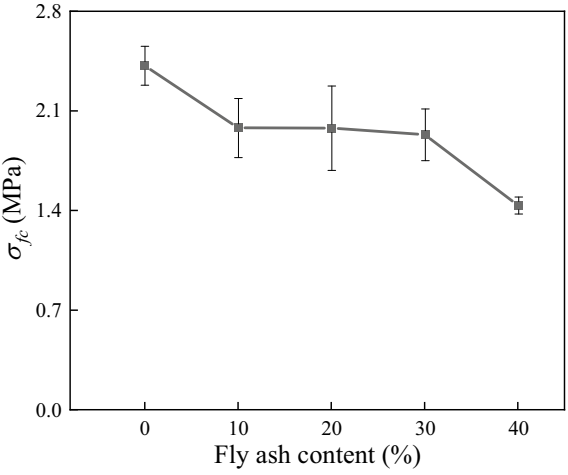

Fig. 4.35 The σ_{fc} of MPC matrix with different FA content

the increase of FA from 0 to 40%, which indicates that the UHDMC with the fly ash of 40% content has a good ability to absorb energy under load.

Figure 4.37 shows the effect of FA content on the E_c of MPC matrix. When the FA content is 10%, the elastic modulus is lower than that of the group without FA, decreasing by 28.6%. When the FA content increases from 10 to 30%, the elastic modulus increases significantly, increasing by 172.9%, while the elastic modulus of MPC matrix decreases by 21.7% with the FA content increasing from 30 to 40%.

Figure 4.38 shows the effect of FA content on the K_m of MPC matrix. With the increase of FA content from 0 to 40%, the K_m increases first and then decreases. When the fly ash content is 20%, the K_m of MPC matrix reaches the maximum, which is 0.64MPa $m^{1/2}$.

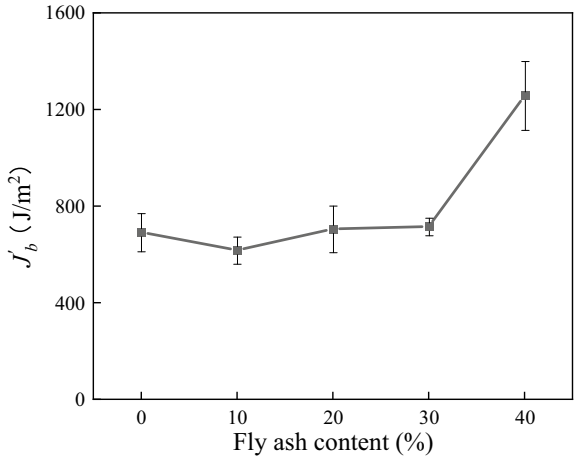

Fig. 4.36 The J_b' of UHDMC with different FA content

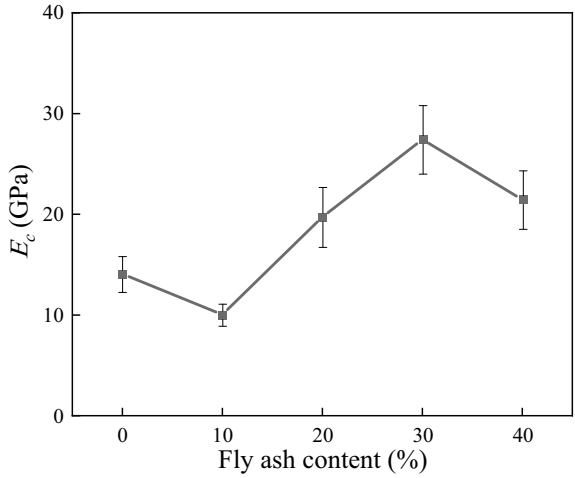

Fig. 4.37 The E_c of MPC matrix with different FA content

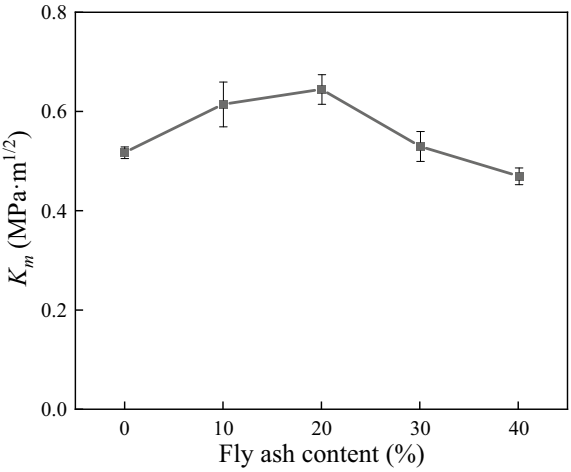

Fig. 4.38 The K_m of MPC matrix with different FA content

Figure 4.39 shows the effect of FA content on the fracture energy J_{tip} of MPC matrix. The fracture energy increases first and then decreases with the increase of fly ash content from 0 to 40%. When increase of FA content from 0 to 10%, the fracture energy reaches the maximum of 41.84 J/m^2, increased by 53.1% compared with the MPC matrix without FA. However, when the FA content exceeds 10%, the fracture energy decreases by 53.4% with the FA content increases from 10 to 40%. This shows that the fracture toughness can be improved by the appropriate content of FA, while the excessive content of FA (more than 10%) will have adverse effects.

Figures 4.40a, b show the effect of FA content on the pseudo strain hardening indices. From Fig. 4.40a, the PSH_σ of UHDMC with different FA content is greater than that of the group without FA except that the FA content is 30%. The PSH_σ

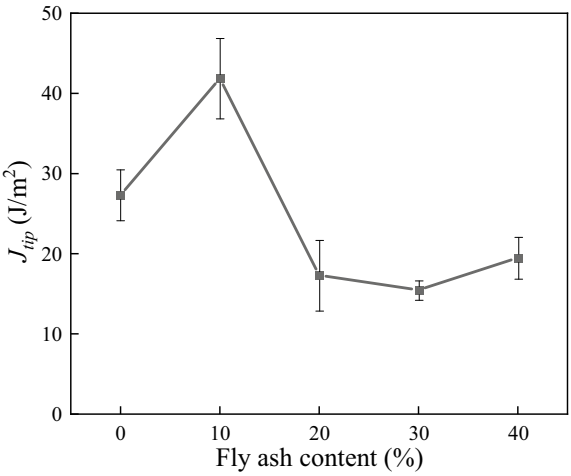

Fig. 4.39 The J_{tip} of MPC matrix with different FA content

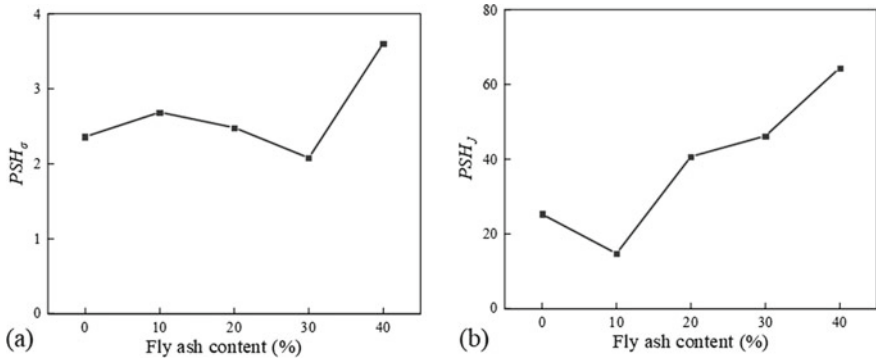

Fig. 4.40 **a** PSH_σ and **b** PSH_J of UHDMC with different FA content

reaches the maximum of 3.61 when the FA content is 40%. From Fig. 4.40b, except for the FA content of 10%, the energy index PSH_J of UHDMC with different FA content is greater than that of the group without FA. And the energy index of UHDMC increases by 58.3% with the increase of FA content from 20 to 40%. In addition, when the FA content is less than 20%, the energy index is relatively small, although the strength index is large, UHDMC still does not show obvious strain hardening performance, which also shows that good strain hardening performance requires a large strength index and energy index at the same time. In summary, when the FA content is 40%, the UHDMC has a good performance, so the FA content of 40% is adopted to continue to explore the influence of fiber content. When exploring the effect of fiber content on UHDMC, the same MPC matrix of the UHDMC with FA content of 40% is used, so the properties of the MPC matrix is no longer repeated discussion in the section.

4.4.4 Effect of Fiber Content

(1) **Compressive strength**

Figure 4.41 shows the effect of fiber content on the compressive strength of UHDMC. The compressive strength gradually increases with the increase of fiber content, increasing 19.7% with increase of the fiber content from 1.2 to 2.0%. This is due to the presence of fiber will limit the development of internal cracks.

(2) **Tensile properties**

Figure 4.42 shows the tensile stress–strain curves of UHDMC with different fiber content. When the fiber content is 1.2%, the strain hardening performance is not significant. However, when the fiber content is 1.4% or above, the UHDMC shows obvious strain hardening performance. And with the increase of fiber content from 1.2 to 2.0%, the strain hardening performance became more obvious.

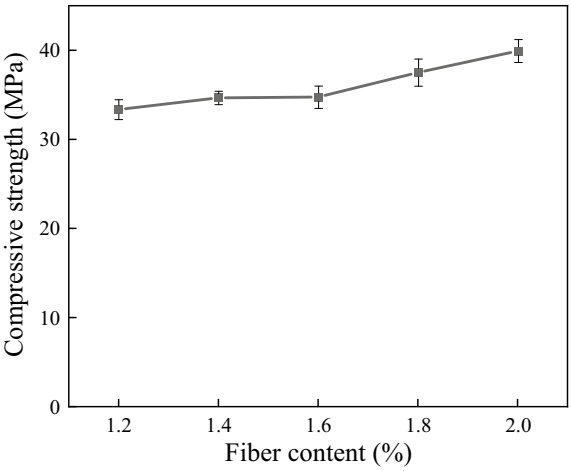

Fig. 4.41 Compressive strength of UHDMC with different fiber content

Figures 4.43a, b show the effect of fiber content on the ultimate tensile stress and ultimate tensile strain of UHDMC. From Fig. 4.43a, the ultimate tensile stress increases by 52.0% with the increase of fiber content from 1.2 to 2.0%, which is due to that the increase of fiber content leads to the increase of the number of bridging fibers at the crack of the specimen, improving fiber bridging ability. In addition, From Fig. 4.43b, with the fiber content increases from 1.2 to 2.0%, the ultimate tensile strain increases from 2.67 to 6.53%, which is also caused by the increase of fibers at the crack interface. This makes the UHDMC specimens after matrix cracking still have large deformation capacity under large tensile load.

(3) **Micromechanical indices**

Figures 4.44a, b show the effect of fiber content on the σ_{cu} and J_b'. From Fig. 4.44a, with the fiber content increases from 1.2 to 2.0%, the σ_{cu} by 102.3%. In addition, From Fig. 4.44b, with the increase of fiber content from 1.2 to 2.0%, the J_b' increases from 426.7 to 1256.4 J/m^2.

Figure 4.45a, b show the effect of fiber content on the pseudo strain hardening indices. From Fig. 4.45a, with the fiber content increases from 1.2 to 2.0%, PSH_σ increases from 1.78 to 3.61. In addition, from Fig. 4.45b, PSH_J increases from 21.88 to 64.35 with the increase of fiber content from 1.2 to 2.0%. This also meets well with the situation that with the increase of fiber content strain hardening performance become more significant. So far, a UHDMC ratio with stable and significant strain hardening performance has been obtained, which is included *M/P* of 1.4, Sd of 150–180 mesh, *S/B* of 0.2, *W/S* of 0.14, FA content of 40%, and fiber content of 2.0%. Then, the effects of curing temperature and curing age on UHDMC with the ratio were tested.

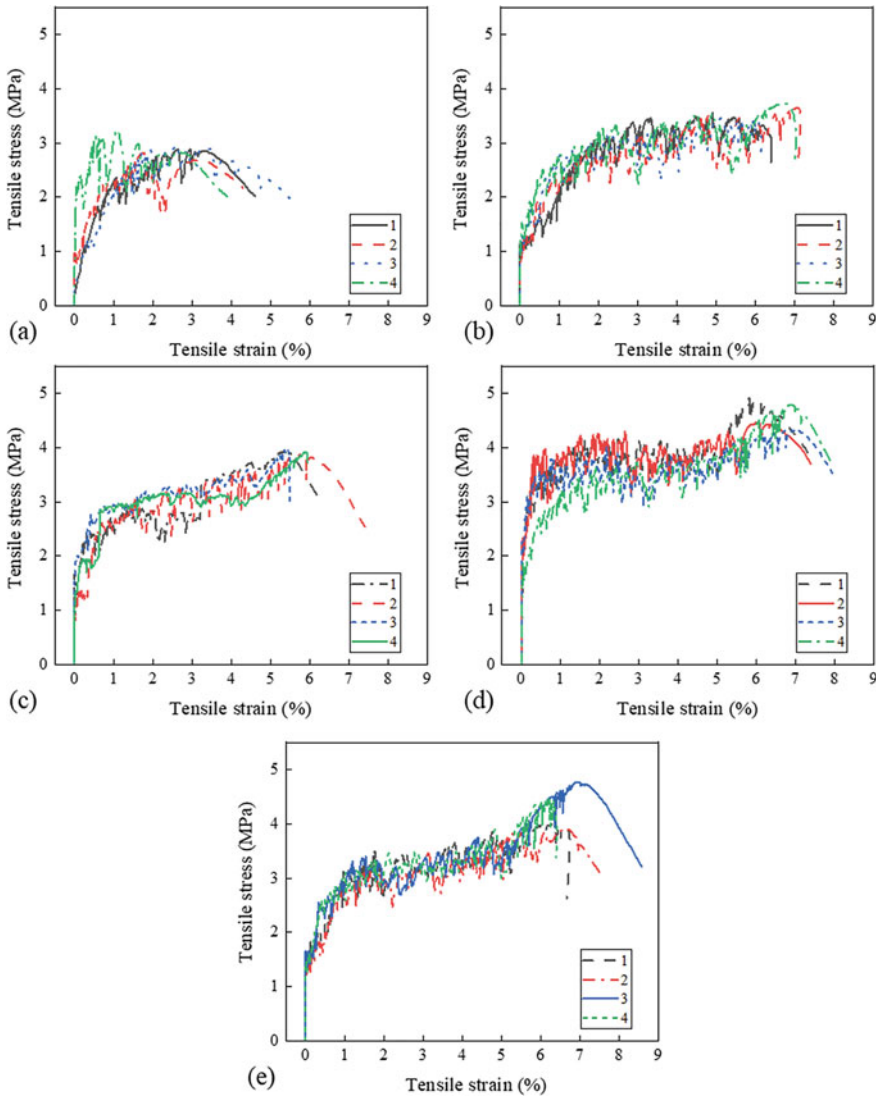

Fig. 4.42 Tensile stress–strain curve with fiber content of **a** 1.2%, **b** 1.4%, **c** 1.6%, **d** 1.8%, **e** 2.0%

4.4.5 Effect of Curing Temperature

(1) **Compressive strength**

Figure 4.46 shows the effect of curing temperatures on the compressive strength of UHDMC. The compressive strength decreases from 39.9 to 19.0 MPa with the

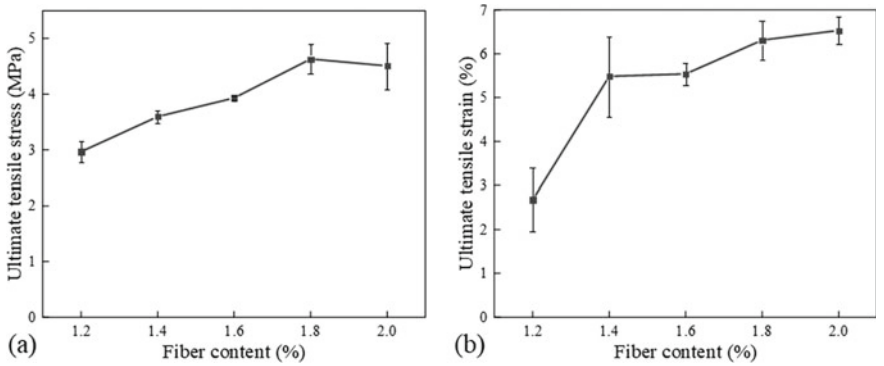

Fig. 4.43 The effect of fiber content on **a** ultimate tensile stress and **b** ultimate tensile strain

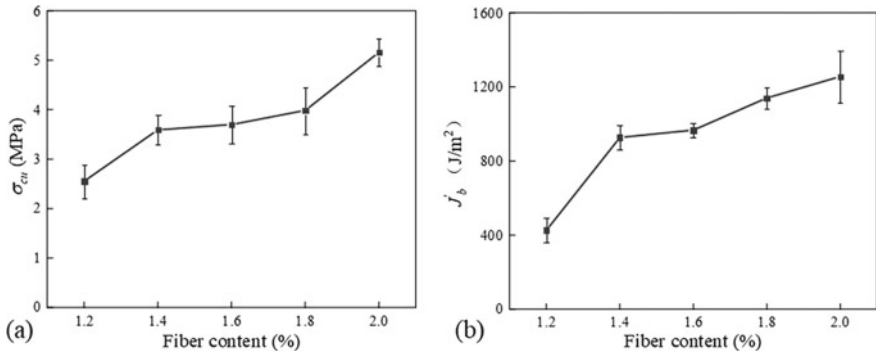

Fig. 4.44 The effect of fiber content on **a** σ_{cu} and **b** J_b'

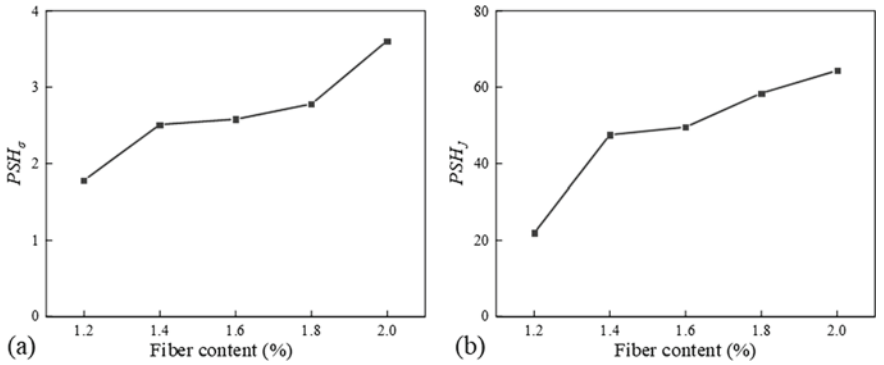

Fig. 4.45 **a** PSH_σ and **b** PSH_J of UHDMC with different fiber content

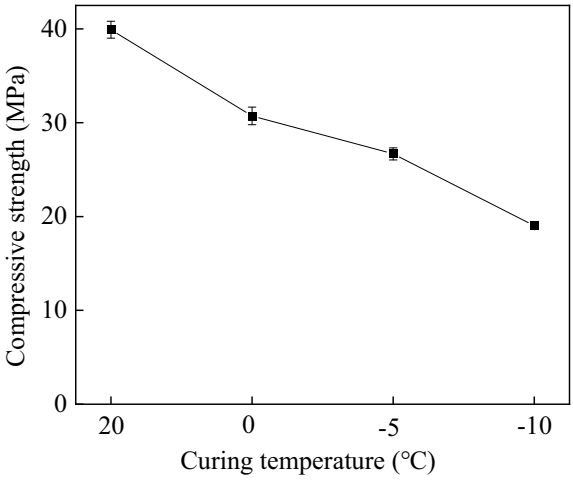

Fig. 4.46 Compressive strength of UHDMC at different curing temperature

temperature decreases from 20 to −10 °C. This is because the decrease of temperature reduces the activity of the material, resulting in a decrease in the degree of hydration, which in turn leads to a decrease in compressive strength. Despite this, the compressive strength can still reach 19.0 MPa after curing 7 days of at −10 °C.

(2) **Tensile properties**

Figure 4.47 shows the tensile stress–strain curves of UHDMC at different curing temperature. From the figure, under low-temperature curing, the UHDMC still have good strain hardening performance.

Figure 4.48a, b show the effect of curing temperature on ultimate tensile stress and ultimate tensile strain. From Fig. 4.48a, the ultimate tensile strength decreases by 61.8% with the decrease of the curing temperature from 20 to −10 °C. There are two main reasons, one of which is that the free water in the pores of UHDMC matrix froze and expanded, then leading to internal microcrack, and the other is that the needle-like $MgKPO_4 \cdot 6H_2O$ (MKP) crystals precipitated under low-temperature conditions, which could grow in the capillary pores and microcracks of the MPC matrix (Hai-He et al., 2014). In addition, from Fig. 4.48b, when the curing temperature is reduced from 20 to −10 °C, although there are some changes in the ultimate tensile strain, it still maintains a large value (exceeds 3%).

4.4.6 Effect of Curing Age

(1) **Compressive strength**

Figure 4.49 shows the effect of curing age on the compressive strength of UHDMC, which increases with the increase of curing age. After 8 h of curing, the compressive

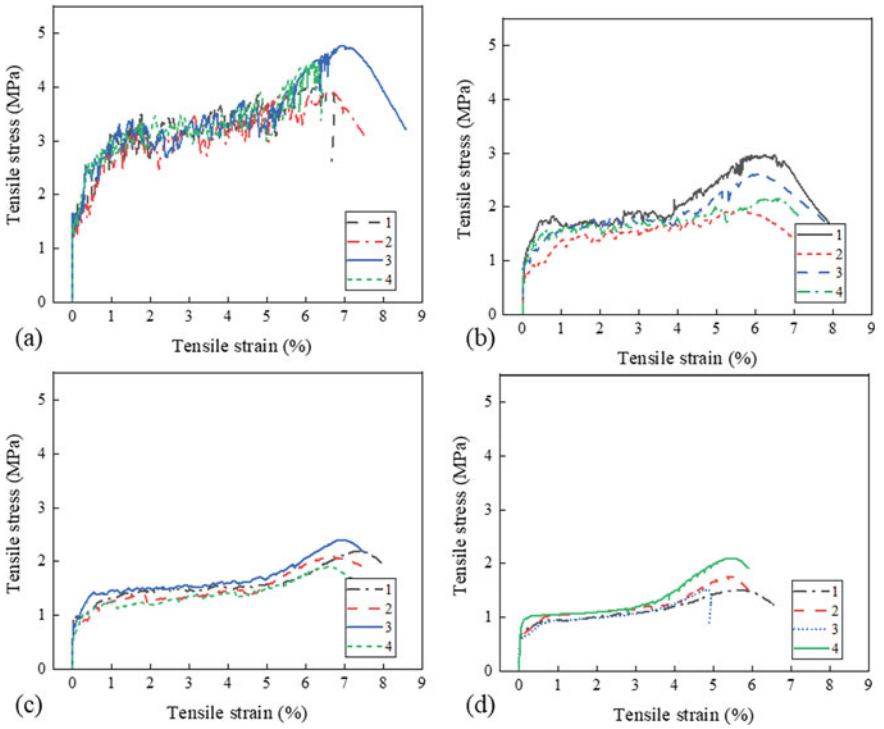

Fig. 4.47 Tensile stress–strain curves at the curing temperature of **a** 20 °C, **b** 0 °C, **c** −5 °C, and **d** −10 °C

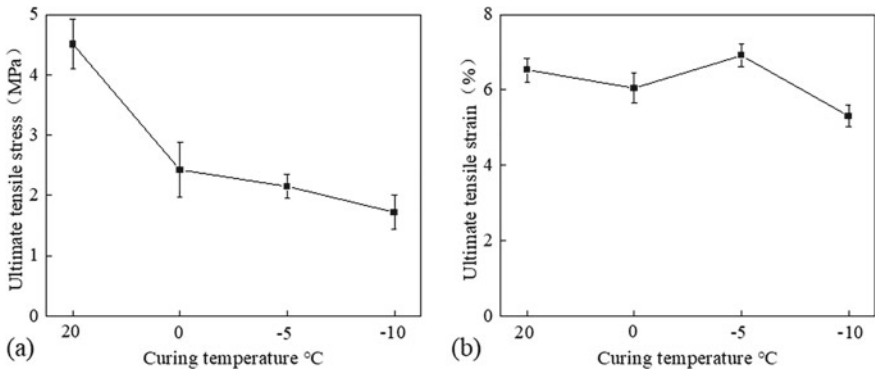

Fig. 4.48 The effect of curing temperature on **a** ultimate tensile stress and **b** ultimate tensile strain

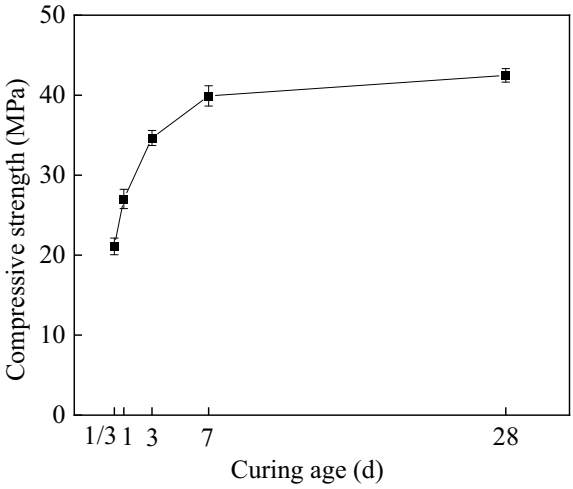

Fig. 4.49 Compressive strength of UHDMC with different curing age

strength can reach 21.09 MPa. In addition, the increase of compressive strength is mainly in the first 7 days. The compressive strength reaches 39.91 MPa when the curing age is 7 days. However, with the curing age increasing from 7 to 28d, the compressive strength only increases by 6.3% (2.57 MPa), which shows that the UHDMC has a good early strength.

(2) **Tensile properties**

Figure 4.50 shows the tensile stress–strain curves of UHDMC at different curing age. The UHDMC has a good strain hardening performance when the curing age is 8h, 1d, 3d and 7d. However, the strain hardening performance decreases slightly at the curing age of 28d.

Figure 4.51a, b show the effect of curing age on the ultimate tensile stress and ultimate tensile strain. From Fig. 4.51a, the ultimate tensile stress can reach 2.73 MPa at 8h. And with the increase of curing age, the ultimate tensile stress reaches a maximum of 4.58 MPa at the age of 7d. With the curing age increasing from 7 to 28 days, the ultimate tensile stress is slightly decreased, decreased by 0.5 MPa. In addition, from Fig. 4.51b, with the increase of curing age, the ultimate tensile strain presents a similar trend, increasing first and then decreasing, reaching a maximum of 6.53% at the curing age of 7 days. However, when the age is increased from 7 to 28 days, the ultimate tensile strain also decreases by 42.3%, which is similar to previous research (Feng et al., 2021b). However, the specific reasons still need to be further explored.

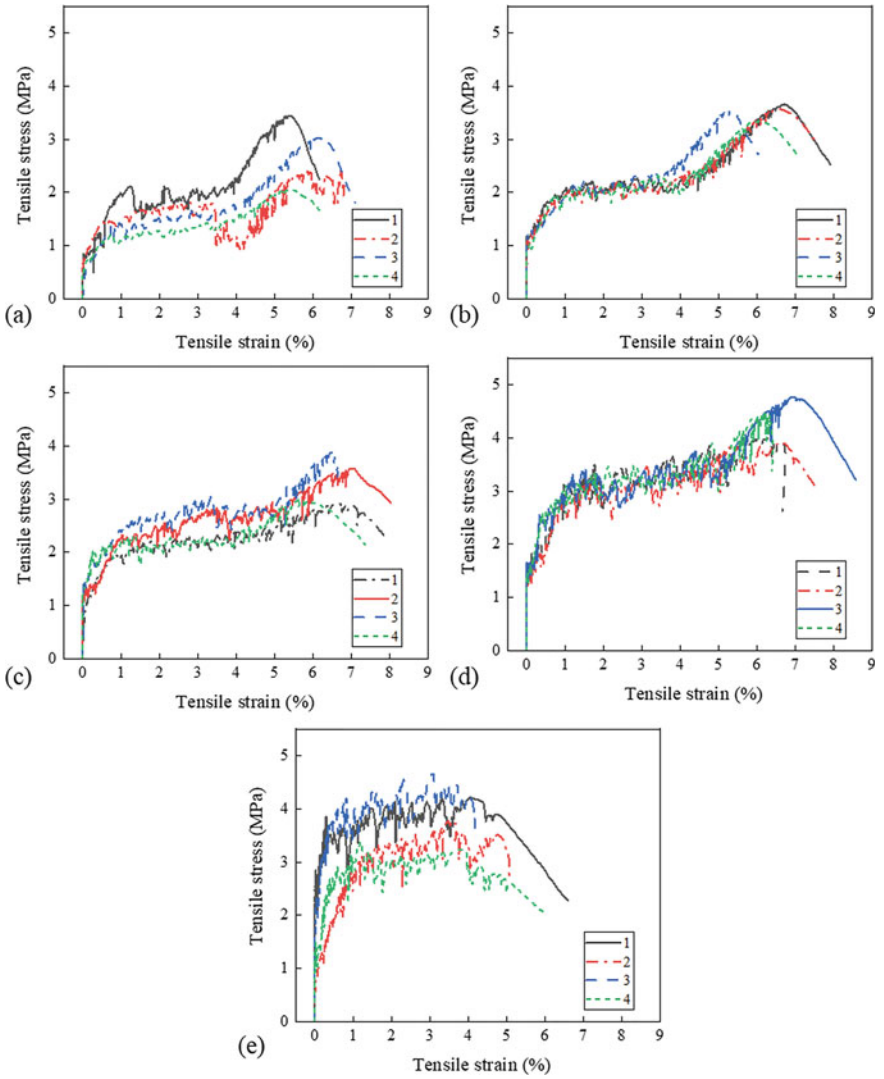

Fig. 4.50 Tensile stress–strain curves at the curing age of **a** 8h, **b** 1d, **c** 3d, **d** 7d, and **e** 28d

4.4.7 Design Method of UHDMC

In order to accurately establish the association model between the pseudo strain-hardening indices and the ultimate tensile strain, the relevant experimental data of UHDMC with PVA fibers from our research group were also used (Lv 2021). Figure 4.52 shows the association model, which is obtained by data fitting. From the figure, the ultimate tensile strain of the UHDMC with PVA fibers is between 0.3

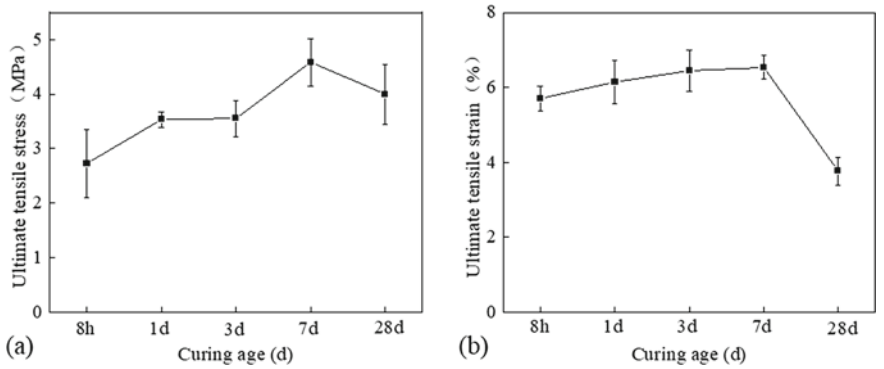

Fig. 4.51 The effect of curing age on **a** ultimate tensile stress and **b** ultimate tensile strain

and 4.1%, while the ultimate tensile strain of the UHDMC with PE fibers is between 0.26 and 6.53%, which indicates that ultra-high ductility UHDMC can be obtained by using PE fibers. In addition, the pseudo strain-hardening indices are positively correlated with the ultimate tensile strain. Therefore, according to the influence laws of various factors on the PSH_σ and PSH_J, as well as the association model, the design of UHDMC with desired ductility is realized.

In addition, previous research shows that when the PSH_σ and PSH_J exceed 2.12 and 21.32, respectively, the UHDMC will have good strain hardening performance (the ultimate tensile strain exceeds 3%) (Feng et al., 2022a, 2022b, 2022c). In this Chapter, the threshold is modified based on more experimental data. Based on data fitting formula (see Fig. 4.52), the PSH_σ and PSH_J should at least reach 2.15 and 25.1, respectively, at the same time.

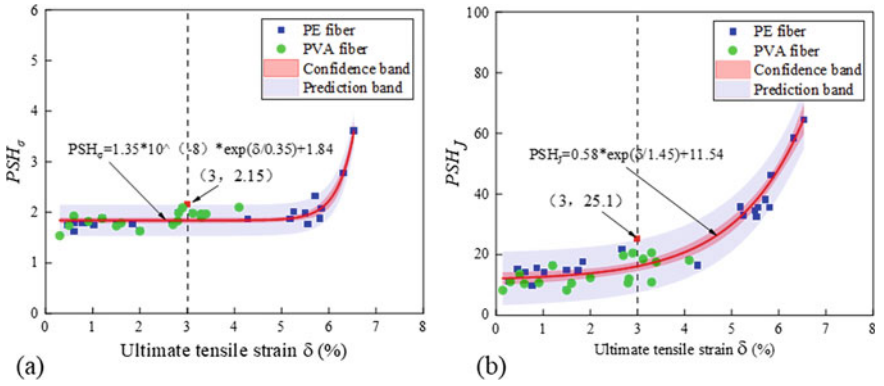

Fig. 4.52 The association model between ultimate tensile strain and **a** PSH_σ and **b** PSH_J

4.5 Conclusions

In this Chapter, the mass ratio of magnesium oxide to potassium dihydrogen phosphate (*M/P*), particle size of quartz sand (Sd), sand to binder mass ratio (*S/B*), water to solid mass ratio (*W/S*), fly ash content (FA), fiber volume fraction (V_f), curing temperature, and curing age are used as the influence factors to develop high performance UHDMC and then establish its systematic design method. The micro-mechanical properties and macro-mechanical properties of composites were tested. The association model between the pseudo strain hardening indices and the ultimate tensile strain is established for the design of high performance UHDMC. The main conclusions are as follows:

(1) The fine quartz sand (200 mesh) has a favorable influence on the compressive strength, ultimate tensile stress, fiber bridging stress capacity, matrix cracking strength and fracture energy of UHDMC. However, the UHDMC with 150–180 mesh quartz sand shows significant strain hardening performance, and its ultimate tensile strain can reach more than 5%. With the increase of *M/P*, the compressive strength of UHDMC increases, but the ultimate tensile stress and fiber bridging stress capacity gradually decrease. In addition, when the particle size of quartz sand is 150–180 mesh, the PSH_σ and PSH_J reach the maximum.

(2) With the increase of *W/S* and *S/B*, the compressive strength and ultimate tensile stress of UHDMC are adversely affected. However, UHDMC shows significant strain hardening performance when the *W/S* is 0.14 or 0.16, and shows high ultimate tensile strain when the *S/B* is 0.2. In addition, with the increase of *W/S*, the fiber bridging stress capacity, matrix cracking strength and matrix fracture energy of UHDMC are adversely affected. The fiber bridging stress capacity of UHDMC decreases with the increase of the *S/B*, but the cracking strength and fracture energy of the matrix reach maximum when the *S/B* is 0.3.

(3) When the FA content is 30%, the compressive strength of UHDMC reaches the maximum. When the FA content is 30% or 40%, the UHDMC has significant strain hardening performance. The addition of FA has adverse effects on the fiber bridging stress capacity and matrix cracking strength. However, the addition of FA has a favorable effect on the pseudo strain hardening indices (strength index and energy index). Especially when the FA content is 40%, the strength index and energy index reach the maximum.

(4) With the increase of fiber content, the compressive strength, the fiber bridging stress capacity, fiber bridging complementary energy, strength index and energy index of UHDMC all increase, and the strain hardening performance also becomes more significant.

(5) With the decrease of curing temperature, the compressive strength and ultimate tensile stress decrease, but the strain hardening performance of UHDMC does not decrease. With the increase of curing age, the compressive strength of UHDMC is gradually increased. Moreover, UHDMC shows obvious strain hardening performance within 7 days of curing age, but the strain hardening performance slightly decreases when the curing age is 28 days.

(6) The UHDMC with significant strain hardening performance is developed in this Chapter. The compressive strength and the ultimate tensile strain can reach 21.1 MPa and 6.1%, respectively, when cured in standard curing environment for only 8h. The compressive strength and the ultimate tensile stress can reach 39.91 and 4.73 MPa, respectively, when cured in standard curing environment for 7 days, especially the ultimate tensile strain can reach 7.1%. In addition, even curing at −10 °C for 7 days, the ultimate tensile strain can reach 5.6%, and the compressive strength can reach nearly 20 MPa.

(7) The association model between the pseudo strain hardening indices and the ultimate tensile strain is established. Based on this association model, the design of UHDMC with desired ductility is realized. The PSH_{σ} and PSH_{J} are recommended to be 2.15 and 25.1, respectively, to ensure that the UHDMC has significant strain hardening performance.

References

Ahmad, M. R., & Chen, B. (2018). Effect of silica fume and basalt fiber on the mechanical properties and microstructure of magnesium phosphate cement (MPC) mortar. *Construction and Building Materials, 190*, 466–478. https://doi.org/10.1016/j.conbuildmat.2018.09.143

Bilginer, B. A., & Erdogan, S. T. (2021). Effect of mixture proportioning on the strength and mineralogy of magnesium phosphate cements. *Construction and Building Materials, 277*(11), 122264. https://doi.org/10.1016/j.conbuildmat.2021.122264

Cabinets, M., Rooms, M., Statements, B., & Mass, D. (2010). Standard test method for compressive strength of hydraulic cement mortars (Using 2-in. or [50 mm] Cube Specimens) 1.

Chen, S. N., Lin, C., Hsu, H. L., Chen, X. H., Huang, Y. C., Hsieh, T. H., Ho, K. S., & Lin, Y. J. (2022). Inorganic flame-retardant coatings based on magnesium potassium phosphate hydrate. *Materials*, *15*(15), Article 5317. https://doi.org/10.3390/ma15155317

Curosu, I., Liebscher, M., Mechtcherine, V., Bellmann, C., & Michel, S. (2017). Tensile behavior of high-strength strain-hardening cement-based composites (HS-SHCC) made with high-performance polyethylene, aramid and PBO fibers. *Cement and Concrete Research, 98*, 71–81. https://doi.org/10.1016/j.cemconres.2017.04.004

Fang, Y., Chen, B., & Oderji, S. Y. (2018a). Experimental research on magnesium phosphate cement mortar reinforced by glass fiber. *Construction and Building Materials, 188*, 729–736. https://doi.org/10.1016/j.conbuildmat.2018.08.153

Fang, Y., Cui, P., Ding, Z., & Zhu, J. X. (2018b). Properties of a magnesium phosphate cement-based fire-retardant coating containing glass fiber or glass fiber powder. *Construction and Building Materials, 162*, 553–560. https://doi.org/10.1016/j.conbuildmat.2017.12.059

Fang, Y., Yin, X. H., Cui, P., Wang, X. D., Zhuang, K. D., Ding, Z., & Xing, F. (2021). Properties of magnesium potassium phosphate cement-expanded perlite composites applied as fire resistance coating. *Construction and Building Materials*, *293*, Article 123513. https://doi.org/10.1016/j.conbuildmat.2021.123513

Feng, H., Sheikh, M. N., Hadi, M. N., Gao, D., & Zhao, J. (2018a). Mechanical properties of micro-steel fibre reinforced magnesium potassium phosphate cement composite. *Construction and Building Materials, 185*, 423–435. https://doi.org/10.1016/j.conbuildmat.2018.07.037

Feng, H., Sheikh, M. N., Hadi, M. N., Feng, L., Gao, D., & Zhao, J. (2018b). Interface bond performance of steel fibre embedded in magnesium phosphate cementitious composite. *Construction and Building Materials, 185*, 648–660. https://doi.org/10.1016/j.conbuildmat.2018.07.107

Feng, H., Sheikh, M. N., Hadi, M. N. S., Feng, L., & Zhao, J. (2019). Pullout behaviour of different types of steel fibres embedded in magnesium phosphate cementitious matrix. *International Journal of Concrete Structures and Materials, 13*(1), 33. https://doi.org/10.1186/s40069-019-0344-1

Feng, H., Nie, S., Guo, A., Shen, S., Gao, D., & Chen, G. (2021a). Flexural behavior of high ductility MPC-based composites under low-temperature curing. *Construction and Building Materials, 300*, 124231. https://doi.org/10.1016/j.conbuildmat

Feng, H., Li, Z., Wang, W., Liu, G., Zhang, Z., & Gao, D. (2021b). Deflection hardening behaviour of ductile fibre reinforced magnesium phosphate cement-based composite. *Cement and Concrete Composites*, *121*(1). https://doi.org/10.1016/j.cemconcomp.2021.104079

Feng, H., Li, L., Wang, W., Cheng, Z., & Gao, D. (2022a). Mechanical properties of high ductility hybrid fibres reinforced magnesium phosphate cement-based composites. *Composite Structures, 284*, 115219. https://doi.org/10.1016/j.compstruct.2022.115219

Feng, H., Nie, S., Guo, A., Lv, L., & Yu, J. (2022b). Evaluation on the performance of magnesium phosphate cement-based engineered cementitious composites (MPC-ECC) with blended fly ash/silica fume. *Construction and Building Materials*, *341*. https://doi.org/10.1016/j.conbuildmat.2022.127861

Feng, H., Nie, S., Guo, A., Lv, L., Chu, L., & Yu, J. (2022c). Fresh properties and compressive strength of MPC-based materials with blended mineral admixtures. *Case Studies in Construction Materials, 17*, e01201. https://doi.org/10.1016/j.cscm.2022.e01201

Feng, H., Liang, J., Guo, A., Lv, L., Sun, Z., Sheikh, M. N., & Liu, F. (2023a). Development and design of ultra-high ductile magnesium phosphate cement-based composite using fly ash and silica fume. *Cement and Concrete Composites, 137*, 104923. https://doi.org/10.1016/j.cemconcomp.2022.104923

Feng, H., Zheng, X., Yu, Z., Chen, B., Zhu, P., Yu, J., & Luo, Z. (2023b). Development of sprayable ultra-high ductility magnesium phosphate cement-based composites based on the rheological properties. *Construction and Building Materials*, *377*. https://doi.org/10.1016/j.conbuildmat.2023.131113

Guang-Jun, Z., Wei-Xuan, Z., & Dao-Yuan, X. U. (2004). A Study on the formulae to test K_(IC) in three-point concrete bending beams. *Journal of Huaihai Institute of Technology*.

Hai-He, Y. I., Yi, Z., Jian-Bing, L. U., & Dong-Xu, L. I. (2014). Failure mechanism of magnesia-phosphate cement under low temperature curing condition. *Bulletin of the Chinese Ceramic Society*. 1001–1625(2014)33:1<197:DWTJXL>2.0.TX;2-Z

Haque, M. A., Chen, B., & Ahmad, M. R. (2019). Mechanical strength and flexural parameters analysis of micro-steel, polyvinyl and basalt fibre reinforced magnesium phosphate cement mortars. *Construction and Building Materials, 235*, 117447. https://doi.org/10.1016/j.conbuildmat

Haque, M. A., & Chen, B. (2019). Research progresses on magnesium phosphate cement: A review. *Construction and Building Materials*, *211*, 885–898. https://doi.org/10.1016/j.conbuildmat.2019.03.304

Jia, L., Zhao, F., Yao, K., & Du, H. (2021). Bond performance of repair mortar made with magnesium phosphate cement and ferroaluminate cement. *Construction and Building Materials*, *279*, Article 122398. https://doi.org/10.1016/j.conbuildmat.2021.122398

Jihui, Q., Jueshi, Q., Zhen, L., Chao, Y., Xiaobing, D., Yanfei, Y., & Yingru, F. (2018). Mechanical properties of basalt fiber reinforced magnesium phosphate cement composites. *Construction and Building Materials, 188*, 946–955. https://doi.org/10.1016/j.conbuildmat.2018.08.044

Kiran, S. R. (2012). Engineered Cementitious Composites (ECC).

Lei, F., Xi-Qing, C., Xiao-Dong, W., Zheng-Ya, Z., & Lv-Yan, S. (2019). Investigating and optimizing the mix proportion of sustainable phosphate-based rapid repairing material. *Construction and Building Materials*, *204*, 550–561. https://doi.org/10.1016/j.conbuildmat.2019.01.195

Li, V. C. (2012). Tailoring ECC for special attributes. *International Journal of Concrete Structures and Materials*. https://doi.org/10.1007/s40069-012-0022-z

Li, D. X., & Feng, C. H. (2011). Study on modification of the magnesium phosphate cement-based material by fly ash. *Advanced Materials Research, 150–151*, 1655–1661. https://doi.org/10.4028/www.scientific.net/AMR.150-151.1655

Liu, K., Jiang, F., Zhang, C., Zhang, B., & Dongxu, L. I. (2012). Failure mechanism of dipotassium hydrogen phosphate modified magnesia-phosphate cements under water curing condition. *Journal of the Chinese Ceramic Society*, *40*(12), 1693–1698(1696). 0454–5648(2012)40:12<1693:SYHTJX>2.0.TX;2-X

Liu, X., Wang, N., & Wang, Z. (2022). Effects of the absorber, thickness and surface roughness on the electromagnetic wave absorption characteristics of magnesium phosphate cement. *Construction and Building Materials*, *344*, Article 128149. https://doi.org/10.1016/j.conbuildmat.2022.128149

Lv, L. (2021). *Experimental study on mechanical properties of high ductility magnesium phosphate cement-based fiber composite material with mineral admixture.* Zhengzhou University.

Ma, C., Liu, Y., Zhou, H., Jiang, Z., Ren, W., & He, F. (2021a). Influencing mechanism of mineral admixtures on rheological properties of fresh magnesium phosphate cement. *Construction and Building Materials*, *288*, Article 123130. https://doi.org/10.1016/j.conbuildmat.2021.123130

Ma, C., Wang, F., Zhou, H., Jiang, Z., Ren, W., & Du, Y. (2021b). Effect of early-hydration behavior on rheological properties of borax-admixed magnesium phosphate cement. *Construction and Building Materials*, *283*, Article 122701. https://doi.org/10.1016/j.conbuildmat.2021.122701

Peng, L., & Chen, B. (2021). Mechanical behavior, durability, thermal performances and microstructure of GGBFS—Modified MPC solidified dredged sludge. *Construction and Building Materials*, *303*, Article 124557. https://doi.org/10.1016/j.conbuildmat.2021.124557

Provis, J. L., Bernal, S. A., Walling, S. A., & Corkhill, C. L. (2015). Characterisation of magnesium potassium phosphate cements blended with fly ash and ground granulated blast furnace slag. *Cement and Concrete Research.* https://doi.org/10.1016/j.cemconres.2015.01.015

Qiao, F., Chau, C. K., & Li, Z. (2010). Property evaluation of magnesium phosphate cement mortar as patch repair material. *Construction and Building Materials, 24*(5), 695–700. https://doi.org/10.1016/j.conbuildmat.2009.10.039

Qin, J., Dai, F., Ma, H., Dai, X., Li, Z., Jia, X., & Qian, J. (2022). Development and characterization of magnesium phosphate cement based ultra-high performance concrete. *Composites Part B-Engineering*, *234*, Article 109694. https://doi.org/10.1016/j.compositesb.2022.109694

Ranade, R., Li, V. C., Stults, M. D., Heard, W. F., & Rushing, T. S. (2013a). Composite properties of high-strength, high-ductility concrete. *Aci Materials Journal*, *110*(4), 413–422.

Ranade, R., Li, V. C., Stults, M. D., Rushing, T. S., Roth, J., & Heard, W. F. (2013b). Micromechanics of high-strength, high-ductility concrete. *Aci Materials Journal*, *110*(4), 375–384.

Shao, H., Zongjin, L., Barbara, B., & Hongyan, M. (2017). Influence of fly ash on compressive strength and micro-characteristics of magnesium potassium phosphate cement mortars. *Cement and Concrete Research.* https://doi.org/10.1016/j.cemconres.2017.05.008

Tang, Z., Chen, D., Wang, X., Han, Z., Tao, R., Zhang, G., Hou, D., Wu, D., & Ding, Q. (2023). Impact of polyethylene fiber on the ductility and durability of magnesium phosphate cement. *Journal of Building Engineering, 68*, 106123. https://doi.org/10.1016/j.jobe.2023.106123

Tonelli, M., Gelli, R., Ridi, F., & Baglioni, P. (2021). Magnesium phosphate-based cements containing Halloysite nanotubes for cracks repair. *Construction and Building Materials*, *301*, Article 124056. https://doi.org/10.1016/j.conbuildmat.2021.124056

Wu, Q., Hou, Y., Mei, J., Yang, J., & Gan, T. (2022). Influence of synthetic limestone sand on the frost resistance of magnesium potassium phosphate cement mortar. *Materials*, *15*(19), Article 6517. https://doi.org/10.3390/ma15196517

Xu, S., & Reinhardt, H. W. (1999). Determination of double-K criterion for crack propagation in quasi-brittle fracture, Part II: Analytical evaluating and practical measuring methods for three-point bending notched beams. *International Journal of Fracture, 98*(2), 151–177. https://doi.org/10.1023/A:1018740728458

Xu, B., Winnefeld, F., Kaufmann, J., & Lothenbach, B. (2019). Influence of magnesium-to-phosphate ratio and water-to-cement ratio on hydration and properties of magnesium potassium

phosphate cements. *Cement and Concrete Research, 123*, 105781. https://doi.org/10.1016/j.cemconres.2019.105781

Yang, E. H., & Li, V. C. (2010). Strain-hardening fiber cement optimization and component tailoring by means of a micromechanical model. *Construction and Building Materials, 24*(2), 130–139. https://doi.org/10.1016/j.conbuildmat.2007.05.014

Yang, Q., Zhu, B., & Wu, X. (2000). Characteristics and durability test of magnesium phosphate cement-based material for rapid repair of concrete. *Materials and Structures, 33*(228), 229–234. https://doi.org/10.1007/bf02479332

Yang, Q. B., Zhang, S. Q., & Wu, X. L. (2002). Deicer-scaling resistance of phosphate cement-based binder for rapid repair of concrete. *Cement and Concrete Research, 32*(1), 165–168. https://doi.org/10.1016/s0008-8846(01)00651-2

Yang, Q. (2013, 2014). Durability and applications of magnesium phosphate material for rapid repair of pavements. In *Advanced Materials Research* [Advanced pavement research]. *3rd International Conference on Concrete Pavements Design, Construction, and Rehabilitation (ICCPDCR 2013).* Shanghai.

Yokota, H., Rokugo, K., & Sakata, N. (2008). *Recommendations for design and construction of high performance fiber reinforced cement composites with multiple fine cracks (HPFRCC).*

Yu, K., Wang, Y., Yu, J., & Xu, S. (2017). A strain-hardening cementitious composites with the tensile capacity up to 8%. *Construction and Building Materials*, *137*, 410–419. https://doi.org/10.1016/j.conbuildmat.2017.01.060

Yu, J., Qian, J., Wang, F., Li, Z., & Jia, X. (2020). Preparation and properties of a magnesium phosphate cement with dolomite. *Cement and Concrete Research*, *138*, Article 106235. https://doi.org/10.1016/j.cemconres.2020.106235

Yue, L., & Bing, C. (2013). Factors that affect the properties of magnesium phosphate cement. *Construction and Building Materials*, *47*, 977–983. https://doi.org/10.1016/j.conbuildmat.2013.05.103

Zhao, J., Hwang, K. H., Lee, J. K., & Kim, M. C. (2012, 2013). Application of magnesia-phosphate cement for chromia/alumina castables. In *Applied Mechanics and Materials* [Materials, mechanical engineering and manufacture, pts 1–3]. *2nd International Conference on Applied Mechanics, Materials and Manufacturing (ICAMMM 2012).* Changsha.

Zheng, D. D., Ji, T., Wang, C. Q., Sun, C. J., Lin, X. J., & Hossain, K. M. A. (2016). Effect of the combination of fly ash and silica fume on water resistance of magnesium-potassium phosphate cement. *106*, 415–421. https://doi.org/10.1016/j.conbuildmat.2015.12.085

Zhou, Y., Xi, B., Sui, L., Zheng, S., Xing, F., & Li, L. (2019). Development of high strain-hardening lightweight engineered cementitious composites: Design and performance. *Cement and Concrete Composites*, *104*. https://doi.org/10.1016/j.cemconcomp.2019.103370

Chapter 5
Water Stability of UHDMC

Abstract The exceptional qualities of magnesium phosphate cement-based ultra-high ductile composites (UHDMC) for repair and reinforcement are fully utilized. However, the broader use of UHDMCs is restrained due to the defective stability of magnesium phosphate cement (MPC) in wet or humid conditions. This chapter presents a sequence of tests to study the influence of factors such as curing age under ambient conditions, duration of immersion in water, water-to-binder (*W/B*) ratio, ratio of magnesium oxide to potassium dihydrogen phosphate (*M/P*), percentage of nano-Al_2O_3 (NA), replacement rate of fly ash (FA), and proportion of water glass (WG) on both mechanical properties and water stability of UHDMCs. A thorough examination of the core properties of UHDMCs, such as workability, resistance to compression, flexural behavior, and stability when exposed to water, is conducted. The operating mechanism explaining these effects is later exposed via Scanning Electron Microscopy (SEM).

Keywords Magnesium phosphate cement · Slump · Compressive strength · Flexural property · Water stability

5.1 Introduction

Magnesium phosphate cement (MPC), a type of cementitious material, was initially introduced by Prosen in 1939 (Prosen, 1939). Its strength is derived from the acid–base neutralizing reaction between magnesium oxide and phosphate, typically using either ammonium dihydrogen phosphate or potassium dihydrogen phosphate (Chau et al., 2011a, 2011b; Mraa et al., 2019). The unique properties of MPC include rapid solidification, exceptional early strength (Chau et al., 2011a, 2011b), good compatibility with ordinary Portland cement (Qiao et al., 2010), minimal shrinkage (Yang et al., 2000), and impressive wear and frost resistance (Wang et al., 2015; Yue et al., 2015). MPC's potential applications span a wide range of fields including bone regeneration (Yu et al., 2020), solidification and stabilization of radioactive metal (Su et al., 2016), natural fiber composite products (Donahue & Aro, 2010), and dental

H. Feng et al., *Ultra-High Ductility Magnesium-Phosphate-Cement-Based Composites (UHDMC)*, https://doi.org/10.1007/978-981-97-0952-6_5

pulp therapies (Mestres et al., 2014). In civil engineering, MPC is employed in areas such as fiber reinforced concrete structures (Ding et al., 2011), 3D printed structures (Weng et al., 2019), grouting material fabrication (Liu & Chen, 2019), and repairing damaged structures (Ban et al., 2020; Ding et al., 2012; Lu & Chen, 2016; Ning & Bing, 2016). However, a significant limitation of MPC is its inherent brittleness (Li & Chen, 2013). This has been counteracted effectively by incorporating polyvinyl alcohol (PVA) fibers into the MPC to achieve high-ductility MPC composites (Li et al., 2001; Yang & Li, 2010). Studies have demonstrated the benefits of adding PVA fibers. For instance, Sun et al. showed PVA fibers' bridging effect slowed crack propagation, enhancing the composite's toughness (Chen & Zhu, 2017). Lee et al. suggested that PVA fibers can manage the expansion and shrinkage of MPC composites, enhancing their strength (Lee et al., 2017). Feng et al. found that introducing PVA fibers into MPC composites mitigates the brittleness issue, enabling superior deflection hardening capability (Feng et al., 2021).

MPC systems are shown to have a noticeable weakness: their strength tends to reduce significantly when exposed to water or moisture. Sarkar revealed a 20% strength loss in magnesium ammonium phosphate cement (MAPC) mortar cured for 28 days in dry conditions after 90 day water immersion (Sarkar, 1990). This loss reduced as curing time increased in a dry environment. When Seehra et al. immersed 28 day cured MAPC mortar in water, they discovered a 17% strength degradation compared to the pre-immersion state (Seehra et al., 1993). On testing the compressive strength after 30 and 90 days of maintaining 7 and 28 day MAPC mortars in water, Yang et al. (2000) found the highest strength loss after 7 day curing and 90 day immersion—approximately 20% (Yang et al., 2000). Li et al. reported a 44.2% reduction in the compressive strength of magnesium potassium phosphate cement (MKPC) paste cured underwater for 28 days compared to air curing (Li et al., 2009).

The primary cause for concern in water environments is the dissolution of hydration products, leading to mass loss within the MPC (Maha et al., 2019). In such conditions, MKP—the main hydration product formed by the acid–base reaction between MgO and KH_2PO_4 (Alberto et al., 2016)—undergoes either dissolution or decomposition, thereby loosening the internal structure of the MKPC and compromising its performance (Chong et al., 2017a, 2017b; Maha et al., 2019). Moreover, unreacted magnesium oxide and phosphate also succumb to dissolution when submerged in water (Chong et al., 2017a, 2017b). As phosphate dissolves, the solution acidifies, impacting the stability of the hydrated product struvite (Xiong et al., 2016), which is soluble under acidic conditions but considerably stable in neutral or alkaline conditions, speeding up the dissolution of the hydration products (Münch & Barr, 2001). As a rapid repair material, the water stability of magnesium potassium phosphate cement directly influences the durability of the foundational structure, potentially impeding its extensive application (Le Rouzic et al., 2017; Li et al., 2009).

Several elements influence the water stability of MPC, including the duration of ambient curing, the *M/P* ratio, and the *W/B* ratio. Concerning curing methods, extending the initial air pre-curing duration allows for a more comprehensive hydration response in MPC, enhancing its initial strength before water immersion and

thereby improving water stability (Chong et al., 2017a, 2017b). Wang observed that specimens cured in air for 28 days demonstrated a significantly smaller rate of strength reduction upon immersion in water than their 7 day air-cured counterparts (Wang, 2006). Moreover, varying the *M/P* ratio impacts MPC's water stability. Li et al.'s research on MPC samples prepared with distinct *M/P* ratios revealed that elevating the *M/P* ratio from 2:1 to 8:1 diminished the compressive strength loss of the samples after a 28 day water immersion period from 65.3 to 12% (Li et al., 2009). This suggests that a higher *M/P* ratio may confer superior water stability. However, an excess of MgO could accelerate the hydration reaction rate, complicating the formation of densely packed reaction products and potentially undermining the structural strength (Hou et al., 2016; Ma et al., 2014). The *W/B* ratio also plays a crucial role, as it can adjust the solidification duration, phase composition, and compressive strength of MPC-based composites. Generally, greater water content results in a more porous matrix, which adversely affects water stability (Ding & Li, 2005; Wang et al., 2013). Given these influences, this chapter will account for the factors of ambient curing age, *M/P* ratio, and *W/B* ratio.

Enhancing the pore structure and structural compactness of the MPC is a critical strategy to improve its water stability. Yue et al. demonstrated that incorporating fly ash (FA) could promote the compactness of MKPC, thereby reducing strength loss in samples (Yue et al., 2016). However, the addition of quartz sand appeared to detrimentally impact the microstructure compactness of MKPC. Lv et al. similarly improved MKPC paste's water resistance by incorporating FA to heighten the microstructure's compactness (Lv et al., 2019). Moreover, Zhang et al. discovered that integrating calcium aluminate cement (CAC) notably bolstered the water stability of MKPC (Zhang et al., 2018). This strengthening happens as struvite-K gets coated by hydration products of CAC, which then densify the structure of MKPC. The optimum water stability was recorded with a 40% inclusion of CAC. In another study, Ge et al. utilized hydraulic sulfoaluminate cement (SAC) as a replacement for some magnesium oxide proportion to strengthen the compactness of the hardened paste (Ge et al., 2017). The hydration of SAC generated amorphous hydration products that provide cohesion between residual unreacted MgO and struvite-K crystals. Wang et al.'s study added 30–40% nickel slag powders to MKPC paste, which notably cut down the total porosity of the hardened MPKC paste (Wang et al., 2019). This reduction was due to the betterment of particle size distribution of base ingredients such as MgO and nickel slag powers, as well as the micro-aggregate of nickel slag powders, and enhanced flowability. Moreover, Haque et al. showed that the combined addition of FA and bauxite to MAPC could fill the matrix's pores and generate a denser microstructure due to the formation of amorphous intermediate crystals (Haque et al., 2020). This resulted in an advancement of the water stability of MAPC mortar. Nevertheless, as of the authors' best knowledge, no studies have been reported thus far that explore the addition of FA and WG to enhance the water stability of UHDMC. Therefore, systematic investigations should be undertaken on the impact of FA and WG on the water stability of UHDMC.

Furthermore, nanomaterials have gained considerable interest for their capacity to enhance the performance of cement-based composites, attributed to their tiny particle size, large surface area, and consistent chemical attributes (Ran & Huirong, 2020). Evidence suggests that integrating nano-Al_2O_3(NA) can boost not only the concrete's strength and elastic modulus (Yuan et al., 2013) and the bond strength between the fibers and the matrix, but it also reinforces the structural compactness (Mohseni et al., 2016). Feng et al. discovered that nano-Al_2O_3(NA) had a positive impact on the crystal structure of MKPC hydrated products and improved the compactness and water stability of structures (Feng et al., 2019). This heightened compactness can enhance both the mechanical properties and the water stability of MKPC-based composites (Feng et al., 2020; Hu et al., 2020). However, the body of research exploring the influence of nano-Al_2O_3 on the water stability and mechanical properties of UHDMC remains limited.

In this chapter, magnesium phosphate cement (MPC) mortars consisting of calcined magnesia (MgO), potassium dihydrogen phosphate (KH_2PO_4), borax ($Na_2B_4O_7 \cdot 10H_2O$), quartz sand, and fly ash (FA) are prepared. To formulate UHDMC, polyvinyl alcohol (PVA) fibers were introduced to the MPC mortars. The first step was to investigate the impact of both ambient curing age (the period of stay in the ambient curing room) and water immersion age (among of time submerged in water after ambient curing) on the water stability and mechanical characteristics of UHDMC, using a benchmark mix proportion. Secondly, to fine-tune the mix proportions, the role of the *M/P* ratio and the *W/B* ratio in influencing the mechanical features and water stability of the UHDMC is examined. The third phase entailed examining the influence of NA content, FA replacement rate, and WG mass proportion on the UHDMC's mechanical properties and water stability. Finally, the scanning electron microscopy (SEM) test was carried out to present a more comprehensive analysis.

5.2 Experimental Program

5.2.1 Raw Materials

The MgO (having a specific gravity of 3.15 g/cm^3) came from Hua Nai Magnesium Industry Co., Ltd., located in Yancheng, Jiangsu, China. Its chemical composition is presented in Table 5.1. Calcination of MgO occurs at 1500 °C. Although a high calcination temperature doesn't largely influence the chemical composition of MgO, it serves to reduce its specific surface area which escalates its reactivity, resulting in an enhanced compressive strength of the MPC sample (Sun et al., 2015). Initially, MgO underwent milling using a ball mill, followed by a sieve process using a sieve with 0.1 mm opening size. The part that remained on the sieve, having a specific surface area around 315.7 m^2/kg, was chosen.

In this study, we utilized two types of potassium dihydrogen phosphates (in the form of white crystals). One version was procured from Tianjin Ding Sheng Xin

Table 5.1 Chemical composition of calcined magnesia (MgO)

Composition	MgO	Fe_2O_3	SiO_2	CaO	Al_2O_3
Mass fraction (%)	≧96	≦0.18	≦1.4	≦1.4	≦0.3

Reproduced from Assessment of the mechanical properties and water stability of nano-Al_2O_3 modified high ductility magnesium potassium phosphate cement-based composites by Hu Feng with permission from Elsevier

Chemical Co., Ltd., with a crystal size within the range of 425–600 μm. Conversely, the other variant was sourced from Wu Jiang Wei Tong Chemical Co., Ltd., possessing a crystal size within the range of 180–315 μm. The MKPC chemical reaction is influenced by the particle size of KH_2PO_4. When the particles of KH_2PO_4 are too large or too small, it either slows down the reaction or speeds it up excessively. Hence, these two industrial grade potassium dihydrogen phosphate were mixed in the proportion of 1:1 and subsequently utilized, with a specific gravity of 2.34 g/cm^3.

The quartz sand, having a particle size between 140 and 198 μm, was obtained from Henan Zhong Bang Environmental Protection Technology Co., Ltd., carrying the technical specifications portrayed in Table 5.2. The Class F fly ash (LOI being 5%) with particle sizes ranging from 0.3 to 48 μm was delivered by Yulian Power Plant of Gongyi, Hennan, China. The chemical composition of this substance can be observed in Table 5.3. The particle gradation curves for MgO, fly ash, and quartz sand are illustrated in Fig. 5.1.

Borax ($Na_2B_4O_7 \cdot 10H_2O$), having a purity of at least 99.5%, was used as a retarder and was acquired from Liaoning Borda Technology Co., Ltd. It has a specific gravity of 1.72 g/cm^3. Nano-Al_2O_3 (Al_2O_3, being at least 99% pure, in a white powder form) which was produced by Zhi Tai Nanotechnology Co., Ltd., was selected, having a particle size range between 30 and 40 nm and a specific surface area of 2×10^5 m^2/kg.

Table 5.2 Technical indicators of quartz sand

SiO_2 (wt.%)	Bulk density (g/cm^3)	Moss hardness	Porosity (%)	Specific gravity (g/cm^3)
99.3	1.8	7.5	43	2.66

Reproduced from Assessment of the mechanical properties and water stability of nano-Al_2O_3 modified high ductility magnesium potassium phosphate cement-based composites by Hu Feng with permission from Elsevier

Table 5.3 Chemical composition of fly ash

Composition	SiO_2	Al_2O_3	Fe_2O_3	CaO	MgO	Na_2O
Mass fraction (%)	53.97	31.15	4.16	4.01	1.01	0.89

Reproduced from Assessment of the mechanical properties and water stability of nano-Al_2O_3 modified high ductility magnesium potassium phosphate cement-based composites by Hu Feng with permission from Elsevier

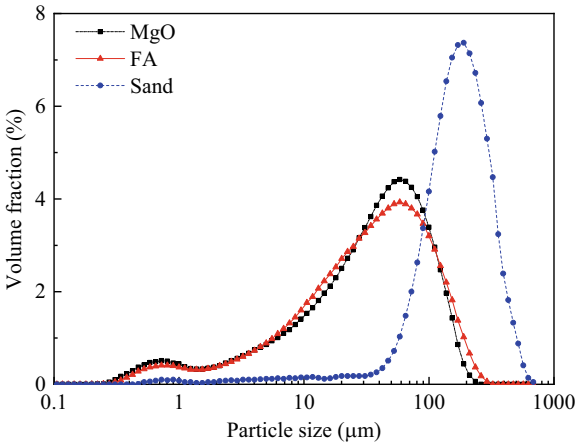

Fig. 5.1 Particle gradation curve of MgO, FA, and quartz sand. Reproduced from Assessment of the mechanical properties and water stability of nano-Al_2O_3 modified high ductility magnesium potassium phosphate cement-based composites by Hu Feng with permission from Elsevier

Table 5.4 Properties of PVA fibers

Diameter (μm)	Length (mm)	Density (g/cm^3)	Young's modulus (GPa)	Tensile strength (MPa)	Elongation (%)
40	12	1.3	41	1560	6.5

Reproduced from Assessment of the mechanical properties and water stability of nano-Al_2O_3 modified high ductility magnesium potassium phosphate cement-based composites by Hu Feng with permission from Elsevier

This study also utilized tap water and monofilament PVA fibers, which were manufactured by the Japan Kuraray Company. The attributes of these PVA fibers can be seen in Table 5.4. Water glass (WG) supplied by Tianjin Damao Chemical Reagent Factory demonstrated a granular appearance, comprising $Na_2SiO_3 \cdot 5H_2O$ with a purity of 99%.

5.2.2 *Mixture Proportions*

The UHDMC fabricated in this study is made up of magnesium potassium phosphate cement (MPC), PVA fibers, and fly ash. The constituents of MPC include magnesium oxide (M), potassium dihydrogen phosphate (P) and borax. Experimental investigations in the authors' research team have indicated that when the *S/B* mass ratio (where *S/B* represents the ratio of sand to binder which comprises MPC + FA) is set at 0.2, borax makes up 6% of the MgO mass, and there's a fiber volume ratio of 1.6%, the produced specimens exhibit commendable mechanical properties and ductility. Hence, in this investigation, these three figures are retained constant in all samples.

Five factors differ: the mass ratio of water to binder (*W/B*), the molar ratio between magnesium oxide and potassium dihydrogen phosphate (*M/P*), the NA (nano-Al_2O_3) content, the FA content, and the WG (water glass) content. It's important to note that the *W/B* ratio is set at 0.14, 0.16, 0.18, and 0.20, respectively; the *M/P* ratio is set at 3, 4, 5, and 6, respectively; the NA makes up 0, 2, 4, 6, 8, and 10% of the MPC by mass, respectively; FA is deployed to substitute for 20, 30, 40, and 50% MPC by mass fraction; the WG represents 0, 1, 2, 3, 4, and 5% of the MPC by mass, respectively. The UHDMC's mix proportions can be viewed in Table 5.5.

Table 5.5 Mixture proportions of UHDMC

	W/B	*M/P*	FA (%)	NA	WG	*S/B*	Borax (%)	V_f (%)
W/B-0.14	0.14	4	20	0	0	0.2	6	1.6
W/B-0.16	0.16							
W/B-0.18	0.18							
W/B-0.20	0.20							
M/P-3	0.13	3	20	0	0	0.2	6	1.6
M/P-4		4						
M/P-5		5						
M/P-6		6						
NA-0	0.13	4	20	0%	0	0.2	6	1.6
NA-2				2%				
NA-4				4%				
NA-6				6%				
NA-8				8%				
NA-10				10%				
FA-20	0.13	4	20	0	0	0.2	6	1.6
FA-30			30					
FA-40			40					
FA-50			50					
WG-0	0.13	4	20	0	0%	0.2	6	1.6
WG-1					1%			
WG-2					2%			
WG-3					3%			
WG-4					4%			
WG-5					5%			

5.2.3 Mixing and Curing

Using a single horizontal shaft mixer (model: HX-15), UHDMC mixtures were concocted. Prior to the mixing process, the mixer's internal surface and blades were dampened with water to prevent the dilution of the mix water. Subsequently, the accurately weighed MgO, KH_2PO_4, quartz sand, borax, and fly ash were consecutively added to the mixer and homogenized for a period of 120 s. For UHDMC mixtures that include NA or WG, these elements are incorporated at this juncture. Following this step, water was introduced, and another 120 s mix was performed. During this phase, PVA fibers were added in a progressive manner to guarantee a satisfactory dispersion of the fibers. The prepared mortar mixture was promptly poured into the test mold, which had been pre-set on a vibrating table. In order to evacuate air from the samples, an initial vibration lasting 60 s was undertaken, followed by a second vibration of 30 s, with the two vibrating procedures separated by a 15 s interval. The specimens then underwent a curing phase in a controlled room environment with a temperature of 25 ± 2 °C and relative humidity of 45 ± 5% for about 2 h. After this time, the mold was taken off.

In order to assess the impacts of ambient curing duration and water immersion period on UHDMC, the samples continued to be conserved in the curing room till they hit a predetermined age (either 7 or 28 days), followed by immersion in a water tank for a predetermined duration (7, 28, or 56 days). To further explore the influence of *W/B*, *M/P*, FA, NA, and WG on UHDMC, the specimens underwent a curing process for 7 days. Following this, half of the cured specimens were removed for immediate testing without water immersion. The remaining half were submerged in tap water for an additional week prior to being subjected to testing.

5.2.4 Slump Test

The slump test was conducted to gauge the UHDMC's workability through the method outlined in China standard JGJ/T283-2012. The time span (T500) that elapses from the moment the slump bucket is lifted until the mixture broadens to a diameter of 500 mm was documented. Once the slurry ceased flowing, its flow diameter (which is the mean value of the measurements taken in two perpendicular directions) was assessed using a steel ruler. Then, the slump was calculated by deducting the slurry's height from the height of the slump cone.

5.2.5 Compressive Test

The compressive test was carried out in accordance with ASTM C109 guidelines. For this test, 50 × 50 × 50 mm^3 plastic molds were utilized to create cube-shaped

samples. Each group had three samples tested, and the mean value of these tests was used. The test deployed a 200T pressure testing machine, applying a load at a rate of 0.9 kN/s.

5.2.6 *Flexural Test*

The primary tool employed for the flexural test was a digital universal testing machine (model: WDW-100, capacity: 100 kN). Figure 5.2 visualizes the blueprints and arrangement of the four-point flexural test. For this test, steel molds with dimensions of $400 \times 100 \times 15\,\text{mm}^3$ were utilized to construct thin plates. Prior to the test, a visual check of the specimens was conducted to confirm they had no damage. The top surface of the samples served as the loading interface, with the supporters arranged in a horizontal line with the pressure head, the off-center value not surpassing 1mm. The pressure sensor (LOAD CELL) and the linear variable differential transformer (LVDTs) were situated at their respective assigned spots (refer to Fig. 5.2a). Throughout the test, a sustained load was applied steadily at 0.3 mm/min. The strain monitoring system autonomously logged the deflection at the mid-span of the specimens and the ongoing load magnitude every 2 s, allowing the creation of load–deflection graphs. The test was halted either when the load–deflection graph revealed a generally falling pattern or when significant fissures emerged at the specimens' base.

A typical strain hardening curve of fiber-reinforced cement-based mixtures is illustrated in Fig. 5.3. The inaugural cracking location is the point A, a shift from the linear stage (curve OA) to the nonlinear phase (curve AB), otherwise known as the limit of proportion (LOP) following ASTM C1018 rules (Abitbol et al., 2016). The load record at the LOP is termed the cracking load (P_{LOP}), while the corresponding deflection is referred to as the cracking deflection (δ_{LOP}). Post the initial cracking, the fiber-reinforced cement-based materials demonstrated enhanced load-support capability. The modulus of rupture (MOR), also recognized as ultimate flexural strength, is established using the softening locus (point B) where a decreasing trend begins to mark the load–deflection trajectory. The load index at MOR gets identified as the ultimate load (P_{MOR}), and the linked deflection is classified as the ultimate deflection (δ_{MOR}).

(1) Strength index

The first-cracking strength, f_{LOP} (MPa), and ultimate flexural strength, f_{MOR} (MPa), are evaluated based on Eqs. 5.1 and 5.2, respectively.

$$f_{LOP} = P_{LOP}\frac{L}{bh^2} \tag{5.1}$$

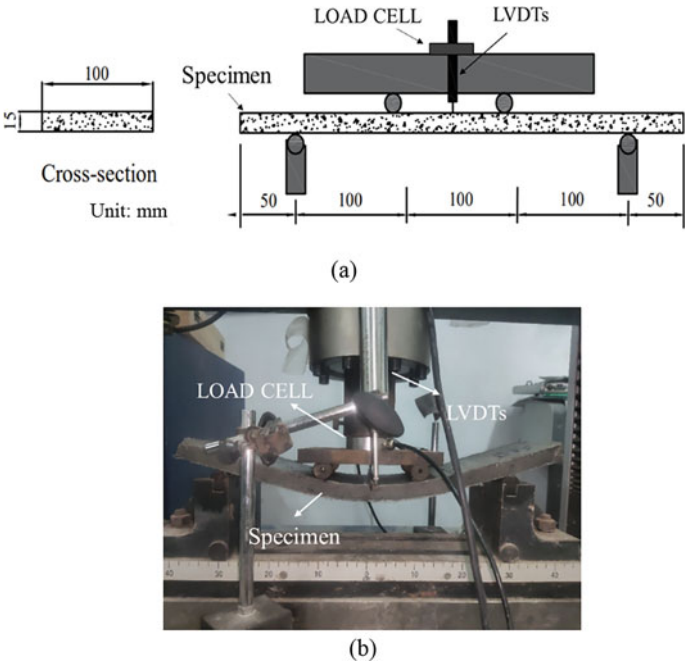

Fig. 5.2 **a** Schematic diagram and **b** setup of four-point flexural test. Reproduced from Assessment of the mechanical properties and water stability of nano-Al_2O_3 modified high ductility magnesium potassium phosphate cement-based composites by Hu Feng with permission from Elsevier

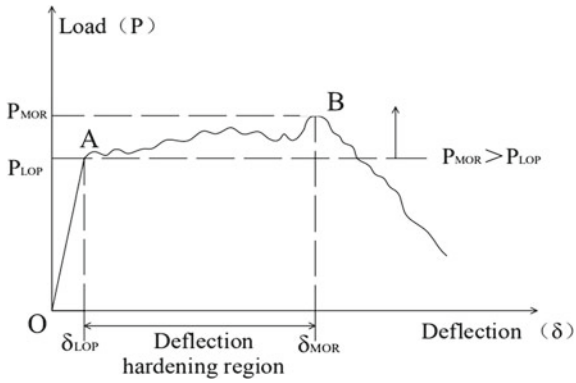

Fig. 5.3 A typical strain hardening curve of fiber reinforced cement-based composites. Reproduced from Assessment of the mechanical properties and water stability of nano-Al_2O_3 modified high ductility magnesium potassium phosphate cement-based composites by Hu Feng with permission from Elsevier

$$f_{MOR} = P_{MOR}\frac{L}{bh^2} \tag{5.2}$$

where P_{LOP} is the cracking load (N), P_{MOR} is the ultimate load (N), L is the span length (mm) of the specimens, and b and h are the width and height (mm) of the specimens, respectively.

(2) Ductility index

The ductility index (DI) is defined as the difference between the ultimate deflection (δ_{MOR}) and the cracking deflection (δ_{LOP}) using Eq. 5.3. The larger the DI value is, the better the ductility of the composite is.

$$DI = \delta_{MOR} - \delta_{LOP} \tag{5.3}$$

where δ_{MOR} is the ultimate deflection (mm), and δ_{LOP} is the cracking deflection (mm).

(3) Toughness index

The ability of fiber-reinforced composites to absorb energy can be quantified by calculating their toughness, which is defined as the area beneath the load–deflection curve up to a pre-defined deflection. The ASTM C1609 standard designates this deflection limit as 1/150 of the sample's span length, as indicated by Onuaguluchi et al. (2014). However, the considerable ductility of the UHDMC necessitates an adjustment to this limit. With flexural-hardening fiber-reinforced composite materials, a deflection limit set at 1/50 of the span length is more appropriate, as proposed by Naaman and Reinhardt in 1996 (Naaman & Reinhardt, 1996). The toughness index (T) is determined by Eq. 5.4 as the difference between the area (T_{MOR}) under the load–deflection curve up to the ultimate deflection, and the area (T_{LOP}) under the load–deflection curve up to the deflection at cracking.

$$T = T_{MOR} - T_{LOP} \tag{5.4}$$

5.2.7 Water Stability Evaluation

The assessment of water stability involves determining the retention rates of compressive strength, first-cracking strength, ultimate flexural strength, ductility index, and toughness index. A higher retention rate corresponds to superior water stability in the specimen. Equations 5.5, 5.6, and 5.7 are used to compute the compressive strength retention rate (k_C), first-cracking strength retention rate (k_{LOP}), and ultimate flexural strength retention rate (k_{MOR}), respectively.

$$k_C = \frac{f_{ct}}{f_{c0}} \times 100\% \tag{5.5}$$

$$k_{LOP} = \frac{f_{LOPt}}{f_{LOP0}} \times 100\% \tag{5.6}$$

$$k_{MOR} = \frac{f_{MORt}}{f_{MOR0}} \times 100\% \tag{5.7}$$

where f_{ct}, f_{LOPt}, and f_{MORt} are the compressive strength (MPa), first-cracking strength (MPa), and ultimate flexural strength (MPa) of the immersed specimens (with 7 day immersion in water after 7 day curing), and f_{c0}, f_{LOP0}, and f_{MOR0} are the compressive strength (MPa), first-cracking strength (MPa), and ultimate flexural strength (MPa) of the non-immersed specimens (without 7 day immersion in water after 7 day curing).

The ductility index retention rate (k_{DI}) is calculated using Eq. 5.8.

$$k_{DI} = \frac{DI_{\mathrm{t}}}{DI_0} \times 100\% \tag{5.8}$$

where DI_0 is the ductility index of non-immersed specimens (without 7 days immersion in water after 7 day curing), and DI_t is the ductility index of immersed specimens (with 7 day immersion in water after 7 day curing).

The toughness index retention rate (k_T) is calculated using Eq. 5.9.

$$k_T = \frac{T_{\mathrm{t}}}{T_0} \times 100\% \tag{5.9}$$

where T_0 is the toughness index of the non-immersed specimens (without 7 day immersion in water after 7 day curing), and T_t is the toughness index of the immersed specimens (with 7 day immersion in water after 7 day curing).

5.2.8 *Microstructure*

Scanning electron microscopy (SEM) test was carried out to inspect the specimens on a microscopic scale. Precision gas cutting machinery was utilized to fracture and resize the specimens to 1 mm^2 before they were scrutinized with a field-emission scanning electron microscope (Zeiss, Oberkochen, Germany). The influence of NA on the flexural properties and water durability of the UHDMC was studied through evaluating alterations in the specimens' microstructure.

5.3 Results and Discussion

5.3.1 *Effect of Ambient Curing Age and Water Immersion Age*

(1) **Compressive strength and compressive strength retention rate**

Figure 5.4a, b displays the compressive strength and compressive strength retention rate of the UHDMC under ambient curing conditions for both 7 and 28 days. The 7 day compressive strength (44.8 MPa) observed in non-immersed UHDMC marginally

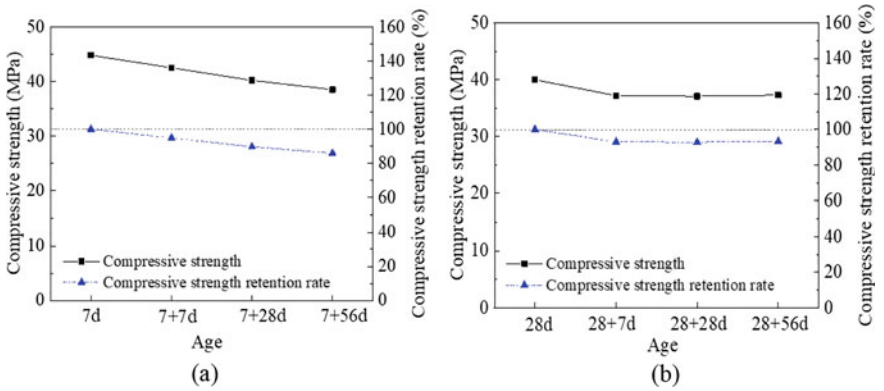

Fig. 5.4 Compressive strength and its retention rate of UHDMC with **a** 7 days and **b** 28 days of ambient curing. Reproduced from Mechanical Properties and Water Stability of High Ductility Magnesium Phosphate Cement-Based Composites (HDMC) by Hu Feng with permission from MDPI

surpasses the strength measured at 28 days, which is 40 MPa. For water-immersed UHDMC, the 7 day curing period consistently results in greater compressive strength irrespective of the duration of water exposure when compared to 28 day curing. Furthermore, as demonstrated in Fig. 5.4, the UHDMC's compressive strength under 7 day curing evidently decreases as the period of water immersion extends from zero to 56 days. However, the compressive strength of the 28 day cured UHDMC reduces marginally, particularly noticeable when the water immersion period ranges from 7 to 56 days.

Figure 5.4 highlights that the UHDMC cured at ambient conditions for 28 days surpasses its 7 day cured variant in terms of compressive strength retention rate, underscoring the water stability enhancement associated with longer curing. This phenomenon stems from the advancement of MPC hydration, denser structure, fewer unreactive phosphates, and minimized phosphate dissolution post-immersion, all resulting from extended ambient curing. Furthermore, Fig. 5.4a showcases a drop in the compressive strength retention rate for the 7 day cured UHDMC as the water immersion duration lengthens, registering at 86% after 56 days. However, Fig. 5.4b illustrates a minimal fluctuation in the compressive strength retention rate for the 28 day cured UHDMC across the 7–56 day water immersion period, remaining stable at roughly 93%. This underscores that the complete hydration attained with 28 day ambient curing attenuates the influence of immersion duration on compressive strength.

(2) **Flexural properties**

Using Eqs. (5.1)–(5.7), the strength index (including first-crack strength and ultimate flexural strength), ductility index, and toughness index can be ascertained for UHDMC with varying ambient curing durations and water immersion periods. The derivation of these parameters, as well as the impact of curing and immersion age

on them, are presented in Fig. 5.5. The figure reveals that the UHDMC cured for 28 days at ambient conditions exhibits higher first-crack strength and ultimate flexural strength only if subjected to either 28 or 56 days of water immersion. Its ductility index is found to be higher when immersed for 7 or 56 days, while the toughness index shows amplification only after 56 days of water immersion. However, comparing the UHDMCs cured for 7 and 28 days at ambient, the latter does not display a markedly improved strength index, ductility index, or toughness index.

Figure 5.5 illustrates that the 7 day ambient-cured UHDMC sees a general reduction in the first-crack strength, ultimate flexural strength, and toughness index with the expansion of the water immersion time, although the ultimate flexural strength slightly increases after 56 days of immersion compared to 28 days. Meanwhile, its ductility index initially experiences an increase, peaking at 22.07 mm after 28 day water immersion, before subsequently decreasing. Regarding the 28 day ambient-cured UHDMC, an upward trend in the first-crack strength is visible as the water immersion age extends. Its ultimate flexural strength drops initially, then starts

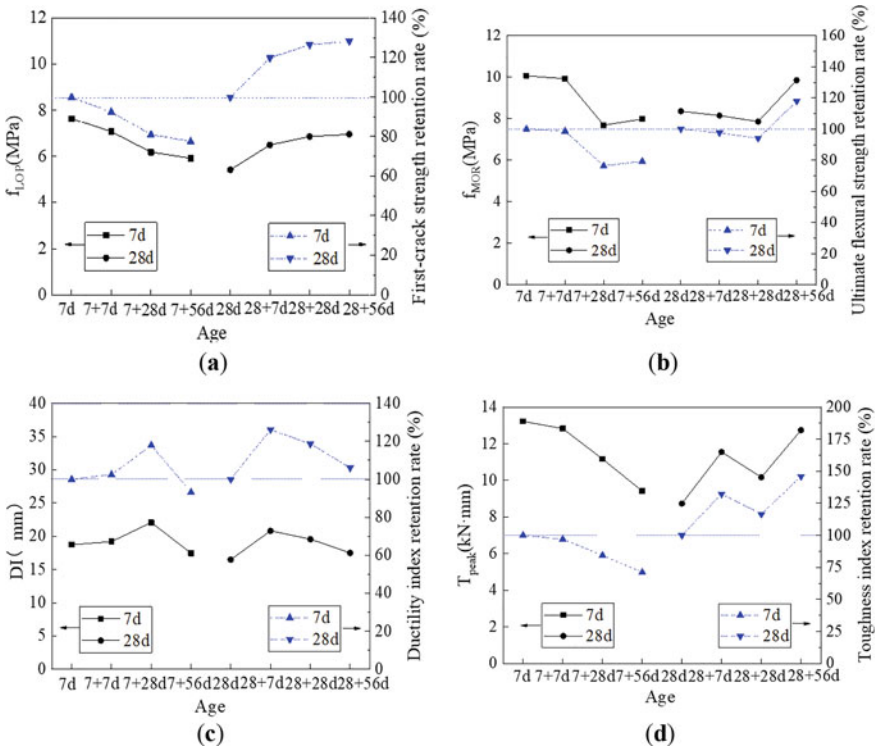

Fig. 5.5 **a** First-crack strength, **b** ultimate flexural strength, **c** ductility index, and **d** toughness index, together with their retention rates, of UHDMC with different ambient curing ages and water immersion ages. Reproduced from Mechanical Properties and Water Stability of High Ductility Magnesium Phosphate Cement Based Composites (HDMC) by Hu Feng with permission from MDPI

growing, reaching a pinnacle of 9.85 MPa after 56 days of water immersion. Interestingly, similar to the 7 day cured UHDMC, the ductility index for the 28 day variety also increases first, peaking at 20.81 mm after 7 day immersion, and then it shrinks. Importantly, the toughness index consistently progresses, maxing out at 12.75 kN mm after 56 days in water. In summary, increased water immersion time generally degrades the strength index, ductility index, and toughness index for the UHDMC that undergoes 7 day ambient curing. Nevertheless, the indexes of the 28 day ambient-cured UHDMC are less vulnerable and often show signs of improvement, particularly when the water immersion period extends to 56 days.

Figure 5.5 presents information that the UHDMC that's undergone ambient curing for 28 days retains its initial first-crack strength, ultimate flexural strength, ductility, and toughness better than its counterpart that's cured for only 7 days, thus demonstrating superior water stability. This outcome can be attributed to the fact that an extended period of ambient curing reduces the quantity of unreacted phosphates within the UHDMC matrix while simultaneously boosting the volume of hydration products. Furthermore, it also contributes to the densification of the matrix structure.

In Fig. 5.5, it's observed that as the water immersion age augments for the UHDMC exposed to 7 days of ambient curing, the retention rates for first-crack strength, ultimate flexural strength, and toughness are on a decreasing trend. Nonetheless, the ductility retention rate initially experiences an increase, peaking at 117.84% at the 28 day immersion mark, and then plunges. Conversely, for UHDMC subjected to 28 days of ambient curing, the first-crack strength retention rate gently escalates with the progression of immersion age, achieving a zenith of 128.23% at the 56 day watermark. The ultimate flexural strength retention rate first slumps slightly before ascending, achieving its apex of 117.87% after 56 days submerged underwater. Ductility retention rate follows a saw-tooth pattern—first rising, then falling—reaching its pinnacle of 126.17% after 7 days of immersion. In a general sense, the toughness retention rate undergoes an upward swing, peaking at 145.95% after 56 days underwater. It becomes apparent that the patterns of strength, ductility, and toughness retention rates match those of corresponding indices. As such, typically, as the water immersion age extends, the water stability for the 7 day ambient-cured UHDMC deteriorates. However, the water stability for the UHDMC with 28 days of ambient curing could be seen to enhance under many conditions, particularly true when at 56 days of immersion.

5.3.2 Effect of W/B Ratio

(1) **Workability**

Table 5.6 illustrates the substantial influence of *W/B* on UHDMC's workability. At 0.14 for the *W/B* ratio, the flow diameter measures only 34.75 cm, with no T500 occurrence, yielding poor fluidity due to uniform fiber dispersion. As the *W/B* ratio elevates to 0.16, it's marked with significant enhancements in T500, slump, and flow

diameter, resulting from fiber uniformity that improves workability. Further, raising the *W/B* to 0.18 or 0.20 enhances water content, leading to even more uniformly dispersed fibers and a modest uplift in the UHDMC's workability.

(2) **Compressive strength and compressive strength retention rate**

The graphic representation in Fig. 5.6 elucidates the relation between the *W/B* ratio and the compressive strength, including its retention rate, for both non-immersed (referred to as "7d") and submerged UHDMC (marked as "7 + 7d"). As the *W/B* ratio grows, there is a noticeable decrease in the compressive strength of 7d UHDMC—from 49.5 down to 43.8 MPa, while the strength in the 7 + 7d case drops from 47.1 to 41.4 MPa. This decline of the compressive strength of the UHDMC is attributed to an increase in the volume of the pores in the matrix, a byproduct of surplus water evaporation when the *W/B* ratio is pushed higher (Ma et al., 2014; Sun et al., 2016).

The information depicted in Fig. 5.6 reveals a compressive strength retention rate in UHDMC that is below one. Under water immersion, the dissolution of certain hydration products, along with some phosphates, results in a diminished hydration level in MgO grains, consequently impeding the creation of additional hydration products. Figure 5.6 further shows a minor reduction in the UHDMC's compressive strength retention rate as the *W/B* ratio increases. At higher *W/B* ratios, though the

Table 5.6 Effect of *W/B* on the workability of UHDMC

Samples	T_{500}(s)	Slump (mm)	Flow diameter		
			Horizontal direction (cm)	Perpendicular direction (cm)	Average value (cm)
W/B-0.14	–	205	36	33.5	34.75
W/B-0.16	3.85	255	49	51	50
W/B-0.18	2.21	265	53.5	54	53.75
W/B-0.20	1.35	280	73	68	70.5

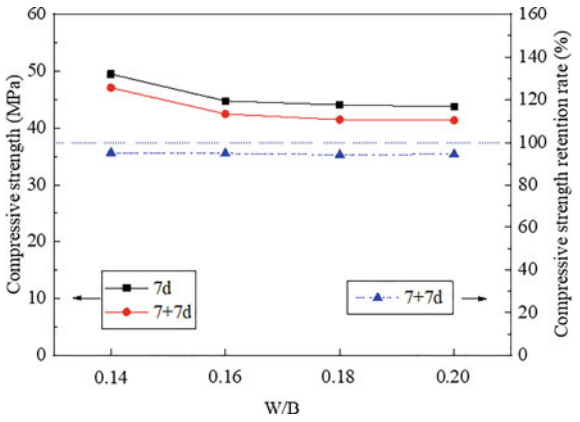

Fig. 5.6 Compressive strength and its retention rate of UHDMC with different *W/B* ratios. Reproduced from Mechanical Properties and Water Stability of High Ductility Magnesium Phosphate Cement-Based Composites (HDMC) by Hu Feng with permission from MDPI

formation of hydration products is reduced and some dissolve, magnifying the matrix defects, there's an increase in unreacted MgO grain presence. The stronger overlapping effect of central particles, compared to the unreacted HDMC matrix, could be the reason why there's only a marginal alteration in the compressive strength retention rate (Yang, 2011).

(3) **Flexural properties**

Equations (5.1)–(5.7) are utilized to measure the strength index (including first-crack strength and ultimate flexural strength), ductility index, toughness index, as well as their respective retention rates. Figure 5.7 demonstrates the influence of the *W/B* ratio over these parameters. Observations indicate that for non-submerged UHDMC, as the *W/B* ratio ascends from 0.14 to 0.20, the first-crack strength first experiences a minor surge before decreasing to its peak value of 7.74 MPa at *W/B* of 0.18; ultimate flexural strength experiences a consistent decrease; ductility index and toughness index rise and subsequently fall, hitting their zenith of 18.73 mm and 13.23 kN mm respectively at a *W/B* ratio of 0.16.

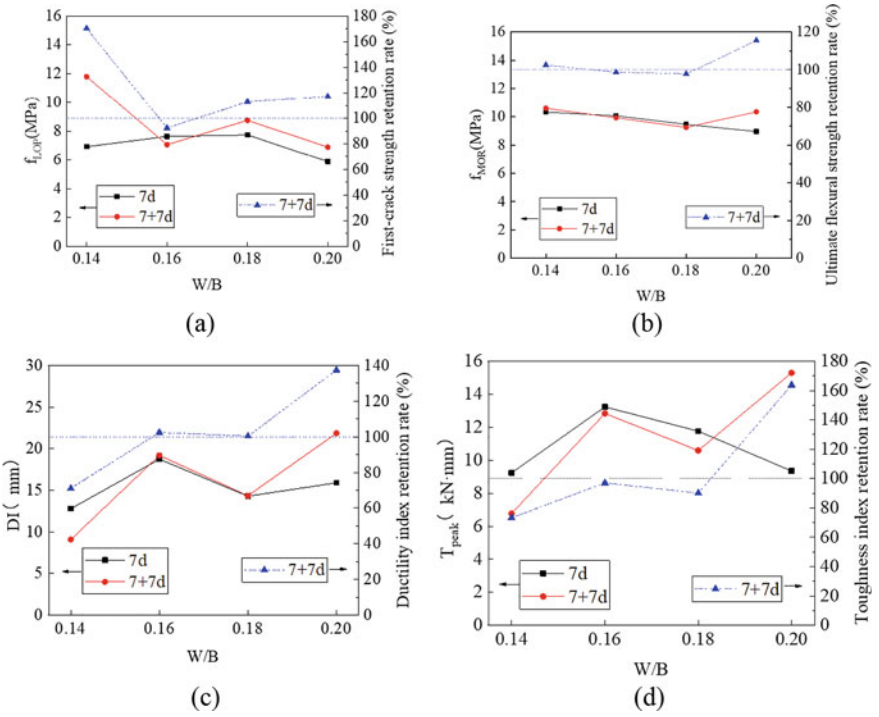

Fig. 5.7 **a** First-crack strength, **b** ultimate flexural strength, **c** ductility index, and **d** toughness index, together with their retention rates, of UHDMC with different *W/B* ratios. Reproduced from Mechanical Properties and Water Stability of High Ductility Magnesium Phosphate Cement-Based Composites (HDMC) by Hu Feng with permission from MDPI

In contrast, for the soaked UHDMC, the *W/B* ratio escalation from 0.14 to 0.20 manifests a downturn in first-crack strength and ultimate flexural strength, whereas the ductility index and toughness index generally illustrate an upward trend except at the *W/B* ratio of 0.18. Therefore, when considering the non-immersed UHDMC, all indexes—strength, ductility, and toughness—yield satisfactory results at a *W/B* ratio of 0.16. On the other hand, for submerged UHDMC, the most optimal strength index has its genesis at the *W/B* ratio of 0.14, the ductility index and toughness index peak at the *W/B* ratio of 0.20, and a *W/B* ratio of 0.16 yields moderate values across all three indexes.

As depicted in Fig. 5.7a, b, the *W/B* ratio's growth initially leads to a decline, and subsequently an ascent, in the retention rates of first-crack strength and ultimate flexural strength. The peak retention rate of first-crack strength occurs at a *W/B* ratio of 0.14, while the retention rate of ultimate flexural strength maximizes at 115.53% when the *W/B* ratio is 0.20. Meanwhile, Figs. 5.7c, d highlight that the retention rates of ductility and toughness overall enhance with the increment of the *W/B* ratio, marking their zenith at 137.48 and 163.7% respectively, at a *W/B* ratio of 0.20.

Typically, the indices for strength, ductility, and toughness are adequate at a *W/B* ratio of 0.16. The peak retention rates for strength, ductility, and toughness appear to be achieved at a *W/B* ratio of 0.20, signifying superior water stability. This is closely trailed by the performance at a *W/B* ratio of 0.16. As such, factoring in both mechanical attributes and water stability, a *W/B* ratio of 0.16 emerges as a highly suitable choice for UHDMC.

5.3.3 Effect of M/P Ratio

(1) **Workability**

Variations in the *M/P* ratio indeed affect the workability of UHDMC, as detailed in Table 5.7. It's observed that with an increase in *M/P*, both the slump and flow diameter initially rise before experiencing a drop. In particular, a T500 time is present only when *M/P* equals to 4, suggesting this is the ratio at which UHDMC displays good flowability and can extend the flow diameter to 50 cm. In contrast, lesser flowability is observed when *M/P* is set to 3, 5, or 6, resulting in a smaller slump and flow diameter. This might also lead to a less uniform distribution of fiber compared to the case of *M/P* being 4.

(2) **Compressive strength and compressive strength retention rate**

Depicted in Fig. 5.8 is both the compressive strength and the corresponding retention rate for UHDMC subjected to immersion and those not, considering varying *M/P* ratios. An upward trend can be discerned for the compressive strength of UHDMC

Table 5.7 Effect of *M/P* on the workability of UHDMC

Samples	T_{500}(s)	Slump (mm)	Flow diameter		
			Horizontal direction (cm)	Perpendicular direction (cm)	Average value (cm)
M/P-3	–	242	43	40	41.5
M/P-4	3.85	255	49	51	50
M/P-5	–	217	38	38.5	38.25
M/P-6	–	215	38	38	38

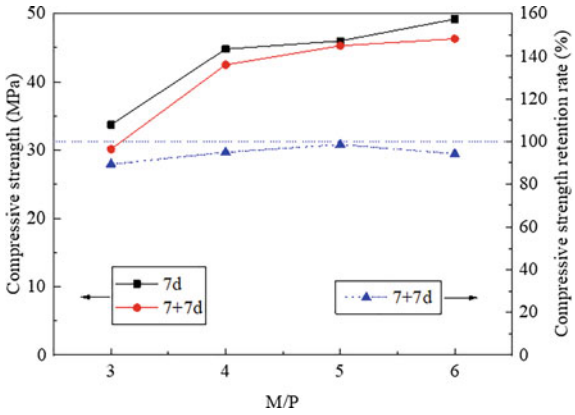

Fig. 5.8 Compressive strength and its retention rate of UHDMC with different *M/P* ratios. Reproduced from Mechanical Properties and Water Stability of High Ductility Magnesium Phosphate Cement-Based Composites (HDMC) by Hu Feng with permission from MDPI

across all *M/P* ratios irrespective of water exposure. Particularly, the compressive strength for the non-immersed UHDMC witnesses a rise from 33.7 to 49.2 MPa as the *M/P* ratio moves from 3 to 6. Similarly, for the immersed UHDMC, the compressive strength witnesses a comparable growth pattern, starting at 30.1 and ending at 46.3 MPa.

Relative to the non-immersed UHDMC, the immersed UHDMC displays a lower compressive strength, which results in a compressive strength retention rate of less than 100%, a fact visually represented in Fig. 5.8. It can also be seen from the same figure that the compressive strength retention rate of the UHDMC initially rises before falling as the *M/P* ratio ascends. Its peak value, 98.5%, is achieved at an *M/P* ratio of 5, underscoring the optimal water stability at this ratio. This could be attributed to the large quantity of MgO making the UHDMC matrix microstructure largely compact. Yet, a minor dip in the compressive strength retention rate is observed when the *M/P* ratio touch 6, possibly due to the overabundance of MgO that completes the early hydration reaction more comprehensively, leading to a more pronounced growth in compressive strength after a week-long ambient curing.

(3) **Flexural properties**

The various indices of strength (including first-crack and ultimate flexural strength), ductility, and toughness for both the non-immersed and the immersed UHDMC at differing *M/P* ratios are depicted in Fig. 5.9. For the non-immersed UHDMC, an incremental *M/P* ratio from 3 to 6 doesn't substantially alter the first-crack strength. The ultimate flexural strength initially elevates and then declines, with a peak value of 12.16 MPa observed at an *M/P* ratio of 5. Similarly, the indices for both ductility and toughness initially rise and later descend, with their apices, 18.73 mm and 14.07 kN mm, captured at *M/P* ratios of 4 and 5, respectively. For the immersed variant of the UHDMC, a rise in the *M/P* ratio from 3 to 6 causes a steady reduction in the first-crack strength. In contrast, the ultimate flexural strength, as well as the ductility and toughness indices, see an initial upswing, followed by a downswing, maxing out at values of 10.28 MPa, 29.36 mm, and 18.11 kN mm correspondingly, all at an *M/P* ratio of 5. Thus, it can be concluded that a satisfactory strength, ductility and toughness index is attained at an *M/P* ratio of 5 for both non-immersed and immersed UHDMC.

As the *M/P* ratio escalates from 3 to 6, a downward trajectory is generally observed in the retention rates for first-crack strength and ultimate flexural strength of UHDMC, with the peak values being 98.51 and 134.58% respectively at an *M/P* ratio of 3. Conversely, the retention rates for ductility and toughness initially shrink, then expand, achieving their zenith at 295.6 and 195.91% correspondingly when the *M/P* ratio is dialed up to 6.

Typically, an *M/P* ratio of 5 leads to satisfactory results in terms of strength, ductility, and toughness indices. However, the water stability of UHDMC at this ratio could be classified as moderate, based on retention rate analysis. For optimal water stability, an *M/P* ratio of 3 is found to yield the best results.

(4) **Microscopic analysis**

The microstructure of UHDMC is revealed through SEM image analysis. The matrix of the UHDMC that's not been immersed, cured in ambient conditions for seven days, is displayed in Fig. 5.10a. The dominance of wedge-shaped struvite-K crystals in the matrix can be observed, which are tightly packed. Figure 5.10b provides insight into the relationship between fibers and the matrix in the same UHDMC. Observing the fibers highlights that their cross-sectional structure remains relatively unchanged. Characteristics on the fiber surface such as scratches, grooves, and the presence of hydration products suggest strong adherence between the fibers and the surrounding matrix. Furthermore, fibers are more likely to be detached from the matrix rather than getting fractured, indicative of good bonding strength.

The UHDMC's matrix, following a 7 day ambient curing period and subsequently a 7 day water immersion, is depicted in Fig. 5.11a. The presence of numerous small particles adjoined to struvite-K crystals is noticeable, which have been identified as either unreacted MgO or MgO derived from struvite-K decomposition. Thus, it implies that the hydration reaction yields less struvite-K; the crystalline interstices are broadened as a result. It highlights that the week-long water immersion exerts

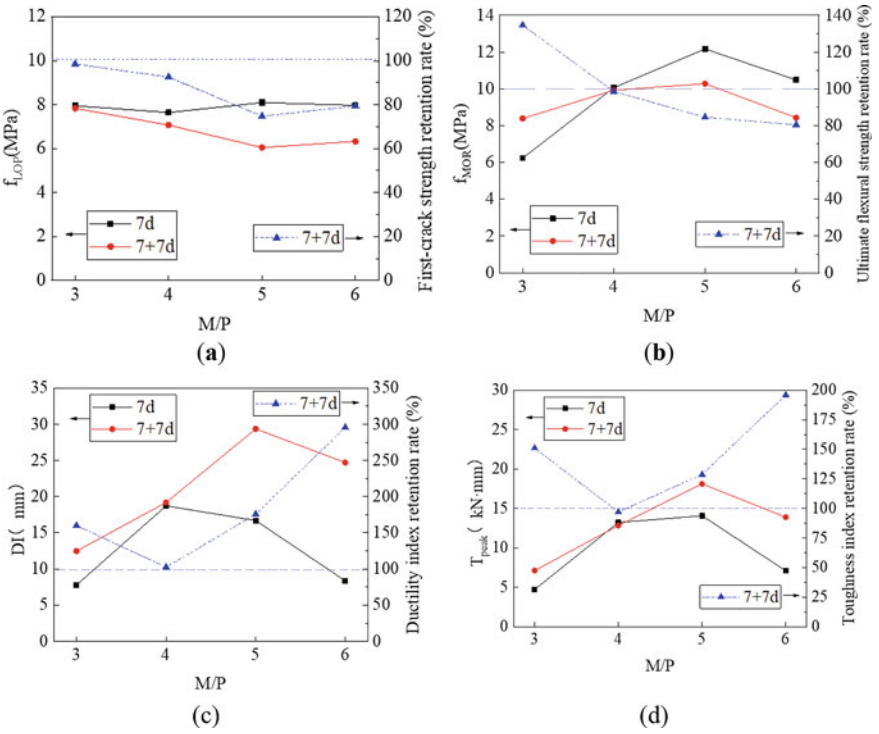

Fig. 5.9 **a** First-crack strength, **b** ultimate flexural strength, **c** ductility index, and **d** toughness index, together with their retention rates, of UHDMC with different *M/P* ratios. Reproduced from Mechanical Properties and Water Stability of High Ductility Magnesium Phosphate Cement-Based Composites (HDMC) by Hu Feng with permission from MDPI

a significant negative impact on the matrix, leading to an indirect reduction in the UHDMC's mechanical properties. This perspective aligns with the reported compressive strength (42.5 MPa) of the water-immersed UHDMC being 5.1% less than the non-immersed variety.

Depicted in Fig. 5.11b is the intermingling of fibers and the matrix in the 7 day water-immersed UHDMC. Post-immersion, the intervals between the fibers and the matrix have increased, indicating suboptimal bonding. The fiber surface is comparatively smoother than that in the non-immersed UHDMC, with a visibly lower quantity of adjoined hydration products. A plausible explanation for this may be the dissolution of unreacted potassium dihydrogen phosphate post-immersion, which renders the solution mildly acidic. This shift triggers a reversal of the hydration reaction, culminating in the decomposition of the hydration product struvite-K. The notion aligns with the slight reduction in the UHDMC's ultimate flexural strength after a 7-day water immersion.

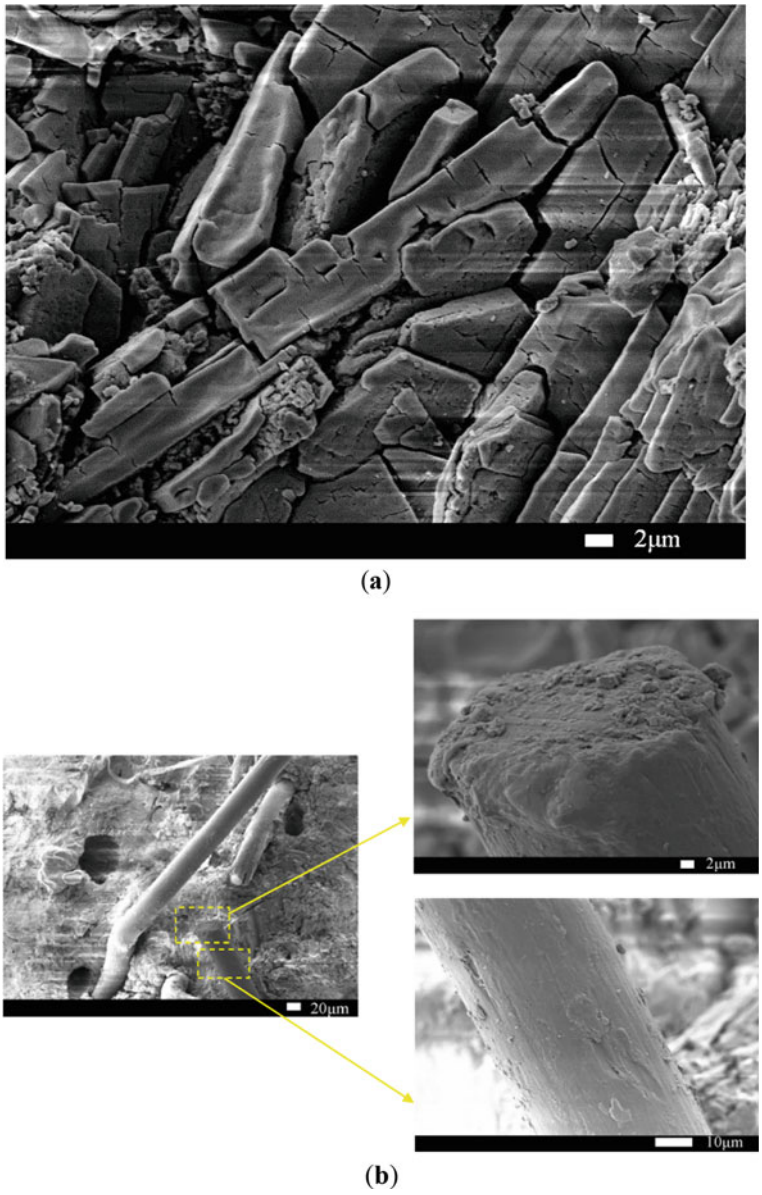

Fig. 5.10 **a** The matrix and **b** its bonding with fibers for non-immersed UHDMC. Reproduced from Mechanical Properties and Water Stability of High Ductility Magnesium Phosphate Cement-Based Composites (HDMC) by Hu Feng with permission from MDPI

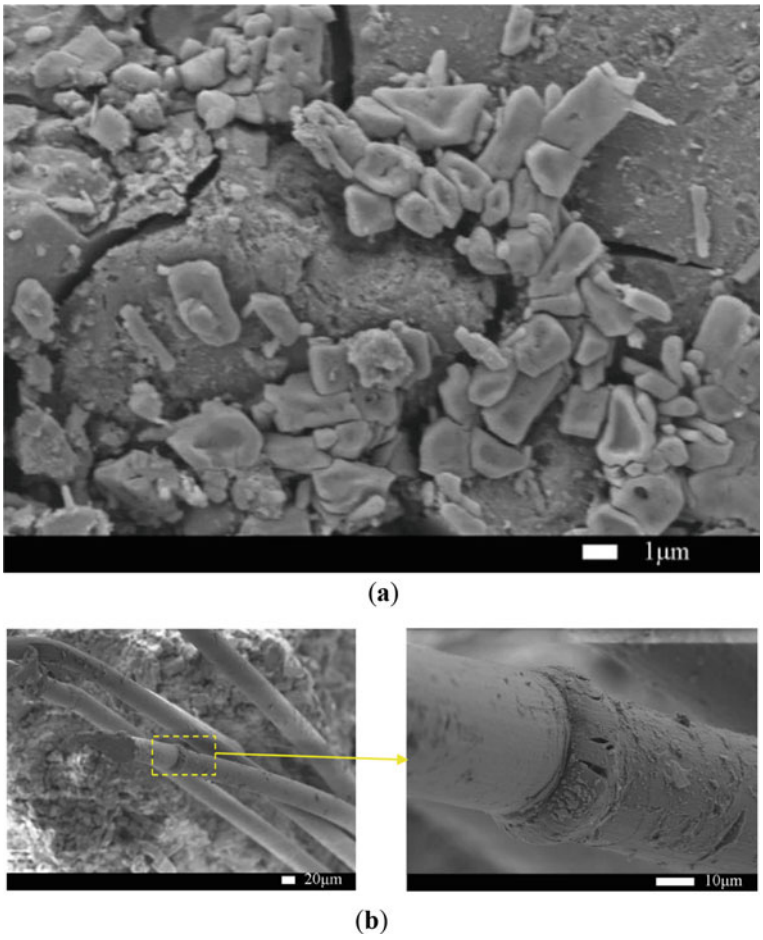

Fig. 5.11 **a** The matrix and **b** its bonding with fibers for UHDMC with 7-day water immersion. Reproduced from Mechanical Properties and Water Stability of High Ductility Magnesium Phosphate Cement-Based Composites (HDMC) by Hu Feng with permission from MDPI

5.3.4 Effect of NA Content

(1) **Workability**

Table 5.8 outlines the influence of NA content on the workability of UHDMC, and the marginal error of all data is capped at five percent. A slightly lower T500 is observed in specimens with NA compared to NA-free ones. Minor fluctuations in the slump and flow diameter of UHDMC occur with an increase of NA content from 0 to 6%, implying a minimal impact of NA content on UHDMC's workability. However, as the NA content escalates to 8% or 10%, the slump and flow diameter shrink, suggesting a more challenging workability. Furthermore, a comprehensive

assessment of the mixtures reveals that all mixtures possess favorable workability, with NA content ranging from 0 to 10%.

(2) **Compressive strength and compressive strength retention rate**

Figure 5.12 presents the impact of NA content on the UHDMC's compressive strength and its capability to retain this property. As it's evident from the figure, the compressive strength in the specimens experiences an initial increase followed by a decline as NA content escalates, with this trend persisting even when the samples have been water-immersed. This boost in compressive strength stems from the high reactivity of nano-Al_2O_3 particles. These tiny particles engage actively in reactions with KH_2PO_4 and MgO, culminating in the formation of $AlPO_4 \times H_2O$ (APH) and $MgAl_2O_4$ (or Spinel)) (Nazari et al., 2010). The resultant crystalline by-products infill the pores, optimizing the aggregate-paste interfacial transition zone and minimizing the MKPC composites' porosity (Yu et al., 2021). However, excessive NA content induces a higher consumption of potassium dihydrogen phosphate, leaving a larger volume of unreacted MgO. This imbalance leads to inadequate hydration products to encase the unreacted MgO surface or accumulate between MgO particles—a factor that causes the structure to lose its compactness and consequently lowers the compressive strength (Yang et al., 2013). The pinnacle of compressive strengths logged in the records—51.8 MPa for non-immersed and 52.7 MPa for immersed samples—is attained when the NA content is at 8%.

It's evident from Fig. 5.12 that the compressive strength of water-immersed samples is lower than the dry samples when there's no NA content (0), yielding a compressive strength retention rate of 94.9%. This suggests that despite further hydration potential for immersed samples, limited water stability restricts the growth in compressive strength. However, upon the addition of NA, an improvement in the compressive strength in soaked samples over dry samples is observed. The compressive strength retention rate value also shows a notable enhancement, surpassing 100% (barring when NA is at 10%). Hence, the incorporation of NA plays a vital role in

Table 5.8 Effect of NA content on the workability of UHDMC

Samples	T_{500}(s)	Slump (mm)	Flow diameter		
			Horizontal direction (cm)	Perpendicular direction (cm)	Average value (cm)
NA-0	3.85	255	49	51	50
NA-2	2.06	257	48.5	49	48.75
NA-4	2.19	260	52.5	55	53.75
NA-6	2.26	255	50	51.5	50. 75
NA-8	2.36	245	46	48	47
NA-10	3.08	243	46	46.5	46.25

Reproduced from Assessment of the mechanical properties and water stability of nano-Al_2O_3 modified high ductility magnesium potassium phosphate cement-based composites by Hu Feng with permission from Elsevier

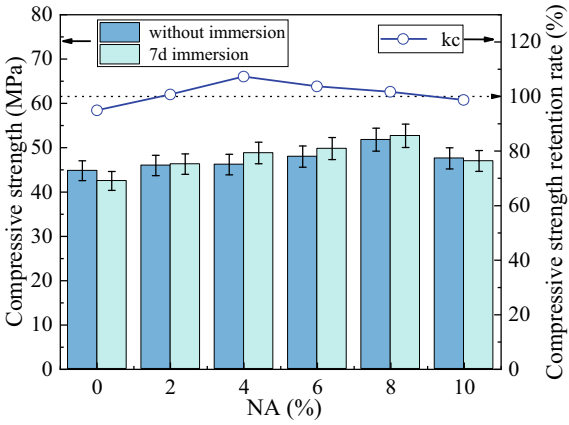

Fig. 5.12 Compressive strength and compressive strength retention rate under different NA contents. Reproduced from Assessment of the mechanical properties and water stability of nano-Al_2O_3 modified high ductility magnesium potassium phosphate cement-based composites by Hu Feng with permission from Elsevier

amplifying the water stability of the UHDMC. Crystalline products like $AlPO_4 \cdot xH_2O$ and $MgAl_2O_4$, facilitated by NA, occupy the voids thus curbing the concrete porosity. This strengthens the compactness, improves the mechanical attributes, restricts permeability of cement-oriented material, and elevates water stability. Moreover, NA elevates the pH value of the solution, thus mitigating the disintegration of struvite-K and bolstering the strength of the soaked matrix (Münch & Barr, 2001). Furthermore, Fig. 5.12 illustrates that the compressive strength retention rate sees a surge before a drop as the NA content increases, peaking at 107.3% when NA is at 4%.

(3) **Flexural properties**

Figure 5.13 presents the flexural load-midspan deflection plots for unsoaked specimens with varying rates of NA. A pattern is evident where the ultimate load sees an initial boost with increasing NA concentrations, drops thereafter, and the peak value (1.012 MPa) is recorded at 6% NA level. The ultimate deflection experiences marginal adjustments across all NA amounts, except when the NA content hits 10%. As we turn our attention to Fig. 5.14, we observe the midspan deflection curves under flexural load for water-immersed samples, measured against different NA levels. Again, it is clear that as NA concentration rises, the ultimate load first experiences an increase, then a decline, while the ultimate deflection initially diminishes, escalates next, and then finally reduces again. The pinnacle for ultimate load is marked at 1.151 MPa when NA content is 2%, and this coincides with a peak deflection of 21.189 mm.

The diagrams in Fig. 5.15 showcase the impact of various NA quantities on the cracking strength, ultimate flexural strength, ductility index, and toughness index of samples, allowing subsequent calculation of these attributes along with their retention rates. For untreated samples, as indicated in the figure, any escalation in NA content prompts a subsequent rise and fall in the cracking and ultimate flexural strength together with ductility and toughness indices. Specifically, maxima for cracking and ultimate flexural strengths are indicated in Fig. 5.15a, b and total at 10.26 and 11.73 MPa with NA concentration at 4%. In turn, Fig. 5.15c, d pinpoint

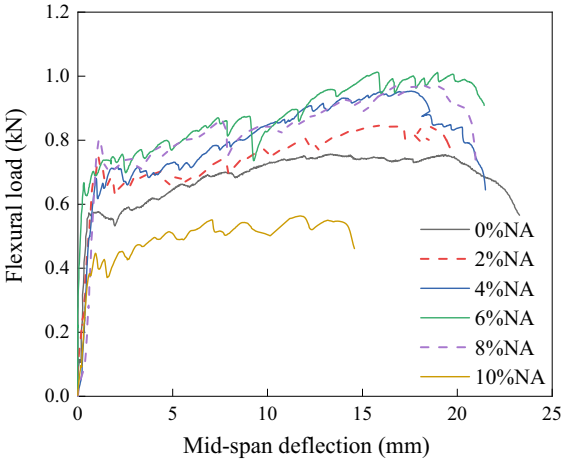

Fig. 5.13 Flexural load–deflection curves of non-immersed samples with different NA contents. Reproduced from Assessment of the mechanical properties and water stability of nano-Al_2O_3 modified high ductility magnesium potassium phosphate cement-based composites by Hu Feng with permission from Elsevier

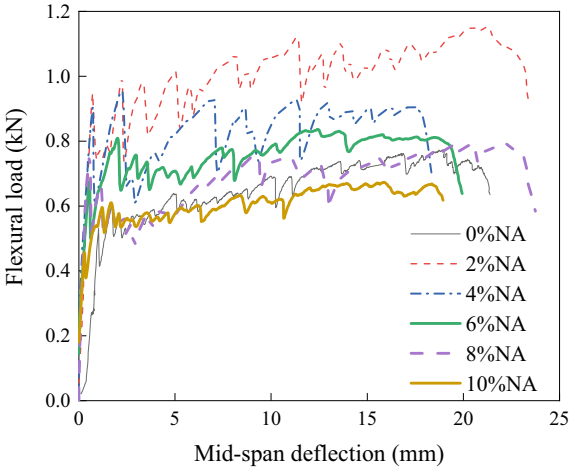

Fig. 5.14 Flexural load–deflection curves of immersed samples with different NA content. Reproduced from Assessment of the mechanical properties and water stability of nano-Al_2O_3 modified high ductility magnesium potassium phosphate cement-based composites by Hu Feng with permission from Elsevier

the highest ductility and toughness measures at 18.12 mm and 14.03 kN·mm as NA content equates to 6%. As for water-soaked samples, it's apparent in Fig. 5.15a, b that augmenting the NA rate boosts cracking and ultimate flexural strengths only until 2% NA, with respective apexes at 11.20 and 13.73 MPa. Consequent to this, a decline becomes perceptible, potentially due to excessive NA shrouding cement particles and curtailing optimal hydration reactions, hence attenuating production of hydration byproducts. Figure 5.15c, d denote that though some irregularities occur as NA content grows, the ductility and toughness indices generally follow a pattern of initial increase and later decline. The maximum ductility level is seen at 18.16 mm with 4% NA, while peak toughness (17.63 kN mm) coincides with usage of 2% NA.

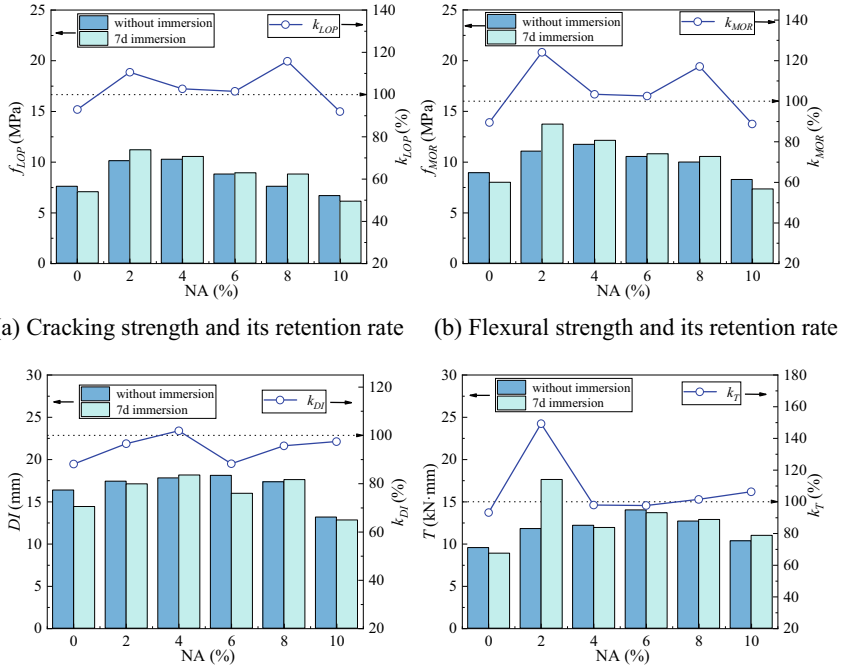

(a) Cracking strength and its retention rate

(b) Flexural strength and its retention rate

(c) Ductility index and its retention rate

(d) Toughness index and its retention rate

Fig. 5.15 Flexural properties and corresponding retention rates of samples with different NA contents. Reproduced from Assessment of the mechanical properties and water stability of nano-Al_2O_3 modified high ductility magnesium potassium phosphate cement-based composites by Hu Feng with permission from Elsevier

Figure 5.15 reveals that the retention rates of different attributes like cracking strength, ultimate flexural strength, ductility index, and toughness index vary as per the increase in NA content. As demonstrated by Fig. 5.15a, b, for the k_{LOP} and k_{MOR} of samples, the values exceed 100%. They peak at NA contents of 8 and 2%, respectively, barring the 10% NA test specimens. This pattern suggests that when the NA content does not exceed 10%, both the cracking strength and the ultimate flexural strength for the submerged specimens surpass those of the dry ones. This could be due to NA modulating the pH value of the solution and slowing down the decomposition of struvite-K, which in turn lends strength to the soaked matrix. However, when the sample contains 10% NA, the retention rates of cracking strength and ultimate flexural strength fall below 100%, even marginally underperforming compared to the NA-free counterparts. On Fig. 5.15c, it's evident that the retention rate of ductility index (k_{DI}) typically remains somewhat below 100%, thus showing that the ductility of soaked samples is somewhat compromised relative to the dry ones. However, in comparison to NA-free samples, a marginal improvement in k_{DI} is shown. Figure 5.15d exhibits that when the NA concentration sits at 2%, the retention rate of the toughness index (k_T) exceeds 100% significantly, but there isn't a notable

change (approximately 100%) for other levels of NA, which implies that toughness indices for soaked and non-soaked samples share a likeness. Compared to the NA-free counterparts, k_T exhibits minor change, except where NA content is 2%. As an overview, the inclusion of 2–6% NA results in superior flexural characteristics and water stability of the UHDMC, but increasing NA content beyond 6% may potentially bring about unfavorable consequences.

(4) **Microscopic analysis**

Our findings from the compressive tests and four-point flexural analyses indicate that, at an 8% proportion of NA, we observe the peak in compressive strength. This value also displays commendable retention in compressive strength while demonstrating satisfactory ductility and toughness indexes post water immersion. As a result, we have chosen the samples with 8% NA for further SEM inspection and evaluation.

The microscopic images of the non-immersed UHDMC without NA and with an 8% NA inclusion are depicted in Figs. 5.16 and 5.17, respectively. Observing Fig. 5.16, it's apparent that the cohesion between the fibers and matrix is subpar, with noticeable gaps. The surface of the fiber appears rough due to the adherence of some hydration products. Additionally, no substantial variation in the fiber's cross-section is noticeable, suggesting that fibers may have been pulled from the matrix, not fractured, thus limiting their ability to fully express superior tensile characteristics. When we examine Fig. 5.17, we note that the incorporation of 8% NA leads to a substantial amount of material, likely hydration products like $MgKPO_4 \cdot 6H_2O$ (struvite-K), $AlPO_4 \cdot xH_2O$, and $MgAl_2O_4$, adhering to the surface of the fibers (Xu et al., 2019). Moreover, visible stretching, along with changes in fiber cross-sectional diameter, is evident at the fiber tips, indicating significant resistance to fiber pull-out. Such recently formed substances likely crystallized as microscopic grains, occupying voids in the matrix, which renders the UHDMC structure denser and the crystal distribution more homogenous (Feng et al., 2020). These hydration products infiltrate the zone of transition between fiber and matrix, reinforcing the density of the bonding region while also enhancing the physical bonding between the fiber and matrix. Consequently, the tensile characteristics of the fibers can be fully utilized, and by implementing NA, the matrix's strength can be enhanced.

Figures 5.18a, b depict the UHDMC matrix's microstructure without NA and with an addition of 8% NA, correspondingly. The morphology can be inferred from Fig. 5.18a, showing that in the absence of NA, the resulting hydration products, primarily struvite-K, exhibit a wedge shape and are tightly configured, yet there remains a presence of voids and cavities. This architecture results in subpar strength and ductility for UHDMC. On the contrary, Fig. 5.18b illustrates the microstructure when NA is deployed. The matrix surface appears smoother lacking evidence of struvite-K and other crystal formations. The resulting hydration products form a more comprehensive attachment to the matrix. This enhanced bonding between the fiber and matrix impedes water penetration into the matrix, thereby fortifying its watertightness and consequently, enhancing the resistance of the matrix to water.

Microscopic visuals of the UHDMC without NA immersed and with 8% NA immersed are represented in Figs. 5.19 and 5.20, respectively. Figure 5.19 reveals

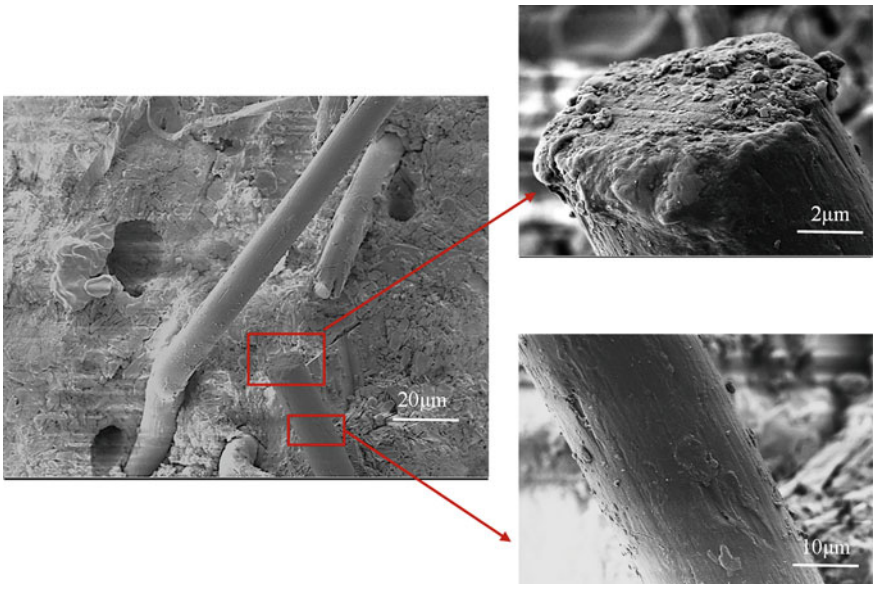

Fig. 5.16 SEM images of non-immersed UHDMC without NA. Reproduced from Assessment of the mechanical properties and water stability of nano-Al_2O_3 modified high ductility magnesium potassium phosphate cement-based composites by Hu Feng with permission from Elsevier

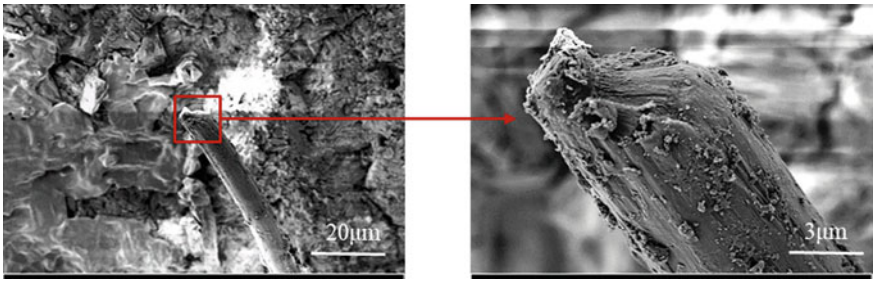

Fig. 5.17 SEM images of non-immersed UHDMC with 8% NA. Reproduced from Assessment of the mechanical properties and water stability of nano-Al_2O_3 modified high ductility magnesium potassium phosphate cement-based composites by Hu Feng with permission from Elsevier

that in comparison to non-immersed instances (Fig. 5.16), there is a reduction in the quantity of hydration by-products produced on the fiber exterior. This is possibly because the potassium dihydrogen phosphate that didn't react is getting dissolved post water submersion of the specimens. As a consequence, the solution's pH decreases, turning it weakly acidic, which causes the hydration reaction to occur in reverse. This results in the decomposition of the hydration product, struvite-K, and diminishes the strength of the matrix (Borgerding, 1972; Bube, 1910).

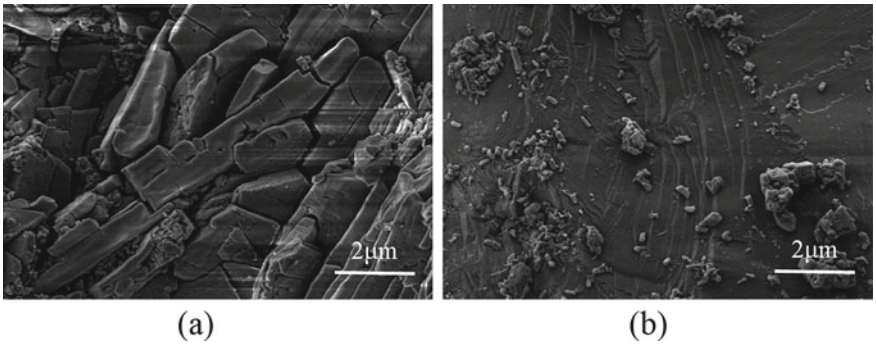

Fig. 5.18 SEM images of the UHDMC matrix **a** without NA and **b** with 8% NA. Reproduced from Assessment of the mechanical properties and water stability of nano-Al_2O_3 modified high ductility magnesium potassium phosphate cement-based composites by Hu Feng with permission from Elsevier

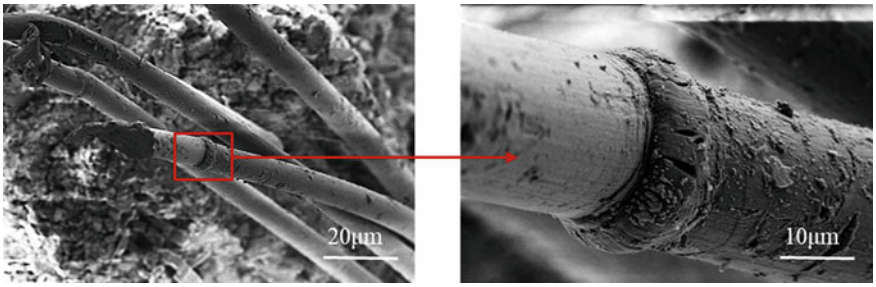

Fig. 5.19 SEM images of the immersed UHDMC without NA. Reproduced from Assessment of the mechanical properties and water stability of nano-Al_2O_3 modified high ductility magnesium potassium phosphate cement-based composites by Hu Feng with permission from Elsevier

Figure 5.20 visibly indicates a noticeable alteration in the fibers' cross-sectional diameter, with the fibers' tips showing fracture phenomena. This establishes that the PVA fibers and the cementitious matrix have a robust bond, enabling the fibers to withstand some tensile force once incorporated into the matrix. Consequently, when NA is integrated, it strengthens the fiber-matrix bond in a watery environment, thereby enhancing the matrix's strength. NA's action of dissolving in the pore solution to regulate the pH contributes to a decline in the decomposition of struvite-K ($MgKPO_4 \cdot 6H_2O$), thus further intensifying the structural adhesion between the matrix and the fibers.

Figure 5.21a, b display the microstructural analysis of the UHDMC matrix in the absence and presence of 8% NA, correspondingly. An analysis of Fig. 5.21a indicates that numerous diminutive elements adhere to the struvite-K crystals, a phenomenon attributed to the ion release into the fluid, a result of struvite-K's breakdown. This process of recrystallization results in the emergence of fresh struvite-K and accompanying microcrystals depositing on the slurry's exterior (Paceagiu &

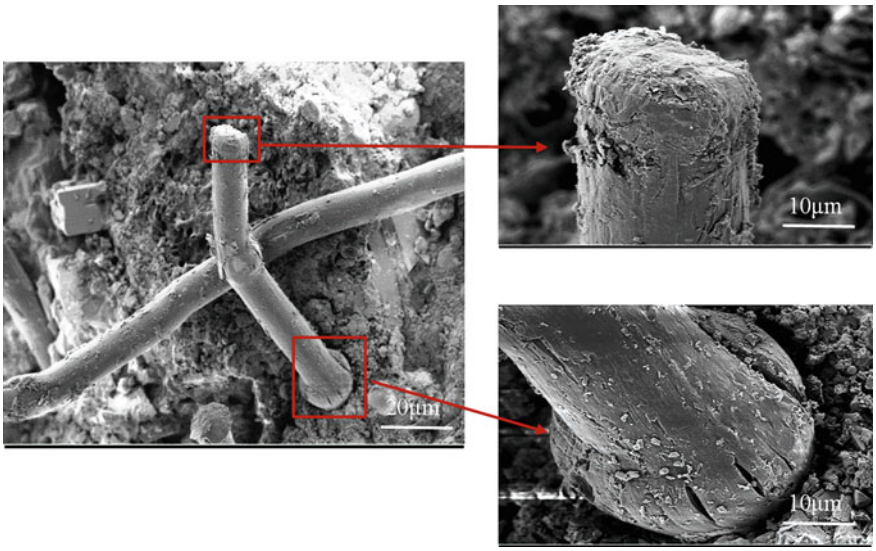

Fig. 5.20 SEM images of the immersed UHDMC with 8% NA. Reproduced from Assessment of the mechanical properties and water stability of nano-Al_2O_3 modified high ductility magnesium potassium phosphate cement-based composites by Hu Feng with permission from Elsevier

Georgescu, 2008). Consequently, less struvite-K is yielded via the hydration reaction, and there's a considerable space interposed between crystals, which is believed to weaken the sample's mechanical properties. Figure 5.21b reveals that the addition of 8% NA results in haptic crystal structuring and robust structural integrity, which significantly enhances UHDMC's mechanical properties. Compared with the NA-free samples (see Fig. 5.21a), cracks are diminished in presence. The SEM micrograph shows a predominantly denser microstructural formation in the presence of nano-Al_2O_3 (Heikal et al., 2015).

5.3.5 Effect of FA Substitution Rate

(1) **Workability**

The impacts of varying FA substitution rates on both the slump and the T500 of UHDMC are displayed in Fig. 5.22. The studied specimen batches contain 20, 30, 40, and 50% FA substitution rates, respectively. There's a clear trend observed that as the FA substitution rate goes up, T500 value increases, shifting from 3.85 to 5.58 s. However, at a 50% substitution rate, the expansion of UHDMC doesn't reach 500 mm, making the T500 data unmeasurable. Concurrently, approximately a 17.64% decline is observed in the slump as the rate of FA substitution goes up. From the results, it can be inferred that FA adversely impacts UHDMC's workability. This could be

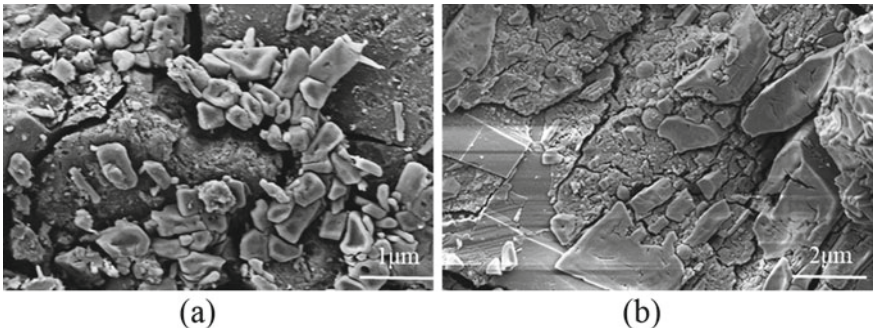

Fig. 5.21 SEM images of the immersed UHDMC matrix **a** without NA and **b** with 8% NA. Reproduced from Assessment of the mechanical properties and water stability of nano-Al_2O_3 modified high ductility magnesium potassium phosphate cement-based composites by Hu Feng with permission from Elsevier

primarily due to the increase of the composite's specific surface area triggered by an increased FA substitution rate, culminating in higher water demand of the matrix and reduced fluidity.

(2) **Compressive strength and compressive strength retention rate**

Figure 5.23 illustrates the impact of FA substitution rate on the compressive strength of UHDMC, both pre- and post-immersion, for specimen series with FA substitution rates of 20, 30, 40, and 50%, respectively. Looking at the figure as a whole, irrespective of immersion status, the specimen's compressive strength witnessed a 40.7% drop when FA substitution rate ascends from 20 to 50%. This steep decline in strength is attributed to the augmentation in hydration derivative generation and the decrement of cement-related materials, thus significantly reducing the specimen's overall compressive strength. Concurrently, the reaction between phosphate on the FA's surface with CaO results in a loosely porous structure, causing a further decline

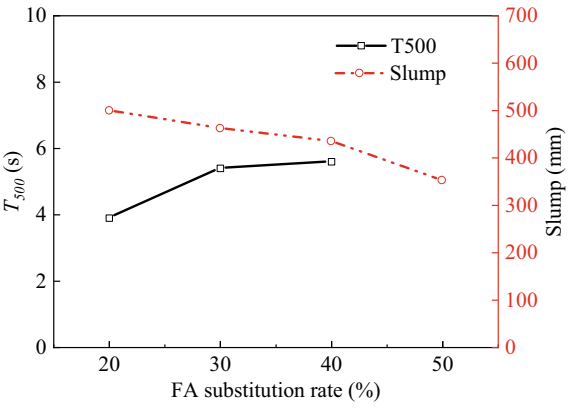

Fig. 5.22 Effects of the FA substitution rate on the workability of UHDMC. Reproduced from Effects of the fly ash and water glass on the mechanical properties and water stability of the high ductile magnesium phosphate cement-based composite by Hu Feng with permission from Elsevier

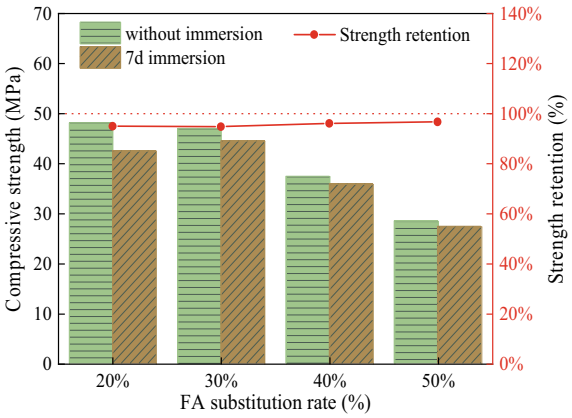

Fig. 5.23 Effects of the FA substitution rate on compressive strength and compressive strength retention of UHDMC. Reproduced from Effects of the fly ash and water glass on the mechanical properties and water stability of the high ductile magnesium phosphate cement-based composite by Hu Feng with permission from Elsevier

in compressive strength. Furthermore, Fig. 5.5 depicts the effect of the FA substitution rate on the compressive strength retention ratio. Observations reveal a trivial change in the compressive strength retention rate with an upsurge in the FA substitution rate, consistently hovering around 95%, which denotes competent water stability. Primarily, this is a result of the reduced porosity of UHDMC and an enhancement in compactness due to the superior filling capability of FA (Haque et al., 2020).

(3) **Flexural properties**

Figure 5.24 depicts the impact of the FA substitution rate on the UHDMC's load-span deflection graph. Generally, the load-mid-span deflection curves of all specimen varieties see three phases: initially, an elastic phase where the load directly corresponds to the mid-span deflection increase; secondly, an elastic–plastic phase where the load escalates not in a straight line but reaches its peak as the mid-span deflection surges; and lastly, a softening phase where the load dwindles in correspondence to the mid-span deflection increment, leading to collapse. The curves of mid-span deflection before immersion for various FA substitution rates are shown in Fig. 5.24a. The observation leads to a finding where the cracking load diminishes by around 36.84% when the FA substitution rate grows from 20 to 50%. The mid-span deflection records its highest at approximately 25mm upon an FA substitution rate of 30%. Figure 5.24b displays the mid-span deflection graph post-immersion with varied FA substitution rates. The results indicate that each specimen type's flexural load and mid-span deflection remain fundamentally identical. Relative to the pre-immersion specimen, there is a measurable increase in the flexural load. In scenarios where the FA substitution rate equals 40%, the specimen's flexural load and mid-span deflection are observed to be the greatest.

Figure 5.25a illustrates the impact of varying FA substitution rates on the cracking strength and its retention in UHDMC. As a general observation, there's a 32.6% decrease in the cracking strength in non-immersed samples when the FA replacement level surges from 20 to 50%. Conversely, Fig. 5.25b highlights the influence of the FA substitution rate on UHDMC's ultimate and retained flexural strength.

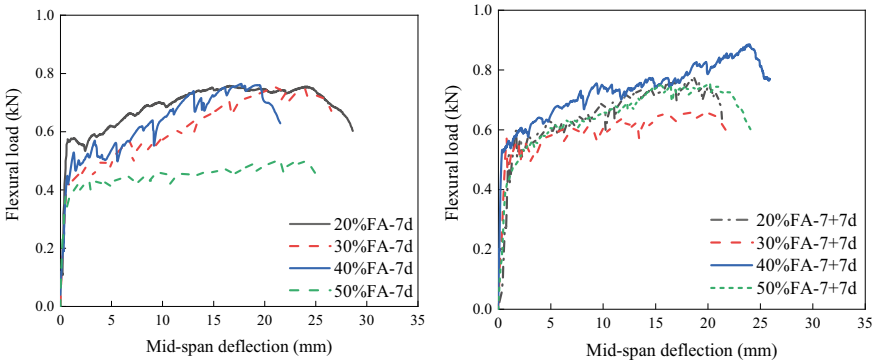

Fig. 5.24 Load-midspan deflection curves of specimens with different FA substitution rates: **a** Before immersion and **b** Immersion. Reproduced from Effects of the fly ash and water glass on the mechanical properties and water stability of the high ductile magnesium phosphate cement-based composite by Hu Feng with permission from Elsevier

From this, it's clear that the ultimate flexural strength is superior in soaked specimens compared to their dry counterparts. Also, a rising trend in flexural strength's retention is noticed with upscaling FA replacement levels. This could be primarily attributed to the fact that increased FA quantities fill the voids inhibiting water absorption, thus alleviating the disintegration of the main hydration compound MKP within the structure. Besides, it reduces the bonding strength loss between the fiber and matrix, enabling the preservation of both cracking and flexural strength at higher levels post-immersion. Figure 5.25c demonstrates the influence of FA replacement on the ductility index and its retention rate. Except for the case with 40% FA substitution, the ductility index of samples prior to immersion generally tops that of samples post-immersion. The ductility retention rate attains its peak, a whopping 123.30%, when the FA replacement is at 40%. Figure 5.25d exhibits the interplay between FA substitution rate and the UHDMC's toughness index and its retention. Generally, the toughness index of pre-immersed samples tends to drop with increasing FA replacement. Hence, FA can diminish the sample's toughness. When FA substitution stands at 40%, the toughness retention hits its pinnacle, reaching a staggering 142.06%. In summary, the non-immersed sample exhibits superior flexural performance at a 20% FA substitution rate, while the immersed ones do so at 40% FA replacement. This suggests that the sample with a 40% FA substitution rate showcases the greatest water stability.

(4) **Microscopic analysis**

a. SEM analysis of the UHDMC matrix

Scanning Electron Microscope (SEM) images of the magnesium phosphate cement (MPC) mortar's microstructure before and after immersion are displayed in

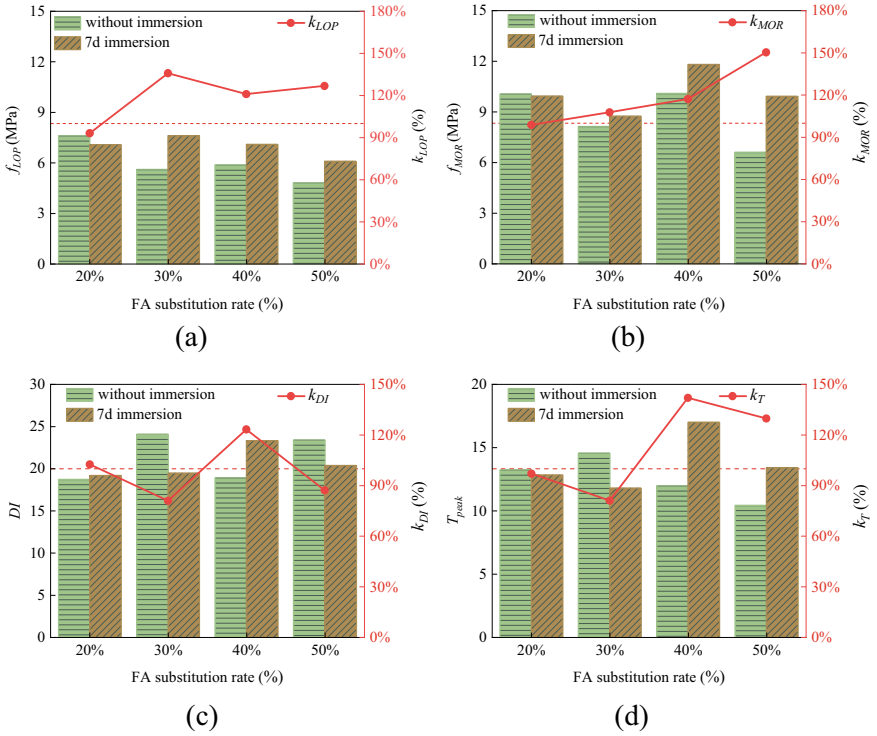

Fig. 5.25 Bending properties of specimens with different FA substitution rates: **a** Cracking strength; **b** Ultimate bending strength; **c** Ductility index and **d** Toughness index. Reproduced from Effects of the fly ash and water glass on the mechanical properties and water stability of the high ductile magnesium phosphate cement-based composite by Hu Feng with permission from Elsevier

Figs. 5.26a, b, respectively. Figure 5.26a reveals a profusion of close-knit, wedge-shaped crystals, the result of cement hydration. Also visible are naturally occurring fissures within the mortar matrix, directing water towards its core. Signs of rapid hydration in the presence of excess heat—manifested as micro-cracks on the hydration products—were also evident (Li & Chen, 2013; Li et al., 2020). On the other hand, Fig. 5.26b illustrates the morphological changes in the MPC mortar after a week-long immersion in water. Here, there is a marked increase in hydration product crystal size compared to Fig. 5.26a, primarily attributed to the swelling of $MgKPO_4 \cdot 6H_2O$ (MKP) after water absorption. This size increase in MKP crystals could be due to the continued hydration of residual MgO and KH_2PO_4 during the 7 day water immersion, with newly generated hydration products adhering to the original MKP crystals. Nevertheless, a point to note is that the water exposure leads to a more porous crystal structure than that of the original, non-immersed specimen. This change results in reduced structural strength of the UHDMC. Furthermore, the matrix and the hydration product surface showcase increased cracking, suggesting

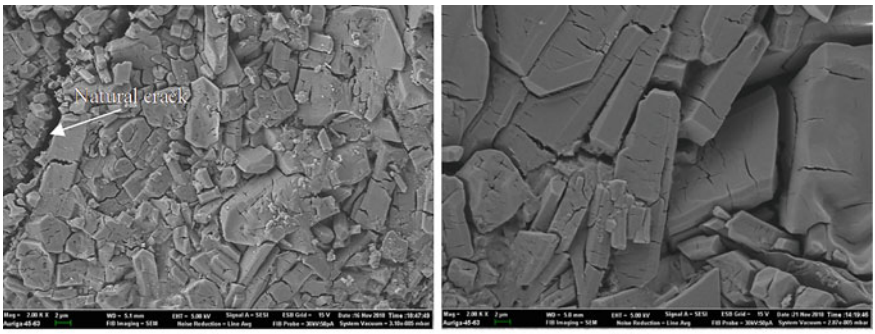

Fig. 5.26 SEM images of MPC mortar: **a** Before immersion and **b** Immersion. Reproduced from Effects of the fly ash and water glass on the mechanical properties and water stability of the high ductile magnesium phosphate cement-based composite by Hu Feng with permission from Elsevier

subpar water stability of the MPC matrix. This susceptibility may be mainly due to the hydration products' propensity to dissolve upon water contact.

The SEM images of specimen types FA-20 matrix and FA-40, both prior to and following immersion, are displayed in Fig. 5.27a, b, c, d. Figure 5.27a illustrates a tight conjunction between the hydration products and FA particles, alongside a few visible micro-cracks on the hydration product surface. After a 7 day immersion period, the microscopic texture of the FA-20 specimen is represented in Fig. 5.27b. Relative to its dry counterpart, the immersed sample exhibits a rougher hydration product surface with amplified micro-cracks, signifying the dissolution of hydration products in water. A greater micro-crack width and the dissolution of hydration products have been identified as principal factors causing the compressive strength loss in the specimen. Figure 5.27c, d depict the SEM visuals of the FA-40 specimen before and after the immersion process. Each specimen shows a plentiful presence of FA particles leading to a compact layout of the cement base. The microstructures of the FA-40 specimen pre- and post-immersion are almost identical. By comparing Figs. 5.26a, and 5.27a, it is determined that a higher FA substitution rate in the UHDMC matrix provids a superior gradation, aiding in barring the water penetration into the matrix interior. Observations from Figs. 5.26b and 5.27b, d suggest that the consolidation of the matrix following immersion notably enhances with a higher FA substitution rate, resulting in better strength retention in the corresponding specimen.

b. SEM analysis of PVA fiber surface texture

Figure 5.28a, b display the alterations in the fracture surface appearance of the FA-40 specimen before and after the immersion process, respectively. Generally speaking, UHDMC displays a uniform distribution of fibers with some hydration by-products detected on the fiber surface. An examination of Fig. 5.28a reveals a fracture that fails along with necking, a hint towards a strong bond property at the interface between the fiber and the matrix. Post a 7 day immersion period, clear signs of pull-out damage are

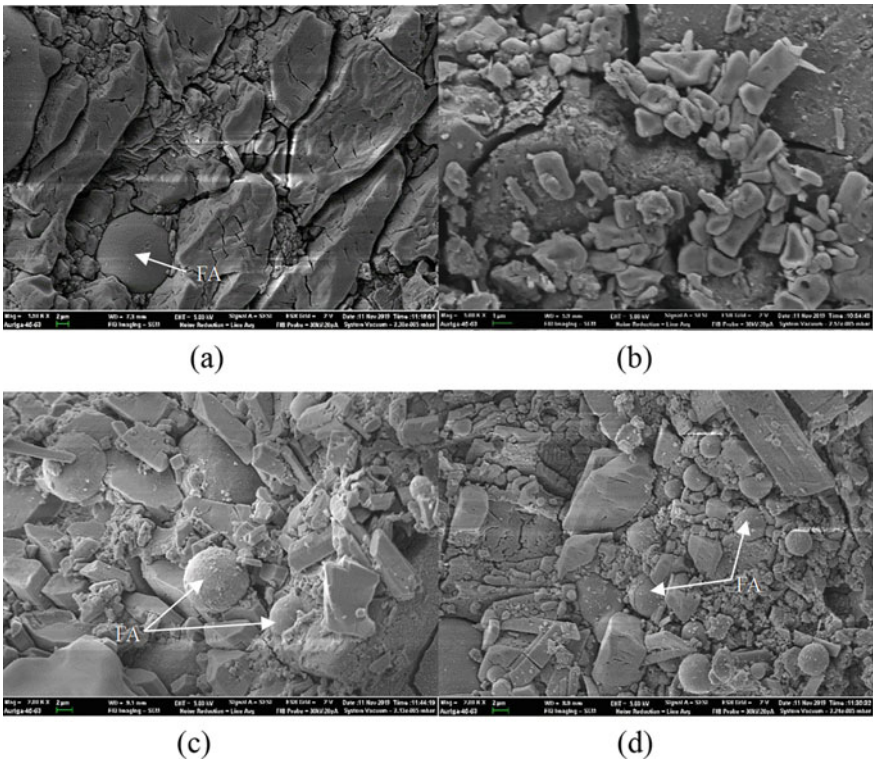

Fig. 5.27 SEM images of UHDMC with the FA substitution rates of 20% and 40%: **a** specimen FA-20 before immersion, **b** specimen FA-20 after immersion, **c** specimen FA-40 before immersion and **d** specimen FA-40 after immersion. Reproduced from Effects of the fly ash and water glass on the mechanical properties and water stability of the high ductile magnesium phosphate cement-based composite by Hu Feng with permission from Elsevier

observed on the fiber, with noticeable fiber pull-out pits evident on the compromised interface, as demonstrated in Fig. 5.28b. These observations make it apparent that the water's influence deteriorates the bonding behavior at the fiber-matrix interface. However, the specimen's ductility could see improvements due to this fiber pull-out failure. In summary, the overall matrix strength of UHDMC and the fiber-matrix interface bonding are weakened, while the deflection of specimen at the mid- span spot shows an increasing trend.

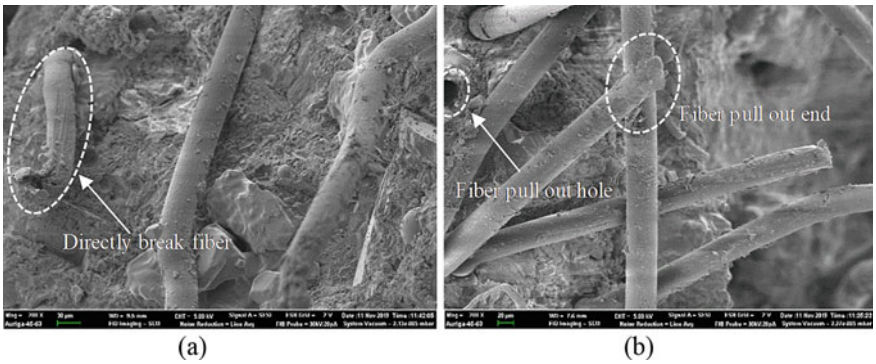

Fig. 5.28 SEM images of UHDMC with a FA substitution rate of 40%: **a** Before immersion and **b** Immersion. Reproduced from Effects of the fly ash and water glass on the mechanical properties and water stability of the high ductile magnesium phosphate cement-based composite by Hu Feng with permission from Elsevier

5.3.6 Effect of WG Mass Fraction

(1) **Workability**

Figure 5.29 illustrates the influence of the WG mass fraction on the UHDMC's workability. It can be noticed that the slump of UHDMC remains virtually unchanged with an increase in the WG mass fraction from 0 to 5%. In contrast to UHDMC devoid of WG, the T500 of UHDMC containing WG mass percentages of 1, 2, 3, and 4% lessens by around 1.41, 1.63, 0.63 and 0.87 s, respectively. However, when the WG mass percentage reaches 5%, the expansion could not hit 500 mm, and the slump is a mere 248 mm, suggesting that too much WG negatively impacts UHDMC workability. Prior research demonstrated that WG had a tendency to hasten the initial hydration of MKPC (Shi et al., 2014), utilizing more water in the initial phase to generate further cementing materials such as struvite-K. Besides, WG may interact with magnesium ions to create some magnesium silicate hydrate gel, thereby consuming more water. As a result of these two factors, the workability of UHDMC indicates a declining trend with a growing rate of WG substitution.

(2) **Compressive strength and compressive strength retention rate**

Figure 5.30 illustrates the impact of the WG mass fraction on the UHDMC's compressive strength, both before and after water submersion. The WG mass fraction for these test samples varies from 0 to 5%. Regardless of whether they were subjected to immersion or not, all variations of samples show a trend where compressive strength initially increases, then declines with a rise in the WG mass fraction. The apex of compressive strength is observed when the WG mass fraction reaches 1%, occurring both prior to and following water exposure. It's important to note that a significant plunge in compressive strength is noticed for all variations of samples when the WG mass fraction exceeds 2%. This can be primarily attributed to a potential reduction

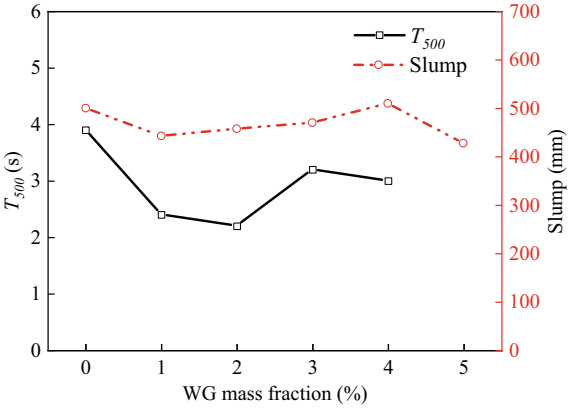

Fig. 5.29 Effects of the WG mass fraction on the workability of UHDMC. Reproduced from Effects of the fly ash and water glass on the mechanical properties and water stability of the high ductile magnesium phosphate cement-based composite by Hu Feng with permission from Elsevier

in cement hydration reaction, as a significant proportion of WG may have enveloped the cement-based material. Additionally, Fig. 5.30 demonstrates the influence of the WG mass fraction on the UHDMC's compressive strength retention rate. The retention rate of compressive strength seems to mildly elevate with the increment of WG mass fraction. Maximum compressive strength retention rate is encountered when WG mass fraction is at 5%, tallying to 106.6%. This implies the capacity of WG to enhance the water stability of the structure. The main reason for this could be the reaction of silicate ion groups in WG with magnesium ions in the solution, forming hydrated magnesium silicate gel as the WG mass fraction rises. This gel could attach to the struvite surface or accumulate within the openings, preventing hydration product decomposition and reinforcing the overall water stability.

(3) **Flexural properties**

Figure 5.31 illustrates the influence of different WG mass fractions on the load-span deflection profile of UHDMC. This load-span deflection pattern of the test sample

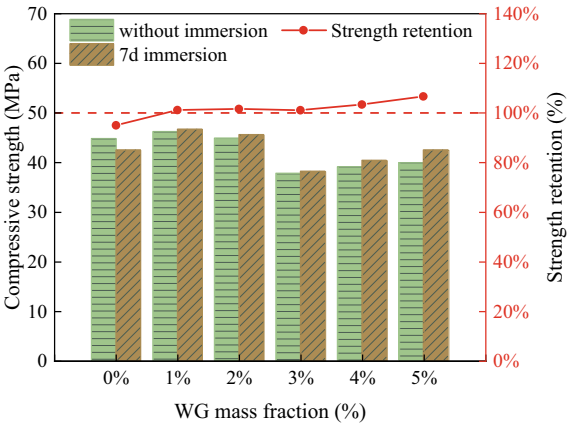

Fig. 5.30 Effects of the WG mass fraction on the compressive strength and compressive strength retention of UHDMC. Reproduced from Effects of the fly ash and water glass on the mechanical properties and water stability of the high ductile magnesium phosphate cement-based composite by Hu Feng with permission from Elsevier

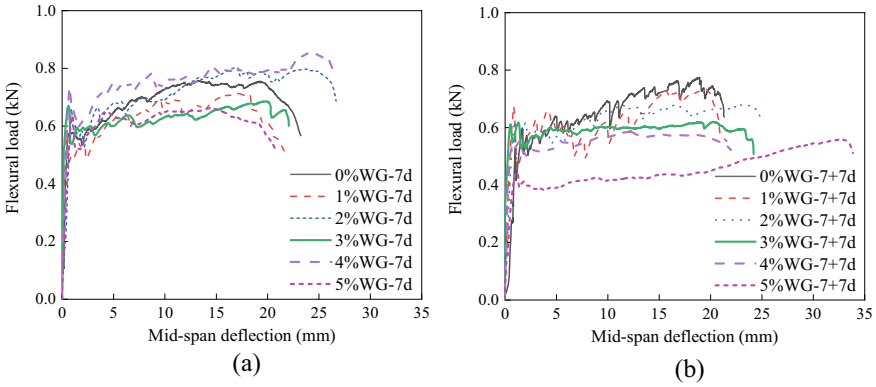

Fig. 5.31 Flexural load—midspan deflection curves of specimens with different WG mass fractions before immersion and immersion: **a** Before immersion and **b** Immersion. Reproduced from Effects of the fly ash and water glass on the mechanical properties and water stability of the high ductile magnesium phosphate cement-based composite by Hu Feng with permission from Elsevier

mimics the three-phase mechanism, encompassing the elastic phase, the elastoplastic phase, and the softening phase. In Fig. 5.31a, we observe the mid-span deflection trajectories for samples with varying WG mass fractions before they undergo immersion. A notable observation is that the cracking load for the sample first escalates and subsequently drops as the WG mass fraction augments. The flexural load and mid-span deflection for the sample both peak when the WG mass fraction is set at 4%. The divergent mid-span deflection trajectories of specimens post-immersion with assorted WG mass fractions are laid out in Fig. 5.31b. Notably, in contrast to pre-immersion samples, the specimens with WG mass fractions of 4 and 5% demonstrate a degree of reduction in the flexural load. It is crucial to highlight that the mid-span deflection for the sample ascends to roughly 34 mm with a WG mass fraction of 5%. This is significantly higher (by about 17 mm) than the deflection observed with specimens not subjected to immersion.

Figure 5.32a outlines the WG mass fraction's impact on the UHDMC's cracking strength and retention rate. Broadly speaking, the pre-immersion specimen's cracking strength rises with the ascending WG mass fraction. In comparison to the 0% WG mass fraction samples, the ones with a WG mass fraction ranging from 2 to 5% experience cracking strength increments of 14.79, 16.75, 28.27, and 10.86%, highlighting that the addition of WG boosts the specimen's cracking strength. Additionally, the post-immersion specimen's cracking strength incrementally increases before experiencing a decrease as the WG mass fraction escalates. However, only the 1% WG mass fraction specimen outperforms the pre-immersion sample in cracking strength after immersion. Figure 5.32b graphs the influence of the WG mass fraction on UHDMC's ultimate flexural strength and ultimate flexural strength retention rate. Pre-immersion, specimens with 2 and 4% WG mass fractions demonstrate a noticeable augmentation in ultimate flexural strength. Post-immersion, the ultimate flexural strength reduces by 25.17% with WG mass fraction advancement from 0 to 5%. A

flexural strength retention rate exceeding 100% is only seen in the 1% WG mass fraction sample. In Fig. 5.32c, the impact of the WG mass fraction on UHDMC's ductility index and ductility retention rate is displayed. For all samples, irrespective of immersion conditions, the ductility index appears roughly stable when the WG mass fraction is within 3%. Specimens with a 4% mass fraction indicates a roughly 24.95% reduction in the immersed sample's ductility index compared to the unimmersed version. Notably, the 5% WG mass fraction specimen exhibits tremendously increased ductility in the immersed state, achieving a ductility retention rate of 172.05%. Figure 5.32d illustrates the effect of the WG mass fraction on UHDMC's toughness index and retention rate. The toughness index remains above 17 for the unimmersed samples at 2 and 4% WG mass fractions, indicating superior strength. For the immersed samples, their toughness indexes remain comparable to the unimmersed ones at 0, 1, and 3% WG mass fraction. However, the toughness index of the immersed samples significantly reduces at 2 and 4% WG mass fraction. Markedly, at 5% WG mass fraction, the immersed samples achieve a higher toughness index and a retention rate of 128.05%. In conclusion, WG incorporation marginally affects the flexural performance of unimmersed specimens. When the WG mass fraction is 5%, the immersed sample delivers optimal flexural performance, with ductility and toughness retention rates surpassing 100%. Hence, the 5% WG mass fraction specimens demonstrate supreme water stability.

(4) **Microscopic analysis**

a. SEM analysis of the UHDMC matrix

The SEM images of WG-2 and WG-5 specimens before and after their submersion are presented in Fig. 5.33a, b, c, d. The dense microstructure typical of all samples can be observed clearly, containing minimal micro-cracks and imperfections. Furthermore, amorphous hydration products become noticeable in WG-2 and WG-5 samples. After being submerged in water for a one-week period, the density of the microstructure in the WG-2 and WG-5 samples remains, as depicted in Fig. 5.33b, d. This suggests that the addition of WG enhances the water stability of the UHDMC matrix. WG has the ability to react with Mg2+, producing magnesium silicate hydrated gel, a substance capable of occupying the pores and cracks within the magnesium phosphate cement. This action results in a reduced dissolution rate of phosphate and hydration product.

b. SEM analysis of PVA fiber surface texture

Figure 5.34a, b illustrate the variation in fracture surface texture for sample WG-5, both pre and post immersion. A close-knit microstructure is shown in the former Fig. 5.34a, without noticeable features like struvite-K crystals. Interestingly, we could notice a fracture event coupled with necking pertinent to PVA fiber, suggesting an impressive interfacial bond with the matrix. Post immersion over a week (Fig. 5.34b), the matrix turned markedly less consolidated. Possible efforts of hydration products partially dissolving due to water exposure may have lessened the bond strength

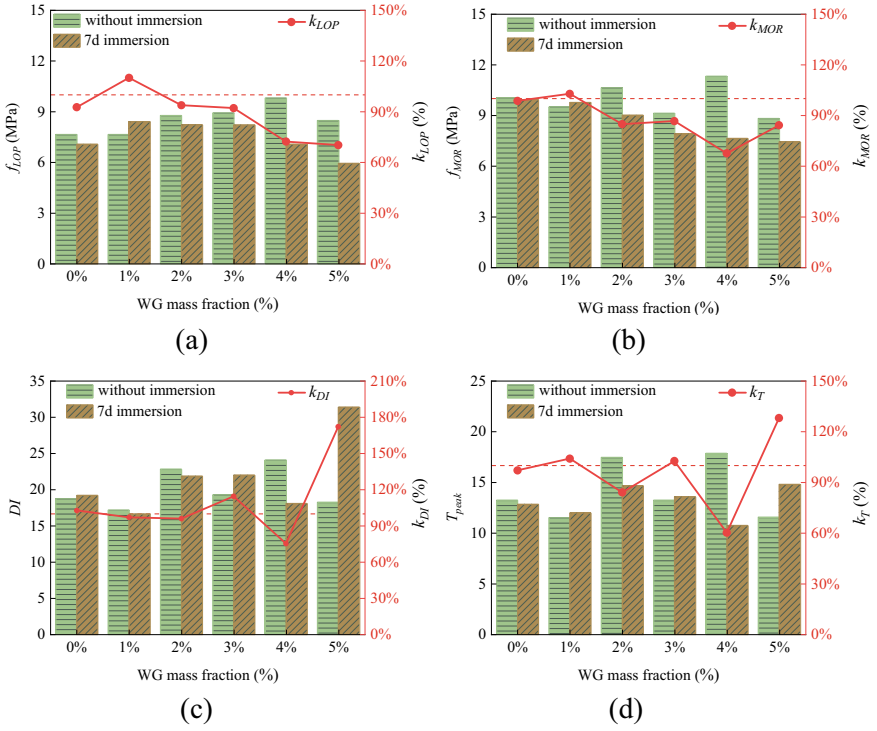

Fig. 5.32 Flexural properties of different WG mass fractions: **a** Cracking strength; **b** Ultimate bending strength; **c** Ductility index and **d** Toughness index. Reproduced from Effects of the fly ash and water glass on the mechanical properties and water stability of the high ductile magnesium phosphate cement-based composite by Hu Feng with permission from Elsevier

amongst the solid granular contents in the matrix. Correspondingly, a slight weakening of the interfacial bond between the fiber and matrix occurred, making it possible for additional fibers to be displaced during a bending load.

5.4 Conclusions

In this chapter, a series of tests—including the slump, compressive, and four-point flexural tests on thin plates—were conducted to determine the influences of several variables. These variables comprised factors such as the duration of ambient curing and water immersion, the ratios of *W/B* and *M/P*, NA content, FA substitution rate, and WG mass fraction. The impacts of these variables on the performance characteristics of UHDMC, which range from workability, compressive strength, flexural behavior to water stability, were analyzed. Additionally, the Scanning Electron Microscopy (SEM) test was used to investigate how these factors affected

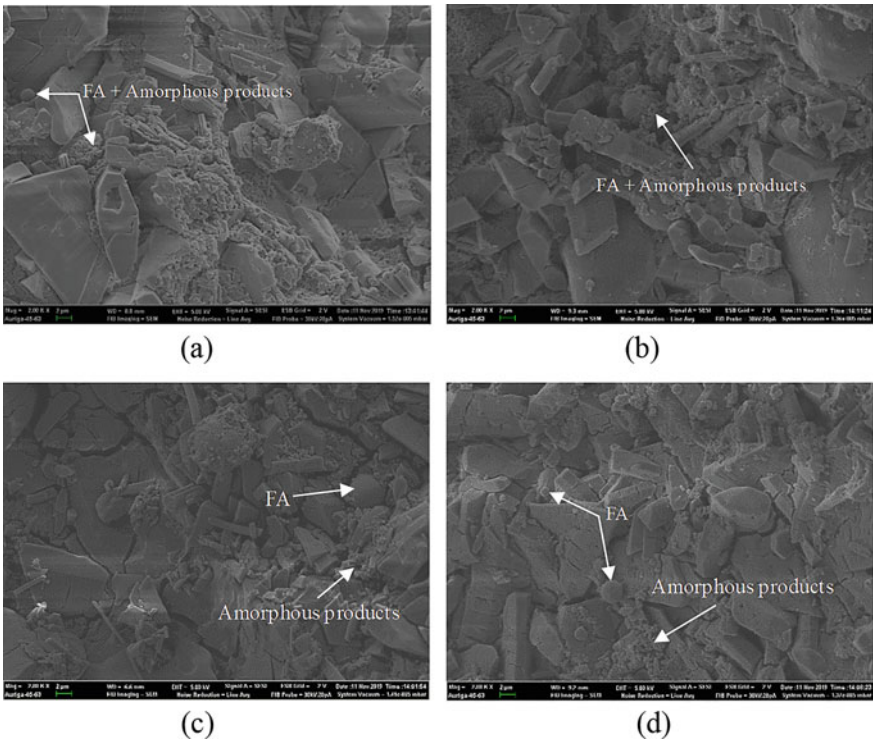

Fig. 5.33 SEM images of UHDMC with the WG mass fraction of 2 and 5%: **a** specimen WG-2 before immersion, **b** specimen WG-2 after immersion, **c** specimen WG-5 before immersion and **d** specimen WG-5 after immersion. Reproduced from Effects of the fly ash and water glass on the mechanical properties and water stability of the high ductile magnesium phosphate cement-based composite by Hu Feng with permission from Elsevier

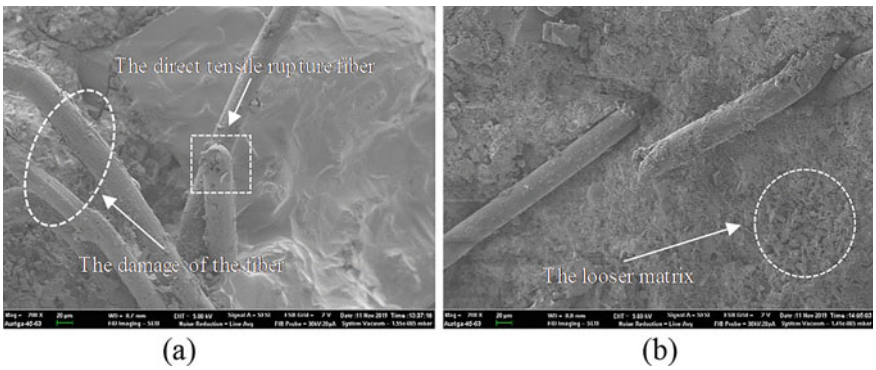

Fig. 5.34 SEM images of UHDMC with a WG mass fraction of 5%: **a** Before immersion and **b** Immersion. Reproduced from Effects of the fly ash and water glass on the mechanical properties and water stability of the high ductile magnesium phosphate cement-based composite by Hu Feng with permission from Elsevier

the UHDMC's microstructure. The primary findings from this research are detailed below.

For UHDMC of identical water immersion timeframes, it can be noted that a curing period of 28 days in an ambient environment culminates in higher retention rates of strength, ductility, and toughness, when compared to a mere seven-day ambient curing process. This demonstrates that protracting the time of curing under ambient conditions improves UHDMC's stability to water; however, there isn't a significant positive impact in UHDMC's mechanical characteristics as an effect of a more extended ambient curing period. As the time of water immersion escalates from zero to 56 days, the UHDMC subject to a seven-day curing process in ambient conditions display a noticeable downgrade in mechanical properties Conversely, the mechanical attributes of the UHDMC undergoing a 28 day ambient curing period seldom exhibit a notable dip and can often demonstrate an upsurge, particularly when the submersion in water lasts for 56 days. Concerning water stability, the alterations proceed in line with the mechanical property transformations. A microscopy examination reveals that in non-submerged UHDMC, the struvite-K crystals predominantly adopt a wedge shape and align fairly tightly in the matrix. The interconnection between fibers and the matrix is fairly solid, with fibers seemingly unfractured and merely extricated from within the matrix. In contrast, for the water-immersed UHDMC, a sizeable gap is discernible amidst struvite-K crystals, and the surface of fibers maintain a polished texture, without substantial adhesion of hydration byproducts, thereby suggesting that immersion negatively impacts the UHDMC, causing a decrease in their mechanical qualities.

As the *W/B* ratio escalates, there's complexity in the modifications of indices related to strength, ductility, and toughness. For unimmersed UHDMC, an optimal balance of the aforementioned indices can be struck with a *W/B* ratio of 0.16. When it comes to immersed UHDMC, an ideal strength index is observed with a 0.14 *W/B* ratio, whilst peak ductility and toughness indices occur at a *W/B* ratio of 0.20; a moderate level of all three is observed at a ratio of 0.16. The highest retention percentages for strength, ductility, and toughness emerge at a ratio of 0.20, suggesting superior water stability, with 0.16 as the next optimal ratio. Thus, taking all indices and their retention percentages into account, it emerges that a *W/B* ratio of 0.16 may represent the most advantageous value for UHDMC.

As the *M/P* ratio rises, the shifts in strength, ductility, and toughness indicators don't necessarily align. However, both dry and water-immersed UHDMC exhibit satisfying performance in these aspects when the *M/P* ratio equals 5. Nevertheless, based on index retention rates, UHDMC's water stability at an *M/P* ratio of 5 is only moderate, achieving optimal water stability at an *M/P* value of 3.

Upon examining both submerged and non-submerged samples, we observed that the compressive strength and its retention rate initially increase, followed by a decrement as the amount of NA rises. More specifically, within the range of 4–8% NA content, both compressive strength and water stability show enhancement. The admixture of NA (less than 8%) is found to elevate the cracking strength and

ultimate flexural strength of the UHDMC, irrespective of the immersion factor. Additionally, the cracking strength and ultimate flexural strength of the immersed specimens appear superior to the non-immersed counterparts, with their strength retention percentages exceeding 100% and noticeably surpassing that of NA-exempt samples. Hence, incorporating up to 8% NA enhances the water stability of the UHDMC. As we increase the level of NA, the ductility and toughness indices follow a trajectory of initial improvement, then diminishing. A NA content of 6% yields the finest ductility and toughness results. Comparisons between submerged and non-submerged specimens reveal no considerable enhancement in the ductility or toughness parameters. The ductility index retention rate is slightly less than 100%, while that of the toughness index is approximately 100%. Be that as it may, these retention rates still bettered when compared to the NA-free samples. Microscopic evaluation highlighs that the UHDMC containing NA is denser than its NA-absent counterpart. The minuscule fractures within the matrix crystals are insignificant, and the overall structural steadfastness is admirable. This density successfully acts as a water barrier, thereby promoting water stability in the UHDMC. Moreover, the addition of NA fosters a stronger bond between MPC matrix and fibers, which in turn heightens the UHDMC's mechanical attributes.

Whether the sample is submerged or not, there is a noticeable reduction in the UHDMC compressive strength with an increase in FA replacement rate. Compressive strength retention rate remains around 95%, demonstrating good water stability. With the introduction of WG, the specimen yields compressive strength retention rates exceeding 100%, depicting excellent water stability. Prior to submersion, the flexural strength of the sample decreases progressively as the FA replacement rate ascends. Once immersed, a specimen with a 40% FA replacement rate exhibits the best flexural performance and water stability. Regardless of whether the sample is submerged or not, the WG enhances the UHDMC's flexural performance. However, only when the WG has a weight fraction of 5%, the maximum mid-span deflection of the immersed specimen is observed, presenting top flexural performance. Microscopic examination suggests that the FA and WG contribute to enhancing the compactness of the matrix. Nevertheless, after a 7 day immersion period, the bond strength at the polyvinyl alcohol (PVA) fiber-matrix interface is diminished due to the dissolution of hydration products. An increase in fiber pullout failures is noted, thus amplifying the deformability of specimens FA-40 and WG-5.

References

Abitbol, T., Rivkin, A., Cao, Y., Nevo, Y., Abraham, E., Ben-Shalom, T., Lapidot, S., & Shoseyov, O. (2016). Nanocellulose, a tiny fiber with huge applications. *Current Opinion in Biotechnology*, *39*, 76–88. https://doi.org/10.1016/j.copbio.2016.01.002

Ban, J., Lca, B., & Bing, C. (2020). Factors assessment of a repair material for brick masonry loaded cracks using magnesium phosphate cement. *Construction Building Materials*, *252*.

Borgerding, J. (1972). Phosphate deposits in digestion systems. *Journal of the Water Pollution Control Federation*, *44*(5), 813–819.

Bube, K. (1910). Ueber Magnesiumammoniumphosphat. *Fresenius' Journal of Analytical Chemistry.*, *49*(9), 525–596.

Chau, C. K., Fei, Q., & Li, Z. (2011a). Microstructure of magnesium potassium phosphate cement. *Construction Building Materials, 25*(6), 2911–2917.

Chau, C. K., Fei, Q., Li, Z. J. C., & Materials, B. (2011). Microstructure of magnesium potassium phosphate cement. *25*(6), 2911–2917.

Chen, S., & Zhu, D. J. (2017). Study on PVA fiber modified phosphate cement-based materials. *China Concrete Cement Products, 16*(2), 44–47.

Chong, L., Yang, J., & Shi, C. (2017a). Effect of curing regime on water resistance of magnesium–potassium phosphate cement. *Construction and Building Materials, 151*, 43–51.

Chong, L., Yang, J., & Shi, C. J. (2017b). Effect of curing regime on water resistance of magnesium–potassium phosphate cement. *Construction Building Materials, 151*, 43–51.

Ding, Z., & Li, Z. (2005). Effect of aggregates and water contents on the properties of magnesium phospho-silicate cement. *Cement and Concrete Composites, 27*(1), 11–18.

Ding, Z., Lu, Z. X., & Li, Y. (2011). Feasibility of basalt fiber reinforced inorganic adhesive for concrete strengtening. *Advanced Materials Research, 287–290*, 1197–1200.

Ding, Z., Dong, B., Xing, F., Han, N., & Li, Z. (2012). Cementing mechanism of potassium phosphate based magnesium phosphate cement. *Ceramics International, 38*(8), 6281–6288.

Donahue, P. K., & Aro, M. (2010). Durable phosphate-bonded natural fiber composite products. *Construction Building Materials, 24*(2), 215–219.

Feng, H., Li, Z., Wang, W., Liu, G., & Gao, D. J. (2021). Deflection hardening behaviour of ductile fibre reinforced magnesium phosphate cement-based composite. *Cement Concrete Composites, 121*(2), 104079.

Feng, H., Zhao, X., Chen, G., Miao, C., Zhao, X., Gao, D., & Sun, G. (2019). The effect of nano-particles and water glass on the water stability of magnesium phosphate cement based mortar. *Materials*, *12*(22).

Feng, H., Shen, S., Pang, Y., Gao, D., & Sheikh, M. N. (2020). Mechanical properties of fiber and nano-Al_2O_3 reinforced magnesium phosphate cement composite. *Construction Building Materials*, *270*(4).

Ge, Z., Li, G., & He, T. (2017). Effects of sulphoaluminate cement on the strength and water stability of magnesium potassium phosphate cement. *Construction Building Materials, 132*, 335–342.

Haque, M. A., Chen, B., & Liu, Y. (2020). The role of bauxite and fly-ash on the water stability and microstructural densification of magnesium phosphate cement composites. *Construction Building Materials, 260*, 119953.

Heikal, M., Ismail, M. N., & Ibrahim, N. S. J. C. (2015). Physico-mechanical, microstructure characteristics and fire resistance of cement pastes containing Al2O3 nano-particles. *Construction Building Materials*, *91*, 232–242.

Hou, D., Yan, H., Zhang, J., Wang, P., & Li, Z. (2016). Experimental and computational investigation of magnesium phosphate cement mortar. *Construction and Building Materials, 112*, 331–342.

Hu, F. A., Ll, A., Yp, A., Zw, A., Dga, B., & Zhe, Z. A. (2020). Experimental study on the effects of the fiber and nano-Fe_2O_3 on the properties of the magnesium potassium phosphate cement composites. *Journal of Materials Research Technology, 9*(6), 14307–14320.

Kim, D. J., Naaman, A. E., & El-Tawil, S. (2008). Comparative flexural behavior of four fiber reinforced cementitious composites. *Cement Concrete Composites, 30*(10), 917–928.

Le Rouzic, M., Chaussadent, T., Stefan, L., & Saillio, M. (2017). On the influence of Mg/P ratio on the properties and durability of magnesium potassium phosphate cement pastes. *Cement Concrete Research, 96*, 27–41.

Lee, H., Lee, I., & Lee, J. (2017). *A experimental study on the hardening and shrinkage characteristics at early age of fiber reinforced MPC mortar*.

Li, D. X., Li, P. X., & Feng, C. H. (2009). Research on water resistance of magnesium phosphate cement. *Journal of Building Materials, 12*(5), 505–510.

Li, J., Zhang, W., & Monteiro, P. J. (2020). Mechanical properties of struvite-K: A high-pressure X-ray diffraction study. *Cement and Concrete Research, 136*, 106171.

Li, Y., & Chen, B. J. C. (2013). Factors that affect the properties of magnesium phosphate cement. *Construction Building Materials*, *47*, 977–983.

Li, V. C., Wang, S., & Wu, C. (2001). Tensile strain-hardening behavior of polyvinyl alcohol engineered cementitious composite (PVA-ECC). *Aci Materials Journal*.

Liu, Y., & Chen, B. (2019). Research on the preparation and properties of a novel grouting material based on magnesium phosphate cement. *Construction Building Materials*, *214*, 516–526.

Lu, X., & Chen, B. (2016). Experimental study of magnesium phosphate cements modified by metakaolin. *Construction Building Materials*, *123*, 719–726.

Lv, L., Huang, P., Mo, L., Deng, M., Qian, J., & Wang, A. J. (2019). Properties of magnesium potassium phosphate cement pastes exposec to water curing: A comparison study on the influences of fly ash and metakaolin. *Construction Building Materials*, *203*, 589–600.

Ma, H., Xu, B., Liu, J., Pei, H., & Li, Z. (2014). Effects of water content, magnesia-to-phosphate molar ratio and age on pore structure, strength and permeability of magnesium potassium phosphate cement paste. *Materials and Design, 64*, 497–502.

Maha, B., Bing, C., Mra, A., & Sfas, A. J. C. (2019). Evaluating the physical and strength properties of fibre reinforced magnesium phosphate cement mortar considering mass loss. *Construction Building Materials, 217*, 427–440.

Mestres, G., Aguilera, F. S., Manzanares, N., Sauro, S., Osorio, R., Toledano, M., & Ginebra, M. P. (2014). Magnesium phosphate cements for endodontic applications with improved long-term sealing ability. *International Endodontic Journal*, *47*(2).

Mohseni, E., Khotbehsara, M. M., Naseri, F., Monazami, M., & Sarker, P. (2016). Polypropylene fiber reinforced cement mortars containing rice husk ash and nano-alumina. *Construction Building Materials, 111*, 429–439.

Mraa, B., Bing, C., & Jiang, Y. A. (2019). A comprehensive study of basalt fiber reinforced magnesium phosphate cement incorporating ultrafine fly ash. *Composites Part B: Engineering, 168*, 204–217.

Münch, E., & Barr, K. J. (2001). Controlled struvite crystallisation for removing phosphorus from anaerobic digester sidestreams. *Water Research, 35*(1), 151–159.

Naaman, A. E., & Reinhardt, H. W. (1996). Characterization of high performance fiber reinforced cement composites. *EFN SPON*.

Nazari, A., Riahi, S., Riahi, S., Shamekhi, S. F., & Khademno, A. (2010). Influence of Al_2O_3 nanoparticles on the compressive strength and workability of blended concrete.

Ning, L., & Bing, C. (2016). Experimental research on magnesium phosphate cements containing alumina. *Construction Building Materials, 121*, 354–360.

Onuaguluchi, O., Panesar, D. K., & Sain, M. (2014). Properties of nanofibre reinforced cement composites. *Construction Building Materials*, *63*, 119–124.

Paceagiu, J., & Georgescu, M. J. (2008). The influence of curing conditions on the physical and mechanical properties of magnesia phosphate cements. *Revista De Chimie-Bucharest-Original Edition, 59*(2), 135–139.

Prosen, E. M. (1939). *Dental investment or refractory material*.

Qiao, F., Chau, C. K., & Li, Z. J. C. (2010). Property evaluation of magnesium phosphate cement mortar as patch repair material. *Construction Building Materials, 24*(5), 695–700.

Ran, L. I., & Huirong, W. (2020). Influence of Nano-particles on durability of shaft concrete. *Safety in Coal Mines, 051*(003), 52–57.

Sarkar, A. K. (1990). Phosphate cement-based fast-setting binders. *American Ceramic Society Bulletin, 69*(2), 234–238.

Seehra, S. S., Gupta, S., & Kumar, S. J. C. (1993). Rapid setting magnesium phosphate cement for quick repair of concrete pavements—characterisation and durability aspects. *Cement Concrete Research, 23*(2), 254–266.

Shi, C., Yang, J., Yang, N., & Chang, Y. (2014). Effect of waterglass on water stability of potassium magnesium phosphate cement paste. *Cement and Concrete Composites, 53*, 83–87.

Su, Y., Yang, J., Liu, D., Zhen, S., Lin, N., & Zhou, Y. (2016). Effects of municipal solid waste incineration fly ash on solidification/stabilization of Cd and Pb by magnesium potassium phosphate cement. *Journal of Environmental Chemical Engineering, 4*(1), 259–265.

Sun, J., Li, J., Li, Y., & Shi, T. J. (2015). Effects of fly ash, retarder and calcination of magnesia on properties of magnesia–phosphate cement. *Advances in Cement Research, 27*(7), 373–380.

Sun, C., Lin, X., & Ji, T. (2016). Influence of the ratio of KH2PO4 to MgO, ratio of water to bind, content change of borax on water resistance of magnesium-potassium phosphate cement. *J. Fuzhou Univ. (Nat. Sci. Ed.), 44*, 856–862.

Viani, A., Peréz-Estébanez, M., Pollastri, S., & Gualtieri, A. F. (2016). In situ synchrotron powder diffraction study of the setting reaction kinetics of magnesium-potassium phosphate cements. *Cement Concrete Research.*

Wang, H. (2006). *Study on the high performance magnesia-phosphate cement based composites.* Chongqing University.

Wang, A.-J., Zhang, J., Li, J.-M., Ma, A.-B., & Liu, L.-T. (2013). Effect of liquid-to-solid ratios on the properties of magnesium phosphate chemically bonded ceramics. *Materials Science and Engineering: C, 33*(5), 2508–2512.

Wang, H., Zhang, S., Ding, J., & Qi, Z. (2015). Study on the influent factors of magnesium phosphate cement repair materials abrasion resistance. *Journal of Functional Materials.*

Wang, Q., Yu, C., Yang, J., Chong, L., Xu, X., & Wu, Q. (2019). Influence of nickel slag powders on properties of magnesium potassium phosphate cement paste. *Construction Building Materials, 205*, 668–678.

Weng, Y., Ruan, S., Li, M., Mo, L., Unluer, C., Tan, M. J., & Qian, S. (2019). Feasibility study on sustainable magnesium potassium phosphate cement paste for 3D printing. *Construction Building Materials, 221.*

Xiong, C., Jiang, L., Xu, Y., Chu, H., Jin, M., & Zhang, Y. (2016). Deterioration of pastes exposed to leaching, external sulfate attack and the dual actions. *Construction Building Materials.*

Xu, B., Winnefeld, F., Kaufmann, J., & Lothenbach, B. J. C. (2019). Influence of magnesium-to-phosphate ratio and water-to-cement ratio on hydration and properties of magnesium potassium phosphate cements. *Cement Concrete Research, 123*, 105781.

Yang, E. H., & Li, V. C. J. C. (2010). Strain-hardening fiber cement optimization and component tailoring by means of a micromechanical model. *Construction Building Materials, 24*(2), 130–139.

Yang, Q., Zhu, B., & Wu, X. J. (2000). Characteristics and durability test of magnesium phosphate cement-based material for rapid repair of concrete. *Materials Structures, 33*(4), 229–234.

Yang, J. M., Shao, Y. X., & Liu, H. (2013). Influences of ratio of acid to base on the properties of magnesium and potassium phosphate cement. *Journal of Building Materials, 16*(6), 923–929.

Yang, J. (2011*). Control on setting time and water stability of magnesium-potassium phosphate cement and mechanism.* Southeast University.

Yu, B., Zhou, J., Cheng, B., & Yang, W. (2021). Compressive strength development and microstructure of magnesium phosphate cement concrete. *Construction Building Materials, 283*(3), 122585.

Yu, L., Xia, K., Gong, C., Chen, J., & Dai, H. (2020). An injectable bioactive magnesium phosphate cement incorporating carboxymethyl chitosan for bone regeneration. *International Journal of Biological Macromolecules, 160.*

Yuan, H., Shi, Y., Xu, Z., Lu, C., Ni, Y., & Lan, X. (2013). Influence of nano-ZrO_2 on the mechanical and thermal properties of high temperature cementitious thermal energy storage materials. *Construction Building Materials*, *48*(Complete), 6–10.

Yue, L., Tongfei, S., Bing, C., & Yaqiang, L. J. (2015). Performance of magnesium phosphate cement at elevated temperatures. *Construction Building Materials, 91*, 126–132.

Yue, L., Shi, T., Li, J. J. C., & Materials, B. (2016). Effects of fly ash and quartz sand on water-resistance and salt-resistance of magnesium phosphate cement. *105*, 384–390.

Zhang, X., Li, G., Niu, M., & Song, Z. J. C. (2018). Effect of calcium aluminate cement on water resistance and high-temperature resistance of magnesium-potassium phosphate cement. *Construction Building Materials, 175*, 768–776.

Chapter 6
Preparation and Performance of Sprayable UHDMC

Abstract This chapter aimed to develop a sprayable ultra-high ductility magnesium phosphate cement-based composite (UHDMC) and explored the effects of starch ether content, water–solid ratio, powder-binder ratio (*P/B*), borax content (*B/M*), fly ash (FA) substitution and polyvinyl alcohol (PVA) fibers volume content on the shootability, rheological and mechanical properties of magnesium phosphate cement-based materials. The correlation between shootability factors (build-up thickness and rebound rate) and rheological parameters (yield stress and plastic viscosity) was established, and the optimum mixture proportion suitable for the sprayed UHDMC was selected and then analyzed by the mechanical properties and pore structure between the cast and sprayed specimens. At the same time, the relationship between pore structure parameters and mechanical properties was established. The results in this chapter will offer valuable theoretical basis and specific guidance for the future application of sprayable UHDMC in engineering projects.

Keywords Ultra-high ductility · Magnesium phosphate cement · Shootability · Rheological properties · Mechanical properties · Pore structure

6.1 Introduction

Shotcrete is a rapidly setting and hardening type of concrete, which is delivered to the nozzle under air pressure through a hose after mixing specific raw materials in a certain proportion, and then sprayed on the target surface at a high speed (Leung et al., 2005). Up to now, shotcrete has found extensive application in tunnel construction, bridge reinforcement, safeguarding rock and soil slopes, and municipal engineering (Chen et al., 2019; Li et al., 2009, 2019; Xu et al., 2019), with its advantages of cost-saving benefits and high work efficiency due to not using special molds (Chen et al., 2019; Li et al., 2019). Generally speaking, several required key factors play a crucial role in concrete spraying technology and its widespread use, such as good fluidity, shootability, high early strength and strong adhesion ability (Li et al., 2009). However, ordinary concrete materials exhibit opposite characteristics, including high

H. Feng et al., *Ultra-High Ductility Magnesium-Phosphate-Cement-Based Composites (UHDMC)*, https://doi.org/10.1007/978-981-97-0952-6_6

brittleness, slow setting time and low early strength, which limits its applicability in shotcrete field. Consequently, a chemical accelerator or a novel material is often necessary.

Given that magnesium phosphate cement (MPC) offers advantages like good fluidity, quick setting time, high early strength and strong adhesion (Haque & Chen, 2019; Xu et al., 2015; Yang & Wu, 1999), it aligns well with the requirements of shotcrete and holds significant potential for application in shotcrete field. However, limited research has explored the use of MPC in shotcrete, and it is known to have some drawbacks related to brittleness. To enhance the broad application of MPC in shotcrete, addressing this brittle behavior is essential. One method for improving this brittle behavior involves incorporating randomly oriented fibers into MPC, leading to a novel materials of magnesium phosphate cement-based engineered cementitious composites (MPC-ECC) (Feng et al., 2018, 2019, 2020, 2022a, 2022b, 2022c, 2021a, 2021b). Based on the previous research, a new type materials of sprayed ultra-high ductility magnesium phosphate cement-based composites (UHDMC) has been progressively developed, which not only has the excellent suitable spraying properties of MPC, but also has the ultra-high ductility (Feng et al., 2021a, 2021b, 2022a, 2022b, 2022c; Li, 2019), along with anti-cracking and anti-spalling properties of ECC (Zhang & Zhang, 2017; Zhu et al., 2020). As for sprayable UHDMC, the main properties to the spraying effect are the shootability and rheology, so relative research should be studied.

Shootability refers to the capability of sprayed materials to adhere to or build-up on the vertical or overhead surface, including the cohesion ability within the materials and the rebounding ability. To achieve good shootability in shotcrete, it's necessary to make materials with strong working performance. This means that they can create higher build-up thickness and lower rebound rate. Numerous studies have highlighted factors that can enhance cohesion in the mixture for shotcrete, including the use of air-entraining admixtures (Beaupre, 1994), silica fume (Yun et al., 2015a, 2015b), accelerants (Pan et al., 2019), tackifiers (Pan et al., 2019), nano admixtures (Ning et al., 2019), fiber type (Kaufmann et al., 2013), and synthetic fibers (Austin et al., 1997; Dufour et al., 2006; Pan et al., 2019), thus increasing the build-up thickness and reducing the rebound rate. However, these factors affecting shootability were mainly focused on conventional cement-based materials, little research on novel sprayed UHDMC.

Rheology is the science that deals with the deformation and flow of materials. In the context of cement-based materials, rheology can be controlled by yield stress and plastic viscosity (Bingham, 1922). Yield stress is the proportional coefficient between the fluid shear stress and the shear rate, reflecting the internal resistance of the slurry (Banfill, 2003; Jiang et al., 2018). When it comes to the pumpability of shotcrete, achieving suitable rheological properties in fresh concrete is crucial. This entails having low yield stress and high plastic viscosity (Beaupre, 1994; Feys et al., 2013, 2016; Yun et al., 2015a, 2015b) to prevent blockages and excessive pumping pressure (Abd El Megid, 2012). Conversely, for good shootability in shotcrete, a high yield stress is necessary to ensure the slurry adheres well to the sprayed surface and resists sagging (Beaupre, 1994; He et al., 2020; Yun et al., 2015a, 2015b).

Therefore, there is a need to balance the values of plastic viscosity and yield stress to ensure both pumpability and shootability in shotcrete. Research has explored the impact of various mineral admixtures (e.g., fly ash, silica fume, metakaolin) on the rheology of shotcrete, presenting that the combination of fly ash with silica fume or metakaolin can enhance pumpability and shootability by reducing plastic viscosity and increasing yield stress (Liu et al., 2021; Yun et al., 2018, 2022). Additionally, the relationship between rheological parameters and shootability factors in shotcrete was also delved, such as, the plastic viscosity and yield stress were negatively related to the rebound rate, while the yield stress was positively correlated with build-up thickness (Pan et al., 2019; Yun et al., 2015a, 2015b). Based on this analysis, the rheological parameters of wet-mix shotcrete can to some extent predict its performance. However, it is not clear whether these relationships still exist in UHDMC, and relative research is necessary to be studied.

This chapter aimed to develop a sprayable UHDMC by investigating shootability, rheological and mechanical properties under various variable factors, including starch ether content, water–solid ratio, powder-binder ratio, borax content (*B/M*), fly ash (FA) substitution, and the volume content of PVA fiber. Furthermore, based on the same spray parameters, a data fitting analysis was conducted to explore the correlation between rheological properties and shootability. The optimal mixture proportion was determined based on rheological and shootability indicators. Finally, a comparison was made between the sprayed and cast samples by assessing compressive strength, tensile properties, and pore structure using MIP testing. Although the spraying process was simulated using a spray gun, the results in this paper still offer valuable theoretical basis and specific guidance for the future application of sprayable UHDMC in engineering projects.

6.2 Experimental Program

6.2.1 Raw Materials

The MPC studied in this research was mixed through the combination of magnesia oxide (MgO), potassium dihydrogen phosphate (KH_2PO_4), and borax ($Na_2B_4O_7 \cdot 10H_2O$). MgO with a specific surface area of 451.0 m^2/kg, was provided by Guizhou Magnesium Phosphorus Materials Co., Ltd. And its chemical composition and particle size distribution was shown in Table 6.1 and Fig. 6.1, respectively.

Two particle size ranges of KH_2PO_4 (white crystal with a purity of ≥99.5%) were used and mixed in a mass ration of 1:1, in which the particle size ranges of 425–600 μm and 180–315 μm were purchased from Tianjin Dingshengxin Chemical Co., Ltd., and Wujiang Weitong Chemical Co., Ltd., respectively. Generally, the particle size of KH_2PO_4 plays a critical role in governing the chemical reaction rate in the MPC, presenting a trend that finer KH_2PO_4 particles lead to faster reactions. Therefore, the

Table 6.1 Chemical composition of MgO (Provided by the supplier)

Ingredient	Mass percent (%)
MgO	97
Fe_2O_3	0.18
SiO_2	0.7
CaO	1.4
Al_2O_3	0.1

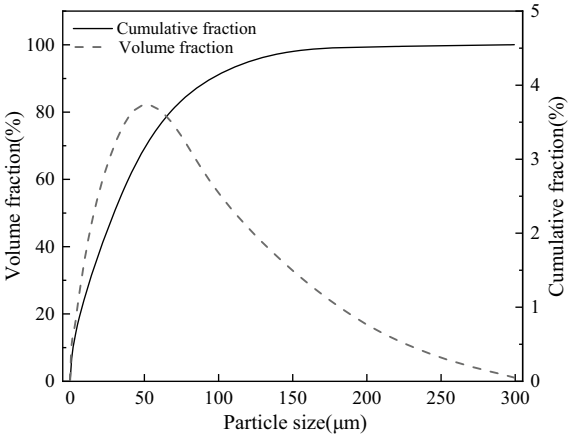

Fig. 6.1 Particle size distribution of MgO

main aim of using two kinds of KH_2PO_4 is to maintain a controlled and reasonable hydration rate. The specific gravity of the mixed KH_2PO_4 was 2.34 g/cm^3.

Industrial-grade borax ($Na_2B_4O_7 \cdot 10H_2O$, 99.5%) with a particle size of 187.5 μm was manufactured by Liaoning Borda Technology Co., Ltd., which was used as a retarder.

Fly ash (FA) with a specific surface area of 850.0 m^2/kg was provided by Henan Kanghui Cement Products Co., Ltd. Its chemical composition and particle size distribution was shown in Table 6.2 and Fig. 6.2, respectively.

The quartz powder, falling within a particle size range of 0–75 μm, was supplied by Henan Zhongbang Environmental Protection Technology Co., Ltd. Its technical indicators and particle size distribution was shown in Table 6.3 and Fig. 6.3, respectively.

Starch ether (SE) utilized is a white powder, specifically hydroxypropyl modified starch ether ($C_{31}H_{56}O_{22}$), and it was manufactured by Guangzhou Jiantubao Building Materials Co., Ltd. The technical indicators of starch ether are shown in Table 6.4.

Polyvinyl alcohol (PVA) fibers produced by Japanese Kuraray Company was used in this study. The technical indicators of PVA fibers are shown in Table 6.5. In addition, the tap water was used as mixing water.

Table 6.2 Chemical composition of fly ash (Provided by the supplier)

Ingredient	Mass fraction (%)
SiO_2	53.97
Al_2O_3	31.15
Fe_2O_3	4.16
CaO	4.01
MgO	1.01
Na_2O	0.89
K_2O	2.49
SO_3	1.61

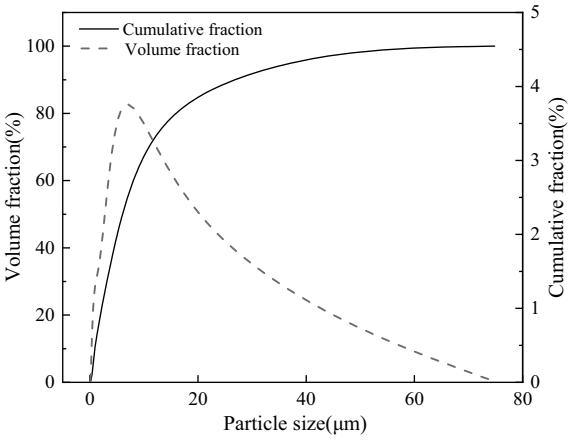

Fig. 6.2 Particle size distribution of FA

Table 6.3 Technical indicators of quartz powder (Provided by the supplier)

SiO_2 content (%)	99.0
Unit weight (g/cm^3)	1.75
Morse hardness	75
Porosity (%)	43
Specific gravity (g/cm^3)	2.67

6.2.2 Mixture Proportions

For magnesium phosphate cement (MPC), the borax content is 6% by weight of magnesium oxide, and the magnesium oxide to phosphate mass ratio (*M/P*) is 4. Based on our team's previous research on UHDMC (Feng et al. 2021a, 2021b, 2022a, 2022b, 2022c) and other researchers' studies on MPC (Li et al., 2014). the mole ratio of MgO to KH_2PO_4 was fixed at 4 in all MPC mixtures. The control mixture

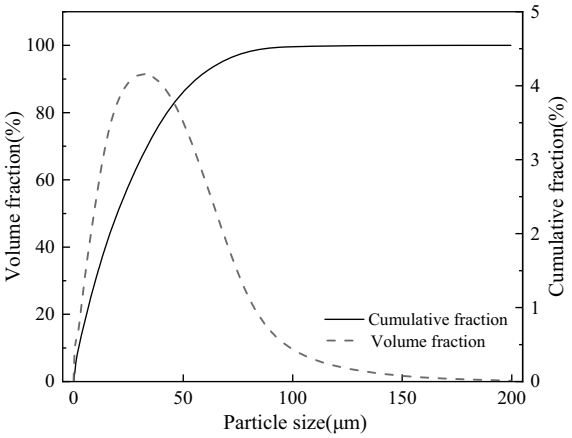

Fig. 6.3 Particle size distribution of quartz powder

Table 6.4 Technical indicators of starch ether (Provided by the supplier)

Bulk density (g/L)	500 ± 100
Water content (%)	<10
PH	4.16
Ash content (750 °C) (%)	10

Table 6.5 PVA fiber performance index (Provided by the supplier)

Diameter (μm)	40
Length (mm)	12
Tensile strength (MPa)	1560
Elastic modulus (GPa)	41
Elongation at break (%)	6.5
Density (g/cm^3)	1.3

proportion of UHDMC is: the starch ether content, water–solid mass ratio, powder-cement mass ratio, borax-MgO mass ratio, substitution rate of FA and PVA fibers volume fraction. The mixture proportions of UHDMC are shown in Table 6.6.

6.2.3 Mixing and Curing

The mixing process involved adding MgO, KH_2PO_4, quartz powder, borax, FA, and starch ether sequentially into the mixer and stirring for a minimum of 120 s. Subsequently, water and PVA fibers were added to the mixture and stirred for an additional 120 s. It's essential to note that fibers in small quantities through multiple

Table . 6 Mixture proportions of UHDMC

Group	SE (%)	*W/S*	*P/B*	*B/M* (%)	FA (%)	PVA (%)
SE-0	0	0.14	0.2	8	30	1.5
SE-0.05	0.05					
SE-0.10	0.10					
SE-0.15	0.15					
SE-0.20	0.20					
W/S-0.12	0.15	0.12	0.2	8	30	1.5
W/S-0.13		0.13				
W/S-0.14		0.14				
W/S-0.15		0.15				
W/S-0.16		0.16				
W/S-0.17		0.17				
P/B-0.0	0.15	0.14	0.0	8	30	1.5
P/B-0.1			0.1			
P/B-0.2			0.2			
P/B-0.3			0.3			
P/B-0.4			0.4			
P/B-0.5			0.5			
B/M-4	0.15	0.14	0.3	4	30	1.5
B/M-6				6		
B/M-8				8		
B/M-10				10		
B/M-12				12		
B/M-14				14		
FA-0	0.15	0.14	0.3	8	0	1.5
FA-10					10	
FA-20					20	
FA-30					30	
FA-40					40	
FA-50					50	
FA-60					60	
PVA-0.0	0.15	0.14	0.3	8	40	0.0
PVA-0.5						0.5
PVA-1.0						1.0
PVA-1.5						1.5
PVA-2.0						2.0
PVA-2.5						2.5
PVA-3.0						3.0

Note Starch ether content is starch ether to all materials weight ratio; *M/P* is the mole ratio of MgO to KH_2PO_4; *W/S* is the weight ratio of water to solid (contain MgO, KH_2PO_4, quartz powder and fly ash); *P/B* is the weight ratio of quartz powder to cement (contain MgO and KH_2PO_4); *B/M* is the weight ratio of borax to MgO; Substitution rate of FA is the percentage of fly ash to cement by weight

Reproduced from Development of sprayable ultra-high ductility magnesium phosphate cement-based composites based on the rheological properties by Hu Feng with permission from Elsevier

Fig. 6.4 Spraying equipment diagram. Reproduced from Development of sprayable ultra-high ductility magnesium phosphate cement-based composites based on the rheological properties by Hu Feng with permission from Elsevier

additions facilitates their uniform distribution within the mixture. Next, the different forming methods were presented as follow.

For the cast UHDMC specimens, the molds filled with UHDMC were placed on a vibration table, and vibration was sustained for at least 60 s to ensure the thorough removal of air bubbles. Finally, the specimens were kept indoors under controlled conditions (temperature: 20 ± 2 °C, relative humidity: 60 ± 5% RH) for approximately 24 h before demolding. After demolding, the specimens were transferred to a standard curing room (temperature: 20 ± 2 °C, relative humidity: 98% RH) for a duration of 7 days.

For the sprayed UHDMC specimens, a spray gun was used for the spray test, whose appearance and spraying principle were shown in the Figs. 6.4 and 6.5, respectively. A standard air compressor with a power rating of 2200 watts and a maximum pressure rating of 0.7 megapascals (MPa) was employed to supply the spray pressure. The spray test process of UHDMC, as illustrated in Fig. 6.6, involved three main steps: (a) Preparations were made for the test site and equipment. The vertical angle of the spray substrate was adjusted to approximately 60°. The air compressor pressure was increased to around 0.7 MPa, and the air compressor was then connected to the spray gun using an air duct; (b) The mixed materials were poured into the spray gun, positioned about 10–15 cm away from the bottom plate. The air pressure at the nozzle was adjusted during the spraying process to achieve the desired spray effect; (c) UHDMC was sprayed into the mold through a series of consecutive sprays, and any excess materials were removed from the mold after spraying.

6.2.4 Shootability Test

Shootability was assessed based on two key parameters: the maximum build-up thickness and the rebound rate. The build-up thickness measures the bonding capacity between the cement-based materials and the structural surface. It is determined by

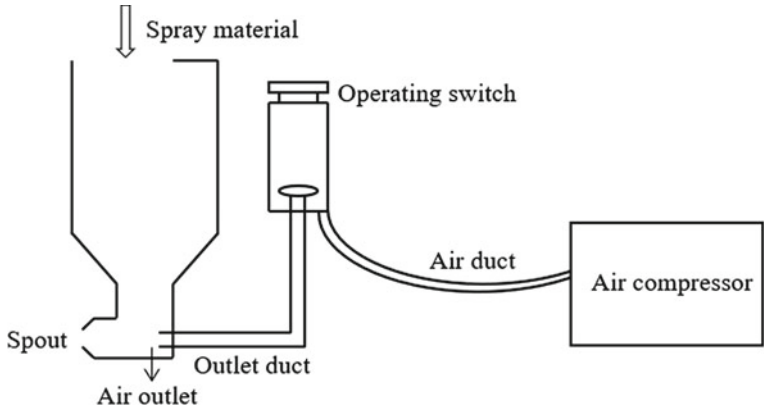

Fig. 6.5 Spraying principle. Reproduced from Development of sprayable ultra-high ductility magnesium phosphate cement-based composites based on the rheological properties by Hu Feng with permission from Elsevier

Fig. 6.6 Experimental process. Reproduced from Development of sprayable ultra-high ductility magnesium phosphate cement-based composites based on the rheological properties by Hu Feng with permission from Elsevier

continuously spraying at a specific base point on the vertical spray surface until the materials naturally detach under their own weight. The measurement method is illustrated in Fig. 6.7.

The rebound rate is a measure of the self-cohesion of the sprayed material and its adhesion to the spray surface. A high rebound rate indicates poor spraying performance and weak material adhesion. Conversely, a low rebound rate suggests good spraying performance, with the material effectively adhering to the sprayed structural

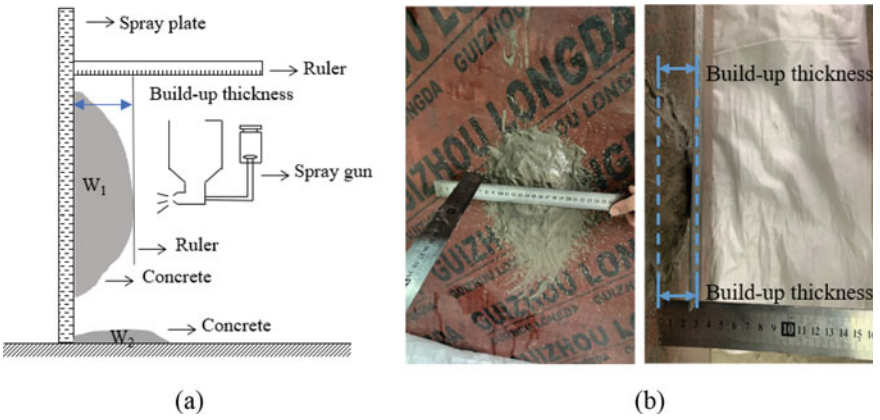

Fig. 6.7 Schematic and physical diagrams of spray thickness test. Reproduced from Development of sprayable ultra-high ductility magnesium phosphate cement-based composites based on the rheological properties by Hu Feng with permission from Elsevier

surface. In this study, the build-up thickness and rebound rate of the slurry in each mixture were tested three times, and the results were averaged. The test method for the rebound rate adhered to the Japanese standard JSCE-F 563–2005 "Test method for the rebound rate of shotcrete." The calculation formula is presented in Eq. 6.1:

$$R = \frac{W_2}{W_1 + W_2} \times 100\% \tag{6.1}$$

in which, R is the rebound rate [%]; W_2 is the weight of the material that rebounded [g]; and W_1 is the weight of the material that stuck onto the rebound panel [g].

6.2.5 Rheology Test

The Bingham model is the most straightforward and widely applied model in the study of rheology for cement-based materials. The yield stress and plastic viscosity are acquired through linear regression analysis of the rheological curve (Yun et al., 2018, 2022), offering a more precise approach to measure the rheological parameters of cement-based materials, aligning with the precision requirements for engineering applications and scientific research in this field. In this study, the determination of the yield stress and plastic viscosity was carried out using this model (Papo & Piani, 2004), and the formula is demonstrated in Eq. 6.2 (Jiao et al., 2017):

$$\tau = \tau_0 + \eta \cdot \gamma \tag{6.2}$$

Fig. 6.8 RVDV-1T rotational viscometer and constant temperature water tank. Reproduced from Development of sprayable ultra-high ductility magnesium phosphate cement-based composites based on the rheological properties by Hu Feng with permission from Elsevier

where τ is the shear stress (Pa), τ_0 is the yield stress (Pa), η is the plastic viscosity (Pa·s) and γ is the shear rate (s^{-1}).

The plastic viscosity of the cement slurry was measured using the RVDV-1T rotational viscometer, manufactured by Shanghai Fangrui Instrument Co., Ltd. This viscometer allows for the setting of the rotation rate and automatically calculates the shear rate corresponding to the rotation rate, as illustrated in Fig. 6.8. To eliminate the temperature effect during the test process, the tests were conducted in a constant-temperature water tank.

Each mixture proportion was subjected to a rheological test to determine the instantaneous viscosity of the slurry at different shear rates (1.04 s^{-1}, 1.25 s^{-1}, 1.67 s^{-1}, 2.50 s^{-1}, 4.18 s^{-1}, 6.27 s^{-1}, 10.45 s^{-1}), which were determined by the corresponding rotation rates. Shear stress was calculated based on these measurements, and the data points of shear rate and shear stress were subjected to linear fitting using the Bingham model formula to obtain the fitted linear equation, thereby calculating τ_0 and η. It's important to note that in this research, the rheological tests were conducted after the spray tests. These tests were independent, but they were performed on slurry composed of the same raw materials and the same mixture proportions, with a time lapse of 1–2 min after slurry mixing.

6.2.6 Compressive Strength Test

According to ASTM C109 (Standard, 2008), the compressive test was conducted on 50 mm × 50 mm × 50 mm cubic specimens by using the 2000 kN pressure testing machine (model: YAW-2000B). The loading rate was set as 0.9 kN/s. From this test, the compressive strength was recorded. The average value of three replicates was adopted.

6.2.7 Tensile Properties Test

The tensile properties of specimens created from the optimal mixture proportions were tested using a universal testing machine. The loading rate was 0.25 mm/min. Figure 6.9 illustrates the dog-shaped bone specimen and the loading procedure of the specimen.

In this testing, two YWC-10 type displacement transducers (LVDTs) manufactured by Liyang Chaoyuan Instrument Factory were utilized to measure the deformation and acquire the corresponding stress–strain curves. For each curing age group, eight dog-bone specimens were tested, comprising 4 poured specimens and 4 sprayed specimens.

The tensile stress and tensile strain of the coupon specimens are computed using Eqs. 6.3 and 6.4. These calculations are based on the recorded tensile load and deformation values, and they are used to plot the direct tensile stress–strain curve. Once the specimen cracks, the tensile load starts to decrease. When the tensile load reaches 85% of the peak tensile load, the corresponding tensile stress and tensile strain are designated as the ultimate tensile stress and ultimate tensile strain, respectively.

$$\delta = \frac{F}{st} \tag{6.3}$$

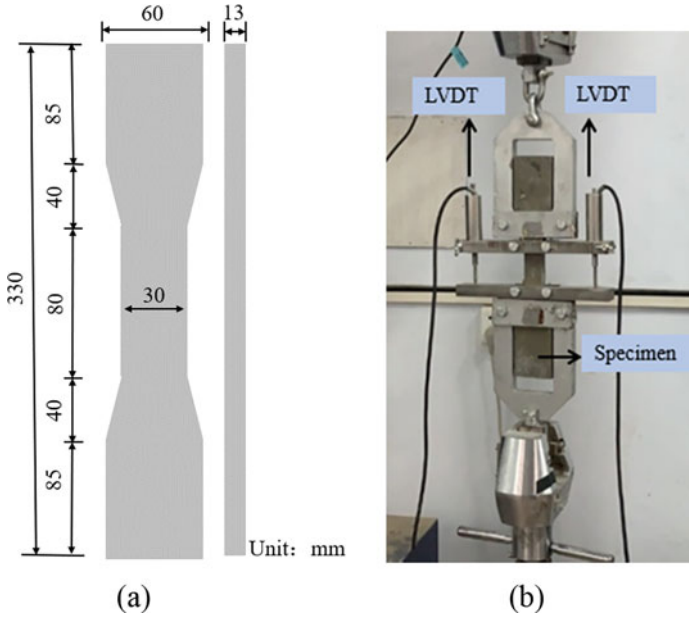

Fig. 6.9 Tensile properties test: **a** specimens and **b** loading diagram. Reproduced from Development of sprayable ultra-high ductility magnesium phosphate cement-based composites based on the rheological properties by Hu Feng with permission from Elsevier

where δ is tensile stress (MPa); s is the width of test piece (40 mm in this study); F is tensile load (N); and t is the thickness of test piece (15 mm in this study).

$$\varepsilon = \frac{L_o}{L} \times 100\% \tag{6.4}$$

where ε is tensile strain (%); L is the specimen gauge length (120 mm in this study); and L_o is the specimen elongation value under tension (mm).

6.2.8 Pore Structure Test

Mercury intrusion porosimetry (MIP) was conducted using a high-performance automatic mercury porosimeter Micro Active Auto Pore V 9600. This method was employed to examine the pore structure of UHDMC, providing information on porosity and pore size distribution. To prepare the samples for testing, 1 cm cubic sections were cut from specimens that had reached the desired curing age. Before conducting the test, these samples were preserved in ethanol to halt hydration and subsequently dried in a freeze dryer until a constant mass was achieved.

6.3 Results and Discussion

6.3.1 Factors Affecting Shootability and Rheological Properties

(1) **Effect of starch ether content**

Figure 6.10 demonstrates the influence of starch ether content on the build-up thickness and rebound rate of UHDMC. As depicted in Fig. 6.10, when the starch ether content was below 0.15%, an increase in starch ether content led to a gradual increase in build-up thickness and a gradual decrease in the rebound rate. However, an opposite trend was observed when the starch ether content exceeded 0.15%, resulting in a 4.5% reduction in build-up thickness and a 6.8% increase in the rebound rate. This phenomenon can be attributed to the formation of a network structure resulting from the interaction between hydrophobic and hydrophilic molecular chains in the starch ether. This network structure can absorb more mortar particles and create a slurry with structural viscosity (Yu et al., 2018). This, in turn, leads to a significant increase in viscosity and yield stress values, as well as improved resistance to sagging (Huang et al., 2014). However, this effect diminishes when the starch ether content exceeds 0.15%. Therefore, the optimal shootability of UHDMC is achieved at a starch ether dosage of 0.15%, resulting in a maximum build-up thickness of 22 mm and a rebound rate of 15.44%.

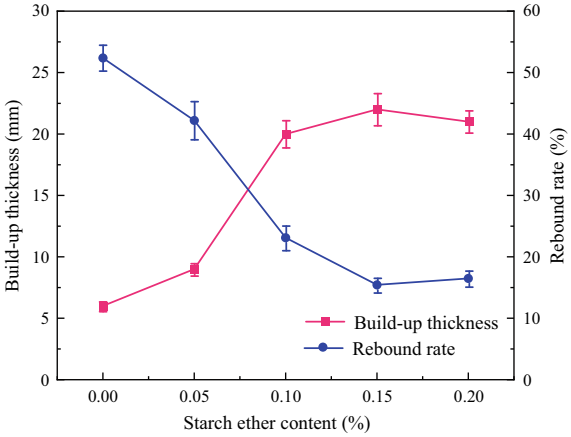

Fig. 6.10 Effect of starch ether content on the shootability factors of UHDMC. Reproduced from Development of sprayable ultra-high ductility magnesium phosphate cement-based composites based on the rheological properties by Hu Feng with permission from Elsevier

Figure 6.11 illustrates the effect of starch ether content on the rheological properties of UHDMC. In Fig. 6.11a, a strong linear relationship between shear stress and shear rate is observed under different starch ether contents, with R^2 values ranging from 0.92 to 0.99. Figure 6.11b presents the effects of various starch ether contents on yield stress and plastic viscosity. The data reveals that, for different starch ether contents, yield stress and plastic viscosity vary between 68.19 to 91.92 Pa and 2.05 to 2.42 Pa·s, respectively. It's notable that the influence of starch ether content on yield stress is more significant than on plastic viscosity. The increase in starch ether content results in the formation of a robust gel in the alkaline pore solution created by starch ether, which enhances the resistance of slurry flow, leading to an increase in yield stress (Peng et al., 2018). Considering the need for optimal shootability and suitable rheological properties, the ideal starch ether content is determined to be 0.15%. At this level, the yield stress and plastic viscosity are 91.64 Pa and 2.42 Pa s, respectively.

(2) **Effect of water–solid ratio**

Figure 6.12 illustrates the effect of the water–solid ratio on the build-up thickness and rebound rate of UHDMC. It's evident that as the water–solid ratio increases, the build-up thickness initially increases and then decreases, while the rebound rate demonstrates the opposite trend. Throughout the test, when the water–solid ratio exceeded 0.16, it became challenging to measure the build-up thickness and rebound rate. This is due to the slurry's high fluidity and low sag resistance at these higher water–solid ratios. Therefore, the optimal water–solid ratio is determined to be 0.13, offering the best shootability. At this ratio, UHDMC achieves a maximum build-up thickness of 26 mm and a minimum rebound rate of 14.38%.

Figure 6.13 depicts the effect of the water–solid ratio on the rheological properties of UHDMC. In Fig. 6.13a, the relationship between shear stress and shear rate at various water–solid ratios shows a strong linear correlation, with R^2 values ranging from 0.88 to 0.99. Figure 6.13b illustrates the effect of different water–solid ratios

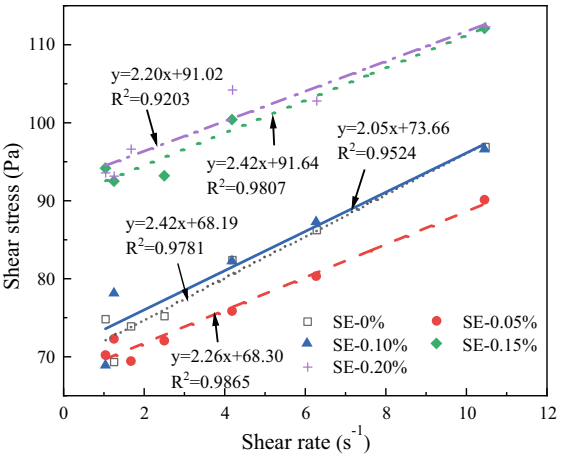

(a) Rheological parameter fitting curves

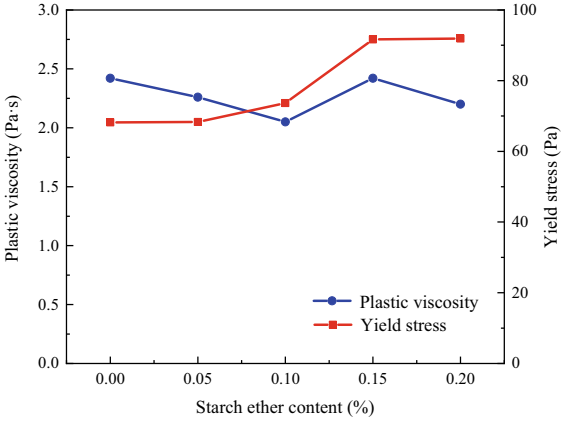

(b) Yield stress and plastic viscosity

Fig. 6.11 Effect of starch ether content on the rheological properties of UHDMC. Reproduced from Development of sprayable ultra-high ductility magnesium phosphate cement-based composites based on the rheological properties by Hu Feng with permission from Elsevier

on yield stress and plastic viscosity. The yield stress and plastic viscosity exhibited ranges of 55.58 to 98.72 Pa and 1.07 to 3.87 Pa s, respectively. Both yield stress and plastic viscosity decreased as the water–solid ratio increased. This can be explained by the increased free water content in the slurry, which led to greater dispersion of structural units and thicker water films on particle surfaces. Consequently, this reduced friction between particles within the slurry, resulting in a notable decrease in yield stress and plastic viscosity (Botsis et al., 2012).

Generally, higher water–solid ratios lead to better rheological performance. However, for the sake of shootability, a water–solid ratio exceeding 0.14 causes excessively good slurry fluidity, significantly reducing the build-up thickness. Conversely, a water–solid ratio below 0.14 makes the slurry too viscous for spraying. Therefore, the optimal water–solid ratio is determined to be 0.14. At this ratio, UHDMC

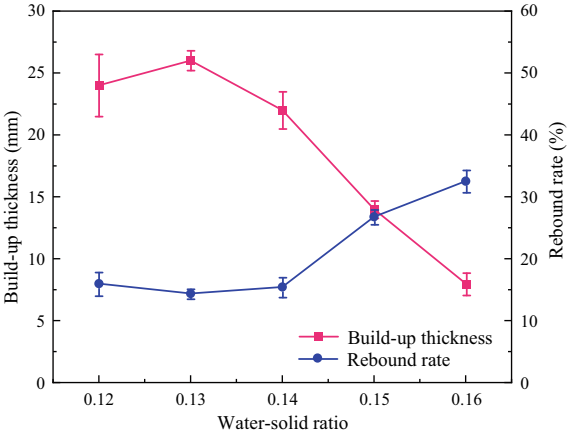

Fig. 6.12 Effect of water–solid ratio on the shootability factors of UHDMC. Reproduced from Development of sprayable ultra-high ductility magnesium phosphate cement-based composites based on the rheological properties by Hu Feng with permission from Elsevier

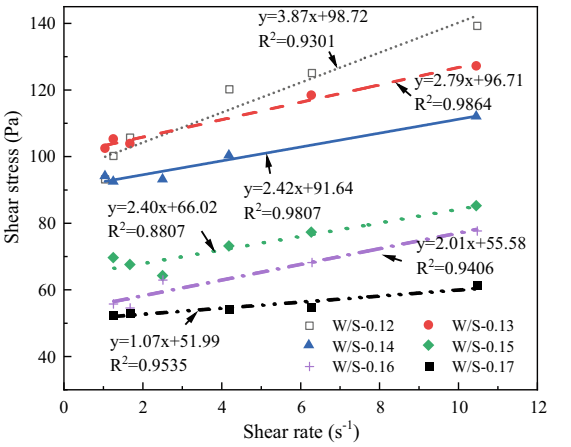

(a) Rheological parameter fitting curves

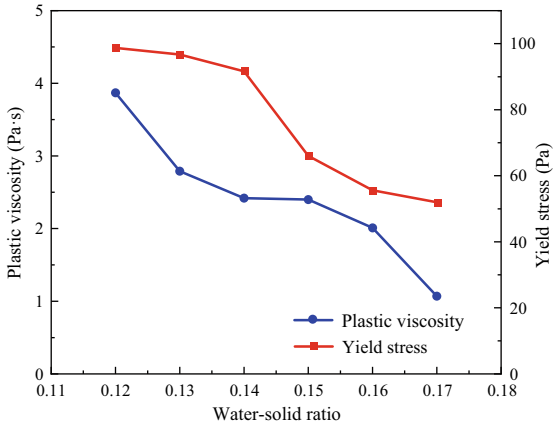

(b) Yield stress and plastic viscosity

Fig. 6.13 Effect of water–solid ratio on the rheological properties of UHDMC. Reproduced from Development of sprayable ultra-high ductility magnesium phosphate cement-based composites based on the rheological properties by Hu Feng with permission from Elsevier

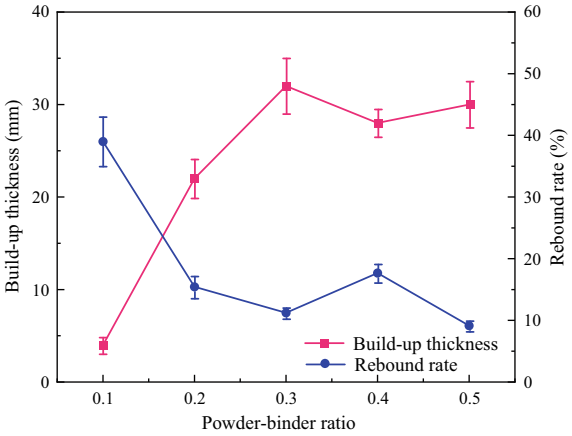

Fig. 6.14 Effect of powder-binder ratio on the shootability factors of UHDMC. Reproduced from Development of sprayable ultra-high ductility magnesium phosphate cement-based composites based on the rheological properties by Hu Feng with permission from Elsevier

achieves a build-up thickness of 22 mm, a rebound rate of 15.44%, and yield stress and plastic viscosity values of 91.64 Pa and 2.42 Pa s, respectively.

(3) **Effect of powder-binder ratio**

Figure 6.14 illustrates the effect of the powder-binder ratio on the build-up thickness and rebound rate of UHDMC. It's evident that when the powder-binder ratio was below 0.4, an increase in this ratio led to an initial increase in build-up thickness followed by a decrease. Conversely, the rebound rate decreased initially and then increased. When the powder-binder ratio exceeded 0.4, both build-up thickness and rebound rate exhibited slight fluctuations. Notably, the most favourable shootability was observed when the powder-to-binder ratio was 0.3, resulting in a build-up thickness of 32 mm and a rebound rate of 11.23%.

Figure 6.15 depicts the effect of the powder-binder ratio on the rheological properties of UHDMC. In Fig. 6.15a, a strong linear relationship between shear stress and shear rate can be observed at different powder-binder ratios, with R^2 values ranging from 0.94 to 0.99. Figure 6.15b illustrates the impact of varying powder-binder ratios on yield stress and plastic viscosity. The data reveal that under different powder-binder ratios, the ranges of variation for yield stress and plastic viscosity were 70.15 to 113.68 Pa and 1.83 to 8.58 Pa s, respectively. Both yield stress and plastic viscosity increased progressively with higher powder-binder ratios. This phenomenon can be attributed to the greater powder content, which increases particle contact and collision probabilities, thus raising yield stress. Simultaneously, the higher powder content results in thinner coatings of cementitious material on powder particle surfaces, increasing the friction force between powder particles and subsequently elevating plastic viscosity (Vance et al., 2013). Consequently, taking the best shootability into account, the optimum powder-binder ratio was determined to be 0.3, resulting in yield stress and plastic viscosity values of 94.64 Pa and 5.51 Pa s, respectively.

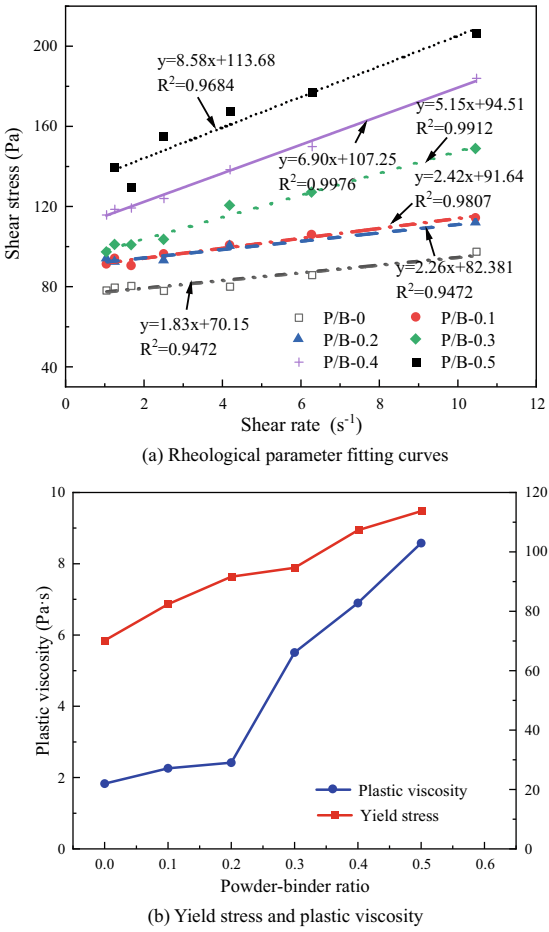

(a) Rheological parameter fitting curves

(b) Yield stress and plastic viscosity

Fig. 6.15 Effect of powder-binder ratio on the rheological properties of UHDMC. Reproduced from Development of sprayable ultra-high ductility magnesium phosphate cement-based composites based on the rheological properties by Hu Feng with permission from Elsevier

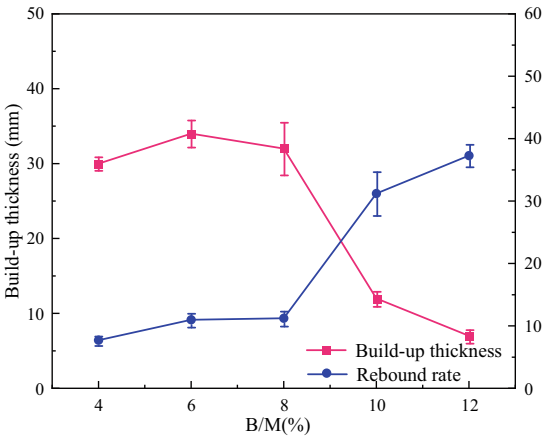

Fig. 6.16 Effect of *B/M* on the shootability factors of UHDMC. Reproduced from Development of sprayable ultra-high ductility magnesium phosphate cement-based composites based on the rheological properties by Hu Feng with permission from Elsevier

(4) **Effect of *B/M***

Figure 6.16 illustrates the effect of borax content on the build-up thickness and rebound rate of UHDMC. It's evident that the build-up thickness initially increased and then decreased with the rising borax content, while the rebound rate exhibited a gradual increase. During testing, when the *B/M* ratio exceeded 14%, it became challenging to measure the build-up thickness and rebound rate due to the improved slurry fluidity and reduced sagging resistance. The optimal shootability was observed with a borax content of 6%, resulting in a maximum build-up thickness of 34 mm and a minimum rebound rate of 10.98%. However, considering that increasing the borax content significantly delays the setting time and extends the working time for spraying, a borax content of 8% was chosen. In comparison to the 6% borax content, the changes in build-up thickness and rebound rate were relatively small, approximately 5.9 and 2.3%, respectively.

Figure 6.17 illustrates the effect of the *B/M* on the rheological properties of UHDMC. As seen in Fig. 6.17a, a strong linear relationship between shear rate and shear stress was observed at different *B/M* ratios, with R^2 values ranging from 0.92 to 0.99. In Fig. 6.17b, the effect of different *B/M* ratios on yield stress and plastic viscosity is presented. It's evident that under various *B/M* ratios, the ranges of variation for yield stress and plastic viscosity were 70.15 to 113.68 Pa and 1.83 to 8.58 Pa·s, respectively. Both yield stress and plastic viscosity exhibited an initial increase followed by a decrease with the rise of the *B/M* ratio. When the borax content in the slurry was less than 6%, the borax could be fully dissolved in an acidic environment, significantly increasing the pH value. This inhibited the dissolution of MgO and led to higher particle concentration in the solution and increased collision and friction among particles, resulting in elevated yield stress and plastic viscosity (Yang & Qian, 2010). Conversely, when the borax content was too high (≥8%), the effective components and hydration products involved in the hydration reaction were significantly reduced. This resulted in a reduction in particle friction due to the generation of numerous unreacted borax crystal particles with smooth surfaces in the slurry, causing a decrease in yield stress and plastic viscosity (Ma et al., 2021). Based on the optimal shootability factors, a *B/M* ratio of 8% was selected, where the yield stress and plastic viscosity were 94.64 Pa and 5.51 Pa·s, respectively.

(5) **Effect of FA substitution**

Figure 6.18 displays the effect of FA substitution on the build-up thickness and rebound rate of UHDMC. It is evident that with the increase of FA substitution, the build-up thickness gradually increases, while the rebound rate exhibits significant fluctuations. Notably, when the FA substitution reaches 60%, the slurry becomes too viscous with poor fluidity. This can be attributed to the increased water absorption caused by fly ash, especially with higher fly ash content. This higher water absorption reduces the amount of free water in the slurry, subsequently increasing the friction among particles and ultimately decreasing the slurry's fluidity (Feng et al., 2022a, 2022b, 2022c; Mo et al., 2018; Xu et al., 2018).

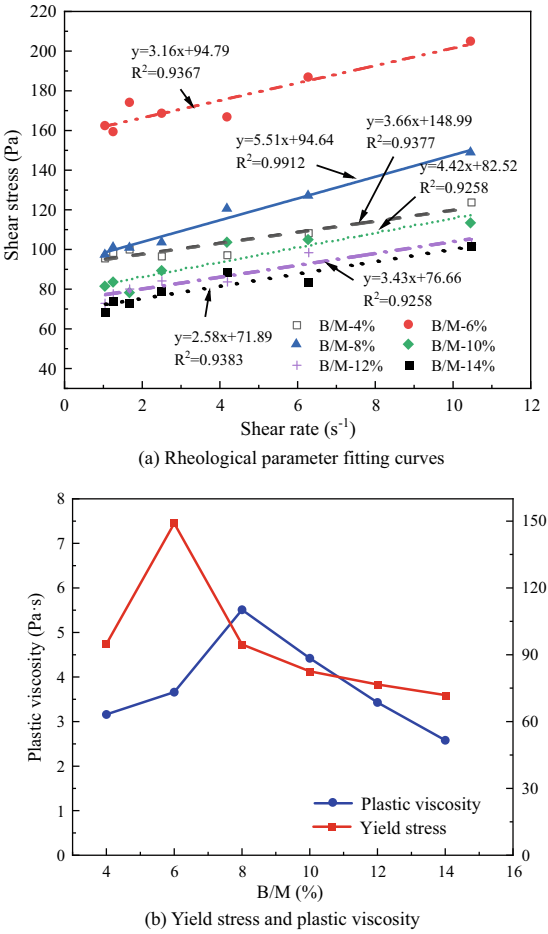

(a) Rheological parameter fitting curves

(b) Yield stress and plastic viscosity

Fig. 6.17 Effect of *B/M* on the rheological properties of UHDMC. Reproduced from Development of sprayable ultra-high ductility magnesium phosphate cement-based composites based on the rheological properties by Hu Feng with permission from Elsevier

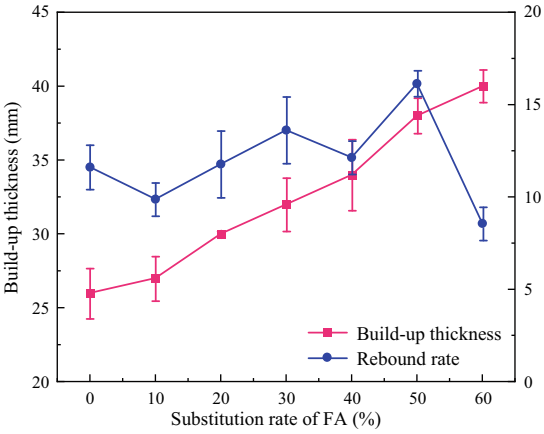

Fig. 6.18 Effect of FA substitution on the shootability factors of UHDMC. Reproduced from Development of sprayable ultra-high ductility magnesium phosphate cement-based composites based on the rheological properties by Hu Feng with permission from Elsevier

Figure 6.19 illustrates the effect of FA substitution on the rheological properties of UHDMC. In Fig. 6.19a, it's evident that there's a strong linear relationship between shear rate and shear stress at various levels of FA substitution, with R^2 values ranging between 0.98 and 0.99. As shown in Fig. 6.19b, the range of variation for both yield stress and plastic viscosity is 92.63 to 118.77 Pa and 4.85 to 7.17 Pa·s, respectively. When the FA substitution is less than 40%, both the yield stress and plastic viscosity gradually decrease with increasing FA substitution. This reduction can be attributed to the lubricating or "ball bearing effect" of fly ash (Vance et al., 2013), which has a spherical particle shape (Feng et al., 2022a, 2022b, 2022c; Mikanovic & Jolicoeur, 2008). This effect makes it easier for particles in the slurry to move relative to each other, reducing flow resistance and friction among particles. However, when the FA substitution exceeds 40%, the increased amount of fly ash leads to greater water absorption, decreasing the content of free water in the slurry. This, in turn, increases friction among particles, resulting in the formation of more network-like or flocculated structures among the particles, and thus the increase of yield stress and plastic viscosity (Felekoğlu et al., 2006; Mo et al., 2018).

Considering the analysis above, it's clear that while a 60% FA substitution results in the best shootability, the rheological properties of the slurry are not optimal. To strike a balance between shootability and rheological properties, a 40% FA substitution is the best choice. At this substitution level, the build-up thickness and rebound rate are 34 mm and 12.14%, respectively, and the yield stress and plastic viscosity are 92.63 Pa and 4.85 Pa·s, respectively.

(6) **Effect of PVA content**

Figure 6.20 demonstrates the effect of PVA (Polyvinyl Alcohol) content on the build-up thickness and rebound rate of UHDMC. As observed, with an increase in PVA content, the build-up thickness initially increased and then decreased, while the rebound rate showed an initial decrease followed by an increase. The optimal shootability factors, with a build-up thickness of 38 mm and a rebound rate of 8.98%, were achieved when the PVA content was 2%. This phenomenon can be explained by the frictional force of randomly distributed PVA fibers and the particles of cementitious material in the slurry, which restricts the flow of the slurry, acting as a thickener for the mixture (Xiong et al., 2018). Additionally, PVA fibers are hydrophilic, which means that they can absorb water molecules, resulting in a reduction of setting time and an increase of the viscosity of the slurry (Li, 2021). However, when the PVA content exceeds 2%, the excessive fibers interferes with the uniform dispersion of fibers in the slurry, resulting in the increases of overlap and agglomeration among fibers and poor bonding properties between fibers and matrix, which increased the rebound rate (Kaufmann et al., 2013).

Figure 6.21 presents the effect of PVA (Polyvinyl Alcohol) content on the rheological properties of UHDMC. As observed in Fig. 6.21a, there was a consistent linear relationship between shear rate and shear stress at different PVA contents, with R^2 values ranging from 0.96 to 0.99. Figure 6.21b demonstrates the effects of different PVA contents on yield stress and plastic viscosity. The results showed that the yield stress exhibited an initial increase followed by a decrease with increasing

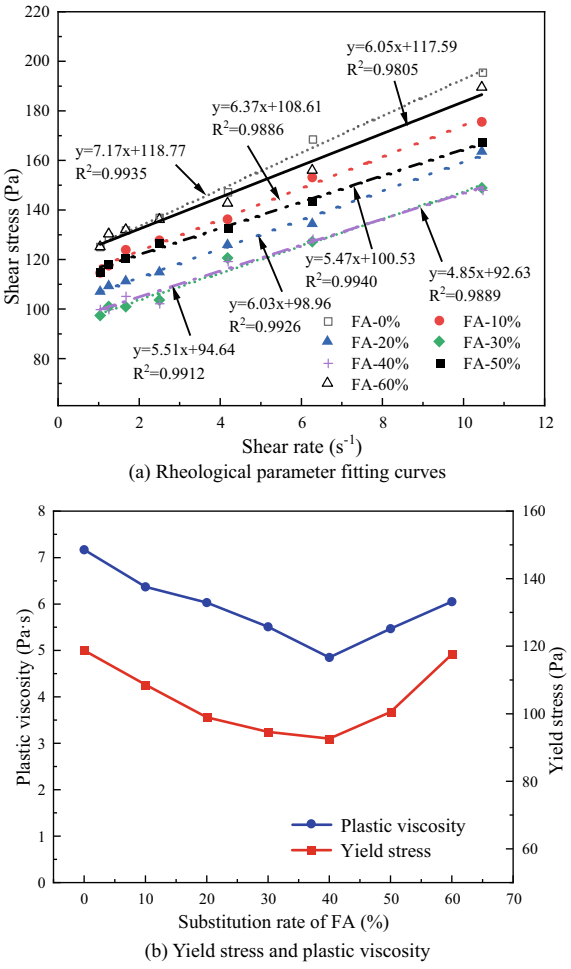

(a) Rheological parameter fitting curves

(b) Yield stress and plastic viscosity

Fig. 6.19 Effect of FA substitution on the rheological properties of UHDMC. Reproduced from Development of sprayable ultra-high ductility magnesium phosphate cement-based composites based on the rheological properties by Hu Feng with permission from Elsevier

PVA content. Plastic viscosity, on the other hand, displayed a rapid increase when the PVA content was below 1.0%, and a slower increase when the PVA content exceeded 1.0%. This phenomenon can be attributed to the water-absorbing property of PVA, which leads to a higher concentration of solid particles in the slurry and a thinner water film thickness on the surface of solid particles, resulting in an increased probability of collision and friction among solid particles. These combined effects lead to an increase in the rheological parameters (Grünewald & Walraven, 2001; Martinie et al., 2010). Based on considerations for optimal shootability factors, a PVA content of 2.0% was selected. At this content, the yield stress and plastic viscosity were 113.04 Pa and 4.95 Pa s, respectively.

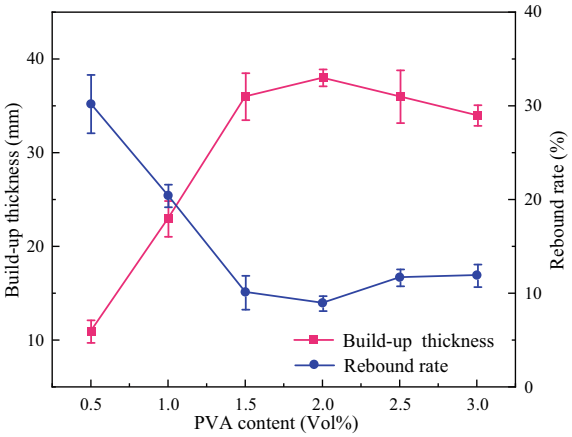

Fig. 6.20 Effect of PVA content on the shootability factors of UHDMC. Reproduced from Development of sprayable ultra-high ductility magnesium phosphate cement-based composites based on the rheological properties by Hu Feng with permission from Elsevier

6.3.2 *Relationship Between Shootability Factors and Rheological Parameters*

Figure 6.22 illustrates the fitting relationship between shootability factors and rheological parameters. In Fig. 6.22a, c, it is evident that the yield stress τ_0 and plastic viscosity η were both positively correlated with the build-up thickness T. The specific fitting equations for these relationships are provided in the following formulas Eqs. 6.5 and 6.6:

$$T = 0.01{\tau_0}^2 + 2.09\tau_0 - 53.08R^2 = 0.8698 \tag{6.5}$$

$$T = 0.207\eta^3 - 4.156\eta^2 + 27.904\eta - 28.360R^2 = 0.7249 \tag{6.5}$$

In Fig. 6.22b, d, it's evident that the yield stress τ_0 and plastic viscosity η were inversely correlated with the rebound rate R, as Pan has concluded (Pan et al., 2019), the specific fitting equations for these relationships are provided in the following formulas Eqs. 6.7 and 6.8:

$$R = 8.37e^{-5}{\tau_0}^2 - 0.03\tau_0 + 1.44R^2 = 0.8539 \tag{6.7}$$

$$R = 0.723\eta^{-1.186}R^2 = 0.6874 \tag{6.8}$$

In general, as the yield stress increases, the minimum stress required for the slurry to flow also increases. This increase in yield stress enhances the sag resistance of the slurry, leading to higher build-up thickness and lower rebound rates. When plastic viscosity increases, it means that the material becomes more resistant to deformation

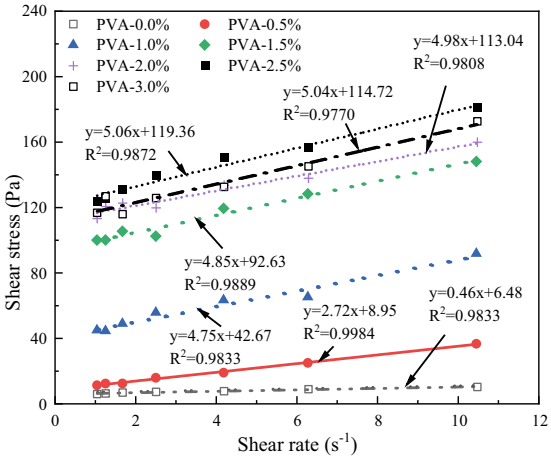

(a) Rheological parameter fitting curves

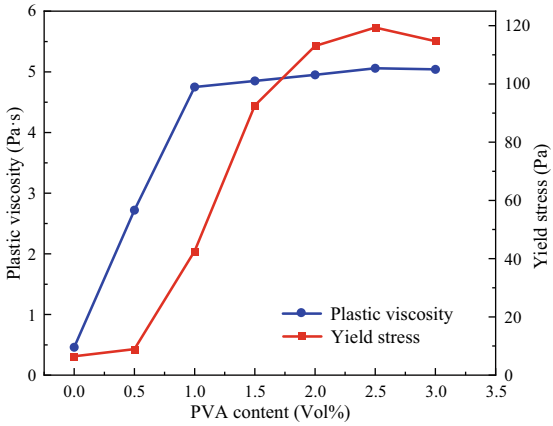

(b) Yield stress and plastic viscosity

Fig. 6.21 Effect of PVA content on the rheological properties of UHDMC. Reproduced from Development of sprayable ultra-high ductility magnesium phosphate cement-based composites based on the rheological properties by Hu Feng with permission from Elsevier

under external forces, and internal friction during material deformation also rises. This increased cohesion among materials leads to higher build-up thickness and reduced rebound rates. The optimal shootability is achieved when the yield stress falls in the range of 91.64–118.77 Pa and the plastic viscosity falls in the range of 4.85–7.17 Pa s, in which the ranges of build-up thickness and the rebound rate were 26–40 mm and 7.7–17.67%, respectively.

The inversely linear relationship between build-up thickness T and the rebound rate R, as demonstrated in Fig. 6.23 and formula Eq. 6.9, further corroborates the fitting equations obtained between shootability and rheological properties shown in Fig. 6.22. A same relationship has been verified by Yun et al. (2015a, 2015b).

$$R = -0.97T + 42.53R^2 = 0.7970 \tag{6.9}$$

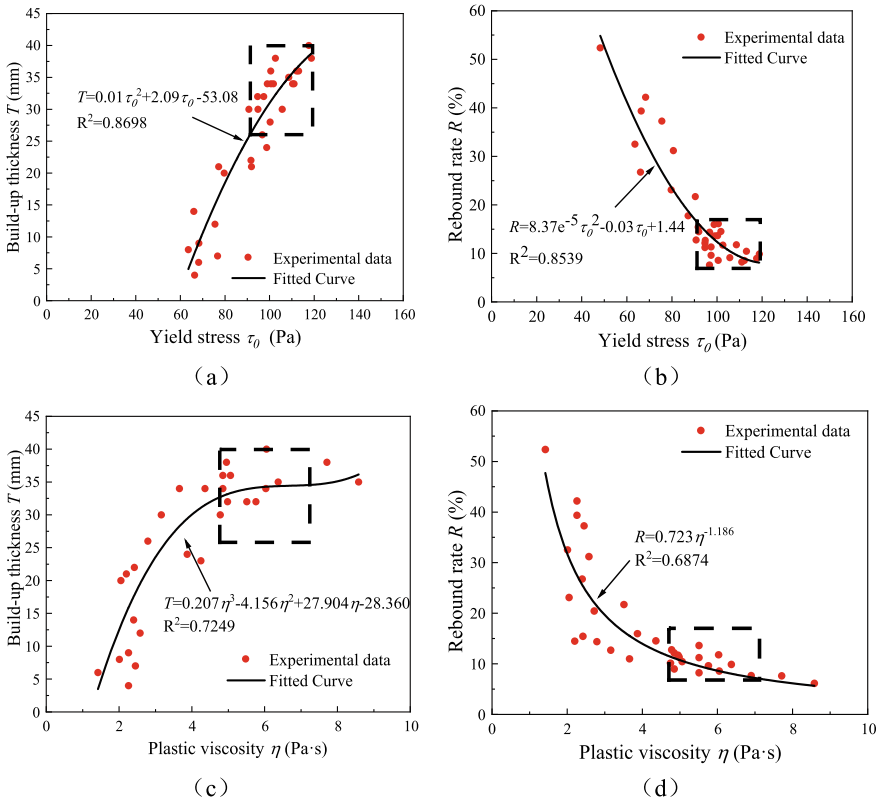

Fig. 6.22 Relationship between rheological parameters and shootability factors (Reproduced from Development of sprayable ultra-high ductility magnesium phosphate cement-based composites based on the rheological properties by Hu Feng with permission from Elsevier)

6.3.3 Factors Affecting Compressive Strength

(1) Effect of starch ether content

Figure 6.24 illustrates the compressive strength of the cast and sprayed UHDMC specimens with different starch ether contents. For cast specimens, the compressive strength decreased as the starch ether content increased. This trend is attributed to the retarding effect of starch ether on cement hydration, which leads to the formation of a thin waterproof polymer layer between latex and cement particles, hampering the development of the cement matrix (Glatthor, 2016). Conversely, for sprayed specimens, the compressive strength of specimens containing starch ether (except at 0.2%) was higher than that of the control group. This can be explained by the increased sag resistance imparted by starch ether, which shows an upward trend with the rising starch ether content within the range of 0–0.15% (Chunyuan et al., 2018; Feng et al., 2023). Furthermore, the strength gap between the cast and sprayed

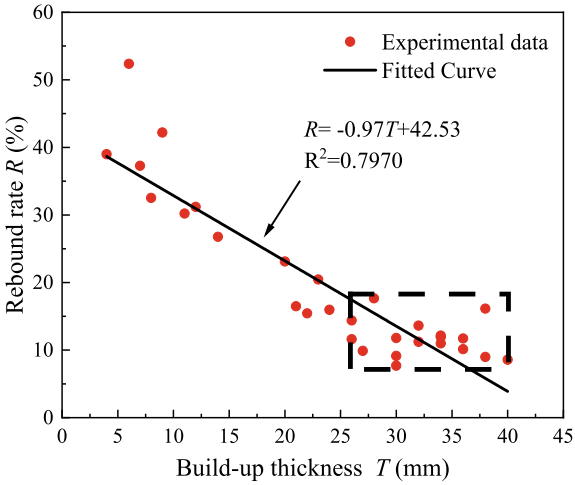

Fig. 6.23 Relationship between build-up thickness and the rebound rate. Reproduced from Development of sprayable ultra-high ductility magnesium phosphate cement-based composites based on the rheological properties by Hu Feng with permission from Elsevier

specimens decreased gradually. In fact, the compressive strength of the sprayed specimens with 0.15% starch ether content even surpassed that of the cast specimens, exceeding 35.0 MPa.

(2) **Effect of water–solid ratio**

Figure 6.25 illustrates the compressive strength of the cast and sprayed UHDMC specimens with different *W/S* ratios. As the *W/S* ratio increased from 0.12 to 0.15, the compressive strengths of the cast and sprayed specimens were decreased by 23 and 33%, respectively. However, the gap in compressive strength between cast and sprayed specimens was minimal when the *W/S* ratio ranged from 0.12 to 0.14. For sprayed specimen, at a *W/S* ratio of 0.15, the paste exhibited good fluidity but poor

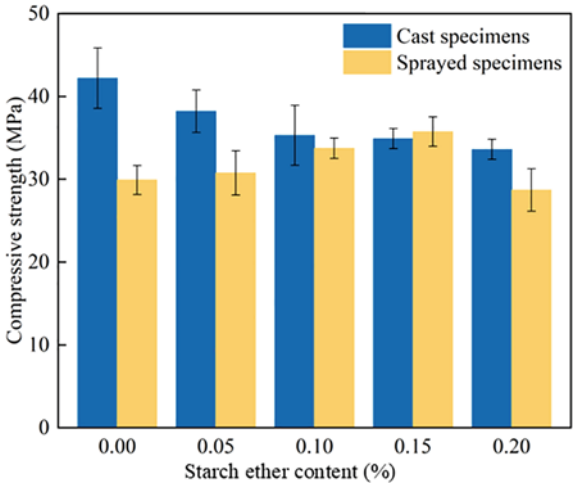

Fig. 6.24 Compressive strength of UHDMC with different SE contents

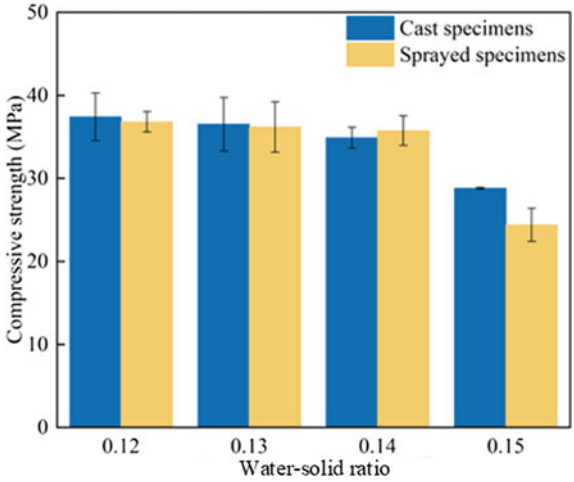

Fig. 6.25 Compressive strength of UHDMC with different W/B ratios

build-up thickness during spraying. Consequently, the compressive strength of the sprayed specimens was lower than that of the cast specimens. On the other hand, when the *W/S* ratio was 0.12, although the sprayed specimens had the highest compressive strength at 36.8 MPa, the paste's poor fluidity led to nozzle clogging issues during spraying. Therefore, maintaining the *W/S* ratio at 0.14 appears to strike a balance, resulting in UHDMC with better compressive strength and suitable fluidity for the spraying process.

(3) **Effect of powder-binder ratio**

Figure 6.26 displays the compressive strength of the cast and sprayed UHDMC specimens with different *P/B* ratios. Notably, the compressive strength of sprayed specimens decreased significantly, reaching a minimum of 17.2 MPa when the *P/B* ratio varied from 0.2 to 0.5. This decrease in compressive strength can be attributed to the reduction in the amount of K-struvite (MKP) generated by MPC, which results in a looser internal structure with the increase of the *P/B* ratio (Feng et al., 2021a, 2021b). Specifically, at a *P/B* ratio of 0.5, the reduction in compressive strength of sprayed specimens was as high as 40%. In addition, when the *P/B* ratio ranged from 0.2 to 0.4, there was little difference in compressive strength between the cast and sprayed specimens. However, when the *P/B* ratio exceeded 0.3, a noticeable "pulse" phenomenon occurred during the spraying process. Considering the need for a smooth and efficient spraying process, it's advisable to control the *P/B* ratio at 0.3.

(4) **Effect of *B/M***

Figure 6.27 displays the compressive strength of the cast and sprayed UHDMC specimens with different *B/M* ratios. For cast specimens, the compressive strength decreased as the *B/M* ratio increased. This decrease can be attributed to the retarding

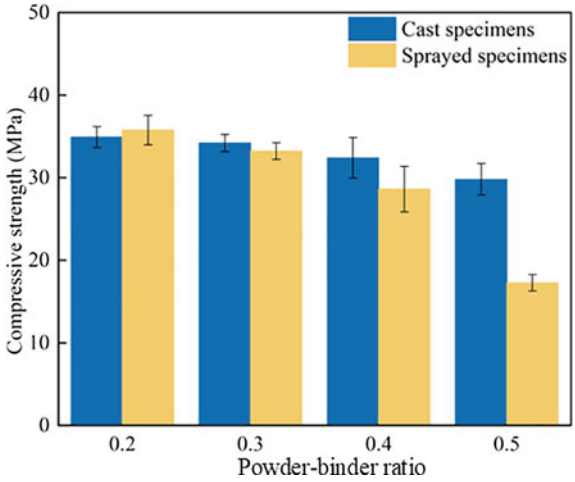

Fig. 6.26 Compressive strength of UHDMC with different *P/B* ratios

effect of borax on the hydration reaction between MgO and phosphate, which hinders the development of strength (Gelli et al., 2022). For sprayed specimens, the compressive strength initially increased and then decreased with the increase in *B/M* ratio. The highest compressive strength was achieved at 10% borax content. This phenomenon is explained by the effect of borax on defect reduction within sprayed specimens at an optimal borax content. However, at higher borax content, the undissolved borax particles negatively impact the bonding strength among the particles, resulting in reduced compressive strength (Fang et al., 2022). Taking into account the combined effects of borax on compressive strength and setting time of sprayed UHDMC, the optimal borax content was determined to be 8%.

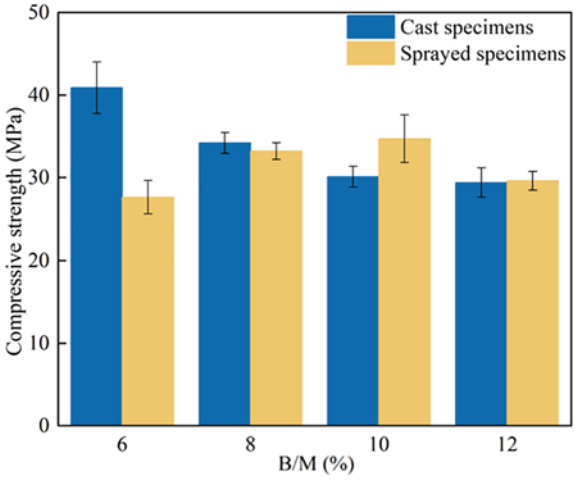

Fig. 6.27 Compressive strength of UHDMC with different *B/M* ratios

(5) **Effect of FA substitution**

Figure 6.28 displays the compressive strength of the cast and sprayed UHDMC specimens with different FA substitution. For cast specimens, the compressive strength initially increased and then decreased with the increase in FA content. The highest strength, approximately 39.1 MPa, was achieved at 20% FA content. For sprayed specimens, the compressive strength exhibited an increasing trend with the addition of FA content, reaching approximately 33.2 MPa at both 30 and 40% FA contents. Based on above analysis, whatever the cast or sprayed specimens, a same increasing trend below 20% FA content was shown. This initial increase can be attributed to the micro-aggregated filling effect and the formation of gelling substances, such as magnesium silicate (Li & Feng, 2011; Lin et al., 2010). These substances enhance the compressive strength by interweaving with the gelling substance (MKP) and solid particles in the matrix. However, this effect begins to diminish beyond 30% FA content, due to its reduction in hydration products and increasing porosity and looser internal structure. Therefore, the optimum FA content was selected at 40%.

(6) **Effect of PVA content**

Figure 6.29 illustrates the compressive strength of the cast and sprayed UHDMC specimens with different PVA fiber volume fractions (V_f). For both cast and sprayed specimens, the compressive strength exhibited a gradual increase as the PVA fiber volume fraction increased from 1.0 to 2.0%. However, an opposite trend was observed at 2.5% PVA fiber volume fraction. This was particularly pronounced for sprayed specimens, where excessive fiber content led to nozzle clogging and disrupted the spraying process. Agglomeration within magnesium phosphate cement-based materials can occur due to the poor dispersion of PVA fibers (Lee et al., 2002; Li et al., 1991), which might explain the decrease in strength at higher fiber fractions. In addition, the highest compressive strengths for cast and sprayed specimens were 36.5 and

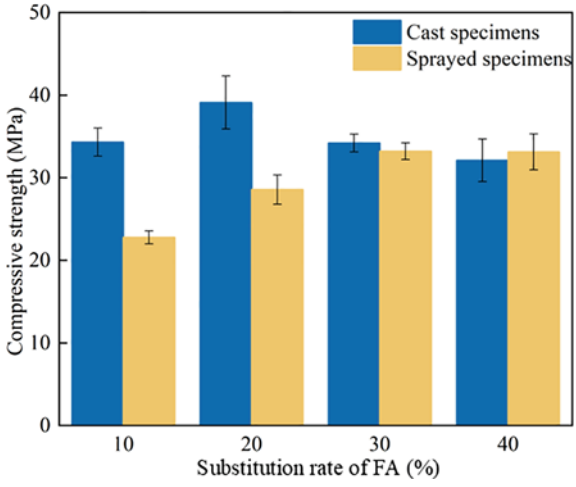

Fig. 6.28 Compressive strength of UHDMC with different FA substitutions

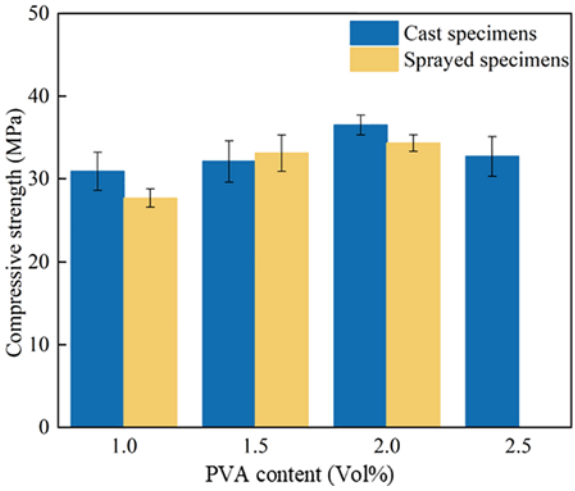

Fig. 6.29 Compressive strength of UHDMC with different PVA contents

35.9 MPa, respectively, both occurring at a 2% PVA fiber volume fraction. When comparing the compressive strengths of cast and sprayed specimens with PVA fiber volume fractions below 2%, there was only a small difference. Therefore, the addition of PVA fibers appeared to be more beneficial for sprayed specimens, as it increased build-up thickness and facilitated the formation of sprayed specimens. Based on this analysis, the optimal PVA fiber volume fraction was selected at 2.0%.

6.3.4 Factors Affecting Tensile Properties

(1) **Effect of starch ether content**

Figure 6.30 presents the tensile properties and crack diagrams of the cast and sprayed UHDMC samples with different starch ether contents. For both cast and sprayed specimens, the ultimate tensile stress and ultimate tensile strain initially increased and then decreased with increasing starch ether content. For cast specimens, the starch ether content had minimal effects on the ultimate tensile stress, with the maximum ultimate tensile stress recorded at 3.8 MPa with 0.10% starch ether content, accompanied by an ultimate tensile strain of 3.6%. For sprayed specimens, the highest tensile strain of 2.5% and ultimate tensile stress of 3.0 MPa were achieved with 0.15% starch ether content. The addition of starch ether can form a network structure by entangling hydrophobic and hydrophilic molecular chains in the pastes, which enhances the strength of the matrix and improves tensile properties (Huan et al., 2018). However, when the starch ether content exceeded 0.15%, the paste became too viscous, and the spraying process became discontinuous. Starch ether acted as a thickener in sprayed UHDMC, significantly improving the sagging resistance of

mortars. With starch ether content exceeding 0.15%, the UHDMC became difficult to spray, resulting in poor spraying effectiveness.

Figure 6.30c reveals that at 0.15% starch ether content, numerous tiny cracks were present in the cast samples. For sprayed specimens, due to the discontinuous spraying process and the occurrence of defects, a primary crack was observed when the sample was damaged.

(2) **Effect of water–solid ratio**

Figure 6.31 displays the tensile properties and crack diagrams of the cast and sprayed UHDMC specimens under different *W/S* ratios. The results show that the ultimate tensile strength and tensile strain were significantly improved within a *W/S* ratio of

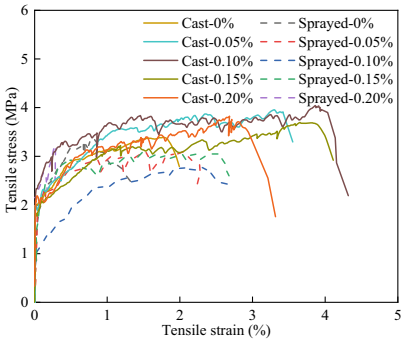

(a) Tensile stress-strain curve

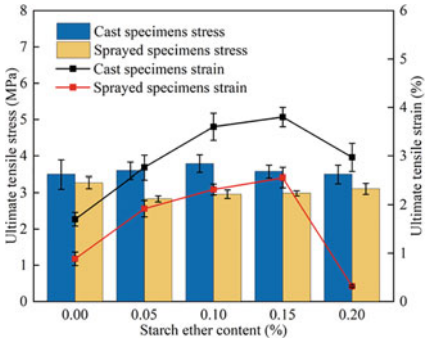

(b) Ultimate tensile strain and stress

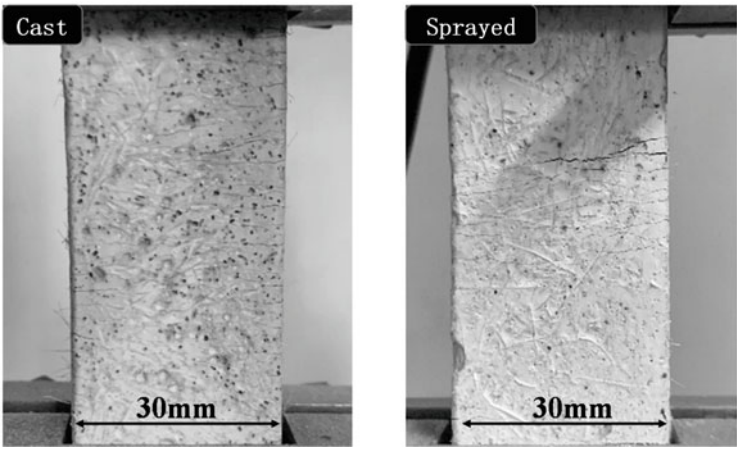

(c) Cracking diagrams of UHDMC with 0.15% SE

Fig. 6.30 Tensile properties and crack diagram of UHDMC with different SE contents. Reproduced from Mechanical properties of sprayable ultra-high ductility magnesium phosphate cement-based composites by Hu Feng with permission from Elsevier

0.14, reaching their maximum values at a *W/S* ratio of 0.14 (3.6 MPa and 3.8%, 3.0 MPa and 2.5%). A *W/S* ratio of 0.12 led to reduced mixed water content, low hydration of magnesium phosphate cement (MPC), and poor workability. As the *W/S* ratio increased, the workability of the pastes improved, making them more suitable for spraying into molds. However, excessive water increased the porosity of the paste, resulting in decreased tensile properties. Cast specimens exhibited better tensile properties than sprayed specimens, which might be attributed to quick hardening due to the prolonged spraying operation time. At a *W/S* ratio of 0.15, the increased free water content led to the formation of more pores within the MPC matrix and reduced cohesion between particles in the slurry (Botsis et al., 2012; Qiao et al., 2010). This decrease in cohesion resulted in reduced tensile properties of UHDMC.

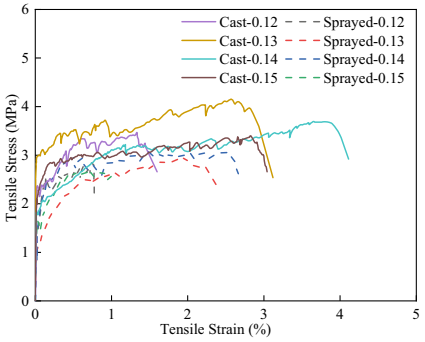

(a) Tensile stress-strain curve

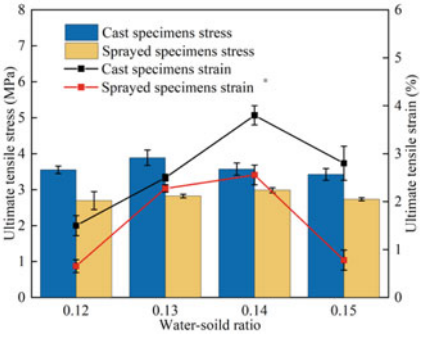

(b) Ultimate tensile strain and stress

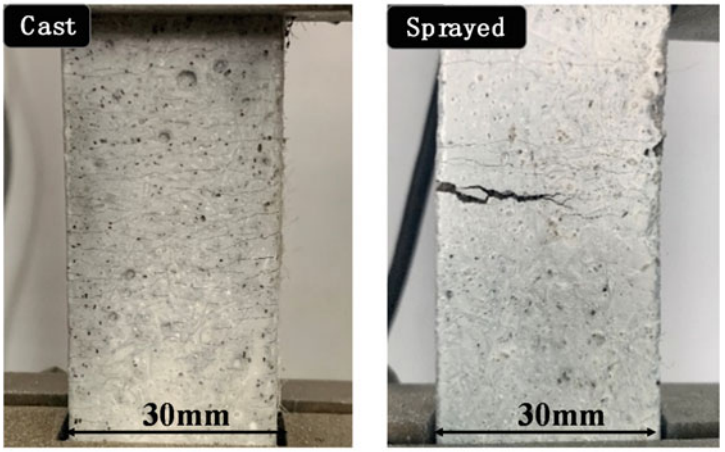

(c) Cracking diagrams of UHDMC with *W/S* of 0.14

Fig. 6.31 Tensile properties and crack diagram of UHDMC with different *W/S* ratios. Reproduced from Mechanical properties of sprayable ultra-high ductility magnesium phosphate cement-based composites by Hu Feng with permission from Elsevier

In Fig. 6.31c, when the *W/S* ratio was 0.14, the cast specimen exhibited relatively dense cracking. However, the sprayed specimens did not show multiple cracking characteristics, and larger cracks appeared when the specimens were damaged.

(3) **Effect of powder-binder ratio**

Figure 6.32 presents the tensile properties and crack diagrams of the cast and sprayed UHDMC specimens under different *P/B* ratios. The data indicate that the sprayed specimens were significantly affected when the *P/B* ratio varied from 0.2 to 0.4. The ultimate tensile stress reached its maximum value of 3.4 MPa, and the tensile strain was 3.9% at a *P/B* ratio of 0.3. For the cast specimens, at a *P/B* ratio of 0.4, the ultimate tensile strain reached 4.2%, and the ultimate tensile stress reached 3.7 MPa. The tensile properties of UHDMC were improved at the *P/B* ratio below 0.3. However, the increase in quartz powder content weakened the cementation of the MPC matrix, due to an increase of the probability of contact and collision between solid particles and a decrease of the consistency of the slurry (Qiao et al., 2010).

In Fig. 6.32c, when the *P/B* ratio was 0.3, there were many dense cracks in both the cast and sprayed specimens. The cracks in the cast specimens were uniformly distributed, while the cracks in the sprayed specimens were denser and less distributed at the bottom.

(4) **Effect of *B/M***

Figure 6.33 displays the tensile properties and crack diagrams of the cast and sprayed UHDMC specimens under different *B/M* ratios. For the cast specimens, the increase of borax gradually reduced the ultimate tensile strain and ultimate tensile stress. However, for the sprayed specimens, the tensile properties initially increased and then declined as the *B/M* ratio increased from 6 to 12%. When the *B/M* ratio was 8%, the ultimate tensile stress and strain reached the highest, presenting 3.4 MPa and 3.9%, respectively. And similar tensile properties were presented in the sprayed and cast UHDMC specimens. While a decrease of the ultimate tensile stress and strain was presented in both the cast and sprayed UHDMC specimens when the *B/M* ratio exceeded 8%. This phenomenon was attributed to the generation of cracks and defects in the hydration product K-struvite (MKP) caused by undissolved borax (Lin et al., 2016, Ming et al., 2010). From Fig. 6.33c, it can be observed that both presented a failure mode of multiple cracks.

(5) **Effect of FA substitution**

Figure 6.34 displays the tensile properties and crack diagrams of cast and sprayed UHDMC specimens under different FA contents. When the FA content was below 30%, the ultimate tensile stress and ultimate tensile strain both increased with the increase of FA content. And at the value of 30% FA, the ultimate tensile stress and tensile strain of sprayed specimens both reached a maximum value of 3.4 MPa, and 3.9%, respectively. While, for the cast specimens, they reached 3.8 MPa and 4.0%, respectively. It's evident that the use of FA improved the tensile properties of UHDMC. This improvement was attributed to FA, especially at lower content (below

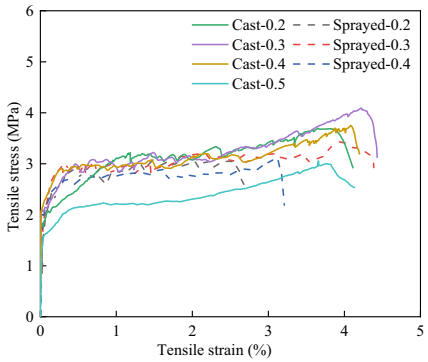

(a) Tensile stress-strain curve

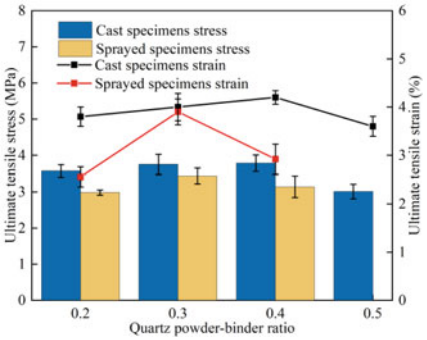

(b) Ultimate tensile strain and stress

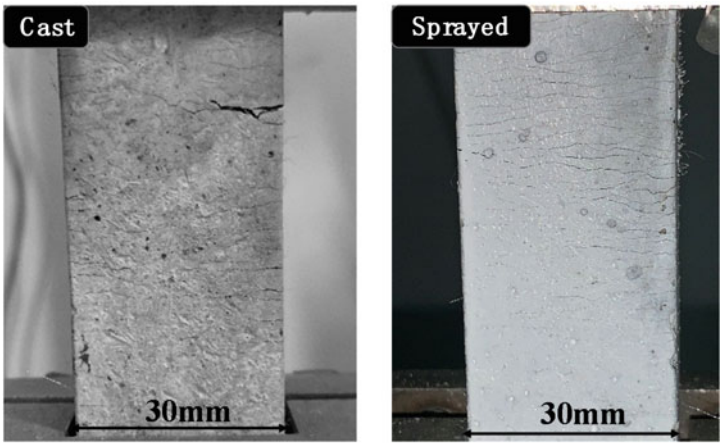

(c) Cracking diagrams of UHDMC with *P/B* of 0.3

Fig. 6.32 Tensile properties and crack diagram of UHDMC with different *P/B*. Reproduced from Mechanical properties of sprayable ultra-high ductility magnesium phosphate cement-based composites by Hu Feng with permission from Elsevier

30%), playing a filling role without reducing hydration products, reducing the pores between the fibers and matrix, and increasing friction, leading to an increase in tensile properties (Yi et al., 2014). However, the filling effect of FA couldn't compensate for the defects caused by the decrease in hydration products at high FA content (above 30%). This resulted in a decrease in tensile properties. Figure 6.34c shows that when 40% FA was used, both sprayed and cast specimens developed many microcracks in the middle of the specimens.

(6) **Effect of PVA content**

Figure 6.35 displays the tensile properties and crack diagrams of cast and sprayed UHDMC specimens under different PVA fibers volume contents (V_f) When V_f was

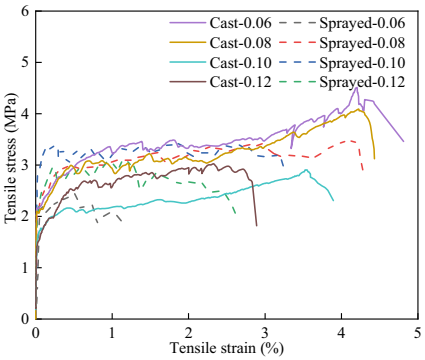

(a) Tensile stress-strain curve

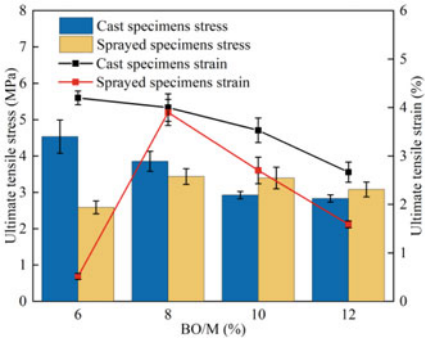

(b) Ultimate tensile strain and stress

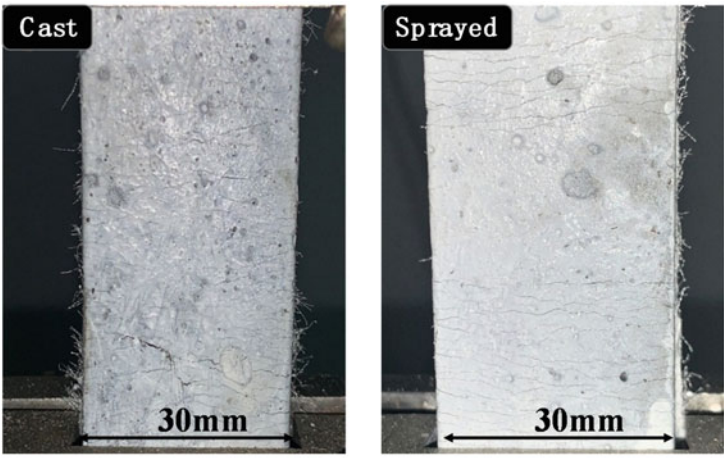

(c) Cracking diagrams of UHDMC with *B/M* of 8%

Fig. 6.33 Tensile properties and crack diagram of UHDMC with different *B/M*. Reproduced from Mechanical properties of sprayable ultra-high ductility magnesium phosphate cement-based composites by Hu Feng with permission from Elsevier

less than 2.0%, the ultimate tensile stress and tensile strain of the cast and sprayed specimens both increased with the increase of PVA fibers volume content. And at the value of 2.0% V_f, the ultimate tensile stress and tensile strain of sprayed specimens both reached a maximum value of 3.7 MPa, and 4.1%, respectively. While, for the cast specimens, they reached 4.2 MPa and 4.1%, respectively. However, when V_f reached 2.5%, the high PVA fibers content caused nozzle clogging during spraying, resulting in extremely poor tensile properties and making it impossible to prepare sprayed UHDMC samples (Ding et al., 2020; Lin, 2017).

Figure 6.35c shows that fewer cracks through observing the crack diagram of the cast and sprayed samples. This indicates similar strain-hardening characteristics. This phenomenon can be explained by the close ultimate tensile stress and ultimate

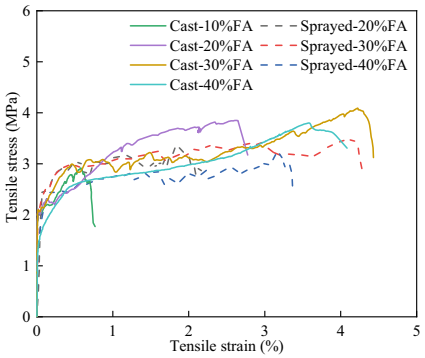

(a) Tensile stress-strain curve

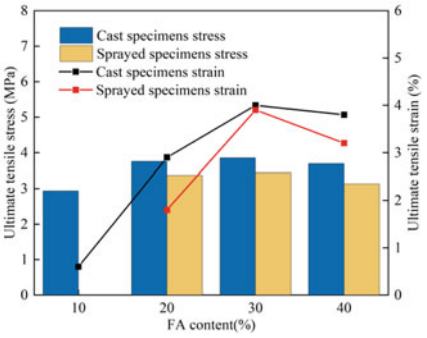

(b) Ultimate tensile strain and stress

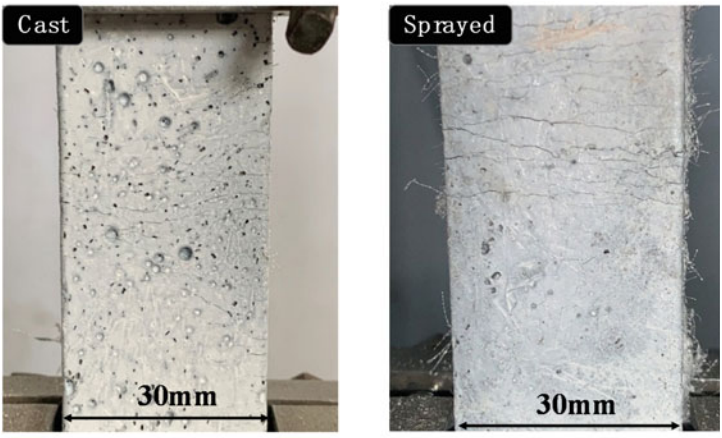

(c) Cracking diagrams of UHDMC with FA of 40%

Fig. 6.34 Tensile properties and crack diagram of UHDMC with different FA. Reproduced from Mechanical properties of sprayable ultra-high ductility magnesium phosphate cement-based composites by Hu Feng with permission from Elsevier

tensile strain of the cast and sprayed specimens at 2.0% V_f, with small gaps of 0.5 MPa and 0%, respectively.

6.3.5 Pore Structure Analysis

(1) **Pore structure parameters analysis**

Based on the mechanical properties, the samples with the optimal value of each variable (SE-0.15%, *W/S*-0.14, *P/B*-0.3, *B/M*-8%, FA-40%, PVA-2.0%) were selected to characteristic the pore structure. Considering the mix proportion of SE-0.15% and

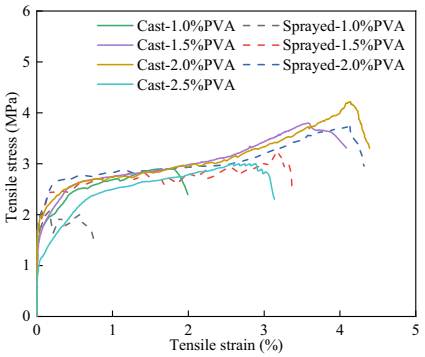

(a) Tensile stress-strain curve

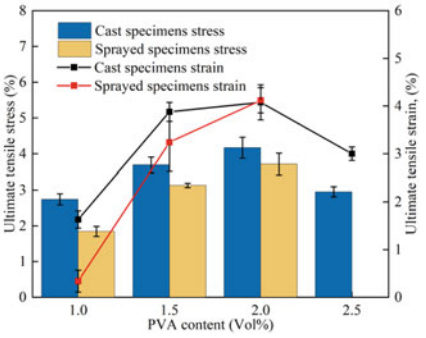

(b) Ultimate tensile strain and stress

(c) Cracking diagrams of UHDMC with V_f of 2.0%

Fig. 6.35 Tensile properties of UHDMC with different PVA content. Reproduced from Mechanical properties of sprayable ultra-high ductility magnesium phosphate cement-based composites by Hu Feng with permission from Elsevier

W/S-0.14 was the same, and the mix proportion of *P/B*-0.3 and BO/M-8% was the same. Therefore, four groups of samples were selected for pore structure analysis. Based on the Odler model, pore structures are classified into the following categories by pore size: (1) Gel pores (<10nm): These primarily affect the shrinkage and creep of cement-based materials. (2) Transition pores (10–100 nm): These mainly affect impermeability, shrinkage, and creep, and also have some influence on mechanical properties. (3) Capillary pores (100–1000 nm): These mainly affect impermeability and have some impact on mechanical properties. (4) Macropores (above 1000 nm): These are harmful and have adverse effects on material properties (Duan et al., 2013; Röβler & Odler, 1985). This simple pore classification can relate certain macroscopic properties of cement-based materials to the distribution of pores.

Figure 6.36 shows the Pore structure parameters of the cast and sprayed UHDMC. From Fig. 6.36a, it seems from that the sprayed UHDMC samples have slightly lower porosity compared to cast samples. From Fig. 6.36b, both sprayed and cast UHDMC have mainly macropores, capillary pores, and transition pores. The volume of macropores in sprayed UHDMC is smaller than in cast UHDMC, while the capillary pores show the opposite pattern. This indicated that the sprayed process gradually transforms the macropores into capillary pores.

Compared with SE-0.15% and *P/B*-0.3, changing the quartz powder content from 0.2 to 0.3 increased the proportion of macropores and decreased the proportion of capillary pores. This change in pore size distribution provides a reason for the decrease in compressive strength. However, the increase in quartz powder content

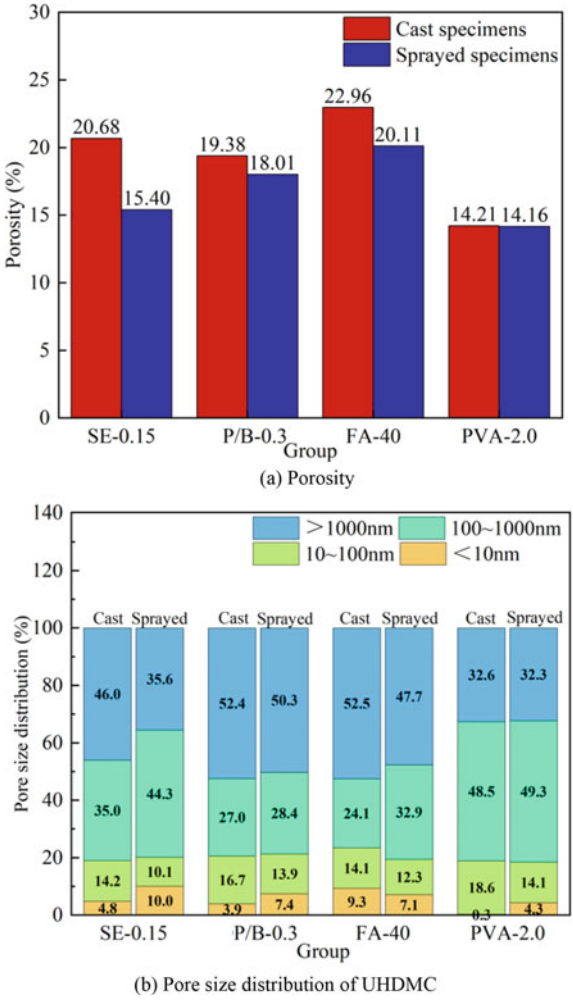

Fig. 6.36 Pore structure parameters of UHDMC. Reproduced from Mechanical properties of sprayable ultra-high ductility magnesium phosphate cement-based composites by Hu Feng with permission from Elsevier

improved the proportion of transition pores, leading to an increase in ultimate tensile strength.

Compared with *P/B*-0.3 and FA-40%, the pore size distribution between *P/B*-0.3 and FA-40% is similar, which explains the small differences in their compressive strength and tensile properties.

Compared with FA-40% and V_f-2.0%, the increase in PVA fibers significantly reduced the proportion of macropores and increased the proportion of transition pores. This is the main reason for the changes in compressive strength and ultimate tensile strength. When V_f was 2.0%, both sprayed and cast UHDMC had similar pore size distribution and porosity.

(2) **Relationship between pore structure and mechanical properties**

Figure 6.37 displays the correlation between mechanical properties and pore structure parameters. As confirmed by much of the literature (Chen et al., 2022; Zhang et al., 2022), gel pores primarily influence the shrinkage and creep of cement-based materials, exerting minimal impact on mechanical properties. Thus, their effect on mechanical properties can be disregarded. To establish a linear relationship with compressive strength and tensile strength, the porosity, macropores, capillary pores, and transition pores were considered. We selected the fitting results with $R^2 > 0.5$ for further analysis, as shown in Fig. 6.37. In Fig. 6.37a, b, c, it can be observed that compressive strength was chiefly associated with porosity, macropores, and capillary pores. Porosity and macropores exhibited a negative correlation with compressive strength, whereas a positive correlation was evident between compressive strength and capillary pores. The specific linear fitting equations are presented in the following formulas Eqs. 6.10, 6.11, and 6.12. In Fig. 6.37d, ultimate tensile stress was predominantly linked to transition pores, as indicated by the linear fitting equation in formula Eq. 6.13.

$$c = -0.43 * \mathrm{P} + 42.16\ \mathrm{R}^2 = 0.8128 \tag{6.10}$$

$$c = -0.16 * \mathrm{P}_{>1000\,\mathrm{nm}} + 41.39\ \mathrm{R}^2 = 0.7942 \tag{6.11}$$

$$c = 0.14 * \mathrm{P}_{100-1000\,\mathrm{nm}} + 29.19\ \mathrm{R}^2 = 0.8229 \tag{6.12}$$

$$f_t = 0.14 * \mathrm{P}_{10-100\,\mathrm{nm}} + 1.57\ \mathrm{R}^2 = 0.9202 \tag{6.13}$$

where c is compressive strength (MPa), f_t is ultimate tensile strength (MPa), P is porosity (%) and P_{xxx} is pore size ratio (%).

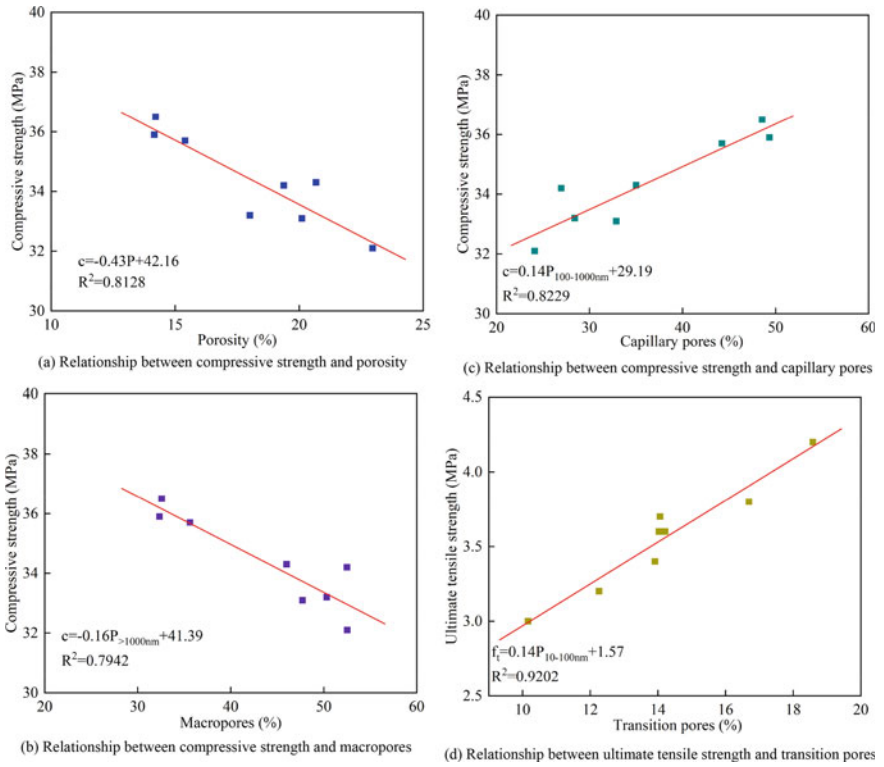

Fig. 6.37 Relationship between mechanical properties and pore structure parameters. Reproduced from Mechanical properties of sprayable ultra-high ductility magnesium phosphate cement-based composites by Hu Feng with permission from Elsevier

6.4 Conclusions

In this chapter, a comprehensive investigation into the influence of starch ether content, water–solid ratio, powder-binder ratio, borax content (*B/M*), FA substitution, and the volume content of PVA fiber on the shootability, rheological and mechanical properties of UHDMC are conducted on. Additionally, the correlation equations between shootability factors and rheological parameters. Additionally, the correlation equations between shootability factors and rheological parameters were developed. Furthermore, the compressive strength, tensile stress and tensile strain of the cast and sprayed UHDMC were compared and analyzed, taking into account the characteristics of pore structures measured using MIP. Through this study, some important conclusions are drawn as follow:

(1) Based on the well shootability, rheological and mechanical properties, the optimum mixture proportion of UHDMC was obtained, just as follows: M/P was 4, starch ether content was 0.15%, water–solid ratio was 0.14, powder-binder ratio was 0.3, borax content (*B/M*) was 8%, FA substitution was 40%, and the volume content of PVA fiber was 2%.
(2) Based on same spray parameters, the ranges of shootability factors and rheological parameters suitable for UHDMC were systematically obtained, in which the ranges of yield stress and plastic viscosity were 91.64–118.77 Pa and 4.85–7.17 Pa s, respectively, and the build-up thickness and the rebound rate were required 26–40 mm and 7.7–17.67%, respectively. These outcomes provide practical implication for the application of UHDMC in spray technology.
(3) The yield stress and plastic viscosity exhibit a positive correlation with build-up thickness while showing a negative correlation with rebound rate. To some extent, these rheological parameters can serve as indicators for characterizing shootability factors.
(4) Under the optimum mixture proportion of sprayed UHDMC, the build-up thickness was 38 mm, the compressive strength was 35.9 MPa, the tensile strength was 3.7 MPa, and the ultimate tensile strain was 4.1%. These properties indicate that the sprayed UHDMC meets the requirements of mechanical properties and ultra-high ductility of ECC.
(5) Compared with cast UHDMC, sprayed UHDMC exhibited a smaller proportion of large pores. The quartz powder can increase the proportion of macropores and decrease the proportion of capillary pores. Under the optimum mixture proportion, the sprayed and cast UHDMC had similar porosity and pore size distribution.
(6) A linear relationship was established between pore structure parameters and mechanical properties. The reduction of compressive strength was related with the porosity and macropores, while the increase of the ultimate tensile strength was related with the transition pores.

References

Abd El Megid, W. (2012). *Effect of rheology on surface quality and performance of SCC*. Université de Sherbrooke.

Austin, S., Peaston, C., & Robins, P. (1997). Material and fibre losses with fibre reinforced sprayed concrete. *Construction and Building Materials, 11*, 291–298.

Banfill, P. F. (2003). The rheology of fresh cement and concrete-a review. In *Proceedings of the 11th international cement chemistry congress* (Vol. 1, pp. 50–62).

Beaupre, D. (1994) Rheology of high performance shotcrete.

Bingham, E. C. (1922). *Fluidity and plasticity* (p. 2).

Botsis, J., Gmür, T., & Wisnom, M. R., et al. (2012). *Composites Part A: Applied Science and Manufacturing, 43*, 1629.

Chen, L., Ma, G., Liu, G., et al. (2019). Effect of pumping and spraying processes on the rheological properties and air content of wet-mix shotcrete with various admixtures. *Construction and Building Materials, 225*, 311–323.

Chen, Y., Liu, P., Sha, F., et al. (2022). Effects of type and content of fibers, water-to-cement ratio, and cementitious materials on the shrinkage and creep of ultra-high performance concrete. *Polymers, 14*, 1956.

Chunyuan, P., Guang, C., Xutao, Y., et al. (2018). Effect of cellulose ether and starch ether on properties of dry-mixed mortar. *GuangDong JianCai, 34*, 13–16.

Ding, C., Guo, L., & Chen, B. (2020). Orientation distribution of polyvinyl alcohol fibers and its influence on bridging capacity and mechanical performances for high ductility cementitious composites. *Construction and Building Materials, 247*, 118491.

Duan, P., Shui, Z., & Chen, W., et al. (2013). Effects of metakaolin, silica fume and slag on pore structure, interfacial transition zone and compressive strength of concrete. *Construction and Building Materials, 44*.

Dufour, J.-F., Trottier, J.-F., & Forgeron, D. (2006). Behaviour and performance of monofilament macro-synthetic fibres in dry-mix shotcrete. *Shotcrete for Underground Support, X*, 194–205.

Fang, B., Hu, Z., & Shi, T., et al. (2022). Research progress on the properties and applications of magnesium phosphate cement. *Ceramics International*.

Felekoğlu, B., Tosun, K., Baradan, B., et al. (2006). The effect of fly ash and limestone fillers on the viscosity and compressive strength of self-compacting repair mortars. *Cement and Concrete Research, 36*, 1719–1726.

Feng, H., Sheikh, M. N., Hadi, M. N., et al. (2018). Interface bond performance of steel fibre embedded in magnesium phosphate cementitious composite. *Construction and Building Materials, 185*, 648–660.

Feng, H., Sheikh, M. N., Hadi, M. N., et al. (2019). Pullout behaviour of different types of steel fibres embedded in magnesium phosphate cementitious matrix. *International Journal of Concrete Structures and Materials, 13*, 1–17.

Feng, H., Li, L., Zhang, P., et al. (2020). Microscopic characteristics of interface transition zone between magnesium phosphate cement and steel fiber. *Construction and Building Materials, 253*, 119179.

Feng, H., Nie, S., Guo, A., et al. (2021a). Flexural behavior of high ductility MPC-based composites under low-temperature curing. *Construction and Building Materials, 300*, 124231.

Feng, H., Li, Z., Wang, W., et al. (2021b). Deflection hardening behaviour of ductile fibre reinforced magnesium phosphate cement-based composite. *Cement and Concrete Composites, 121*, 104079.

Feng, H., Liang, J., Pang, Y., et al. (2022a). Effects of the fly ash and water glass on the mechanical properties and water stability of the high ductile magnesium phosphate cement-based composite. *Construction and Building Materials, 333*, 127395.

Feng, H., Li, L., Wang, W., et al. (2022b). Mechanical properties of high ductility hybrid fibres reinforced magnesium phosphate cement-based composites. *Composite Structures, 284*, 115219.

Feng, H., Nie, S., Guo, A., et al. (2022c). Evaluation on the performance of magnesium phosphate cement-based engineered cementitious composites (MPC-ECC) with blended fly ash/silica fume. *Construction and Building Materials, 341*, 127861.

Feng, H., Zheng, X., Yu, Z., et al. (2023). Development of sprayable ultra-high ductility magnesium phosphate cement-based composites based on the rheological properties. *Construction and Building Materials, 377*, 131113.

Feys, D., De Schutter, G., & Verhoeven, R. (2013). Parameters influencing pressure during pumping of self-compacting concrete. *Materials and Structures, 46*, 533–555.

Feys, D., Khayat, K. H., & Khatib, R. (2016). How do concrete rheology, tribology, flow rate and pipe radius influence pumping pressure? *Cement and Concrete Composites, 66*, 38–46.

Gelli, R., Tonelli, M., Martini, F., et al. (2022). Effect of borax on the hydration and setting of magnesium phosphate cements. *Construction and Building Materials, 348*, 128686.

Glatthor, A. (2016). Performance of starch ethers in drymix mortars. In *Proceedings of the XVIII international scientific conference. modern technologies of dry mixtures in construction.* MixBuild.

Grünewald, S., & Walraven, J. C. (2001). Parameter-study on the influence of steel fibers and coarse aggregate content on the fresh properties of self-compacting concrete. *Cement and Concrete Research, 31*, 1793–1798.

Haque, M. A., & Chen, B. (2019). Research progresses on magnesium phosphate cement: A review. *Construction and Building Materials, 211*, 885–898.

He, S., Lai, J., Wang, L., et al. (2020). A literature review on properties and applications of grouts for shield tunnel. *Construction and Building Materials, 239*, 117782.

Huan, Y., Benshan, Z., & Zhehui, Q. (2018). Application study of hydroxypropyl starch ether in cement-based putty. *New Building Materials, 45*, 129–132.

Huang, L., Sun, G., & Sun, Z. (2014). Effect of modified starch ether on the properties of fresh mortar. *New Building Materials*, 26–29.

Jiang, S., Shan, B., Ouyang, J., et al. (2018). Rheological properties of cementitious composites with nano/fiber fillers. *Construction and Building Materials, 158*, 786–800.

Jiao, D., Shi, C., Yuan, Q., et al. (2017). Effect of constituents on rheological properties of fresh concrete-A review. *Cement and Concrete Composites, 83*, 146–159.

Kaufmann, J., Frech, K., Schuetz, P., et al. (2013). Rebound and orientation of fibers in wet sprayed concrete applications. *Construction and Building Materials, 49*, 15–22.

Lee, Y., Lee, S., Youn, J., et al. (2002). Characterization of fiber orientation in short fiber reinforced composites with an image processing technique. *Materials Research Innovations, 6*, 65–72.

Leung, C. K., Lai, R., & Lee, A. Y. (2005). Properties of wet-mixed fiber reinforced shotcrete and fiber reinforced concrete with similar composition. *Cement and Concrete Research, 35*, 788–795.

Li, D. X., & Feng, C. H. (2011). Study on modification of the magnesium phosphate cement-based material by fly ash. *Advanced Materials Research, 150*, 1655–1661.

Li, V. C., Wang, Y., & Backer, S. (1991). A micromechanical model of tension-softening and bridging toughening of short random fiber reinforced brittle matrix composites. *Journal of the Mechanics and Physics of Solids, 39*, 607–625.

Li, Y., Sun, J., & Chen, B. (2014). Experimental study of magnesia and M/P ratio influencing properties of magnesium phosphate cement. *Construction and Building Materials, 65*, 177–183.

Li, V. C., Fischer, G., & Lepech, M. D. (2009) Shotcreting with ECC.

Li, P., Zhou, Z., & Chen, L., et al. (2019). Research on dust suppression technology of shotcrete based on new spray equipment and process optimization. *Advances in Civil Engineering.*

Li, V. C. (2019). Engineered cementitious composites (ECC): bendable concrete for sustainable and resilient infrastructure.

Li, X. (2021). Research on the influence of different fibers on the early performance of magnesium phosphate cement mortar. *Railway Construction Technology.*

Lin, W., Sun, W., & Li, Z.-J. (2010). Study on the effects of fly ash in magnesium phosphate cement.

Lin, Q. H., Yan, G., & Li, B. W., et al. (2016). Effect of borax on compressive strength of magnesium phosphate cement. *Bulletin of the Chinese Ceramic Society, 35*, 4252–4255+4260. https://doi.org/10.16552/j.cnki.issn1001-1625.2016.12.060

Lin, T. (2017). Research on mechanical properties of fiber reinforced magnesium-potassium phosphate cement mortars. Chinese. *J. Fuzhou Univ. (Natl. Sci. Ed.), 45*, 528–534.

Liu, X., Li, Q., & Wang, L., et al. (2021). cBonding behavior of spray-based 3D printing magnesium phosphate cement and concrete. *Portland Bulletin, 40*,18.

Ma, C., Wang, F., Zhou, H., et al. (2021). Effect of early-hydration behavior on rheological properties of borax-admixed magnesium phosphate cement. *Construction and Building Materials, 283*, 122701.

Martinie, L., Rossi, P., & Roussel, N. (2010). Rheology of fiber reinforced cementitious materials: Classification and prediction. *Cement and Concrete Research, 40*, 226–234.

Ming, Y. J., Xiang, Q. C., & Xiang, J. B. et al. (2010). Effects of retardant borax on hydration and harden process of magnesia-phosphate cement pastes. *Journal of Materials Science and Engineering, 28*, 31–35+75.https://doi.org/10.14136/j.cnki.issn1673-2812.2010.01.030

Mikanovic, N., & Jolicoeur, C. (2008). Influence of superplasticizers on the rheology and stability of limestone and cement pastes. *Cement and Concrete Research, 38*, 907–919.

Mo, L., Lv, L., Deng, M., et al. (2018). Influence of fly ash and metakaolin on the microstructure and compressive strength of magnesium potassium phosphate cement paste. *Cement and Concrete Research, 111*, 116–129.

Ning, F. W., Cai, Y. B., Bai, Y., et al. (2019). Research on rebound rate of nano-scale admixture wet-mix shotcrete. *IOP Conference Series: Materials Science and Engineering, 678*, 012109.

Pan, G., Li, P., Chen, L., et al. (2019). A study of the effect of rheological properties of fresh concrete on shotcrete-rebound based on different additive components. *Construction and Building Materials, 224*, 1069–1080.

Papo, A., & Piani, L. (2004). Effect of various superplasticizers on the rheological properties of Portland cement pastes. *Cement and Concrete Research, 34*, 2097–2101.

Peng, J., Peng, C., Chen, G., et al. (2018). Effect of cellulose ether and starch ether on performance of dry mixed mortar. *Guangdong Building Materials, 8*

Qiao, F., Chau, C., & Li, Z. (2010). Property evaluation of magnesium phosphate cement mortar as patch repair material. *Construction and Building Materials, 24*, 695–700.

Röβler, M., & Odler, I. (1985). Investigations on the relationship between porosity, structure and strength of hydrated portland cement pastes I. Effect of porosity. *Cement and Concrete Research, 15*, 320–330.

Standard, A. (2008). ASTM C109-standard test method for compressive strength of hydraulic cement mortars. ASTM International, West Conshohocken.

Vance, K., Kumar, A., Sant, G., et al. (2013). The rheological properties of ternary binders containing Portland cement, limestone, and metakaolin or fly ash. *Cement and Concrete Research, 52*, 196–207.

Xiong, Z., Ou, Z., & Wang, J., et al. (2018). Influence of hybrid PVA fibers on the fluidity and mechanical properties ofsprayed ultra high toughness cementitious composites. *Concrete,* 71–73.

Xu, B., Ma, H., & Li, Z. (2015). Influence of magnesia-to-phosphate molar ratio on microstructures, mechanical properties and thermal conductivity of magnesium potassium phosphate cement paste with large water-to-solid ratio. *Cement and Concrete Research, 68*, 1–9.

Xu, B., Lothenbach, B., & Ma, H. (2018). Properties of fly ash blended magnesium potassium phosphate mortars: Effect of the ratio between fly ash and magnesia. *Cement and Concrete Composites, 90*, 169–177.

Xu, S., Mu, F., Wang, J., et al. (2019). Experimental study on the interfacial bonding behaviors between sprayed UHTCC and concrete substrate. *Construction and Building Materials, 195*, 638–649.

Yang, J., & Qian, C. (2010). Effect of borax on hydration and hardening properties of magnesium and pottassium phosphate cement pastes. *Journal of Wuhan University of Technology-Materials Science Edition, 25*, 613–618.

Yang, Q., & Wu, X. (1999). Factors influencing properties of phosphate cement-based binder for rapid repair of concrete. *Cement and Concrete Research, 29*, 389–396.

Yi, H., Yi, Z., Lu, J., et al. (2014). Failure mechanism of magnesia-phosphate cement under low temperature curing condition. *Bulletin of the Chinese Ceramic Society, 33*, 197–201.

Yu, H., Zhang, B., & Qu, Z. (2018). Application study of hydroxypropyl starch ether in cement-based putty. *New Building Materials, 45*, 129–132.

Yun, K.-K., Choi, P., & Yeon, J. H. (2015a). Correlating rheological properties to the pumpability and shootability of wet-mix shotcrete mixtures. *Construction and Building Materials, 98*, 884–891.

Yun, K.-K., Choi, S.-Y., & Yeon, J. H. (2015b). Effects of admixtures on the rheological properties of high-performance wet-mix shotcrete mixtures. *Construction and Building Materials, 78*, 194–202.

Yun, K.-K., Choi, P., & Yeon, J. H. (2018). Rheological characteristics of wet-mix shotcrete mixtures with crushed aggregates and mineral admixtures. *Ksce Journal of Civil Engineering, 22*, 2469–2479.

Yun, K. K., Kim, J. B., Song, C. S., et al. (2022). Rheological behavior of high-performance shotcrete mixtures containing colloidal silica and silica fume using the bingham model. *Materials, 15*, 428.

Zhang, Z., & Zhang, Q. (2017). Self-healing ability of Engineered Cementitious Composites (ECC) under different exposure environments. *Construction and Building Materials, 156*, 142–151.

Zhang, L., Lin, G., Qian, X., et al. (2022). Unveil the role of nano-$CaCO_3$ in early shrinkage and tensile properties of cement paste: From experimental work to modeling. *Composites Part b: Engineering, 243*, 110185.

Zhu, H., Zhang, D., Wang, T., et al. (2020). Mechanical and self-healing behavior of low carbon engineered cementitious composites reinforced with PP-fibers. *Construction and Building Materials, 259*, 119805.